Enhancing Osseointegration and Preventing Implant-Associated Infections Through Biomimetic Nano-Modifications

By

Richard Bright

BSc. Hons. MSc Applied Science (Immunology)

Thesis

Submitted to Flinders University

for the degree of

Doctor of Philosophy (PhD)

College of Medicine and Public Health

25/01/2024

TABLE OF CONTENTS

ABSTRACT

The increasing need for titanium-based implants has caused a rise in implant-related infections and inadequate integration. To tackle this problem, scientists are creating new anti-infective technologies that can reduce the risk of infection and enhance host integration. These technologies involve the use of antimicrobial coatings, nanomaterials, and drug-eluting coatings. The implementation of these technologies is anticipated to enhance the safety and effectiveness of implants based on titanium, thereby leading to improved outcomes for patients. Scientists are drawing inspiration from the intricate nanostructures present on the wings of cicadas and dragonflies to design synthetic materials capable of eradicating bacteria upon contact. By imitating and enhancing these nanostructures, researchers can develop materials that exhibit superior antibacterial properties and facilitate bone integration. Several methods have been employed to replicate and enhance the natural antimicrobial characteristics of these surfaces, paving the way for the creation of materials that hold promise in addressing these concerns. Alkaline hydrothermal etching is a process used to etch a variety of materials, such as titanium, silicon, and other semiconductor materials. The process entails submerging the material in a heated alkaline solution, commonly sodium hydroxide (NaOH) or potassium hydroxide (KOH). The alkaline solution initiates a reaction with the material, leading to its controlled dissolution. The etching rate is typically regulated by modifying the temperature and concentration of the alkaline solution. This research project aimed to evaluate the applicability of hydrophilic hydrothermally etched nanostructured surfaces for use in orthopedic and dental implants. The investigation focused on strategies to enhance, suppress, or shape the immune response, as they are crucial in various biomedical applications, including biomaterials. The project's objective was to further examine the viability of implementing a hydrothermally etched nanomodified surface on titanium-based implants, to reduce implant-related infections and improve osteointegration.

DECLARATION

I certify that this thesis:

1. does not incorporate without acknowledgment any material previously submitted for a degree or diploma in any university

2. and the research within will not be submitted for any other future degree or diploma without the permission of Flinders University; and

3. to the best of my knowledge and belief, does not contain any material previously published or written by another person except where due reference is made in the text.

Richard J Bright
Date 25/01/2024

ACKNOWLEDGEMENTS

This thesis would not have been possible without the invaluable help and support of many people. I would like to express my sincere gratitude to my supervisor Professor Krasimir Vasilev, for his direction, advice, and guidance throughout my research, and his immense patience and enthusiasm. Thank you for giving me the personal space to develop myself. I would also like to thank Professor David Haynes and Dr Dennis Palms for their invaluable input and feedback on my work. Their comments and suggestions were crucial to the successful completion of this project. I would also like to acknowledge the entire Vasilev group, Biomedical Nanoengineering Laboratory for their support and contributions. I am extremely thankful for the funding and in-kind support from Corin Australia and Flinders University, College of Medicine and Public Health. I would also like to acknowledge the instruments and scientific and technical assistance of Microscopy Australia and ANFF. I am deeply grateful to my family and friends for their unconditional love and support throughout this process. Finally, I thank all the people who have been part of my journey, directly or indirectly and have helped me reach this milestone.

My heartfelt gratitude to all of you!

CHAPTER 1:

1. INTRODUCTION:

Enhancing Osseointegration and Preventing Implant-Associated Infections Through Biomimetic Nano-Modifications

Abstract

Bio-inspired nanomaterials are materials that are designed and synthesized based on the structures and functions of biological systems. These materials have unique properties, such as high strength, flexibility, and biocompatibility, making them suitable for various applications in fields such as medicine, energy, and electronics. Bio-inspired nanomaterials are often made through bottom-up approaches, such as self-assembly or template-assisted methods, and they mimic the hierarchical structures and functions found in nature. The development of these materials has been facilitated by advances in nanotechnology and materials science, leading to new possibilities for the creation of sustainable and environmentally friendly products. Orthopedic and dental surgeries often employ commercially pure titanium and its alloys due to their exceptional mechanical properties, chemical stability, and biocompatibility. However, successful bone healing and regeneration after implant surgery can be challenging, as foreign body reactions and implant-related infections can impede the process. The fate of a biomaterial is determined by a cascade of events that take place immediately after surgical implantation. The initial interactions between proteins, blood components, and the implant surface influence the formation of a clot. Platelets respond to the foreign surface by adhering, spreading, aggregating, and undergoing intracellular and biochemical changes. The fibrin clot acts as a scaffold, known as osteoconduction, facilitating the migration and differentiation (osteoinduction) of osteogenic cells within the healing area. These cells produce osteoid tissue and new woven bone, which eventually remodels into lamellar bone directly in contact with the implant surface, promoting osteointegration. The development of a bioinspired hydrothermally etched nanosurface with dual properties, including antibacterial effects and improved osteoconduction, holds promise in preventing prosthetic implant infections and facilitating favourable bone healing around the implant.

1.1 Background

Enhancing osseointegration and preventing infection through nanomodifications have gained significant importance in the medical field, as they have the potential to enhance implant success rates. Ongoing research is focused on studying and developing bioinspired nanomodifications to mitigate infection risks and improve the overall success of implants. This review aims to explore the current advancements in nanomodifications and their applicability in enhancing the success of osseointegrated implants. Additionally, it will address the associated challenges with this technology and discuss the potential for future advancements. Osseointegration refers to the process of securely attaching a medical device, such as an implant, to living bone [1]. This process involves the natural process of bone remodelling and formation, as well as the formation of a bond between the implant and the living bone. This bond is highly durable and can last for a long time, depending on the material and the patient's health.

Nano modifications are modifications made to the surface of an implant to improve its success rate [2]. These modifications can be made in a variety of ways, such as coating the implant with a nano-layer or using nanoscale particles to control the surface properties of the implant. This technology is becoming increasingly popular as it can provide greater control of the implant surface, leading to improved implant success rates. The use of nanomodifications to enhance osseointegration and prevent infection has been studied extensively in the past few years [3]. Studies have shown that nano modifications can provide greater control of the implant surface and lead to improved implant success rates [4]. Studies have also shown that nano modifications can reduce the risk of infection by providing a more uniform surface, as well as by reducing the surface area for bacteria to attach to [4]. One of the most common nanomodifications used to enhance osseointegration is the use of nano-coatings. These coatings are typically made from biocompatible materials, such as titanium dioxide or hydroxyapatite. These coatings can provide a uniform surface and can also help to reduce the risk of infection by providing a barrier between the implant and the surrounding tissue. Another type of nano modification is the use of nanoscale particles to control the surface properties of the implant. These particles can be used to control the hydrophobicity, roughness, and other surface properties of the implant [5, 6]. By controlling these properties, the implant can be more effectively osseointegrated and can also reduce the risk of infection.

Although nanomodifications have the potential to improve the success of implants, there are still many challenges associated with this technology. One of the main challenges is the difficulty of controlling the surface properties of the implant. As the nano-coatings and particles are so small, it is difficult to accurately predict how they will affect the surface properties of the implant. Additionally, the cost of these modifications can be high and there is a risk of damage to the implant if the modifications are not done appropriately. One more challenge is the lack of data on the long-term effects of these modifications.

As the technology is still relatively new, there is limited data on the long-term effects of nanomodifications on osseointegration. It is also unclear how these modifications will interact with the patient's body over time. Nano modifications have the potential to enhance osseointegration and reduce the risk of infection. However, there are still challenges associated with this technology, such as the difficulty of controlling the surface properties of the implant and the lack of data on the long-term effects of these modifications. Despite these challenges, nano modifications have the potential to dramatically improve the success of implants and reduce the risk of infection in the future.

With the rapid development of biomaterials and medical implants, titanium (Ti) [7], and its alloys have been widely used in applications such as skeleton structure fixation, joint function repair implants [8, 9] dental implants [10-12]. Due to its exceptional mechanical properties, chemical stability and good biocompatibility, Ti has been widely used for implant manufacturing for decades [8, 13, 14]. Biofilm-associated orthopaedic implant infections (IAI) are clinically important due to the morbidity, significant expense for follow-up healthcare, quality of life and socioeconomic burden that they cause [15]. Unquestionably, implant materials play a pivotal role in orthopaedic diseases and their infection risk [16-18]. The global infection rate for orthopaedic implants is 2-5% [19], however as high as 30% in open fractures [20, 21], and is expected to significantly increase due to ageing [22, 23].

The common causative agents responsible for IAI are *Staphylococcus aureus* and *Staphylococcus epidermidis* [15, 24], normally part of the skin micro-flora [25]. Biofilm secret an organic matrix known as extra polymeric substance (EPS), responsible for the protection, host evasion and adhesion of biofilms to both organic and inorganic surfaces [26]. Remarkably, biofilm evades the host immune response by several mechanisms including acting as a physical barrier, actively suppressing the proinflammatory host immune cells, and activating or suppressing genetic response regulators [27, 28]. IAI is difficult to treat with systemic antibiotics, having a diminishing effect (up to 1000X more resistant), with obvious cytotoxic consequences to the patient if high dose regimes are required [29-31]. Together with a self-perpetuating inflammatory response, IAI is problematic to treat with the last resort being surgical revision, which may lead to further complications [32].

Surface modifications aimed at modulating the host immune system to mitigate inflammation and promote osteointegration can be a valuable approach in addressing infection rates. By facilitating the rapid colonization of the surface by host cells, the risk of bacterial colonization and persistent infections, also known as the "race to the surface," [10] can be mitigated. Such modifications have the potential to create a more favourable environment that discourages bacterial colonization and facilitates successful integration of the implant [33-35]. In the realm of orthopedic and dental implants, a surface modification that possesses both antibacterial properties and promotes osteointegration would offer significant advantages.

However, this dual functionality can be considered a "double-edged sword." Following the invasion of exogenous pathogens, the immune response becomes a crucial factor in determining the level of inflammation and the subsequent healing process at the implantation site. The specific types of host immune cells recruited to the site play a pivotal role in shaping these responses [36-40].

An attractive approach may be the development of antibacterial/osteogenic characteristics directly on the surface of the biomaterial currently used in the clinic [41]. Evidence suggests that to achieve a lasting relationship between the implant and the host, Ti implants must have an optimal surface [42], and there must be an adequate healing capacity of the host [43, 44].

Monocytes/macrophages play a crucial role in the initial interaction with orthopedic and dental implants, setting the stage for subsequent events that influence the performance of osseointegration. Recent studies have highlighted the significant impact of M1/M2 macrophage phenotypes on this process [45, 46]. Our comprehension of the immune response and the eventual fate of implantable biomaterials is not thoroughly understood, particularly in terms of understanding how the physicochemical properties can be modified to achieve a favorable outcome. In this review, the emphasis will be on exploring the immunomodulatory properties of Ti surfaces. Additionally, the potential of nano-level surface modifications to enhance these factors will be discussed, with the goal of improving osteointegration and mitigating biofilm-associated infections.

1.2 Strategies Using Biomimetics for Medical Implants

In recent years, there has been a surge of research focused on biomaterial design, aiming to create implantable materials that closely mimic the properties of natural substances. This approach, known as biomimicry or biomimetics, draws inspiration from the remarkable regenerative capabilities of bone and its unique characteristics throughout the healing process. By incorporating these aspects into biomimetic biomaterial design, researchers aim to develop materials that closely resemble the natural healing properties of bone [47]. The development of implant materials with osteoconductive, anti-inflammatory and angiogenic potential, with suitable physicochemical and mechanical properties, poses a great challenge for researchers [48]. Interestingly, over the last twenty years, there has been immense attention on bioinspired surfaces for medical implants such as lotus leaves [49], shark [50], gecko skin [51], and cicada wings [52, 53] showing remarkable antibacterial/antibiofouling properties. Interestingly, there is limited research on the osteogenic capabilities of such surfaces.

1.2.1 Surface Modification on Ti Implants

The advantageous properties of Ti, including exceptional corrosion resistance and compatibility with hard tissues, establish it as a favoured material in the field of bioengineering. These qualities make Ti highly desirable for various bioengineering applications [54]. Additionally, the application of Ti can be extended when alloyed with other elements, such as aluminium and vanadium. The most used biomaterials are commercially pure (CP-Ti), Ti6Al7Nb and Ti-6Al-4V-an alpha-beta Ti alloy with high specific strength and excellent corrosion resistance [8]. While Ti and its alloys are sought for their bulk material/chemical properties their surface characteristics can pose challenges. One major challenge is the inability to interact with the surrounding host tissue, known as biocompatibility.

Without proper implant-host tissue integration, a fibrotic layer-foreign body response may form at the interface [55], resulting in loosening and device failure [56, 57].

To tackle the challenge of insufficient integration and hindering biofilm attachment, modifications to the surface morphology or chemistry have been explored. The aim is to enhance integration and facilitate favourable cellular interactions. Implant surfaces have been engineered with functionalized surfaces, modified chemistry, and micro/nano-sized pores or structures to promote cell growth and improve biocompatibility on the implant surface. The structure and chemistry of the surface play a critical role in governing cellular adhesion, differentiation, as well as gene and protein expression. By optimizing these factors, researchers seek to enhance the overall performance and biocompatibility of implant surfaces [58]. Both the physical aspects and the chemistry of the material surface are of utmost importance when it comes to the functionality of biomaterials. These factors play a crucial role in determining the performance and effectiveness of biomaterials in various applications.

1.2.3 Physical Modifications

Physical modifications affect the topography, however, cause little or no change to the chemistry such as plasma spraying [59], nano-3D printing [60], grit-blasting [61], acid/alkaline etching [62, 63], electron beam lithography [64] and machining [54]. Most physical modification techniques are cost-effective and relatively straightforward compared to the chemical modifications mentioned below. These physical modifications offer a practical and accessible approach to altering biomaterial properties.

1.2.4 Chemical Modifications of the Implant Surface

Chemical modification of the implant surface involves altering its chemical properties to promote specific interactions between cell surface molecules and the implant surface, resulting in improved healing and osteointegration outcomes. However, it is important to note that many chemical modification techniques are intricate in their preparation and tend to be costly. Despite their complexity and expense, these techniques hold promise in enhancing the performance and integration of implants. The current implant surface research focuses on composition control, multilayer structural design, multi-scale coatings, or coatings with novel surface morphologies [65]. Some well know techniques include plasma and chemical vapour deposition [66, 67], atomic layer deposition [68], and electrochemical deposition [69]. Chemical treatments can result in surface functionalization [70], ion infusion, single/multilayer coatings [6, 71] and oxidizing the surface [72, 73].

1.3 Factors Affecting Biocompatibility

While several crucial factors have been identified, the precise parameters necessary to promote osseointegration are still being investigated. The quest to uncover the exact requirements for optimal osseointegration is ongoing, with researchers continuously working to expand our understanding in this field. *Figure 1* demonstrates factors that affect the biocompatibility of implantable devices for hard tissue implants. Surface chemistry plays a significant role in determining the biocompatibility of material, including factors such as the choice of material, its treatment or modification, and its interactions with host cells and tissues. These aspects have a direct influence on the material's ability to interface effectively with the biological environment and promote favourable biological responses.

1 Surface Roughness: Roughness of the material surface can influence the adhesion of cells and tissue. A rougher surface may cause more inflammation, while a smoother surface may be more conducive to healing [8].

2 Mechanical Properties: Mechanical properties such as elasticity and stiffness can affect biocompatibility. Materials that are too hard or too soft may cause stress or damage to cells and tissue [8].

3 Biodegradability: If a material is biodegradable, it will be broken down by the body, reducing inflammation and promoting healing [8].

4 Toxicity: Toxicity can be an issue with some materials, as they may release toxins into the body [8].

5 Foreign Body Reaction: If the body does not recognize the material as being compatible with its tissues, it may mount an immune response, leading to inflammation and other issues [8].

Modifying the surface chemistry and topography of implantable materials can lead to improved bio-inertness and enhanced osseointegration. Ti and its alloys are widely recognized for their excellent biocompatibility compared to other metals used in implants. These materials have demonstrated a high degree of acceptance by the body, making them favourable choices for various implant applications.

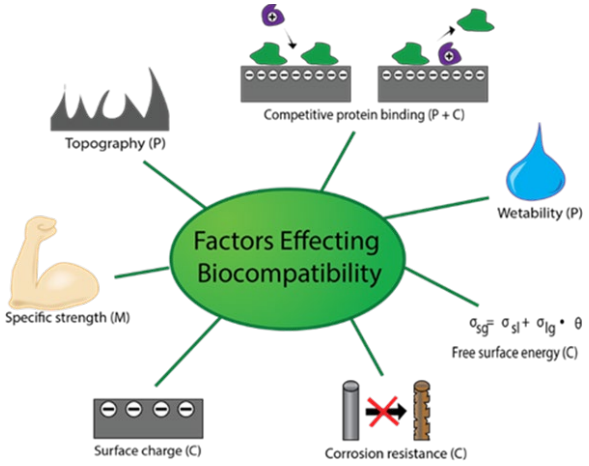

Figure 1. *Factors Affecting the Biocompatibility of Titanium include specific strength, surface charge, topography, wettability, free surface energy, corrosion resistance and competitive protein binding.*

1.4 Hydrothermally Etched Ti (HTE-Ti) Nanostructures: A Promising Surface Modification to Enhanced Biocompatibility

Numerous techniques have been developed to create nanoscale titania layers on the surface of Ti. These methods enable precise control over the thickness and characteristics of the titania layer. Some commonly employed techniques include:

1. Anodization: This electrochemical process involves applying an electric current to the Ti surface immersed in an electrolyte solution. It forms a controlled titania layer with nanoscale features [19].
2. Sol-Gel Method: This method involves the hydrolysis and condensation of precursor molecules to form a titania layer. It allows for the incorporation of various additives and can be used to create nanoscale structures [19].
3. Atomic Layer Deposition (ALD): ALD is a precise and self-limiting process that involves depositing thin titania layers atom by atom. It offers excellent control over layer thickness and uniformity [19].
4. Hydrothermal Synthesis: This method utilizes high-temperature and pressure conditions in an aqueous solution to generate nanoscale titania layers on the Ti surface [19].
5. Plasma Treatment: Plasma-based techniques such as plasma immersion ion implantation (PIII) and plasma-enhanced chemical vapour deposition (PECVD) can be used to create nanoscale titania layers by modifying the surface properties through plasma interactions [19].

Indeed, while hydrothermal etching is a relatively straightforward method, many other techniques for generating nanoscale titania layers on Ti surfaces require complex fabrication steps. These steps often involve the use of chemicals, which can raise environmental concerns, especially during large-scale implementation. Furthermore, the scalability of these techniques may be limited, posing challenges to their widespread application [65, 74]. Ti surfaces with nanostructured features such as nanopillars, nanospikes, nanorods, nanowires, nanoneedles, nanoleaves, and nanoscaffolds, generated through hydrothermal etching (HTE), have demonstrated enhanced protein adsorption capabilities and varying degrees of biocompatibility. These nanostructured Ti surfaces exhibit favourable interactions with proteins, highlighting their potential for promoting cellular responses and improving the biocompatibility of implantable materials [63]. Furthermore, HTE nanostructures bioinspired from cicada and dragonfly wings, have been shown to prevent bacterial growth (*Figure 2*) [53, 75]. Recent studies reported nanoprotrusions fabricated by HTE enhanced biocompatibility [76]. HTE involves modifying the surface by growing a hydrothermal oxide layer (TiO_2) on a chemically etched Ti layer.

Two common etchants used to generate nanostructured structures are NaOH and KOH. By modifying the variables (etchants/alkali, concentrations of etchants, reaction temperature, and etching time), the desired effects can be achieved [77, 78]. For example, Anitha, and Banerjee [79] reported, small discreet nanostructures formed with random orientation using low-molarity alkaline solutions. Furthermore, the resultant nanostructures are also dependent on the temperature of the HTE process. Higher temperatures tend to produce discrete nanorods, however, lower temperatures result in nanoplatelet-like features [79]. Additionally, the etching time also influences the nanoarchitecture [78]. Jaggessar and Mathew [80] reported a model to predict nanostructure height and diameter by altering the NaOH concentration, etching time and reaction temperature.

In a previous study by Jaggessar and Mathew [81] the influence of various parameters such as etchant (NaOH) concentration, reaction time, and reaction temperature on the nanostructures generated through hydrothermal etching (HTE) was investigated. This research aimed to understand the effects of these factors on the formation and characteristics of the HTE nanostructures. Samples fabricated from 1M NaOH showed nano-textured surfaces with reduced strength, however, the 2M NaOH samples displayed mesh-like nanostructures with superior mechanical properties. Remarkably, small hydrophilic nanostructures approximately 300 nm in length, improved human osteoblast cell growth over 24 h compared to unetched Ti-Alloy and showed good antibacterial potential [81]. Vishnu, V [76] confirmed, hydrothermally treating commercially pure (CP)-Ti at 225 °C for 5 h, resulting in a novel nanostructure, exhibiting no mammalian cell cytotoxicity. These types of models will help address biocompatibility and infection of Ti implants.

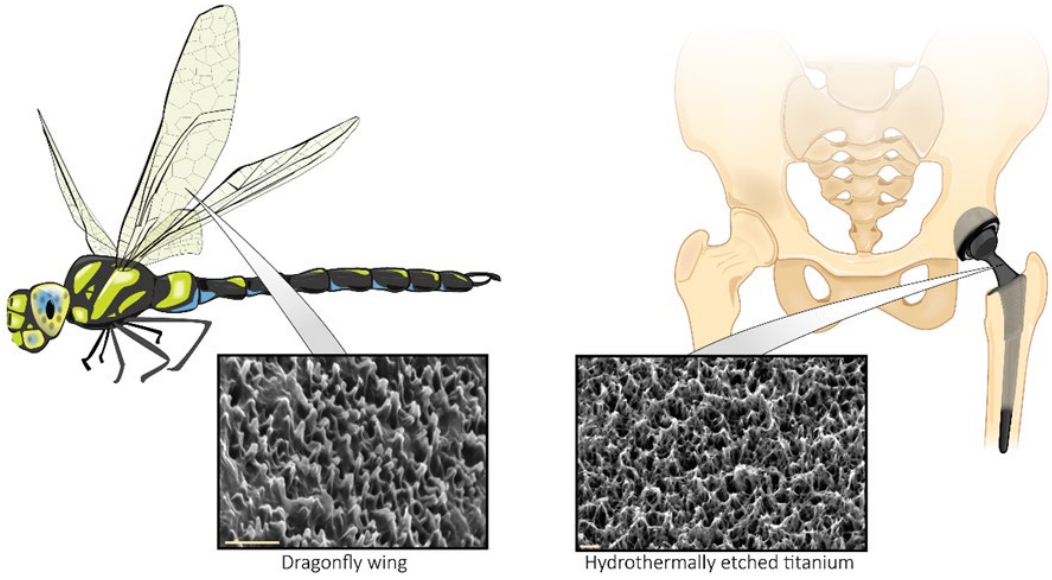

Figure 2. *Demonstrates the biomimetic nanostructures HTE- titanium. Scale bars on scanning electron microscope images represent 1 µm.*

1.5 Biocompatibility and Bactericidal Properties of HTE-Ti a "Double-Edged Sword"

Implant infections are a common and serious complication that can occur after surgical implantation of medical devices, such as joint replacements, dental implants, pacemakers, and other devices [16]. These infections can occur at the site of the implant or in the surrounding tissue and can cause pain, swelling, redness, and fever. In severe cases, implant infections can lead to the failure of the implant, requiring additional surgeries or even the removal of the implant [82].

Bacterial contamination during or following surgery is the primary underlying cause of implant infections. Several common bacterial strains, including *Staphylococcus aureus*, *Staphylococcus epidermidis*, *Pseudomonas aeruginosa*, *Escherichia coli*, *Enterococcus faecalis*, and various *Streptococcus* species, are frequently associated with implant infections [82]. These bacteria can contribute to the development of complications and pose challenges to the successful outcome of implant procedures. Other pathogens such as *Mycobacterium tuberculosis*, fungi, and viruses have also been implicated in implant infections. The risk of infection can be heightened by various factors, including inadequate hygiene practices, a compromised immune system, and underlying health conditions such as diabetes, cancer, and autoimmune disorders. In the event of implant infections, treatment typically involves the administration of antibiotics. However, in certain instances, it may be necessary to remove the infected implant to effectively address the infection and promote healing [82]. To prevent implant infections, proper sterilization and aseptic techniques should be followed during surgery, and patients should be vigilant about their health. The implications of such infections can be severe, underscoring the importance of taking preventive measures and seeking immediate treatment if any signs of infection arise. By prioritizing hygiene and promptly addressing any concerns, patients can play an active role in safeguarding against implant infections and ensuring the long-term success of their implants.

Recently, Ti nanostructures have been shown to have a differential response to bacterial and mammalian cells [29, 75, 77, 78]. HTE surface treatment is effective against both Gram-positive and Gram-negative bacteria and allows eukaryotic cells to survive [79-81], with enhanced biocompatibility potential [71]. This may be due to eukaryotic cells being far less rigid than bacteria or prokaryotes, allowing them to accommodate deformational stress imposed by Ti-nanostructures. (*Figure 3*) [29, 82]. Another significant difference is the magnitude, with bacteria being around 0.5 - 5 μm and eukaryotes ranging from 10 – 100 μm. Being significantly larger than bacteria, eukaryotic cells can distribute downward pressure, evenly, over a larger area on the nanostructured surface leading to a "bed of nails "effect (*Figure 4*).

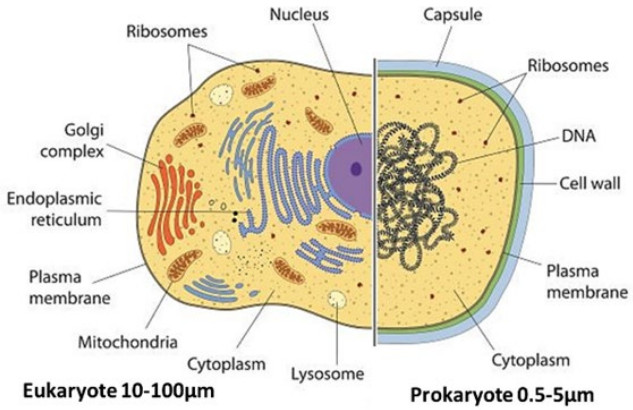

Figure 3. *Mammalian cells (eukaryotes) do not have a ridged cell wall and are much larger than bacteria (eukaryotes). The cell wall of eukaryotes consists of a rigid peptidoglycan layer. Thus, the cell wall rigidity of bacterial cells is the main aspect that affects the vulnerability of bacteria to the mechano-bactericidal action of nanopillar surfaces [80, 83, 84].*

Determining the optimal spacing, height, and diameter of individual nanostructures is critical to achieving the dual goals of bactericidal activity and successful attachment of eukaryotic cells, while also modulating the inflammatory response to facilitate rapid healing and osseointegration. Furthermore, by carefully adjusting the chemical and physical properties of the nanomorphology, it becomes possible to regulate the immune response, leading to desired outcomes in biomedical applications. It is essential to explore these parameters to harness the full potential of nanostructures for promoting favourable biological responses and improving therapeutic efficacy. Luo, Ge [91] reported a bactericidal effect and decreased inflammation of 2D graphene-like silicon nanosheets in a mouse model. Others have investigated *in vivo* accelerated osseointegration by measuring the upregulation of sialoprotein gene expression [92]. There are limited *in-vitro* and *in-vivo* studies reporting the comparative biological response in the presence of infection and the ability of the nanostructured surfaces to minimize the infection.

Figure 4. *Schematic of bacterial cell versus mammalian cell attached to nanospikes, spreading the downward pressure experienced by the cells over a larger area, thus preventing mechanical rupture as seen in the bacterial cells-this phenomenon is known as the "bed of nails" effect.*

1.6 Immunomodulation and Cellular Response to Ti-Implants

1.6.1 Host Cell Response to Biomaterials

The mammalian immune system comprises two components: the innate immune system and the adaptive immune system. The innate immune system provides a rapid, nonspecific response upon the immediate recognition of biomaterials. It involves various cell types, including polymorphonuclear cells, mononuclear phagocytic cells (such as dendritic cells, monocytes, and macrophages), and lymphocytes (such as natural killer cells, T-cells, and innate lymphoid cells). Together, these components work in coordination to mount an immune response against foreign materials and maintain overall immune homeostasis within the body. The adaptive immune system serves as the second line of defence and plays a crucial role in mounting highly specific responses against non-self insults. It possesses the remarkable ability to generate long-term memory, enabling a rapid and targeted immune response upon re-exposure to the same pathogen or antigen. This system involves specialized immune cells known as B lymphocytes (B cells) and T lymphocytes (T cells), which work together to recognize specific antigens and orchestrate an adaptive immune response tailored to eliminate the identified threat [93].

The development of an immune response necessitates a tightly regulated and coordinated interplay between the innate and adaptive immune systems. This intricate communication involves the exchange of chemical signals, including cytokines and chemokines, as well as the involvement of the cellular subsets mentioned earlier. Through this close interaction, the innate and adaptive immune systems work together to effectively detect, respond to, and eliminate foreign pathogens or antigens, thereby maintaining immune balance and promoting overall immune function. This early immune response is pivotal in osseointegration and foreign body response. Historically, hydroxyapatite (HA; $Ca_{10}(PO_4)6(OH)_2$) has been the benchmark Ti implant surface treatment to improve osteointegration. Multiple studies have demonstrated that coatings composed of hydroxyapatite (HA) offer a beneficial microenvironment for the interaction between implant surfaces and bone tissue. These HA-based coatings facilitate enhanced osseointegration of implants, promoting a more rapid and robust integration with the surrounding bony tissue. The presence of HA in these coatings contributes to improved biocompatibility and creates an environment conducive to successful implant integration, ultimately leading to improved clinical outcomes [94-96]. However, HA coating methods exhibited weak adhesion strength on a metal surface and lack antibacterial properties [97] HTE treated implants have emerged as a promising solution, demonstrating the potential for both antibacterial properties and osteoconductive capabilities. These implants, modified through the HTE process, exhibit the ability to inhibit bacterial growth and promote the integration of bone tissue. By harnessing the benefits of HTE treatment, these implants offer a dual advantage, addressing the risk of infections while facilitating successful bone healing and integration. This advancement holds promise in improving the overall performance and longevity of implants in various biomedical applications. [4, 98, 99]. To comprehensively comprehend the sequence of events, a series of subheadings have been formulated to specifically address it:

1.6.2 Protein Adsorption

Following implantation, the surface of biomaterials undergoes rapid protein adsorption [100]. Cellular interactions with biomaterials are mediated by the type and conformation of the adsorbed proteins that interact with specific integrins expressed by host cells (*Figure 5*). The hydrophobicity of the surface plays a crucial role in influencing these phenomena, as it is dependent on the surface composition of the biomaterial [5, 101]. The composition of this adsorbed protein layer is a crucial mediator of cellular recruitment and their response to the biomaterial [102]. Nanostructured features could influence the type, amount, distribution and conformation of the adsorbed proteins, allowing a surface to be tuned, resulting in an improved biomaterial host integration [103].

Platelets are the initial cells to adhere to the protein matrix, responding to different stimuli and releasing cytokines/chemokines that regulate inflammatory processes, such as leukocyte recruitment and migration, phagocytosis, and the generation of reactive oxygen species (ROS) [104, 105]. Numerous in vitro studies have been conducted using specific proteins, such as bovine serum albumin and fibrinogen. However, it is worth noting that these studies do not encompass the complexity of a complete plasma mixture found in real-life conditions [106-109].

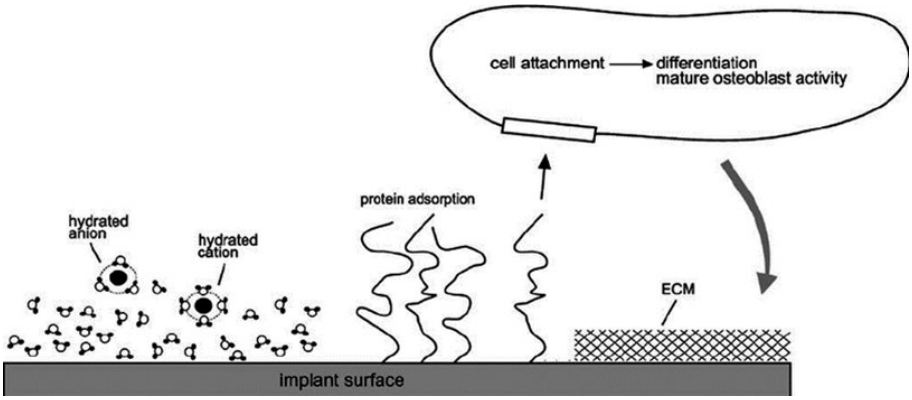

Figure 5. *Schematic representation of events sequentially taking place at the surface after implantation into living bone tissue. Water binds to the surface, followed by the incorporation of hydrated ions, adsorption, and desorption of proteins, eventually leading to cell attachment. After differentiation, mature osteoblasts produce the extracellular matrix (ECM) [106].*

1.6.3 Complement activation on biomaterial surfaces

The complement system plays a crucial role as a host defence mechanism, responsible for interacting with and eliminating foreign substances. However, the activation of the complement system and its subsequent reactions can lead to detrimental antagonistic side effects during interactions between blood and medical devices. Additionally, there exists a close interplay between the various cascade systems, leukocytes, and platelets, which collectively contribute to clotting and inflammation induction [111].

1.6.4 Host Immune Early Cellular Response

Neutrophils are the initial immune cells to invade an implantation site and have a crucial role in the immune response to biomaterial-based implants. They initiate inflammation by releasing pro-inflammatory cytokines that trigger the recruitment of other immune cells, particularly pro-inflammatory M1 macrophages [112]. Consequently, the design of biomaterials should prioritize the modulation of neutrophil activation and elicitation of the appropriate response from other effector cells, such as monocytes, macrophages, dendritic cells, and more [113]. The interaction between neutrophils and implant materials is a critical early event, and their response, primarily influenced by the biomaterial and microenvironment, can significantly impact subsequent processes. Neutrophils can polarize in response to specific signals, similar to macrophage polarization, leading to distinct phenotypes (proinflammatory N1 and anti-inflammatory N2) that exert different effects on the immune system [114]. Recent studies have indicated that specific surface chemistries can influence the adhesion and fusion of monocytes and macrophages. Hydrophilic, non-ionic, and anionic surfaces have been found to significantly decrease the adhesion and fusion of macrophages, thereby inhibiting the formation of foreign body giant cells and osteoclasts, which are associated with bone resorption [115, 116], resulting in orthopaedic implant loosening [117].

1.6.5 Macrophage Polarization and Fibroblastic Interaction

Despite extensive research in the field, the development of biomaterials that do not induce a foreign body response (FBR) remains a challenge. A major obstacle in addressing FBR is the limited understanding of the ideal behaviour of macrophages, which play a crucial role in innate inflammation. Macrophages derived from monocytes are white blood cells that engulf and digest cellular debris and foreign substances. Proinflammatory M1 macrophages are generally involved in early tissue responses, subsiding after a few days post-implant surgery [118], followed by a switch to an anti-inflammatory M2 macrophage phenotype, involved in wound healing and repair (*Figure 6*) [119]. Failure of macrophages to transition from M1 to M2 phenotype has been associated with dysregulated functions including chronic inflammation, foreign body reaction, granulation tissue formation and eventual encapsulation (*Figure 7*) [57].

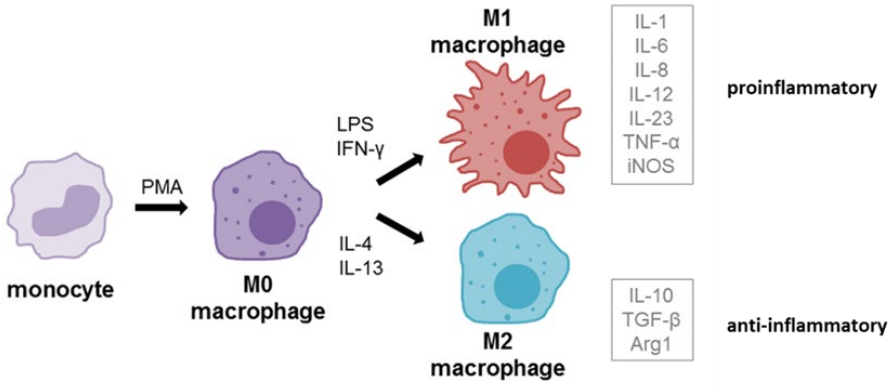

Figure 6. *In vivo macrophage differentiation and polarization. Monocytes can be differentiated into macrophages (non-activated, M0) using 12-myristate 13-acetate (PMA). M0 macrophages can then be further polarized into M1 (pro-inflammatory) phenotype using LPS and IFN-γ or M2 (anti-inflammatory) using IL-4 and IL-13 treatment. The boxes beside polarization phenotypes show the cytokines that are predominately secreted by the respective phenotypes [120].*

Macrophages, platelets, and other cells near the implant site release growth factors with profibrotic and angiogenic properties. These growth factors include vascular endothelial growth factors (VEGF), platelet-derived growth factors (PDGF), and transforming growth factor-beta (TGF-β), which attract and activate fibroblastic cells [121]. Myofibroblasts are the main contributors to the formation of scar tissue that characterizes peri-implant fibrosis and together with other fibroblast cell types, become the major cell population in the extracellular matrix (ECM) around implants. In a worst-case scenario, the dense fibrotic capsule encompasses and isolates the implanted material from the local tissue environment, possibly serving as our body's last defence mechanism against the foreign object [122]. A bioinert surface seeks to promote the transition from M1 to M2 macrophage phenotype, preventing fibrotic encapsulation and enhancing osteointegration.

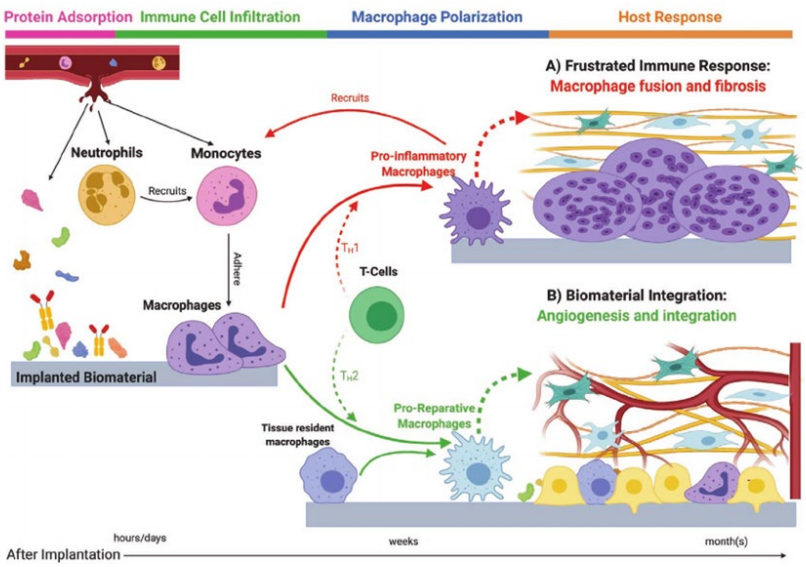

Figure 7. *Schematic representing the inflammatory response that occurs after biomaterial implantation. First, plasma proteins adhere to the biomaterial's surface and there is a rapid and considerable infiltration of platelets followed by neutrophils. Next, there is an infiltration of circulating monocytes. These monocytes generally differentiate toward proinflammatory macrophages (M1) when interacting with materials, causing a foreign body reaction that finally provokes biomaterial rejection (A). This process is fostered by a TH1 response. However, biomaterial integration can be achieved by promoting anti-inflammatory (M2) macrophage phenotypes and tissue-resident macrophages, fostered through a TH2 response (B) [123].*

1.7 Biomaterials Osseointegration

Osseointegration refers to the direct and strong bond between living bone and an implant surface. Inadequate osseointegration can result in the formation of fibrous tissue and subsequent implant loosening. Moreover, a surface that integrates effectively with the surrounding bone is crucial for preventing osteolysis [124]. As mentioned previously, bone healing around implants involves a cascade of cellular and extracellular events, taking place at the interface between host tissue and implant surface [125].

1.8 Osteoblasts and Stem Cell

Osteoblasts and mesenchymal cells migrate to the implant interface very early post-implantation, expressing bone-related proteins and producing a non-collagenous matrix layer on the implant surface that assists cell adhesion and binding of minerals. This matrix is a pre-bone tissue, consisting of a calcified fibrillar acellular cementum-like layer on the implant surface [126]. Several researchers have reported the efficiency of TiO2 nanotubular layer on *in vitro* cell adhesion and proliferation, protein adsorption, and osseointegration in an *in vivo* setting [127-129]. Not only did the Ti nanotubes enhance the surface roughness and hydrophilicity, but also activates angiogenic factors. Olivares-Navarrete, Hyzy [130] reported factors produced by osteoblasts grown on micro-structured hydrophilic Ti surfaces were sufficient to induce co-cultured MSC differentiation to osteoblasts.

1.9 Interaction Between Host, Bacteria and Biomaterial

The host immune response to microorganisms is via the innate and acquired immune responses, however, some bacteria can evade the immune system by producing a biofilm or by becoming internalised into a host cell. Particularly relevant in orthopaedic and dental implants is the internalisation of bacteria by osteoblasts, macrophages, and epithelial cells [131-134]. Further research is required to understand the host, bacteria and biomaterial surface interactions will help to improve the treatment of IAI. The ideal biomaterial will reduce bacterial colony formation and promote an anti-inflammatory cellular response [135], prevent fibrous encapsulation [136] and maintain long-term implant osseointegration [137].

1.10 Outlook and Conclusion

Osteointegration refers to the biological process, where an implant becomes fused with the bone, resulting in the long-term stability of the prosthesis. The implant is usually made of Ti or Ti alloy, which is a metal that is especially well-suited for the process. Once the implant is in place, the natural healing process begins, and the body begins to form a strong bond with the metal implant. Surface roughness and the chemistry of the implant surface play a major role in driving the biological mechanisms at the interface.

There are numerous fabrication methods to generate nanomodified surfaces on implantable devices, however, the alkaline HTE method is the most appealing due to its cost-effectiveness, simplicity, and potential for scale-up. It is still unclear what is the optimal surface modification to show a favourable immune response leading to good osteointegration, however, the literature points toward hydrophilic nano-modified surfaces. Further studies are required to elucidate the cascade of events that occur after implant surgery. Understanding these cellular events may help to design improved implant surfaces resulting in favourable osteointegration and preventing implant infection.

1.11 Gaps in Knowledge

There have been numerous studies on the antibacterial properties of various nanomodified Ti surfaces [4, 85, 138, 139], however little is known of the mechanism leading to biomaterial immune response, and how to enhance a favourable response. Hydrophilic nanomodified surfaces have been shown to reduce inflammation [140-142], however further work is required to explain the mechanisms at play. Furthermore, macrophages are shown to promote osteogenic signalling on the hydrophilic surface [143]. To date, there has been minimal research on the crosstalk between the various immune cells, specifically involved in a favourable osteoconductive outcome because of nanomodified Ti implants. The interplay between bacteria-host cells and implant materials, termed “race to the surface” requires further understanding to prevent implant-associated infections [34, 35, 144]. Furthermore, there has been little research on long-term and dose-response studies about antibacterial efficacy. The major research questions that will be addressed in this current research project are related to mechanistically understanding the interaction between bacteria, and host cells on the nanostructured surface. The answers to these questions will enable us to create a more complete picture of the inflammatory reaction to an implanted biomaterial, resulting in accelerated and improved bone healing together with a lower incidence of implant infections.

1.12 Research Questions

1. What is the optimal protocol to fabricate nanostructured surfaces to maximise biocompatibility and antimicrobial properties?
2. Will the mechano-bactericidal activity of nanostructured surfaces have decreased antibacterial efficacy in a dose and time-dependent manner?
3. Does the surface preserve its antimicrobial properties over time?
4. Does the addition of a clinically relevant antibiotic dose enhance the antibacterial efficacy of the HTE?
5. Macrophages will outcompete *S. aureus* when co-cultured on the HTE nanostructured surface.

1.13 Project Aims and Objectives

The objective of this research project was to evaluate the applicability of hydrophilic HTE nanostructured surfaces for orthopaedic and dental implants. The investigation aimed to explore strategies for enhancing, suppressing, or modulating the immune response, which is crucial for various biomedical applications, including biomaterials. The project will focus on further examining the feasibility of implementing an HTE nanomodified surface on Ti-based implants to reduce the risk of implant-related infections and promote improved osseointegration.

1.14 Expected Outcomes:

1. Optimisation of the hydrothermal etching process
2. Determine the biocompatibility against several mammalian cell types.
3. Quantify the antimicrobial ability of the surface to kill implant-related pathogens over time and in a dose-response manner.
4. Elucidate the mechanism if synergy is detected between the nanostructured surface and antibiotics against *S. aureus*.
5. Investigate the ability of macrophages to out-compete bacteria and identify the underlying mechanisms that contribute to the outcome.

1.15 References

1. Hao, C.-P., et al., The osseointegration and stability of dental implants with different surface treatments in animal models: a network meta-analysis. Scientific Reports, 2021. 11(1): p. 13849.
2. Souza, J.C.M., et al., Nano-scale modification of titanium implant surfaces to enhance osseointegration. Acta Biomater, 2019. 94: p. 112-131.
3. Taylor, E. and T.J. Webster, Reducing infections through nanotechnology and nanoparticles. Int J Nanomedicine, 2011. 6: p. 1463-73.
4. Liu, J., et al., Nano-Modified Titanium Implant Materials: A Way Toward Improved Antibacterial Properties. Front Bioeng Biotechnol, 2020. 8: p. 576969.
5. Visalakshan, R.M., et al., Biomaterial Surface Hydrophobicity-Mediated Serum Protein Adsorption and Immune Responses. ACS Applied Materials & Interfaces, 2019. 11(31): p. 27615-27623.
6. Vasilev, K., et al., Controlled release of levofloxacin sandwiched between two plasma polymerized layers on a solid carrier. ACS Appl Mater Interfaces, 2011. 3(12): p. 4831-6.
7. Sam Froes, F.H., Titanium for medical and dental applications-An introduction. Titan. Med. Dent. Appl, 2018: p. 3–21.
8. Kaur, M. and K. Singh, Review on titanium and titanium-based alloys as biomaterials for orthopaedic applications. Mater Sci Eng C Mater Biol Appl, 2019. 102: p. 844-862.
9. Guillemot, F., Recent advances in the design of titanium alloys for orthopedic applications. Expert Rev Med Devices, 2005. 2(6): p. 741-8.
10. Tharani Kumar, S., et al., Review of Metallic Biomaterials in Dental Applications. J Pharm Bioallied Sci, 2020. 12(Suppl 1): p. S14-s19.
11. Xi, D. and L. Wong, Titanium and implantology: a review in dentistry. J Biol Regul Homeost Agents, 2021. 35(1 Suppl. 1): p. 63-72.
12. Alzahrani, K.M., Implant Bio-mechanics for Successful Implant Therapy: A Systematic Review. J Int Soc Prev Community Dent, 2020. 10(6): p. 700-714.
13. Sidambe, A.T., Biocompatibility of Advanced Manufactured Titanium Implants-A Review. Materials (Basel, Switzerland), 2014. 7(12): p. 8168-8188.
14. Kim, K.T., et al., General review of titanium toxicity. Int J Implant Dent, 2019. 5(1): p. 10.
15. Ribeiro, M., F.J. Monteiro, and M.P. Ferraz, Infection of orthopedic implants with emphasis on bacterial adhesion process and techniques used in studying bacterial-material interactions. Biomatter, 2012. 2(4): p. 176-194.
16. Arciola, C.R., D. Campoccia, and L. Montanaro, Implant infections: adhesion, biofilm formation and immune evasion. Nat Rev Microbiol, 2018. 16(7): p. 397-409.
17. Zimmerli, W., Clinical presentation and treatment of orthopaedic implant-associated infection. J Intern Med, 2014. 276(2): p. 111-9.
18. Trampuz, A. and A.F. Widmer, Infections associated with orthopedic implants. Curr Opin Infect Dis, 2006. 19(4): p. 349-56.

19. Chouirfa, H., et al., Review of titanium surface modification techniques and coatings for antibacterial applications. Acta Biomater, 2019. 83: p. 37-54.
20. Tornetta, P., 3rd, et al., Risk Factors Associated With Infection in Open Fractures of the Upper and Lower Extremities. Journal of the American Academy of Orthopaedic Surgeons. Global research & reviews, 2020. 4(12): p. e20.00188-e20.00188.
21. Patzakis, M.J. and J. Wilkins, Factors influencing infection rate in open fracture wounds. Clin Orthop Relat Res, 1989(243): p. 36-40.
22. Castano-Betancourt, M.C., et al., Identification of high-risk groups for complication after arthroplasty: predictive value of patient's related risk factors. J Orthop Surg Res, 2018. 13(1): p. 328.
23. Sloan, M., A. Premkumar, and N.P. Sheth, Projected Volume of Primary Total Joint Arthroplasty in the U.S., 2014 to 2030. J Bone Joint Surg Am, 2018. 100(17): p. 1455-1460.
24. Shah, M.Q., et al., Surgical Site Infection In Orthopaedic Implants And Its Common Bacteria With Their Sensitivities To Antibiotics, In Open Reduction Internal Fixation. J Ayub Med Coll Abbottabad, 2017. 29(1): p. 50-53.
25. Cogen, A.L., V. Nizet, and R.L. Gallo, Skin microbiota: a source of disease or defence? The British journal of dermatology, 2008. 158(3): p. 442-455.
26. Muhammad, M.H., et al., Beyond Risk: Bacterial Biofilms and Their Regulating Approaches. Front Microbiol, 2020. 11: p. 928.
27. Yamada, K.J. and T. Kielian, Biofilm-Leukocyte Cross-Talk: Impact on Immune Polarization and Immunometabolism. J Innate Immun, 2019. 11(3): p. 280-288.
28. González, J.F., M.M. Hahn, and J.S. Gunn, Chronic biofilm-based infections: skewing of the immune response. Pathog Dis, 2018. 76(3).
29. Khatoon, Z., et al., Bacterial biofilm formation on implantable devices and approaches to its treatment and prevention. Heliyon, 2018. 4(12): p. e01067.
30. Ciofu, O., et al., Antibiotic treatment of biofilm infections. Apmis, 2017. 125(4): p. 304-319.
31. Donlan, R.M. and J.W. Costerton, Biofilms: survival mechanisms of clinically relevant microorganisms. Clin Microbiol Rev, 2002. 15(2): p. 167-93.
32. Lenguerrand, E., et al., Risk factors associated with revision for prosthetic joint infection following knee replacement: an observational cohort study from England and Wales. The Lancet. Infectious diseases, 2019. 19(6): p. 589-600.
33. Subbiahdoss, G., et al., Microbial biofilm growth vs. tissue integration: "the race for the surface" experimentally studied. Acta Biomater, 2009. 5(5): p. 1399-404.
34. Shiels, S.M., L.H. Mangum, and J.C. Wenke, Revisiting the "race for the surface" in a pre-clinical model of implant infection. Eur Cell Mater, 2020. 39: p. 77-95.
35. Pham, V.T.H., et al., “Race for the Surface”: Eukaryotic Cells Can Win. ACS Applied Materials & Interfaces, 2016. 8(34): p. 22025-22031.
36. Garg, K., et al., Macrophage functional polarization (M1/M2) in response to varying fiber and pore dimensions of electrospun scaffolds. Biomaterials, 2013. 34(18): p. 4439-51.

37. Taraballi, F., et al., Biomimetic collagenous scaffold to tune inflammation by targeting macrophages. J Tissue Eng, 2016. 7: p. 2041731415624667.
38. Hotchkiss, K.M., N.M. Clark, and R. Olivares-Navarrete, Macrophage response to hydrophilic biomaterials regulates MSC recruitment and T-helper cell populations. Biomaterials, 2018. 182: p. 202-215.
39. Chen, M., et al., The osteoimmunomodulatory effect of nanostructured TiF(x)/TiO(x)coating on osteogenesis induction. Biomed Mater, 2021. 16(4).
40. Chen, Y., et al., Improved Immunoregulation of Ultra-Low-Dose Silver Nanoparticle-Loaded TiO(2) Nanotubes via M2 Macrophage Polarization by Regulating GLUT1 and Autophagy. Int J Nanomedicine, 2020. 15: p. 2011-2026.
41. Damiati, L., et al., Impact of surface topography and coating on osteogenesis and bacterial attachment on titanium implants. J Tissue Eng, 2018. 9: p. 2041731418790694.
42. Hamlet, S. and S. Ivanovski, Inflammatory Cytokine Response to Titanium Surface Chemistry and Topography, in The Immune Response to Implanted Materials and Devices, B. Corradetti, Editor. 2017, Springer, Cham: Switzerland. p. 151–167.
43. Irandoust, S. and S. Müftü, The interplay between bone healing and remodeling around dental implants. Sci Rep, 2020. 10(1): p. 4335.
44. Kučera, T., et al., Bone healing capacity in patients undergoing total hip arthroplasty. Acta Chir Orthop Traumatol Cech, 2012. 79(1): p. 52-8.
45. Kzhyshkowska, J., et al., Macrophage responses to implants: prospects for personalized medicine. J Leukoc Biol, 2015. 98(6): p. 953-62.
46. Wang, X., et al., The role of macrophages in osseointegration of dental implants: An experimental study in vivo. J Biomed Mater Res A, 2020. 108(11): p. 2206-2216.
47. Ng, J., et al., Biomimetic Approaches for Bone Tissue Engineering. Tissue engineering. Part B, Reviews, 2017. 23(5): p. 480-493.
48. Yu, X., et al., Biomaterials for Bone Regenerative Engineering. Advanced healthcare materials, 2015. 4(9): p. 1268-1285.
49. Han, K., et al., Combinational Biomimicking of Lotus Leaf, Mussel, and Sandcastle Worm for Robust Superhydrophobic Surfaces with Biomedical Multifunctionality: Antithrombotic, Antibiofouling, and Tissue Closure Capabilities. ACS Appl Mater Interfaces, 2019. 11(10): p. 9777-9785.
50. Dundar Arisoy, F., et al., Bioinspired Photocatalytic Shark-Skin Surfaces with Antibacterial and Antifouling Activity via Nanoimprint Lithography. ACS Appl Mater Interfaces, 2018. 10(23): p. 20055-20063.
51. Watson, G.S., et al., A gecko skin micro/nano structure - A low adhesion, superhydrophobic, anti-wetting, self-cleaning, biocompatible, antibacterial surface. Acta Biomater, 2015. 21: p. 109-22.
52. Zhang, G., et al., Cicada wings: a stamp from nature for nanoimprint lithography. Small, 2006. 2(12): p. 1440-3.

53. Ivanova, E.P., et al., Natural Bactericidal Surfaces: Mechanical Rupture of Pseudomonas aeruginosa Cells by Cicada Wings. Small, 2012. 8(16): p. 2489.
54. Hanawa, T., Titanium-Tissue Interface Reaction and Its Control With Surface Treatment. Front Bioeng Biotechnol, 2019. 7: p. 170.
55. Puleo, D.A. and A. Nanci, Understanding and controlling the bone-implant interface. Biomaterials, 1999. 20(23-24): p. 2311-21.
56. Noskovicova, N., B. Hinz, and P. Pakshir, Implant Fibrosis and the Underappreciated Role of Myofibroblasts in the Foreign Body Reaction. Cells, 2021. 10(7).
57. Anderson, J.M., A. Rodriguez, and D.T. Chang, Foreign Body Reaction to Biomaterials. Semin. Immunol., 2008. 20(2): p. 86.
58. Rahmati, M., et al., Biological responses to physicochemical properties of biomaterial surface. Chem Soc Rev, 2020. 49(15): p. 5178-5224.
59. Wypych, A., et al., Titanium Plasma-Sprayed Coatings on Polymers for Hard Tissue Applications. Materials (Basel), 2018. 11(12).
60. Qin, J., et al., Micro- and nano-structured 3D printed titanium implants with a hydroxyapatite coating for improved osseointegration. J Mater Chem B, 2018. 6(19): p. 3136-3144.
61. Lewallen, E.A., et al., Surface roughness of titanium orthopedic implants alters the biological phenotype of human MSCs. Tissue Eng Part A, 2021.
62. Ban, S., et al., Surface modification of titanium by etching in concentrated sulfuric acid. Dent Mater, 2006. 22(12): p. 1115-20.
63. Camargo, W.A., et al., Effect of surface alkali-based treatment of titanium implants on ability to promote in vitro mineralization and in vivo bone formation. Acta Biomater, 2017. 57: p. 511-523.
64. Shahali, H., et al., A systematic approach towards biomimicry of nanopatterned cicada wings on titanium using electron beam lithography. Nanotechnology, 2021. 32(6): p. 065301.
65. Xue, T., et al., Surface Modification Techniques of Titanium and its Alloys to Functionally Optimize Their Biomedical Properties: Thematic Review. Front Bioeng Biotechnol, 2020. 8: p. 603072.
66. Roy, M., A. Bandyopadhyay, and S. Bose, Induction plasma sprayed Sr and Mg doped nano hydroxyapatite coatings on Ti for bone implant. J Biomed Mater Res B Appl Biomater, 2011. 99(2): p. 258-65.
67. Mani, N., et al., Single-Step Fabrication Method toward 3D Printing Composite Diamond-Titanium Interfaces for Neural Applications. ACS Appl Mater Interfaces, 2021.
68. Devlin-Mullin, A., et al., Atomic Layer Deposition of a Silver Nanolayer on Advanced Titanium Orthopedic Implants Inhibits Bacterial Colonization and Supports Vascularized de Novo Bone Ingrowth. Adv Healthc Mater, 2017. 6(11).
69. El-Wassefy, N.A., F.M. Reicha, and N.S. Aref, Electro-chemical deposition of nano hydroxyapatite-zinc coating on titanium metal substrate. Int J Implant Dent, 2017. 3(1): p. 39.

70. Zhang, Y., et al., Smart Titanium Coating Composed of Antibiotic Conjugated Peptides as an Infection-Responsive Antibacterial Agent. Macromol Biosci, 2021. 21(1): p. e2000194.
71. Blanco Carcache, P.J., et al., Regulation of Reversible Conformational Change, Size Switching, and Immunomodulation of RNA Nanocubes. Rna, 2021.
72. Wang, G., et al., Surface thermal oxidation on titanium implants to enhance osteogenic activity and in vivo osseointegration. Sci Rep, 2016. 6: p. 31769.
73. Yang, H., et al., Hydrothermally grown TiO2-nanorods on surface mechanical attrition treated Ti: Improved corrosion fatigue and osteogenesis. Acta Biomater, 2020. 116: p. 400-414.
74. Ou, H.-H. and S.-L. Lo, Review of titania nanotubes synthesized via the hydrothermal treatment: Fabrication, modification, and application. Separation and Purification Technology, 2007. 58(1): p. 179-191.
75. Bandara, C.D., et al., Bactericidal Effects of Natural Nanotopography of Dragonfly Wing on Escherichia coli. ACS Appl Mater Interfaces, 2017. 9(8): p. 6746-6760.
76. Vishnu, J., et al., Hydrothermal treatment of etched titanium: A potential surface nano-modification technique for enhanced biocompatibility. Nanomedicine, 2019. 20: p. 102016.
77. Tsimbouri, P.M., et al., Osteogenic and bactericidal surfaces from hydrothermal titania nanowires on titanium substrates. Sci Rep, 2016. 6: p. 36857.
78. Wandiyanto, J.V., et al., Tunable morphological changes of asymmetric titanium nanosheets with bactericidal properties. J Colloid Interface Sci, 2020. 560: p. 572-580.
79. Anitha, V.C., et al., Morphology-dependent low macroscopic field emission properties of titania/titanate nanorods synthesized by alkali-controlled hydrothermal treatment of a metallic Ti surface. Nanotechnology, 2015. 26(35): p. 355705.
80. Jaggessar, A., et al., Bacteria Death and Osteoblast Metabolic Activity Correlated to Hydrothermally Synthesised TiO_2 Surface Properties. Molecules, 2019. 24(7).
81. Jaggessar, A., et al., Mechanical, bactericidal and osteogenic behaviours of hydrothermally synthesised TiO(2) nanowire arrays. J Mech Behav Biomed Mater, 2018. 80: p. 311-319.
82. VanEpps, J.S. and J.G. Younger, Implantable Device-Related Infection. Shock, 2016. 46(6): p. 597-608.
83. Tripathy, A., et al., Natural and bioinspired nanostructured bactericidal surfaces. Adv Colloid Interface Sci, 2017. 248: p. 85-104.
84. Zhu, Y., et al., Hierarchical micro/nanostructured titanium with balanced actions to bacterial and mammalian cells for dental implants. Int J Nanomedicine, 2015. 10: p. 6659-74.
85. Ivanova, E.P., et al., The multi-faceted mechano-bactericidal mechanism of nanostructured surfaces. Proc Natl Acad Sci U S A, 2020. 117(23): p. 12598-12605.
86. Li, X., Bactericidal mechanism of nanopatterned surfaces. Phys Chem Chem Phys, 2016. 18(2): p. 1311-6.
87. Bright, R., et al., In Vitro Bactericidal Efficacy of Nanostructured Ti6Al4V Surfaces is Bacterial Load Dependent. ACS Appl Mater Interfaces, 2021. 13(32): p. 38007-38017.

88. Trichet, L., et al., Evidence of a large-scale mechanosensing mechanism for cellular adaptation to substrate stiffness. Proc Natl Acad Sci U S A, 2012. 109(18): p. 6933-8.
89. Pogodin, S., et al., Biophysical Model of Bacterial Cell Interactions With Nanopatterned Cicada Wing Surfaces. Biophys. J., 2013. 104(4): p. 835.
90. Xue, F., et al., Theoretical study on the bactericidal nature of nanopatterned surfaces. J Theor Biol, 2015. 385: p. 1-7.
91. Luo, Y., et al., Anti-Infective Application of Graphene-Like Silicon Nanosheets via Membrane Destruction. Adv Healthc Mater, 2020. 9(3): p. e1901375.
92. Hao, J., et al., Biological and Mechanical Effects of Micro-Nanostructured Titanium Surface on an Osteoblastic Cell Line In vitro and Osteointegration In vivo. Appl Biochem Biotechnol, 2017. 183(1): p. 280-292.
93. Alberts B, J.A., Lewis J, et al, Molecular Biology of the Cell., in The Adaptive Immune System. 2002, Garland Science: New York.
94. Samavedi, S., A.R. Whittington, and A.S. Goldstein, Calcium phosphate ceramics in bone tissue engineering: a review of properties and their influence on cell behavior. Acta Biomater, 2013. 9(9): p. 8037-45.
95. Łukaszewska-Kuska, M., et al., Hydroxyapatite coating on titanium endosseous implants for improved osseointegration: Physical and chemical considerations. Adv Clin Exp Med, 2018. 27(8): p. 1055-1059.
96. Oonishi, H., Orthopaedic applications of hydroxyapatite. Biomaterials, 1991. 12(2): p. 171-8.
97. Tsui, Y.C., C. Doyle, and T.W. Clyne, Plasma sprayed hydroxyapatite coatings on titanium substrates. Part 1: Mechanical properties and residual stress levels. Biomaterials, 1998. 19(22): p. 2015-29.
98. Jäger, M., et al., Antimicrobial and Osseointegration Properties of Nanostructured Titanium Orthopaedic Implants. Materials (Basel), 2017. 10(11).
99. Orapiriyakul, W., et al., Antibacterial surface modification of titanium implants in orthopaedics. J Tissue Eng, 2018. 9: p. 2041731418789838.
100. Hlady, V.V. and J. Buijs, Protein adsorption on solid surfaces. Current opinion in biotechnology, 1996. 7(1): p. 72-77.
101. Jia, S., et al., Enhanced Hydrophilicity and Protein Adsorption of Titanium Surface by Sodium Bicarbonate Solution. Journal of Nanomaterials, 2015. 2015: p. 536801.
102. Ngandu Mpoyi, E., et al., Protein Adsorption as a Key Mediator in the Nanotopographical Control of Cell Behavior. ACS Nano, 2016. 10(7): p. 6638-47.
103. Planell, J.A., et al. Materials Surface Effects on Biological Interactions. in Advances in Regenerative Medicine: Role of Nanotechnology, and Engineering Principles. 2010. Dordrecht: Springer Netherlands.
104. Rendu, F. and B. Brohard-Bohn, The platelet release reaction: granules' constituents, secretion and functions. Platelets, 2001. 12(5): p. 261-73.

105. Chen, Y., et al., Role of platelet biomarkers in inflammatory response. Biomark Res, 2020. 8: p. 28.
106. Jia, E., et al., Protein adsorption on titanium substrates and its effects on platelet adhesion. Applied Surface Science, 2020. 529: p. 146986.
107. Yang, Y., R. Cavin, and J.L. Ong, Protein adsorption on titanium surfaces and their effect on osteoblast attachment. J Biomed Mater Res A, 2003. 67(1): p. 344-9.
108. Rockwell, G.P., L.B. Lohstreter, and J.R. Dahn, Fibrinogen and albumin adsorption on titanium nanoroughness gradients. Colloids Surf B Biointerfaces, 2012. 91: p. 90-6.
109. Allouni, Z.E., et al., The effect of blood protein adsorption on cellular uptake of anatase TiO2 nanoparticles. International journal of nanomedicine, 2015. 10: p. 687-695.
110. de Jonge, L.T., et al., Organic-inorganic surface modifications for titanium implant surfaces. Pharm Res, 2008. 25(10): p. 2357-69.
111. Nilsson, B., et al., The role of complement in biomaterial-induced inflammation. Mol Immunol, 2007. 44(1-3): p. 82-94.
112. Selders, G.S., et al., An overview of the role of neutrophils in innate immunity, inflammation and host-biomaterial integration. Regen Biomater, 2017. 4(1): p. 55-68.
113. Hussen, J., et al., Neutrophil degranulation differentially modulates phenotype and function of bovine monocyte subsets. Innate Immun, 2016. 22(2): p. 124-37.
114. Mantovani, A., et al., Neutrophils in the activation and regulation of innate and adaptive immunity. Nat Rev Immunol, 2011. 11(8): p. 519-31.
115. Anderson, J.M., Exploiting the inflammatory response on biomaterials research and development. J Mater Sci Mater Med, 2015. 26(3): p. 121.
116. Khan, U.A., et al., Foreign body giant cells and osteoclasts are TRAP positive, have podosome-belts and both require OC-STAMP for cell fusion. J Cell Biochem, 2013. 114(8): p. 1772-8.
117. Greenfield, E.M., et al., The role of osteoclast differentiation in aseptic loosening. J Orthop Res, 2002. 20(1): p. 1-8.
118. Zhu, Y., et al., Regulation of macrophage polarization through surface topography design to facilitate implant-to-bone osteointegration. Sci Adv, 2021. 7(14).
119. Sheikh, Z., et al., Macrophages, Foreign Body Giant Cells and Their Response to Implantable Biomaterials. Materials (Basel, Switzerland), 2015. 8(9): p. 5671-5701.
120. Bezold, V., et al., Glycation of macrophages induces expression of pro-inflammatory cytokines and reduces phagocytic efficiency. Aging (Albany NY), 2019. 11(14): p. 5258-5275.
121. Hinz, B., The role of myofibroblasts in wound healing. Curr Res Transl Med, 2016. 64(4): p. 171-177.
122. Veiseh, O. and A.J. Vegas, Domesticating the foreign body response: Recent advances and applications. Adv Drug Deliv Rev, 2019. 144: p. 148-161.

123. Huyer, L.D., et al., Advanced Strategies for Modulation of the Material–Macrophage Interface. Advanced Functiional Materials, 2020. 30.
124. Mavrogenis, A.F., et al., Biology of implant osseointegration. J Musculoskelet Neuronal Interact, 2009. 9(2): p. 61-71.
125. Fini, M., et al., Osteoporosis and biomaterial osteointegration. Biomed Pharmacother, 2004. 58 (9): p. 487-93.
126. Murai, K., et al., Light and electron microscopic studies of bone-titanium interface in the tibiae of young and mature rats. J Biomed Mater Res, 1996. 30(4): p. 523-33.
127. Das, K., S. Bose, and A. Bandyopadhyay, TiO2 nanotubes on Ti: Influence of nanoscale morphology on bone cell-materials interaction. J Biomed Mater Res A, 2009. 90(1): p. 225-37.
128. Yao, C., E.B. Slamovich, and T.J. Webster, Enhanced osteoblast functions on anodized titanium with nanotube-like structures. J Biomed Mater Res A, 2008. 85(1): p. 157-66.
129. Beltrán-Partida, E., et al., Improved in vitro angiogenic behavior on anodized titanium dioxide nanotubes. J Nanobiotechnology, 2017. 15(1): p. 10.
130. Olivares-Navarrete, R., et al., Direct and indirect effects of microstructured titanium substrates on the induction of mesenchymal stem cell differentiation towards the osteoblast lineage. Biomaterials, 2010. 31(10): p. 2728-35.
131. Wen, Q., et al., The Process of Osteoblastic Infection by Staphylococcus Aureus. Int J Med Sci, 2020. 17(10): p. 1327-1332.
132. Bish, S.E., W. Song, and D.C. Stein, Quantification of bacterial internalization by host cells using a beta-lactamase reporter strain: Neisseria gonorrhoeae invasion into cervical epithelial cells requires bacterial viability. Microbes Infect, 2008. 10(10-11): p. 1182-91.
133. Dowling, A.J., G.E. Hill, and C. Bonneaud, Multiple differences in pathogen-host cell interactions following a bacterial host shift. Sci Rep, 2020. 10(1): p. 6779.
134. Mitchell, G., C. Chen, and D.A. Portnoy, Strategies Used by Bacteria to Grow in Macrophages. Microbiol Spectr, 2016. 4(3).
135. Lebaudy, E., et al., Recent Advances in Antiinflammatory Material Design. Adv Healthc Mater, 2021. 10(1): p. e2001373.
136. Horejs, C., Preventing fibrotic encapsulation. Nature Reviews Materials, 2021. 6(7): p. 554-554.
137. Ko, S.Y., et al., Osteoconductivity of Porous Titanium Structure on Implants in Osteoporosis. J Dent Res, 2021: p. 220345211023724.
138. Linklater, D., et al., Mechanical inactivation of Staphylococcus aureus and Pseudomonas aeruginosa by titanium substrata with hierarchical surface structures. Materialia 2019. 5.
139. Liu, X., et al., Biocompatibility evaluation of antibacterial Ti-Ag alloys with nanotubular coatings. Int J Nanomedicine, 2019. 14: p. 457-468.
140. Abaricia, J.O., et al., Hydrophilic titanium surfaces reduce neutrophil inflammatory response and NETosis. Biomater Sci, 2020. 8(8): p. 2289-2299.

141. Zhao, Y., et al., Regulation of endothelial functionality through direct and immunomodulatory effects by Ni-Ti-O nanospindles on NiTi alloy. Mater Sci Eng C Mater Biol Appl, 2021. 123: p. 112007.
142. El Kholy, K., et al., Investigating the Response of Human Neutrophils to Hydrophilic and Hydrophobic Micro-Rough Titanium Surfaces. Materials (Basel), 2020. 13(15).
143. Hamlet, S.M., et al., Hydrophilic titanium surface-induced macrophage modulation promotes pro-osteogenic signalling. Clin Oral Implants Res, 2019. 30(11): p. 1085-1096.
144. Martínez-Pérez, M., et al., The "Race for the Surface" experimentally studied: In vitro assessment of Staphylococcus spp. adhesion and preosteoblastic cells integration to doped Ti-6Al-4V alloys. Colloids Surf B Biointerfaces, 2019. 173: p. 876-883.

nanomaterials MDPI

(IF 5.72)

Bright R, Hayles A, Wood J, Ninan N, Palms D, Visalakshan RM, Burzava A, Brown T, Barker D, Vasilev K. Bio-Inspired Nanostructured Ti-6Al-4V Alloy: The Role of Two Alkaline Etchants and the Hydrothermal Processing Duration on Antibacterial Activity. Nanomaterials (Basel). 2022 Mar 29;12(7):1140. DOI: 10.3390/nano12071140 . PMID: 35407257; PMCID: PMC9000892.

CHAPTER 2:

BIO-INSPIRED NANOSTRUCTURED TI-6AL-4V ALLOY: THE ROLE OF TWO ALKALINE ETCHANTS AND THE HYDROTHERMAL PROCESSING DURATION ON ANTIBACTERIAL ACTIVITY

Richard Bright [1], Andrew Hayles [1], Jonathan Wood [1], Neethu Ninan [1], Dennis Palms [1], Rahul M. Visalakshan [2], Anouck Burzava [1], Toby Brown [3], Dan Barker [3] and Krasimir Vasilev [1,4,*]

[1] Academic Unit of STEM, University of South Australia, Mawson Lakes, Adelaide, 5095, South Australia, Australia. [2] Corin Australia, Baulkham Hills, NSW 2153, Australia.
[3] College of Medicine and Public Health, Flinders University, Bedford Park 5042, South Australia, Australia

(*Corresponding author email: krasimir.vasilev@unisa.edu.au)

1.1 Graphical Abstract

2.2 Abstract

Inspired by observations that the natural topography observed on cicada and dragonfly wings may be lethal to bacteria, researchers have sought to reproduce these nanostructures on biomaterials to reduce implant-associated infections. Titanium and its alloys are widely employed biomaterials with excellent properties but are susceptible to bacterial colonisation. Hydrothermal etching is a simple, cost-effective procedure that fabricates nanoscale protrusions of various dimensions upon titanium, depending on the etching parameters used. We investigated the role of etching time and the choice of cation (sodium and potassium) in the alkaline heat treatment on the topographical, physical, and bactericidal properties of the resulting modified titanium surfaces. Optimal etching times were 4 h for sodium hydroxide (NaOH) and 5 h for potassium hydroxide (KOH). NaOH etching for 4 h produced dense but somewhat ordered, surface nanofeatures with 75 nanospikes per μm^2. In comparison, KOH etching for 5 h resulted in sparser but disordered surface morphology with only 8 spikes per μm^2. The NaOH surface was more effective at eliminating Gram-negative pathogens, while the KOH surface was more effective against the Gram-positive strains. These findings may guide further research and development of bactericidal titanium surfaces which are optimised for the predominant pathogens associated with the intended application.

2.3 Introduction

Worldwide, there is a growing demand for implantable medical devices, in part due to an aging population made possible by advancements in medicine and technology [1]. Titanium and its alloys are the materials of choice in the field of orthopaedics, mainly due to their biocompatibility, excellent strength, and corrosion resistance [2]. While there is a high success rate for total joint replacement surgeries, implant failure is a pervasive and unrelenting threat. The primary cause of implant failure is due to bacterial contamination, and it is estimated that 1.5–2.5% of orthopaedic implants become a site of infection [3]. Implant-associated infection (IAI) is a devastating complication that is associated with severe morbidity and a mortality rate between 2.7 and 18% [4–6]. Evidence suggests that the presence of an implant reduces the minimal inoculum of bacteria required to cause infection by a factor of greater than 100,000 [7,8]. IAI can occur through multiple paths of pathogenesis. In one setting, bacteria residing on the patient's skin can translocate to the implanted device during surgery [9,10]. Alternatively, an infection can arise from the haematogenous transfer, whereby bacteria at distal sites of infection travel through the bloodstream and encounter the implanted device [11,12]. In another mode of pathogenesis, contiguous spread from infected tissue (e.g., trauma, pre-existing osteomyelitis, and soft tissue lesions) acts as a reservoir for pathogens to transfer to the implanted device [9,13]. Regardless of the route of pathogenesis, bacterial attachment, and colonisation of the implant surface, IAI is the unfortunate outcome. Bacteria residing on the implanted device strongly attach to the surface and proliferate to form a biofilm in a sequence of stages. Biofilm formation can be characterised by 3 broad phases: attachment, maturation, and dispersal [14]. Primary attachment is reversible and involves van der Waals and electrostatic forces [15].

Attachment is gradually strengthened by the presence of proteins, known as adhesins, which facilitate the covalent linkage of the cell to the surface. The maturation phase of biofilm formation is marked by the production and secretion of extracellular polymeric substance (EPS), which contains polysaccharides, proteins, lipids, extracellular DNA, and quorum-sensing molecules [16,17]. EPS is multifunctional, acting as a structural support, a medium for the exchange of molecules, and a defence against antimicrobial compounds and phagocytic cells. Once a biofilm has progressed through the maturation phase, it is exceedingly difficult to treat with antibiotics, and mature biofilms are known to be up to 1000× more resistant to antibiotics compared to their planktonic counterparts [18–20]. Due to this, IAI usually requires surgical intervention to remove or replace the implanted device [21]. When fully matured, the biofilm acts as a reservoir of cells that can be readily dispersed into the neighbouring environment, potentially causing further infection in sites around the body, or lethal septicaemia [22–24].

To tackle the burden of IAI, much research has focused on the modification of implanted biomaterials to grant them anti-infective properties. For example, surfaces can be coated with antimicrobial peptides or drug-eluting compounds [25–28]. An alternative strategy is to modify the nanoscale topography of the surface itself to generate protruding structures that are hostile to bacteria but accommodating to host cells. Bacteria attaching to nanoscale protrusions have their cell membrane perturbed and penetrated, and this mechanical interaction is associated with induced oxidative stress and cell death [29]. The bactericidal effect of nanoscale protrusions was first observed on cicada wings by Ivanova and colleagues [30] and has since served as inspiration for the fabrication of a new generation of anti-infective surfaces. Bioinspired nanoscale protrusions have been successfully fabricated on silicon [31] and titanium [32,33] using a range of techniques. Hydrothermal etching is one such technique that has been used to modify titanium surfaces. It is attractive due to its simplicity, cost-effectiveness, and potential for large-scale manufacture [34]. The process of hydrothermal etching involves submerging a sample in an alkaline solution at high temperatures to form an oxide layer with nanoscale architecture [35]. The morphology of the resultant nanostructure is influenced by the combination of fabrication parameters used in the process including primarily etching duration, temperature, and alkaline etchant.

The purpose of this study is to examine the role of etchant type and processing time on the morphology of the resultant surfaces and their antibacterial capacity. Potassium hydroxide (KOH) and sodium hydroxide (NaOH) were used as etchants. Etching time was 1, 3, 4, and 5 h. The modified surface was challenged with three clinically relevant pathogens: *Staphylococcus aureus* (*S. aureus*), *Escherichia coli* (*E. coli*), and *Pseudomonas aeruginosa* (*P. aeruginosa*). The Gram-positive coccus *S. aureus* was chosen due to its ubiquitous association with IAIs [9], and well-documented resilience to mechanical killing [36] combined with its capacity to develop antibiotic resistance [37]. *E. coli* and *P. aeruginosa* were chosen as representative Gram-negatives which frequently appear in implant infections [38,39].

P. aeruginosa rods are typically longer than *E. coli* rods (up to 5 μm and up to 2 μm, respectively) [40,41] which makes them good examples to study the relationship between pathogen morphological characteristics and nanostructure topographical dimensions.

2.4 Materials and Methods

2.4.1 Fabrication of Hydrothermally Etched Ti-6Al-4V

Ti-6Al-4V discs (10 mm in diameter, 3 mm in height, and a surface area of 0.78 cm^2) were received and polished at a Ra of 0.5 μm (Hamagawa Industrial (M) SDN BHD, Kedah, Malaysia). To create the nanostructured surface, the discs were hydrothermally etched at 150 °C, using either 1 M KOH or 1 M NaOH in a stainless-steel reactor (Parr Instrument Company, Moline, IL, USA). Next, the reactors were cooled, and the samples were cleaned in ultrapure water. Ti-6Al-4V discs were then dried, followed by heat treatment inside an oven and allowed to cool down overnight. The as-received titanium alloy discs were used as controls (AR-Ti) and hydrothermally etched discs, using 1 M NaOH and 1 M KOH aqueous etching solutions, were then cleaned and sterilised at 121 °C for 20 min before use. Samples were fabricated using both alkaline solutions, (1 M KOH and 1 M NaOH) with etching times of 1, 3, 4, and 5 h.

2.4.2 Characterisation of the Surface Nanotopography

Scanning electron microscope (SEM) characterisation was performed on samples fabricated using both alkaline etchant solutions (1 M KOH and 1 M NaOH) with etching times of 1, 3, 4, and 5 h. The morphology and distribution of nanostructures upon the surface of the titanium substrate were analysed on a field emission gun scanning electron microscope Zeiss Merlin FEG-SEM (Zeiss, Jena, Germany), equipped with a secondary electron (SE) detector, at 2 KV with magnification from 5–50 K. The stage was tilted at 45 degrees for imaging of the nanostructures, and orthogonal when analysing the density of individual nanostructures and imaging bacteria on the surfaces. The height of the nanostructures was determined by the linear distance between a basal plane and the highest point of each spike (n = 20), whereas the diameter was measured at mid-height in parallel orientation with the basal plane, and a correction factor of x/cos (45°) to amend dimensional distortion during linear measurements, where x equals the length of nanostructures. Spike height and diameter at mid-height were expressed as mean ± standard deviation, and n = 5. The spacing between nanostructures was determined from four zero-degree tilted SEM images, considering the nanostructure tips in a 25 μm^2 area and presented as mean ± standard deviation. Density was calculated by counting spike tips and expressing them as nanostructures per μm^2. The nanostructure dimensions were determined using ImageJ software version 1.53f51 (NIH, Bethesda, MD, USA).

2.4.3 Atomic Force Microscopy of 1M NaOH-Etched for 4 h (NaOH-4 h) and 1M KOH-Etched for 5 h (KOH-5 h) Samples

Atomic force microscopy (AFM) was used to acquire 25 μm^2 images in the air using a JPK NanoWizard III with instrument-specific software v5. An NT-MDT NSG03 silicon nitride cantilever with a conical tip rated by the manufacturer at a radius less than 10 nm and a half side angle of 18° was used to perform tapping mode on annealed AR-Ti and the optimal bactericidal etched samples, NaOH-4 h and KOH-5 h. Initial calibration of the cantilever on a glass microscope slide derived a normal spring constant of 1.8 N/m at just off the first resonant frequency of 84.5 kHz. Scanning parameters over a scan rate of 0.7 Hz were at a set point of 22 nm and a drive amplitude of 1.24 Volts. Roughness values were calculated, and images were acquired using Gwyddion data analysis software v2.54 (http://gwyddion.net/, accessed on 30/08/2021).

2.4.4 Surface Analysis by X-ray Photoelectron Spectroscopy (XPS)

The chemical composition of the upper 10 nm layer of AR-Ti, NaOH-4 h, and KOH-5 h was analysed using X-ray photoelectron spectroscopy (XPS). XPS survey spectra were collected using a Kratos AXIS Ultra DLD spectrometer (Kratos Analytical Ltd., Manchester, UK) equipped with a magnetically confined charge compensation system, with monochromatic AlKα radiation (hv = 1486.7 eV). The sample area analysed was 300 μm × 700 μm at a pass energy of 160 eV. Data analysis was performed with CasaXPS software (Casa Software Ltd., Teignmouth, UK). All binding energies were referenced to the low energy, aliphatic C 1 s peak at 285.0 eV.

2.4.5 Contact Angle of NaOH-4 h and KOH-5 h

Surface wettability was evaluated for AR-Ti, NaOH-4 h, and KOH-5 h using a contact angle evaluated by the sessile drop method using a contact angle goniometer model RD-SDM02 (RD Support, Scotland, UK). The contact angle from probe liquid and ultrapure water (4 uL) was measured by a tangent fitting method using the plugin Contact_Angle.jar for Image J software version 1.53f51 (NIH, Bethesda, MD, USA).

2.4.6 Bacterial Cultures

Escherichia coli ATCC 11303 (*E. coli*), *Pseudomonas aeruginosa* ATCC 15692 (*P. aeruginosa*), and *Staphylococcus aureus* ATCC 25923 (*S. aureus*) were cultured in tryptic soy broth (TSB; Oxoid, ThermoFisher, Waltham, MA, USA) and incubated overnight at 37 °C. Before starting the bacterial experiments, it was determined that an optical density of 1 measured at 600 nm (OD_{600}) was approximately 1×10^9 CFU/mL.

2.4.7 LIVE/DEAD BacLight Bacterial Viability

To compare the different etching times (1, 3, 4, and 5 h) and etchants (NaOH and KOH), overnight cultures of bacteria were adjusted to a concentration of 1 × 10^6 CFU/mL, and 1 mL added to wells containing titanium discs (AR-Ti, NaOH, and KOH-etched samples) in triplicate, and incubated for 20 h at 37 °C in a humid chamber. Next, the samples were stained with LIVE/DEAD® BacLight™ Bacterial Viability Kit (ThermoFisher Scientific, Waltham, MA, USA) as per the manufacturer's instructions and analysed by an Olympus FV3000 laser confocal microscope (CLSM; Olympus, Tokyo, Japan). Samples were inverted onto a glass coverslip and four randomly selected regions were imaged. SYTO 9 and propidium iodide fluorescence excitation/emissions were monitored at 480/500 nm and 490/635 nm, respectively. The viability was determined using ImageJ software v1.53a (NIH, Bethesda, MD, USA).

2.4.8 Bacteria–Nanotopography Interaction by SEM

Overnight cultures of *E. coli*, *P. aeruginosa*, and *S. aureus* incubated on AR-Ti, NaOH-, and KOH-etched samples were fixed for 1 h with 4% paraformaldehyde, 1.25% glutaraldehyde, and 4% sucrose in PBS. Following fixation, they were washed in PBS, followed by dehydration in an ascending ethanol order from 50% (*v*/*v*) to absolute ethanol and further dried using hexamethyldisilazane (HMDS; Sigma-Aldrich, St. Louis, MI, USA). After the dehydration process, the discs were mounted on aluminium stubs using double-sided carbon tape, sputter-coated with 2 nm platinum, and examined using a Zeiss Merlin FEG-SEM (Zeiss, Jena, Germany).

2.4.9 Cytocompatibility Analysis of NaOH-4 h and KOH-5 h Surfaces

Primary human-derived dermal fibroblast cells (HDF) were seeded on AR-Ti, NaOH-4 h, and KOH-5 h samples in a 48-well plate. Cultures were maintained in Dulbecco's modified Eagle medium (DMEM; Life Technologies, Carlsbad, CA, USA) supplemented with 10% *v*/*v* foetal bovine serum (FBS; Life Technologies, Carlsbad, CA, USA) and 1% (*v*/*v*) penicillin/streptomycin (Life Technologies, Carlsbad, CA, USA). Tissue culture plate (TCP) and AR-Ti discs were used as positive controls. HDF cells were seeded at a density of 2.5 × 10^4 cells/well. The short-term cytocompatibility was assessed using the resazurin assay (Resazurin sodium salt, R7017, Sigma Aldrich, St. Louis, MI, USA). A stock solution of 100 µg/mL resazurin was prepared in phosphate-buffered saline (PBS) and diluted to a final working concentration of 10 µg/mL. Briefly, the cells were incubated on TCP, AR-Ti, NaOH-4 h, and KOH-5 h for 48 h at 37 °C and 5% CO_2, after which the culture medium was replaced with 250 µL media containing 10% resazurin of the stock solution and incubated for 1 h. Next, 100 µL of the supernatant was transferred into a 96-well plate and the fluorescent intensity was recorded using a plate reader. Resazurin is a fluorescent assay that detects cellular metabolic activity. The blue nonfluorescent resazurin reagent is reduced to highly fluorescent resorufin by dehydrogenase enzymes in metabolically active cells.

The resorufin formed in the assay was quantified by measuring the fluorescent intensity using a plate reader (Ex = 530–570 nm, Em = 590–620 nm). The percent of cell viability is calculated using the following formula, $\frac{\boldsymbol{Fluorescent\ intensity\ of\ treated}}{\boldsymbol{Fluorescent\ intensity\ of\ control}} \times \mathbf{100}$, normalised to TCP control. To investigate changes in HDF cell morphology after 48 h incubation upon the surfaces, Phalloidin (Alexa Fluor 488 phalloidin, A12379, Thermo Fisher Scientific, Waltham, MA, USA) was used to stain actin and DAPI (4′,6-Diamidino-2-Phenylindole, Dihydrochloride, D1306, Thermo Fisher Scientific, MA, USA) to visualise the nucleus following recently published work [42]. Samples were washed in PBS, inverted onto a glass coverslip, and imaged by an Olympus FV3000 confocal laser scanning microscope (CLSM; Olympus, Tokyo, Japan).

2.4.10 Statistical Analysis

Statistical analysis for surface parameters and viability was carried out using one-way ANOVA or Student's *t*-test followed by post hoc analysis using Tukey's multiple comparisons tests. To compare nanostructure topographical dimensions, a student's *t*-test was performed. Statistical analysis was performed using GraphPad Prism version 8.3.0 (GraphPad Software, San Diego, CA, USA., www.graphpad.com, accessed on 8/12/2021). All experiments were undertaken in triplicate and reported as mean and standard deviation. In all experiments, significance was set at $p < 0.05$.

2.5 Results

2.5.1 Morphology and Dimensional Analysis of NaOH- and KOH-Etched Samples

A range of surface nanostructures was created on titanium alloy discs using hydrothermal etching with either NaOH or KOH aqueous solutions. Surfaces were etched for 1, 3, 4, or 5 h to investigate the changes in geometrical and morphological characteristics to investigate the nanostructure evolution with time. Surfaces were then annealed to improve corrosion resistance, alloy plasticity, abrasion resistance, and potential for bone on-growth, and reduce surface stress developed during fabrication [43,44]. The SEM micrographs presented in Figure 1 shows the formation of nanostructures, resembling those found in nature such as on dragonfly wings (Figure S1) [45,46], observed on both NaOH- (Figure 1A–E) and KOH-etched surfaces (Figure 1F–J). Although displaying an overall similar "spike-like" shape, architectural differences could be observed between the two etching solutions tested. Nanostructures on NaOH-etched surfaces appeared more densely packed, straighter (Figure 1 A–E), and shorter than those formed on KOH-etched surfaces (Figure 1E–J). The nanostructures formed on the KOH-etched samples appeared to be arranged in a hierarchal disordered format (Figure 1F–J) [47].

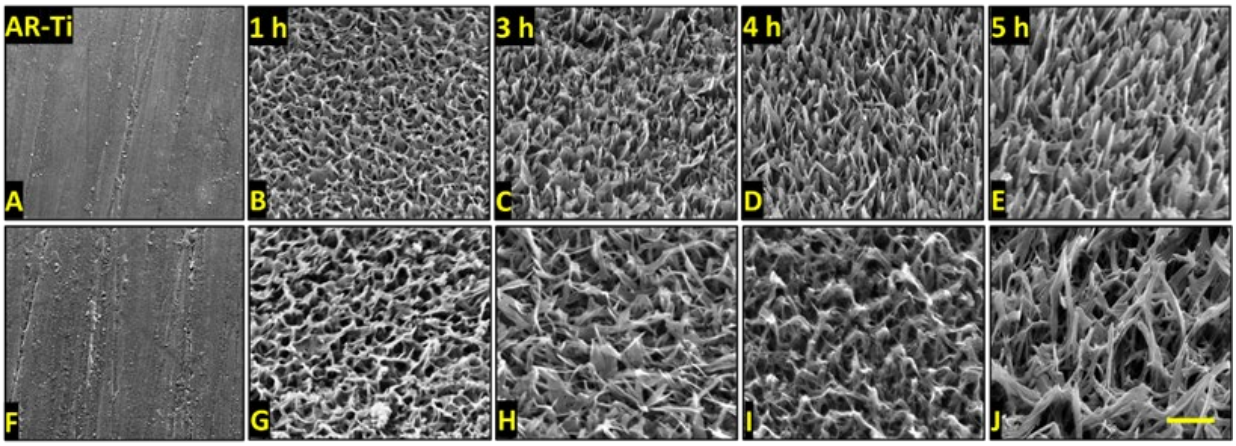

Figure 1. *SEM micrographs showing the morphology and distribution of nanoarchitecture obtained after etching the surface for 0 (AR-Ti), 1, 3, 4, and 5 h using either NaOH (A–E) and KOH (F–J) aqueous-based etching solutions. Images were acquired at 50,000x magnification with 45° stage tilt, the scale bar bottom left panel represents 500 nm.*

The SEM micrographs were used to measure spike height, diameter at mid-height, spacing between, and density per μm^2. The results are presented in Figure 2A and Table S1 for the NaOH-etched samples and Figure 2B and Table S1 for the KOH-etched samples. The spike height significantly increased as the etching time increased between 1 and 5 h for both NaOH- and KOH-etched surfaces ($p < 0.0001$). The nanostructure diameter at mid-height, followed an upward trend for NaOH, with a significant increase between 1 h and 3 h etching times (30 ± 4 nm and 94 ± 33 nm, respectively, $p < 0.0001$), and 1 h and 5 h etching times (30 ± 4 nm at 1 h and 83 ± 30 nm, respectively, $p < 0.0001$). However, the nanostructures' diameter at mid-height remained almost constant from 1 to 5 h in the case of KOH-etching (65 ± 10 nm and 83 ± 32 nm, respectively, $p = 0.02$). The spacing between nanostructures remained unchanged for etching times on the NaOH-etched surfaces (1 h and 5 h etching times, 185 ± 41 nm, and 224 ± 55 nm, respectively, $p = 0.02$), and increased on KOH-etched surfaces (1 h and 5 h etching times, 330 ± 83 nm, and 544 ± 150 nm, respectively, $p < 0.0001$). This indicates that there was no new nanostructure formation over time, only the evolution of those that had already formed at the beginning of the hydrothermal process, the main outcome being the increase in nanostructure height. The density of the nanostructures was lower on the KOH-etched surface (8 ± 2 spikes/ μm^2 at 5 h etching time) compared to the NaOH-etched surface (32 ± 9 spikes/μm^2 at 5 h etching time).

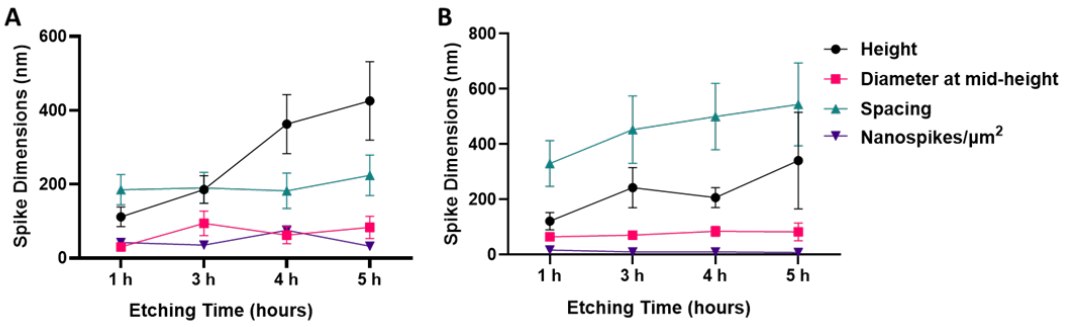

Figure 2. *Nanostructures' dimensions for NaOH-etched samples (A) and KOH-etched titanium samples (B) were measured from four etching times (1, 3, 4, and 5 h), and data points represent mean ± SD. Details of nanostructure height, diameter at mid-height, spacing and density can be found in Table S1.*

2.5.2 Analysis of Bacterial Morphology Using SEM

The interactions between the nanostructures and *E. coli*, *P. aeruginosa*, and *S. aureus* on the surfaces generated by NaOH and KOH hydrothermal etching for 1, 3, 4, and 5 h are shown in Figures 3 and 4. We observed morphologically disturbed cells on all treated surfaces (highlighted by yellow arrows). We observed the highest proportions of dead cells on NaOH-4 h and KOH-5 h. Overall, the two Gram-negative species were more frequently observed to be damaged and flattened against the surfaces compared to the Gram-positive *S. aureus*. This is somewhat expected as Gram-positive bacteria possess a thicker peptidoglycan layer which confers greater structural support compared to the relatively fragile Gram-negative species [34]. However, despite the greater rigidity of *S. aureus*, a high proportion of damaged cells were observed on the KOH-5 h surface (Figure 4).

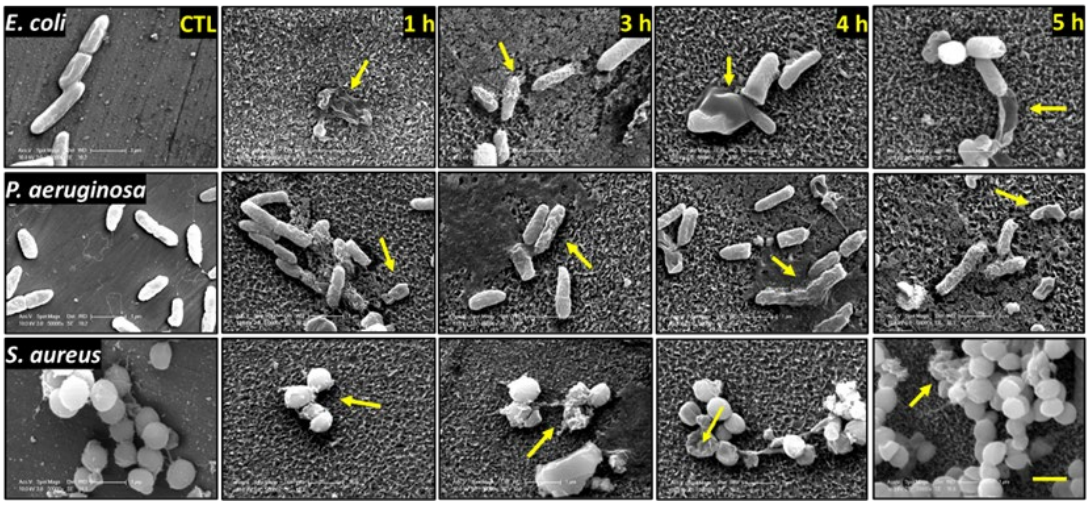

Figure 3. *SEM micrographs of E. coli, P. aeruginosa, and S. aureus following 20 h incubation on the NaOH-etched samples (1, 3, 4, and 5 h etching time). Yellow arrows indicate damaged bacteria. SEM micrographs were acquired at 50,000x magnification, and the scale bar bottom right image represents 1 µm.*

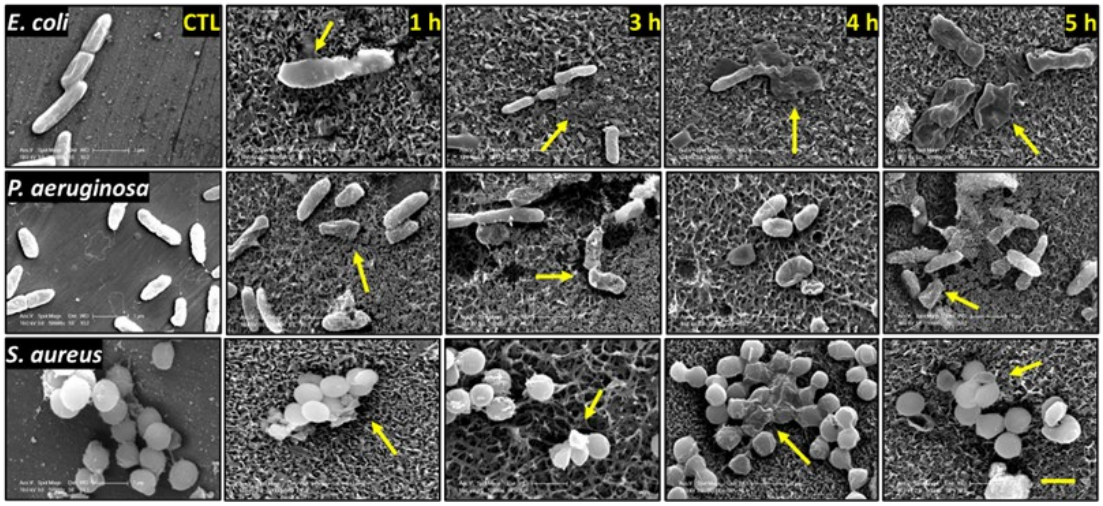

Figure 4. *SEM micrographs of E. coli, P. aeruginosa, and S. aureus following 20 h incubation on the KOH-etched samples (1, 3, 4, and 5 h etching time). Yellow arrows indicate damaged bacteria. SEM images were acquired at 50,000x magnification. The scale bar bottom right image represents 1 µm.*

2.5.6 Bacterial Analysis by Live/Dead Assay

Live/Dead fluorescence analysis for the target bacterial species is shown in Figures 5 and 6, with the percentage viabilities for each pathogen on each surface shown in Figure 7. The two Gram-negative species were notably more vulnerable to nanostructure-induced cell death compared to *S. aureus*. For *P. aeruginosa*, viability ranged from 3.5 ± 2.0% to 6.7 ± 2.7% on the NaOH-etched surfaces. On the KOH-etched surfaces, *P. aeruginosa* viability ranged from 4.6 ± 0.8 to 16.7 ± 1.0%. The most effective surface against *P. aeruginosa* was NaOH-4 h, which reduced viability to 3.5 ± 2.0%. For *E. coli*, viability ranged from 20.7 ± 3.6% to 32.4 ± 2.5% on the NaOH-etched surfaces. On the KOH-etched surfaces, *E. coli* viability ranged from 38.1 ± 4.0% to 60.3 ± 4.1%. The most effective surface against *E. coli* was NaOH-4 h, which reduced viability to 20.7 ± 3.6%. For the Gram-positive *S. aureus*, viability ranged from 45.2 ± 2.0% to 91.1 ± 7.0% on the NaOH-etched surfaces. On the KOH-etched surfaces, the *S. aureus* viability ranged from 38.5 ± 4.8% to 73.2 ± 6.3%. The most effective surface against *S. aureus* was KOH-5 h, which reduced *S. aureus* to 38.5 ± 4.8%.

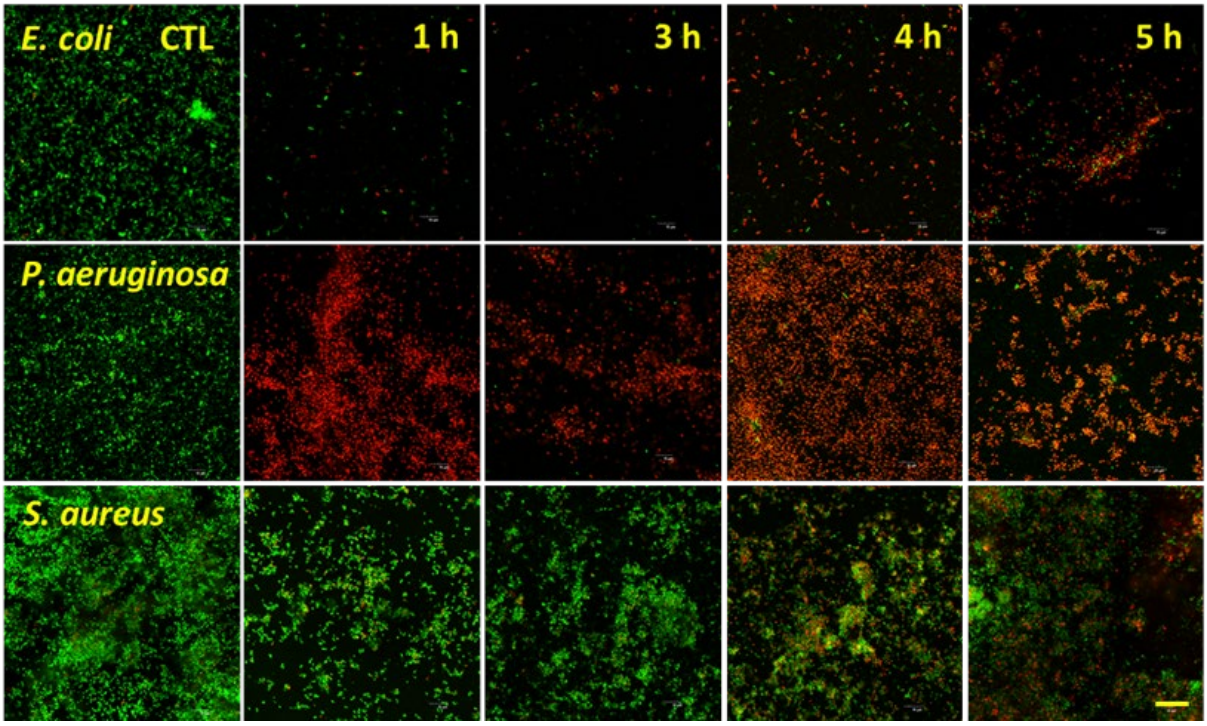

Figure 5. *Confocal microscopy micrographs of E. coli, P. aeruginosa, and S. aureus incubated on the surfaces of the titanium etched using 1 M NaOH for 1, 3, 4, and 5 h. Bacteria were inoculated on the etched samples at a concentration of 10^6 CFUs and incubated for 20 h. Cells were stained with a LIVE/DEAD BacLight™ bacterial viability kit. The scale bar represents 20 μm.*

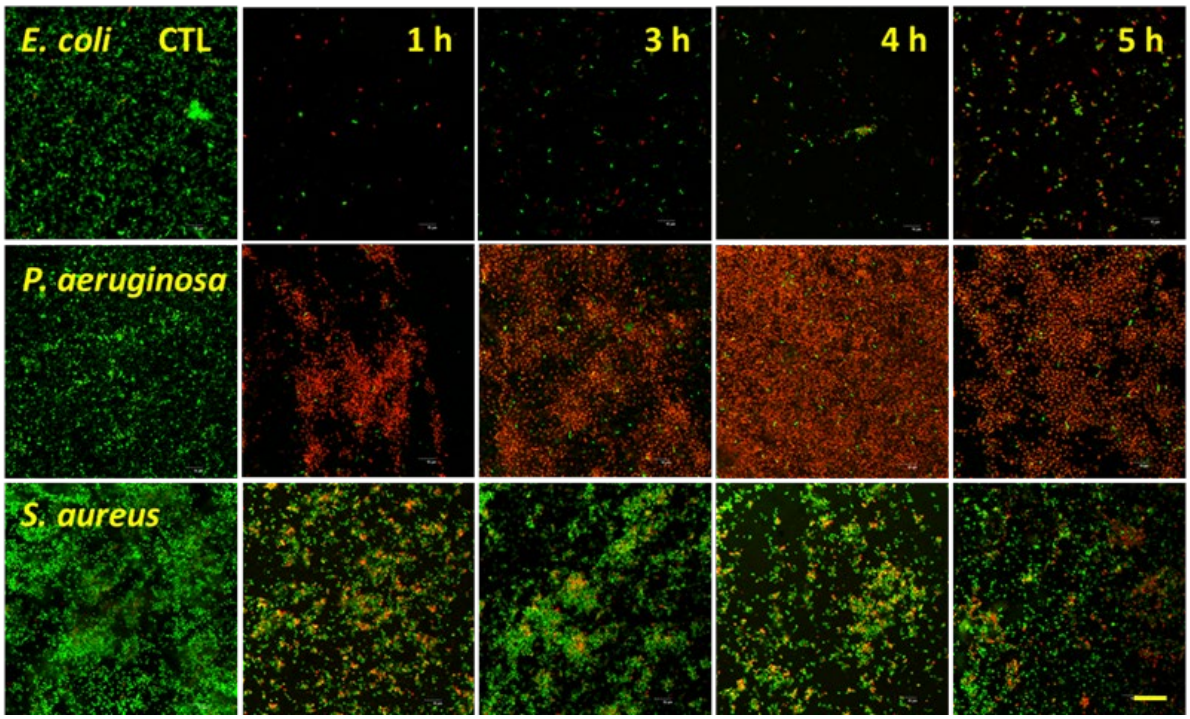

Figure 6. *Confocal microscopy images of E. coli, P. aeruginosa, and S. aureus incubated on the surfaces of the titanium etched using 1 M KOH for 1, 3, 4, and 5 h. Bacteria were inoculated on the etched samples at a concentration of 10^6 CFUs and incubated for 20 h. Cells were stained with a LIVE/DEAD BacLight™ bacterial viability kit. The scale bar represents 20 µm.*

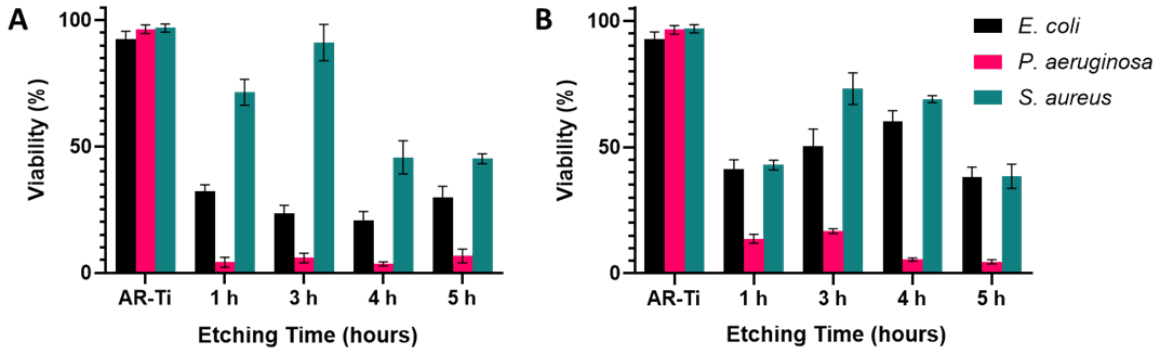

Figure 7. *Percentages of viability observed across the three bacteria test strains, after 20 h incubation on both NaOH-etched (A) and KOH-etched (B) for 1, 3, 4, and 5 h etching time, with an initial seeding concentration of 10^6 CFUs (mean ± SD, n = 3).*

Based on the above data, the etching duration that produces nanotopography with the highest bactericidal activity for NaOH was 4 h, whereas for KOH it was 5 h. Additionally, it can be noted that the NaOH-4 h surface was more effective at eliminating the two Gram-negative pathogens, while the KOH-5 h surface was more effective at eliminating the Gram-positive *S. aureus* [48]. We, therefore, selected these two etching parameters for further surface property characterisation to understand their differing bactericidal activity.

2.5.7 Characterisation of the NaOH-4 h and KOH-5 h Samples

To find a potential explanation for the observed bactericidal selectivity between NaOH-4 h and KOH-5 h, we first compared the spike dimensions of the fabricated nanostructures (Table 1). We found no statistical difference between the height and diameter at mid-height of the nanostructures (p = 0.81 and p = 0.41, respectively). However, although the spike heights were not significantly different, the KOH-5 h shows a much greater range in measured nanostructure height (175 nm) compared to the NaOH-4 h (80 nm). This irregularity of spike heights can be observed in both the SEM and AFM micrographs (Figures 1 and 8, respectively). The NaOH-4 h surface had significantly lower structure spacing (p = 0.02) and greater spike density (p = 0.0001) when compared to the KOH-5 h surface.

Table 1. *Topography dimensional comparison between NaOH-4 h and KOH-5 h.*

Parameter	NaOH-4 h	KOH-5 h	Significance (*p*)
Height (nm)	367 ± 80	340 ± 175	0.81
Diameter at mid-height (nm)	62 ± 23	83 ± 32	0.41
Spacing (nm)	182 ± 48	544 ± 150	0.02
Spike density (spikes/μm^2)	75 ± 8	8 ± 2	< 0.0001

Elemental composition detected on the AR-Ti, NaOH-4 h, and KOH-5 h surface using XPS is presented in Figure 8A. There was an increase in oxygen concentration of 5.6% on the NaOH-4 h surface and 7.6% on the KOH-5 h surface compared to the AR-Ti control. This is consistent with the thickening of the oxide layer (TiO_2) occurring during the hydrothermal etching process. Furthermore, the thicker oxide layer also resulted in a reduction in the surface concentration of vanadium and aluminium as the XPS sampling depth is limited to the outermost 10 nm of the surface. This may prove to be advantageous for implantable biomaterials as wear particles and leaching of vanadium and aluminium from Ti-6Al-4V have raised concerns due to their potential toxicity and DNA-damaging effects [49–51]. Additionally, small levels of sodium and potassium were incorporated within the NaOH-4 h and KOH-5 h surface, respectively, consistent with the use of sodium and potassium as cations for the alkaline treatment.

To compare the hydrophilicity of samples before and after hydrothermal etching, water contact angles (WCA) were measured. The WCA for NaOH-4 h surface (7.6° ± 1.2°) and KOH-5 h (9.7° ± 1.1°) was significantly lower than that for the AR-Ti surface (76.0° ± 5.0°), $p < 0.0001$, indicative of significantly increased hydrophilicity (Figure 8B). There was no significant difference in water contact angle between the NaOH-4 h and KOH-5 h surface treatments ($p > 0.05$). Such superhydrophilic behaviour is the result of the combination of surface roughness at the nanoscale and a hydrophilic TiO_2 surface layer, consistent with the Wenzel and Cassie Baxter theory [52–54]. An increase in hydrophilicity is an imperative characteristic of the hydrothermally etched surface since the phenomenon is generally associated with improved biocompatibility and enhanced bactericidal properties [55,56].

The surface area and roughness measurements calculated from the AFM analysis can be found in Table S2. AFM images confirmed marks due to the polishing process on the AR-Ti surface (Figure 8C). Nanostructures were observed on the NaOH-4 h and KOH-5 h samples (Figure 8D and 8E, respectively); however, fine details of nanostructures such as those seen by SEM were not observed by AFM. It should be noted that the tip convolution effect resulting from the cantilever geometry and scan velocity reduced the measured surface roughness values, particularly towards nanostructures with comparable magnitude to the tip radius [57]. AFM analysis for NaOH-4 h and KOH-5 h showed greater roughness and surface area compared to the AR-Ti surface.

The root mean square (RMS), arithmetic roughness average (Ra), and surface area (SA) calculated from the AFM images for the AR-Ti surface were 10.1 nm, 6.6 nm, and 25.2 μm² respectively, whereas, for the NaOH-4 h surface, these parameters were 88.4 nm, 71.4 nm, and 79.9 μm², respectively. Compared to the NaOH-4 h surface, the KOH-5 h surface had a similar RMS value of 88.5 nm, and a decrease in both Ra and SA (61.5 nm and 50.3 μm², respectively, Figure 8F).
The relative surface area measurements between NaOH-4 h and KOH-5 h are consistent with the measured structure dimensions and the greater surface area of NaOH-4 h is reflective of more densely packed nanospikes compared to KOH-5 h.

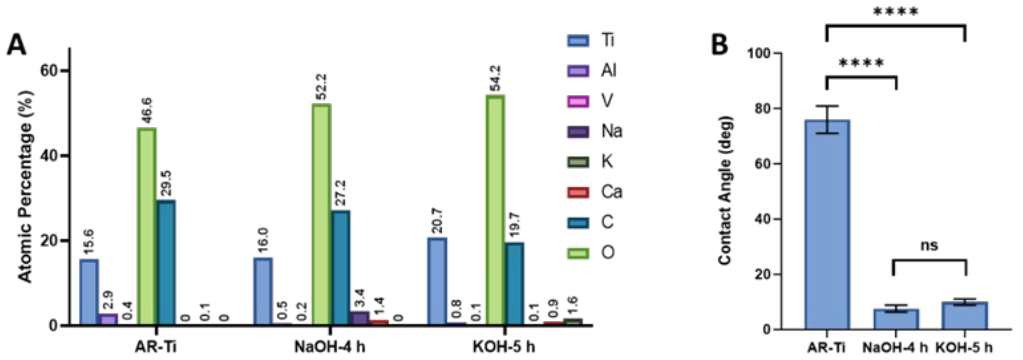

F

	RMS (nm)	Ra (nm)	SA (μm²)
AR-Ti	10.1	6.6	25.2
NaOH-4 h	88.4	71.4	79.9
KOH-5 h	88.5	61.5	50.3

Figure 8. *Surface analysis of NaOH-4 h and KOH-5 h, by XPS survey spectra (A), surface wettability (B), mean ± SD and n = 3, **** p < 0.001, ns = non-significant, and AFM 3D nanotopological features of a 25 μm² region on AR-Ti, NaOH-4 h, and KOH-5 h samples (C–E), scale bars represent 1 μm. The root mean square (RMS), arithmetic roughness average (Ra), and surface area (SA) for AR-Ti, NaOH-4 h, and KOH-5 h samples, were calculated using Gwyddion data analysis software from the AFM data (F).*

Based on the above data, it can be noted that there are only two considerable differentiating characteristics between the NaOH-4 h and KOH-5 h surfaces. The first is the nonuniformity of nanostructures length on KOH-5 h, which creates a chaotic array of spikes of different heights, reminiscent of the dragonfly wing (Figure S1).

In contrast, the nanospikes observed on NaOH-4 h were relatively uniform and had similar heights. The chaotic arrangement of spikes with nonuniform heights on the KOH-5 h surface may therefore allow it to pierce bacteria from multiple angles rather than just from the bottom. The other perhaps more important differing characteristic is the spacing between nanospikes. On the NaOH-4 h surfaces, the spikes are densely packed with a mean of 75 spikes per μm^2, compared to the sparser KOH-5 h surfaces with a density of approximately 8 spikes per μm^2.

These data suggest that the NaOH-4 h nanoarchitecture supports bactericidal activity against Gram-negative rods, while a KOH-5 h nanoarchitecture supports a high bactericidal efficacy of Gram-positive cocci. This may prove to be an important finding which could guide research and the development of nanostructures with specific functional outcomes. In the case of implantable biomaterials in the orthopaedic field, the KOH-5 h surface may be preferred over the NaOH-4 h surface due to its spike density favouring bactericidal activity against Gram-positive cocci, such as the clinically relevant *S. aureus*. As *S. aureus* is one of the most predominant bacterial pathogens in orthopaedic implant infections, implant manufacturers may benefit from treating titanium implants with the KOH-5 h procedure described in the present report.

2.5.8 *In Vitro* Short-Term Cytocompatibility

The cytoskeleton and nuclei of HDF cells on the nanostructured surfaces (AR-Ti, NaOH-4 h and KOH-5 h) incubated for 48 h are shown in Figure 9. The HDF cells incubated on the AR-Ti surface exhibited a polarised phenotype manifested by an elongated cell body (Figure 9A), whereas the cells incubated on NaOH-4 h and KOH-5 h surfaces were somewhat less polarised, with cells showing spreading upon the surfaces due to the interaction with the nanostructures [58]. This suggests the HDF cells incubated on these surfaces exhibit strong adhesion [59]. Cell viability determined via the resazurin method is shown in Figure 9C. The HTE-treated surface did not cause any cytotoxicity as the viability of the cells was 84.6 ± 16.4% on the NaOH-4 h and 87.5 ± 16.9 on the KOH-5 h, compared to the AR-Ti 82.1 ± 7.5%, $p > 0.05$ (Tables S3). These results indicate good viability and cell attachment on the nanostructured surfaces, indicating adequate cytocompatibility and biocompatibility.

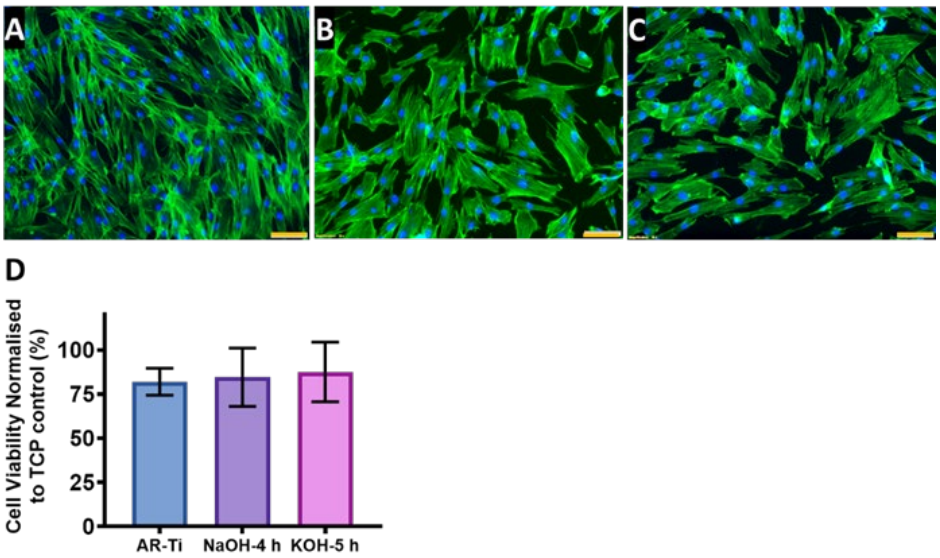

Figure 9. *Confocal micrographs demonstrating cellular morphology of HDF stained with Phalloidin (green) and DAPI (blue) incubated on AR-Ti (A), NaOH-4 h (B), and KOH-5 h samples (C). Percentage cell viability normalised to TCP control (D), mean ± SD, n = 3 and scale bars in Figure 9A–C represent 100 µm. p-values may be found in Table S3.*

2.6 Conclusion

We investigated the role of alkaline etchants and hydrothermal processing duration on the resultant surface nanotopography outcomes for titanium alloy discs. Nanostructured surfaces were challenged with three clinically relevant pathogens to determine their bactericidal potential. Our bacteriological analysis allowed us to narrow down the etching parameters to two favourable processing conditions involving either NaOH-etching for 4 h or KOH-etching for 5 h. NaOH-4 h treatment exhibited spikes that are densely packed with a mean of 75 spikes per μm^2, compared to the sparser KOH-5 h with a density of approximately 8 spikes per μm^2 suggesting that a greater density of spikes supports bactericidal activity against Gram-negative rods, while a sparser nanostructures array supports the killing of Gram-positive cocci. A short-term in vitro cytocompatibility study using HDF cells incubated on NaOH-4 h and KOH-5 h surfaces showed no unfavourable effects on morphology, viability, and proliferation. Further research is required to fully understand the mechanisms supporting the antibacterial properties of the nanostructured surface. However, this study highlights that with appropriate optimisation, substrates with selective antibacterial activity could be potentially achieved.

2.7 Supplementary Materials

The following supporting information can be downloaded at: https://www.mdpi.com/article/10.3390/nano12071140/s, Figure S1: SEM micrographs comparing nanostructures from a dragonfly wing and hydrothermally etched nanostructures.

Table S1: Geometry and distribution of the nanospikes fabricated using both NaOH and KOH etchant solutions and 1, 3, 4, and 5 h etching times. Table S2: AFM roughness measurements. Table S3: Mean difference, confidence intervals, and *p*-values for in vitro short-term cytocompatibility of HDF.

2.8 Author Contributions

R.B. designed, planned and performed the experiments. R.B. and A.H. analysed data and drafted the manuscript. J.W., D.P., N.N., R.M.V., and A.B. performed the surface characterisation and participated in data analysis. R.B., K.V., D.B., and T.B. conceptualised, designed, and planned the study and revised the manuscript. K.V. supervised the study and revised the manuscript. All authors have read and agreed to the published version of the manuscript.

2.9 Funding

This study was co-funded by the Department of Industry, Science, Energy and Resources (Innovative Manufacturing CRC Ltd., Carlton, VIC 3053, Australia) Global Orthopaedic Technology Pty Ltd., Bella Vista, NSW 2153, Australia (IMCRC/GOT/130318).

2.10 Data Availability Statement

The datasets generated and/or analysed during the current study are available from the corresponding author upon reasonable request.

2.11 Acknowledgments

The authors acknowledge the funding and in-kind support from Corin Australia and the University of South Australia. The authors would also like to acknowledge the instruments and scientific and technical assistance of Microscopy Australia at the University of South Australia, Mawson Lakes Campus, a facility that is funded by the University, and State and Federal Governments. The authors would also like to acknowledge Daniel Fernandes for fabricating samples. K.V. thanks NHMRC for Fellowship GNT1194466 and ARC for grant DP180101254.

Conflicts of Interest: The authors listed above declare no conflict of interest or personal relationships that could have appeared to influence the work reported in this paper.

2.12 Supplementary Materials

Bio-Inspired Nanostructured Ti-6Al-4V Alloy: The Role of Two Alkaline Etchants and the Hydrothermal Processing Duration on Antibacterial Activity

Richard Bright [1], Andrew Hayles [1], Jonathan Wood [1], Neethu Ninan [1], Dennis Palms [1], Rahul M. Visalakshan [2], Anouck Burzava [1], Toby Brown [3], Dan Barker [3] and Krasimir Vasilev [1,4,*]

[1] Academic Unit of STEM, University of South Australia, Mawson Lakes, Adelaide, SA 5095, Australia;
richard.bright@unisa.edu.au (R.B.); andrew.hayles@unisa.edu.au (A.H.); jonathan.wood@mymail.unisa.edu.au (J.W.); neethun.ninan@gmail.com (N.N.); dennis.palms@unisa.edu.au (D.P.); anouck.burzava@unisa.edu.au (A.B.)

[2] Division of Biomaterials and Biomechanics, Department of Restorative Dentistry, School of Dentistry,
Oregon Health and Science University, Portland, OR 97201, USA; madathip@ohsu.edu

[3] Corin Australia, Baulkham Hills, NSW 2153, Australia; tobydbrown@gmail.com (T.B.); dan.barker@coringroup.com (D.B.)

[4] College of Medicine and Public Health, Flinders University, Bedford Park, SA 5042, Australia

* Correspondence: krasimir.vasilev@unisa.edu.au

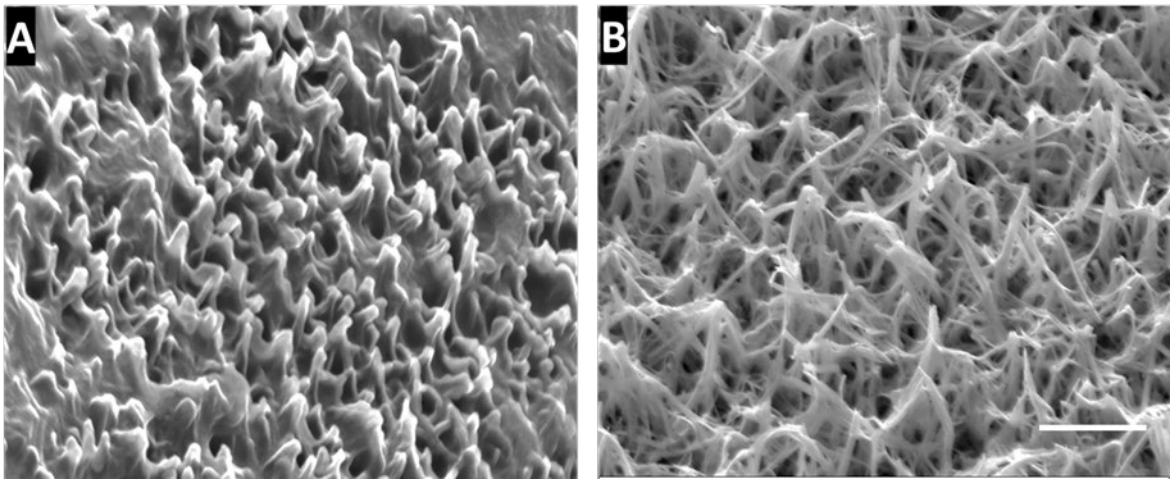

Figure S1. *SEM micrographs comparing nanostructures from a dragonfly wing (A) and hydrothermally etched nanostructures (B). The scale bar represents 500 nm.*

Table S1. *Geometry and distribution of the nanospikes prepared on the surface of Ti6Al4V by KOH and NaOH-aqueous etching solutions over different periods. The values were presented in means ± standard deviation from at least 20 spikes by analyzing at least four fields of view. Spacing distances were calculated from the SEM micrographs with the stage at the orthogonal position. Highlighted measures represent the best antibacterial activity for the two alkaline etching solutions (NaOH and KOH).*

Etching Solution	**NaOH**				**KOH**			
Etching Time:	**1 h**	**3 h**	**4 h**	**5 h**	**1 h**	**3 h**	**4 h**	**5 h**
Height (nm)	112 ± 27	185 ± 38	367 ± 80	425 ± 107	122 ± 107	242 ± 73	207 ± 37	340 ± 175
Diameter at mid-height (nm)	30 ± 4	94 ± 33	62 ± 23	83 ± 30	65 ± 10	71 ± 11	85 ± 18	83 ± 32
Spacing (nm)	185 ± 41	190 ± 42	182 ± 48	224 ± 55	330 ± 83	453 ± 122	500 ± 120	544 ± 150
Density(spike/μm^2)	42 ± 4	35 ± 7	75 ± 8	32 ± 9	17 ± 6	10 ± 2	10 ± 3	8 ± 2

Table S2. *AFM roughness measurements and calculated surface area. RMS = root mean square, R_a = average roughness and SA = calculated surface area.*

Treatment	**RMS (nm)**	**R_a (nm)**	**SA (μm^2)**
AR-Ti	10.1	6.6	25.2
NaOH-4h	88.4	71.4	79.9
KOH-5h	88.5	61.5	50.3

2.13 References

1. Sato, Y.; Kitagawa, N.; Isobe, A. Implant treatment in ultra-aged society. *Jpn. Dent. Sci. Rev.* **2018**, *54*, 45–51.
2. Geetha, M.; Singh, A.K.; Asokamani, R.; Gogia, A.K. Ti based biomaterials, the ultimate choice for orthopaedic implants—A review. *Prog. Mater. Sci.* **2009**, *54*, 397–425.
3. Cataldo, M.A.; Petrosillo, N.; Cipriani, M.; Cauda, R.; Tacconelli, E. Prosthetic joint infection: Recent developments in diagnosis and management. *J. Infect.* **2010**, *61*, 443–448.
4. Khatoon, Z.; McTiernan, C.D.; Suuronen, E.J.; Mah, T.F.; Alarcon, E.I. Bacterial biofilm formation on implantable devices and approaches to its treatment and prevention. *Heliyon* **2018**, *4*, e01067.
5. Berbari, E.F.; Hanssen, A.D.; Duffy, M.C.; Steckelberg, J.M.; Ilstrup, D.M.; Harmsen, W.S.; Osmon, D.R. Risk factors for prosthetic joint infection: Case-control study. *Clin. Infect. Dis.* **1998**, *27*, 1247–1254.
6. Moriarty, T.F.; Kuehl, R.; Coenye, T.; Metsemakers, W.J.; Morgenstern, M.; Schwarz, E.M.; Riool, M.; Zaat, S.A.J.; Khana, N.; Kates, S.L.; et al. Orthopaedic device-related infection: Current and future interventions for improved prevention and treatment. *EFORT Open Rev.* **2016**, *1*, 89–99.
7. An, Y.H.; Friedman, R.J. Concise review of mechanisms of bacterial adhesion to biomaterial surfaces. *J. Biomed. Mater. Res.* **1998**, *43*, 338–348.
8. Montanaro, L.; Speziale, P.; Campoccia, D.; Ravaioli, S.; Cangini, I.; Pietrocola, G.; Giannini, S.; Arciola, C.R. Scenery of Staphylococcus implant infections in orthopedics. *Future Microbiol.* **2011**, *6*, 1329–1349.
9. Ribeiro, M.; Monteiro, F.J.; Ferraz, M.P. Infection of orthopedic implants with emphasis on bacterial adhesion process and techniques used in studying bacterial-material interactions. *Biomatter* **2012**, *2*, 176–194.
10. Potapova, I. Functional Imaging in Diagnostic of Orthopedic Implant-Associated Infections. *Diagnostics* **2013**, *3*, 356–371.
11. Shiels, S.M.; Bedigrew, K.M.; Wenke, J.C. Development of a hematogenous implant-related infection in a rat model. *BMC Musculoskelet. Disord.* **2015**, *16*, 255.
12. Zimmerli, W. Clinical presentation and treatment of orthopaedic implant-associated infection. *J. Intern. Med.* **2014**, *276*, 111–119.
13. Seebach, E.; Kubatzky, K.F. Chronic Implant-Related Bone Infections-Can Immune Modulation be a Therapeutic Strategy? *Front. Immunol.* **2019**, *10*, 1724.
14. Rabin, N.; Zheng, Y.; Opoku-Temeng, C.; Du, Y.; Bonsu, E.; Sintim, H.O. Biofilm formation mechanisms and targets for developing antibiofilm agents. *Future Med. Chem.* **2015**, *7*, 493–512.
15. Palmer, J.; Flint, S.; Brooks, J. Bacterial cell attachment, the beginning of a biofilm. *J. Ind. Microbiol. Biotechnol.* **2007**, *34*, 577–588.

16. Vu, B.; Chen, M.; Crawford, R.J.; Ivanova, E.P. Bacterial extracellular polysaccharides involved in biofilm formation. *Molecules* **2009**, *14*, 2535–2554.
17. Preda, V.G.; Sandulescu, O. Communication is the key: Biofilms, quorum sensing, formation and prevention. *Discoveries* **2019**, *7*, e100.
18. Olsen, I. Biofilm-specific antibiotic tolerance and resistance. *Eur. J. Clin. Microbiol. Infect. Dis.* **2015**, *34*, 877–886.
19. Potera, C. Antibiotic Resistance: Biofilm Dispersing Agent Rejuvenates Older Antibiotics. *Environ. Health Perspect.* **2010**, *118*, A288.
20. Sharma, D.; Misba, L.; Khan, A.U. Antibiotics versus biofilm: An emerging battleground in microbial communities. *Antimicrob. Resist. Infect. Control* **2019**, *8*, 76.
21. Aggarwal, V.K.; Rasouli, M.R.; Parvizi, J. Periprosthetic joint infection: Current concept. *Indian J. Orthop.* **2013**, *47*, 10–17.
22. Fleming, D.; Rumbaugh, K. The Consequences of Biofilm Dispersal on the Host. *Sci. Rep.* **2018**, *8*, 10738.
23. Minasyan, H. Sepsis: Mechanisms of bacterial injury to the patient. *Scand. J. Trauma Resusc. Emerg. Med.* **2019**, *27*, 19.
24. Penesyan, A.; Paulsen, I.T.; Kjelleberg, S.; Gillings, M.R. Three faces of biofilms: A microbial lifestyle, a nascent multicellular organism, and an incubator for diversity. *NPJ Biofilms Microbiomes* **2021**, *7*, 80.
25. Cavallaro, A.; Taheri, S.; Vasilev, K. Responsive and “smart” antibacterial surfaces: Common approaches and new developments (Review). *Biointerphases* **2014**, *9*, 029005.
26. Eaninwene, G., 2nd; Yao, C.; Webster, T.J. Enhanced osteoblast adhesion to drug-coated anodized nanotubular titanium surfaces. *Int. J. Nanomed.* **2008**, *3*, 257–264.
27. Griesser, S.S.; Jasieniak, M.; Vasilev, K.; Griesser, H.J. Antimicrobial Peptides Grafted onto a Plasma Polymer Interlayer Platform: Performance upon Extended Bacterial Challenge. *Coatings* **2021**, *11*, 68.
28. Vasilev, K.; Griesser, S.S.; Griesser, H.J. Antibacterial Surfaces and Coatings Produced by Plasma Techniques. *Plasma Processes Polym.* **2011**, *8*, 1010–1023.
29. Jenkins, J.; Mantell, J.; Neal, C.; Gholinia, A.; Verkade, P.; Nobbs, A.H.; Su, B. Antibacterial effects of nanopillar surfaces are mediated by cell impedance, penetration and induction of oxidative stress. *Nat. Commun* **2020**, *11*, 1626.
30. Ivanova, E.P.; Hasan, J.; Webb, H.K.; Truong, V.K.; Watson, G.S.; Watson, J.A.; Baulin, V.A.; Pogodin, S.; Wang, J.Y.; Tobin, M.J.; et al. Natural bactericidal surfaces: Mechanical rupture of Pseudomonas aeruginosa cells by cicada wings. *Small* **2012**, *8*, 2489–2494.
31. Ivanova, E.P.; Hasan, J.; Webb, H.K.; Gervinskas, G.; Juodkazis, S.; Truong, V.K.; Wu, A.H.; Lamb, R.N.; Baulin, V.A.; Watson, G.S.; et al. Bactericidal activity of black silicon. *Nat. Commun*. **2013**, *4*, 2838.

32. Hasan, J.; Jain, S.; Chatterjee, K. Nanoscale Topography on Black Titanium Imparts Multi-biofunctional Properties for Orthopedic Applications. *Sci. Rep.* **2017**, 7, 41118.
33. Bhadra, C.M.; Truong, V.K.; Pham, V.T.; al Kobaisi, M.; Seniutinas, G.; Wang, J.Y.; Juodkazis, S.; Crawford, R.J.; Ivanova, E.P. Antibacterial titanium nano-patterned arrays inspired by dragonfly wings. *Sci. Rep.* **2015**, *5*, 16817.
34. Hayles, A.; Hasan, J.; Bright, R.; Palms, D.; Brown, T.; Barker, D.; Vasilev, K. Hydrothermally etched titanium: A review on a promising mechano-bactericidal surface for implant applications. *Mater. Today Chem.* **2021**, *22*, 100622.
35. Anitha, V.C.; Banerjee, A.N.; Joo, S.W.; Min, B.K. Morphology-dependent low macroscopic field emission properties of titania/titanate nanorods synthesized by alkali-controlled hydrothermal treatment of a metallic Ti surface. *Nanotechnology* **2015**, *26*, 355705.
36. Tripathy, A.; Sen, P.; Su, B.; Briscoe, W.H. Natural and bioinspired nanostructured bactericidal surfaces. *Adv. Colloid Interface Sci.* **2017**, *248*, 85–104.
37. Lee, A.S.; de Lencastre, H.; Garau, J.; Kluytmans, J.; Malhotra-Kumar, S.; Peschel, A.; Harbarth, S. Methicillin-resistant Staphylococcus aureus. *Nat. Rev. Dis. Primers* **2018**, *4*, 18033.
38. Cremet, L.; Broquet, A.; Brulin, B.; Jacqueline, C.; Dauvergne, S.; Brion, R.; Asehnoune, K.; Corvec, S.; Heymann, D.; Caroff, N. Pathogenic potential of Escherichia coli clinical strains from orthopedic implant infections towards human osteoblastic cells. *Pathog. Dis.* **2015**, *73*, ftv065.
39. Brouqui, P.; Rousseau, M.C.; Stein, A.; Drancourt, M.; Raoult, D. Treatment of Pseudomonas aeruginosa-infected orthopedic prostheses with ceftazidime-ciprofloxacin antibiotic combination. *Antimicrob. Agents Chemother.* **1995**, *39*, 2423–2425.
40. Gangan, M.S.; Athale, C.A. Threshold effect of growth rate on population variability of Escherichia coli cell lengths. *R. Soc. Open Sci.* **2017**, *4*, 160417.
41. Diggle, S.P.; Whiteley, M. Microbe Profile: Pseudomonas aeruginosa: Opportunistic pathogen and lab rat. *Microbiology* **2020**, *166*, 30–33.
42. Wang, L.; Luo, Q.; Zhang, X.; Qiu, J.; Qian, S.; Liu, X. Co-implantation of magnesium and zinc ions into titanium regulates the behaviors of human gingival fibroblasts. *Bioact Mater.* **2021**, *6*, 64–74.
43. Maarof, S.K.M.; Rusop, M.; Abdullah, S. Effect of Annealing Temperature on TiO_2 Nanostructured Prepared by Sol-Gel Method. *Nanosci. Nanotechnol. Nanoeng.* **2014**, *832*, 763–766.
44. Du, Z.; Ma, Y.; Liu, F.; Xu, N.; Chen, Y.; Wang, X.; Chen, Y.; Gong, T.; Xu, D. The Influences of Process Annealing Temperature on Microstructure and Mechanical Properties of near beta High Strength Titanium Alloy Sheet. *Materials* **2019**, *12*, 1478.
45. Bandara, C.D.; Singh, S.; Afara, I.O.; Wolff, A.; Tesfamichael, T.; Ostrikov, K.; Oloyede, A. Bactericidal Effects of Natural Nanotopography of Dragonfly Wing on Escherichia coli. *ACS Appl. Mater. Interfaces* **2017**, *9*, 6746–6760.

46. Chopra, D.; Gulati, K.; Ivanovski, S. Bed of nails: Bioinspired nano-texturing towards antibacterial and bioactivity functions. *Mater. Today Adv.* **2021**, *12*, 100176.
47. Bright, R.; Fernandes, D.; Wood, J.; Palms, D.; Burzava, A.; Ninan, N.; Brown, T.; Barker, D.; Vasilev, K. Long-term antibacterial properties of a nanostructured titanium alloy surface: An in vitro study. *Mater. Today Bio* **2022**, *13*, 100176.
48. Bright, R.; Hayles, A.; Fernandes, D.; Visalakshan, R.M.; Ninan, N.; Palms, D.; Burzava, A.; Barker, D.; Brown, T.; Vasilev, K. In Vitro Bactericidal Efficacy of Nanostructured Ti6Al4V Surfaces is Bacterial Load Dependent. *ACS Appl. Mater. Interfaces* **2021**, *13*, 38007–38017.
49. Gomes, C.C.; Moreira, L.M.; Santos, V.J.; Ramos, A.S.; Lyon, J.P.; Soares, C.P.; Santos, F.V. Assessment of the genetic risks of a metallic alloy used in medical implants. *Genet. Mol. Biol.* **2011**, *34*, 116–121.
50. Costa, B.C.; Tokuhara, C.K.; Rocha, L.A.; Oliveira, R.C.; Lisboa-Filho, P.N.; Costa Pessoa, J. Vanadium ionic species from degradation of Ti-6Al-4V metallic implants: In vitro cytotoxicity and speciation evaluation. *Mater. Sci. Eng. C Mater. Biol. Appl.* **2019**, *96*, 730–739.
51. Sansone, V.; Pagani, D.; Melato, M. The effects on bone cells of metal ions released from orthopaedic implants. A review. *Clin. Cases Miner. Bone Metab.* **2013**, *10*, 34–40.
52. Wenzel, R.N. Surface Roughness and Contact Angle. *J. Phys. Colloid Chem.* **1949**, *53*, 1466–1467.
53. Cassie, A.B.D.; Baxter, S. Wettability of porous surfaces. *Trans. Faraday Soc.* **1944**, *40*, 546–550.
54. Webb, H.K.; Crawford, R.J.; Ivanova, E.P. Wettability of natural superhydrophobic surfaces. *Adv. Colloid Interface Sci.* **2014**, *210*, 58–64.
55. Prabu, V.; Karthick, P.; Rajendran, A.; Natarajan, D.; Kiran, M.S.; Pattanayak, D.K. Bioactive Ti alloy with hydrophilicity, antibacterial activity and cytocompatibility. *RSC Adv.* **2015**, *5*, 50767–50777.
56. Quinn, J.; McFadden, R.; Chan, C.W.; Carson, L. Titanium for Orthopedic Applications: An Overview of Surface Modification to Improve Biocompatibility and Prevent Bacterial Biofilm Formation. *iScience* **2020**, *23*, 101745.
57. Shen, J.; Zhang, D.; Zhang, F.H.; Gan, Y. AFM tip-sample convolution effects for cylinder protrusions. *Appl. Surf. Sci.* **2017**, *422*, 482–491.
58. Dalby, M.J.; Gadegaard, N.; Riehle, M.O.; Wilkinson, C.D.; Curtis, A.S. Investigating filopodia sensing using arrays of defined nano-pits down to 35 nm diameter in size. *Int. J. Biochem. Cell Biol.* **2004**, *36*, 2005–2015.
59. Chowdhury, A.K.; Tavangar, A.; Tan, B.; Venkatakrishnan, K. Biofunctionalized 3-D Carbon Nano-Network Platform for Enhanced Fibroblast Cell Adhesion. *Sci. Rep.* **2017**, *7*, 44250.

ACS APPLIED MATERIALS & INTERFACES

(IF 10.38)

Bright R, Hayles A, Fernandes D, Visalakshan RM, Ninan N, Palms D, Burzava A, Barker D, Brown T, Vasilev K. In Vitro Bactericidal Efficacy of Nanostructured Ti6Al4V Surfaces is Bacterial Load Dependent. ACS Appl Mater Interfaces. 2021 Aug 18;13(32):38007-38017. DOI: 10.1021/acsami.1c06919 .1c06919. Epub 2021 Aug 10. PMID: 34374279.

CHAPTER 3:

THE *IN VITRO* BACTERICIDAL EFFICACY OF NANOSTRUCTURED TI6AL4V SURFACES IS BACTERIAL LOAD DEPENDENT

Richard Bright[1,2], Andrew Hayles[1,2], Daniel Fernandes[1], Rahul M Visalakshan[1], Neethu Ninan[1], Dennis Palms[1], Anouck Burzava[1], Dan Barker[3], Toby Brown[3], *Krasimir Vasilev[1,2].

[1]STEM, University of South Australia, Mawson Lakes, Adelaide, 5095, South Australia, Australia. [2]Future Industries Institute, University of South Australia, Mawson Lakes, Adelaide, 5095, South Australia, Australia. [3]Corin Australia, Baulkham Hills, NSW 2153, Australia.
(*Corresponding author email: krasimir.vasilev@unisa.edu.au)

3.1 Graphical Abstract

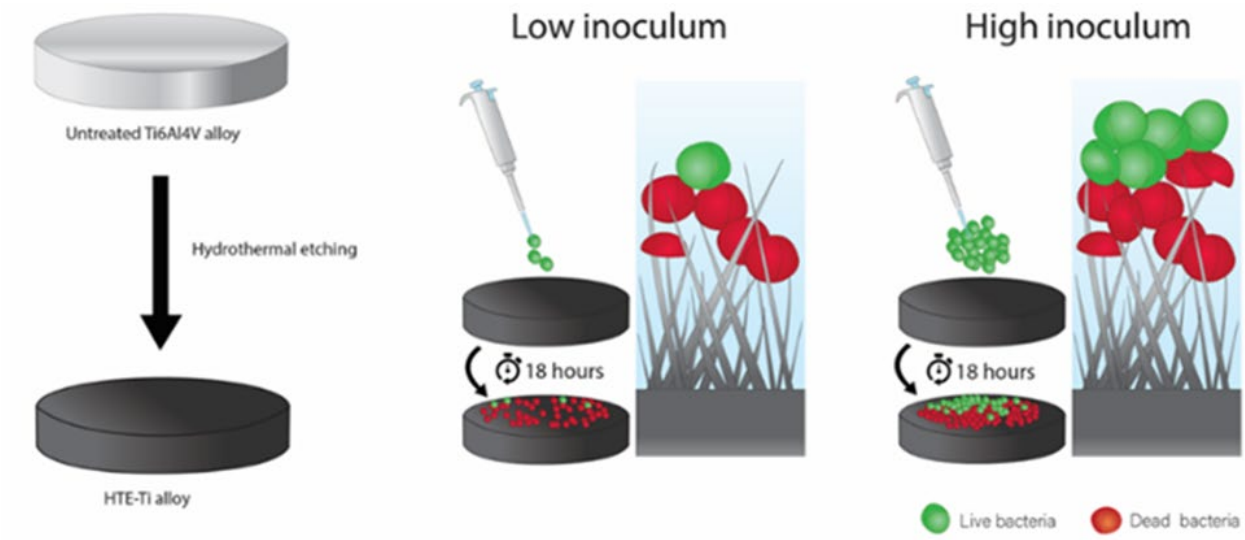

3.2 Abstract

The demand for medical implants globally has increased significantly, due to an aging population amongst other reasons. Despite an overall increase in the survivorship of Ti6Al4V implants, implant infection rates are increasing due to factors such as diabetes, obesity, and bacterial resistance to antibiotics. Two commonly found bacteria implicated in implant infections are *Staphylococcus aureus* (*S. aureus*) and *Pseudomonas aeruginosa* (*P. aeruginosa*). Based on prior work that showed nanostructured surfaces might have the potential to passively kill these bacterial species, we developed a hierarchical, hydrothermally etched, nanostructured titanium surface. To evaluate the antibacterial efficacy of this surface, etched and as-received surfaces were inoculated with *S. aureus* or *P. aeruginosa* at concentrations ranging from 10^2 to 10^9 colony-forming units per disc. Live/dead staining revealed there was a 60% decrease in viability for *S. aureus* and a greater than 98% decrease for *P. aeruginosa* on etched surfaces at the lowest inoculum of 10^2 CFU/disc when compared to the control surface. Bactericidal efficiency decreased with increasing bacterial concentrations in a stepwise manner, with decreases in bacterial viability noted for *S. aureus* above 10^5 CFU/disc and above 10^6 CFU/disc for *P. aeruginosa*. Surprisingly, biofilm depth analysis revealed a decrease in bacterial viability in the 2µm layer furthest from the nanostructured surface. The nanostructured Ti6Al4V surface developed here holds the potential to reduce the rate of implant infections.

Keywords

Hydrothermally Etched, Titanium Implants, Nanostructures, Nanospikes, Antimicrobial, Antibiofilm, Orthopedic, Prosthetic Joint Infection.

3.3 Introduction

Despite increases in the survivorship of titanium alloy (Ti6Al4V) implants for applications such as joint and tooth replacement, implant-associated infection (IAI) remains a substantial clinical challenge. [1-3] Periprosthetic joint infections (PJIs), for example, are associated with devastating complications, increased costs and hospital admissions, and increased morbidity and mortality. [4-5] The rate of IAI can vary from 0.5% to 2% [6-7] for joint replacement, and as high as 30% in orthopedic implant trauma cases. [8-10] IAIs involve complex interactions between bacteria, the implant surface, and the host surrounding tissues. [11] It has been well established that surfaces of prosthetic implants provide an ideal substrate for bacterial adhesion, formation of a mature biofilm and establishment of a chronic infection. [12] Biofilms can also occur on bone cement, implant screws, peri-implant bone, connective tissue and in the synovial fluid. [13-15] Factors influencing implant biofilm formation include chemical composition, surface roughness, hydrophilicity, electrostatic charge (Z potential) and surface free energy. [16-19]

The pathogenesis of IAI is multimodal. Infection can occur directly by contamination of the implant during the surgical procedure, or via a contiguous route, with bacteria seeding the implant from the surgical site, an open traumatic wound, an adjacent site of infection, or through hematogenous seeding. [20-23] Several measures, such as the use of topical antimicrobials, shaving body hair, use of surgical gowns, gloves, drapes and masks, aseptic technique, and HEPA filters in the operating theatre, have been employed to reduce the incidence of IAI and biofilm formation. [24-25] However, once a biofilm has formed, implant removal is usually required, in part because bacteria within a biofilm are up to 1000-fold more antibiotic-resistant than planktonic cells [26] and protected from the host immune response. [4] The use of high-dose antibiotics to treat IAIs can also lead to systemic toxicity to organs such as the liver and kidneys. [27] The inability of current measures to prevent IAIs has led to novel and innovative strategies, including modification of the implant surface to render it antimicrobial. [28-29]

Recently, nanostructured surfaces mimicking the morphology found on insect wings have attracted substantial interest. [30-32] Such surfaces were first fabricated on silica by Ivanova, *et al*. [33] and later titanium, [34] and were shown to significantly reduce bacterial colonization by killing bacteria upon contact. As with most surface modifications, antibacterial testing was conducted using inoculum concentrations in the range of 10^5 – 10^6 colony-forming units per (CFU/cm^2), which is consistent with current regulatory standards. [35] The clinical relevance of testing with such high concentrations is, however, questionable. For example, antiseptic skin preparation alone has been shown to reduce CFU counts on the skin from 10^7 CFU/cm^2 to less than 10 CFU/cm^2. [36-37] Other variables affecting the potential inoculating concentration include the type of device, surgical procedure, and operating environment. [38-39]

The relationship between the bactericidal efficacy of nanostructured surfaces and inoculum concentration is unknown. Furthermore, it is unknown if there is an upper limit to the inoculum concentration on nanostructured surfaces, above which there is limited bactericidal efficacy. This study aimed to determine the bactericidal efficacy of a nanostructured Ti6Al4V surface challenged with a range of bacterial inoculum concentrations of clinically relevant Gram-positive and Gram-negative bacterial pathogens and whether there was an upper limit in inoculum concentration, above which the surface would be ineffective at killing bacteria.

3.4 Methods and Materials

3.4.1 Fabrication of Ti6Al4V hydrothermally etched antibacterial samples (AM)

Coupons of Ti6Al4V (discs 10 mm in diameter, 0.78cm^2 and 3 mm in height) were mirror-polished (Ra = 0.5 µm) and etched in a stainless-steel reactor (Parr Instrument Company, USA), using 1M KOH aqueous solutions. Based on our preliminary optimization experiments to investigate the generation of distinct nanospikes, reactors were kept sealed at 150°C inside an oven for 5 h. After the etching process, the vessels were cooled down in flowing water and the samples were rinsed and immersed in ultrapure water.

After drying, discs were heat treated inside a tubular furnace and cooled down overnight until room temperature. Before undertaking bacteriological analysis, the samples were cleaned and then sterilized in an autoclave at 121°C for 20 min.

3.4.2 Scanning electron microscopy (SEM) to determine the surface morphology

The morphology and dimensions of the nanostructures formed on the surface following etching and heat treatment were analysed using SEM (Zeiss Merlin FEG-SEM, Zeiss, Jena, Germany) at 2KV, 4.5 mm working distances with magnification from 5-50K with the stage tilted at 45 degrees. A distinctive branched network of nanospikes was observed. The height of the nanospikes was determined from five images, by the linear distance between a basal plane and the highest point of each spike, while the width was measured at mid-height in parallel orientation with the basal plane, and a correction factor of x/cos (45°) to amend dimensional distortion during linear measurements, where x equals the length of nanospike. Spike height and width at mid-height were expressed as mean ± standard deviation. To determine the spacing between nanospikes, four zero-degree tilted SEM images were analysed, considering nanospike tips in a 5 um^2 field. The density of the nanospikes was performed using ImageJ software v1.53a (NIH, Maryland, USA). To calculate the mean spacing between nanospikes, the square root of density divided by the area (25 μm) and multiplied by 1000 (to express measurement in nanometers) was determined, presented as mean and standard deviation.

3.4.3 Contact angle analysis

The contact angle, θ, is a quantifiable measure of the wetting of a solid by a liquid. The as-received control (CTL) and AM surfaces were evaluated by the sessile drop method using a contact angle goniometer model RD-SDM02 (RD Support, Scotland, UK). Contact angles were measured at a minimum of five different areas across triplicate samples. The contact angle from Milli-Q water (4uL) was measured in triplicate by a tangent fitting method using the plugin Contact_Angle.jar for Image J software (NIH, Maryland, USA).

3.4.4 Surface chemistry analysis by X-ray photoelectron spectroscopy (XPS)

XPS is a technique to measure the elemental composition, empirical formula, chemical state, and electronic state of the elements within a material. A Kratos AXIS Ultra DLD spectrometer (Kratos Analytical Ltd, Manchester, UK) was used with a monochromatic Al source run at 15 keV and 15 mA. Survey spectra were collected with a pass energy of 160 eV and high-resolution spectra were obtained using a 20-eV pass energy. Survey spectra were recorded over a 0−1100 eV range in 0.5 eV steps. The processing of spectra after curve fitting was performed using Casa XPS software and all binding energies were referenced to the neutral carbon peak at 285.0 eV.

3.4.5 Primary derived human dermal fibroblast (HDF) cell culture

HDF cultures were maintained in fibroblast culture medium (FCM) consisting of Dulbecco's modified Eagle medium supplemented with 10% v/v fetal bovine serum (FBS; Life Technologies, California, USA), 1% (v/v) penicillin/streptomycin (Life Technologies, California, USA). Cells were maintained at 37°C and 5% CO_2 with 95% humidity. The medium was changed every 3 days until the cells reached 80% confluency.

3.4.6 Determination of cell viability

The short-term cytocompatibility was assessed by cell viability, determined using the resazurin cell viability assay (Resazurin, Sigma Aldrich, Missouri, USA). The blue non-fluorescent resazurin reagent is reduced to highly fluorescent resorufin by dehydrogenase enzymes in metabolically active cells. A stock solution of 100 µg/mL (440µM) resazurin was prepared in PBS pH 7.4 and filter sterilized using a 0.2 mm filter. HDF cells were seeded on titanium discs in triplicate (AM and CTL) in a 48-well plate and tissue culture plate at a density of 2.5 x 10^4 cells/well. The cells were incubated for 48 h at 37°C and 5% CO_2, after which the culture medium was replaced with 250µL media containing 25µL of the stock resazurin solution in 250µL FCM and incubated for 1h. Next, 100 µL of the culture medium was transferred into a 96-well plate and the fluorescent intensity was recorded using a FLUOstar Omega plate reader (BMG Lab Tech, Victoria, Australia) at excitation of 530nm and emission of 590nm. Cell viability was calculated using the following formula: *% cell viability = fluorescent intensity of treated/fluorescent intensity of control x 100*.

3.4.7 Proliferation, adhesion, and cell morphology of HDF

To confirm the cell viability and show the spread and morphology of cells on the AM and CTL surfaces post 48 h incubation, cells were fixed using 4% paraformaldehyde for 2 hours. Next, cells were rinsed in PBS and permeabilized with 0.1 % Triton-X (Sigma Aldrich, Missouri, USA) then stained with phalloidin (Alexa Fluor 488 phalloidin, ThermoFisher Scientific, MA, USA) to stain actin filaments and nuclei stained by DAPI (4',6-Diamidino-2-Phenylindole, Dihydrochloride, ThermoFisher Scientific, Massachusetts, USA), following manufacturer's protocol. Samples were inverted onto a coverslip and imaged by an Olympus FV3000 confocal laser scanning microscope (CLSM; Olympus, Tokyo, Japan).

3.4.8 Bacterial cultures

S. aureus ATCC 25923 and *P. aeruginosa,* ATCC 15692 cultures were inoculated in modified tryptone soy broth (Oxoid, ThermoFisher, Massachusetts, USA) supplemented with 5% fetal calf serum (TSBFCS) (Gibco, ThermoFisher, Massachusetts, USA), and incubated overnight at 37°C. Fetal calf serum provides an ideal environment to facilitate bacterial adhesion, somewhat replicating *in vivo* conditions. [40-41]

Bacterial cultures were diluted in TSBFCS to produce 50µl aliquots containing cell quantities decreasing 10-fold from 1.3 x 10^9 CFU/cm^2 down to 1.3 x10^2 CFU/cm^2 (henceforth for simplicity 10^9 to 10^2 CFU/disc, see table S1 for conversions) and incubated for 18 h at 37°C. An optical density reading of 1 measured at 600 nm (OD_{600}) was determined to be approximately 1x10^9 CFU/mL by calibrating against colony enumeration for S. aureus and *P. aeruginosa* before beginning the study.

3.4.9 Surface inoculation

CTL and AM discs (n = 3) were aseptically placed into the wells of a sterile 24-well tissue culture plate. The prepared bacteria were inoculated directly onto the surface of the discs. They were then incubated in a humid chamber at 37°C for 3 h to allow for cell attachment. Discs were gently rinsed with phosphate-buffered saline (PBS) to remove unattached bacteria, immersed in 1 ml TSBFCS, and incubated at 37°C for a further 18 h on an orbital shaker at 70 RPM.

3.4.10 Live/Dead BacLight bacterial viability assay

The culture medium was removed, and bacterial cells that remained attached to the surface were stained by Live/Dead® BacLight™ (Invitrogen, ThermoFisher, Massachusetts, USA), containing Syto9 and Propidium Iodide (PI) in equal proportions at 1.5µl/ml in phosphate-buffered saline (PBS). Samples were immersed in the mixture and incubated in the dark at room temperature. Syto9 is taken up by all cells and binds with nucleic acids, staining the cell green. Whereas PI has a higher affinity for nucleic acid than Syto9, which is unable to pass through the intact plasma membrane and is therefore only taken up by structurally damaged and dead cells. Discs were inverted on a glass coverslip and imaged by an Olympus FV3000 CLSM (Olympus, Tokyo, Japan). The excitation/emission maxima for STYO9 and PI were 480/500 nm and 490/635 nm, respectively. Single-plane fluorescence micrographs were taken in triplicate from randomly chosen areas at the interface between the titanium alloy surface and bacteria. Viability was quantified from single-plane images by counting red and green stained cells using ImageJ software v1.53a (NIH, Maryland, USA). Full biofilm thickness images (Z-stacks) were analyzed for biomass and spatial distribution of live and dead cells within the biofilm on the four highest inoculum concentrations for both *S. aureus* and *P. aeruginosa.* The viability and biomass for the Z-stacks were analysed using Imaris 3D analysis software (Version 9.3.0, Bitplane, Zürich, Switzerland).

3.4.11 Colony Enumeration (CFU)

The standard method to compare the bactericidal efficacy of competing surfaces is colony enumeration. The AM and CTL discs were transferred to sterile tubes containing 1ml PBS at pH 7.4, and vortexed for 15 seconds, followed by 2-minute sonication and a further 15-second vortex. Serial dilutions were plated out on tryptic soy agar plates and incubated for 20 h at 37°C.

The following day, colonies were counted, and log reduction scores were calculated from the difference in the number of CFUs on CTL and AM discs. [42] After CTL and AM samples were processed for CFU counts, they were imaged by SEM to confirm the removal of all bacteria.

3.4.12 SEM imaging of biofilm

Samples were fixed for 2 h with 1.25% glutaraldehyde and 4% paraformaldehyde in PBS containing 4% sucrose. Next, they were washed in PBS, followed by dehydration in an ascending ethanol order from 50% (v/v) to absolute ethanol. The samples were then chemically dried using Hexamethyldisilazane (HMDS; Sigma-Aldrich, Missouri, USA) and mounted on aluminium stubs using double-sided carbon tape, sputter coated with 2nm platinum, and examined in a Zeiss Merlin FEG- SEM (Carl Zeiss, Jena, Germany).

3.5 Results and Discussion

3.5.1 Characterization of the AM samples

SEM images were acquired at different magnifications for the CTL and AM discs are shown in Figures 1A and 1B. The surface of CTL discs showed the presence of machining and polishing marks at both the microscale and nanoscale magnifications. AM discs exhibited sharp spike-like structures at the nanoscale uniformly covering the entire surface. Nanospikes were found to be preferentially orthogonal to the surface, with a mean height of 348 ± 152 nm and a mean diameter at mid-height of 98 ± 60 nm. The mean spacing between the nanostructured tips was 437 ± 46 nm.

The HT etched surface modification acted as a hardened overlay and reduced the penetration of the pin under a load of 1N for the same number of revolutions (Figure S1). Lower penetration could suggest the reduced probability of debris generation compared to the as-received control.

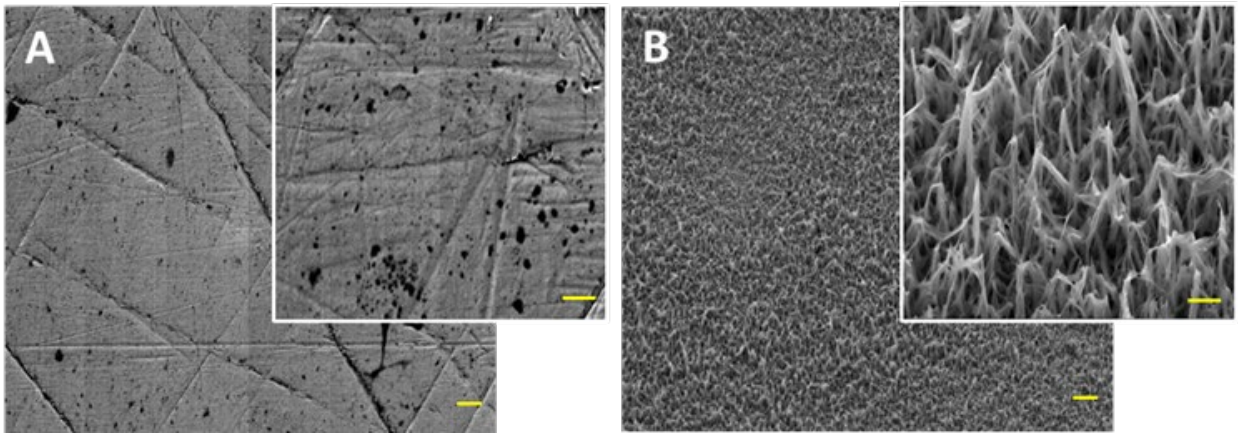

Figure 1. *SEM images of untreated (A), and hydrothermally etched Ti6Al4V alloy discs (B) were used throughout this study. Working distance 4mm, EHT 2.0kV and signal A = SE2. Scale bar =2 µm and inset image 500 nm. Lower power images were 5000 X magnification and inset images were 50,000 X magnification.*

The water contact angle for AM discs (5° ± 0.8 degrees) was significantly lower than that for CTL samples (61° ± 8 degrees) p=0.0003, indicative of significantly increased hydrophilicity (Figure 2). The increase in hydrophilicity is an important characteristic of the AM surface since the phenomenon is generally associated with improved biocompatibility, [43-44] enhanced antibacterial [45-46] and antifungal properties. [47]

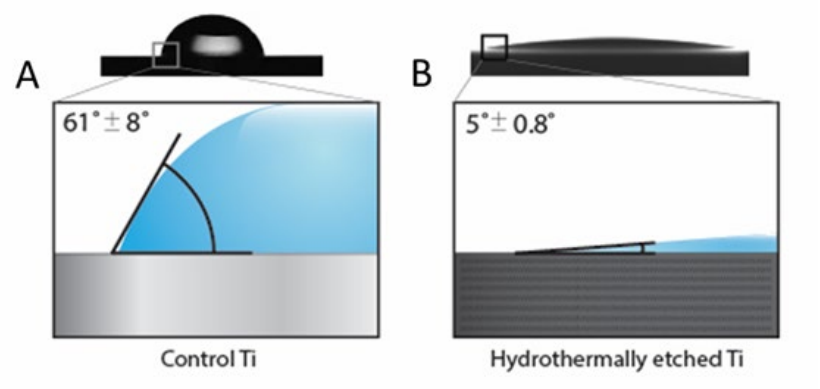

Figure 2. *The wettability of non-etched CTL (A) and AM (B) titanium alloy surfaces was evaluated by a static sessile drop technique. Illustrations under images show contact angle in mean degrees ± SD (n = 3).*

The chemical elements detected on the surface using XPS are presented in Table 1. A notable finding was the increase in oxygen concentration of 6.4% on the AM disc surfaces compared to the unetched CTL. These results are consistent with the thickening of the oxide layer occurring during hydrothermal etching. The thicker oxide layer also caused a reduction in the measured surface concentration of vanadium and aluminium, as XPS is limited to the outermost 10 nm of the surface. The concentration of common environmental contaminants such as carbon and nitrogen was reduced after hydrothermal etching. Additionally, small levels of potassium were incorporated within the AM surface, consistent with the use of potassium as the cation for the alkaline treatment. Small traces of magnesium and silicon were detected on both CTL and AM disc surfaces, consistent with unavoidable environmental contamination that occurs during the processing of Ti-alloy.

Table 1. *Atomic percentages of the non-annealed CTL and AM surfaces were quantified from the XPS survey spectra (n = 3).*

	Survey spectra - Atomic percentages									
Surface	O 1s	C 1s	Ti 2p	V 2p	Al 2p	K 2p	N 1s	Mg 2s	Si 2p	Ca 2p
Control (non-annealed)	48.7	30.2	15.1	0.2	2.9	-	1.5	0.6	0.8	-
AMK (annealed)	55.1	18.6	20.1	-	0.7	0.6	0.5	1.3	2.0	1.1

3.5.2 The short-term cytocompatibility of human-derived fibroblast on the AM surface.

Viability using the resazurin method is shown in Figure 3A, AM treated surface did not cause any cytotoxicity as the viability of the cells was 92.5 ± 2.6% compared to the CTL 100 ± 8.3%, p=0.21. Merged fluorescent images stained with phalloidin, a highly bicyclic peptide used to stain actin filaments and nuclei staining with DAPI demonstrated the HDF cells incubated on the AM surface (Figure 3C) were confluent and had normal fibroblast morphology comparable to the CTL samples (Figure 3B). These data demonstrate good viability and cell attachment on the AM surface, thus confirming the nanostructured surface is cytocompatible with HDF cells.

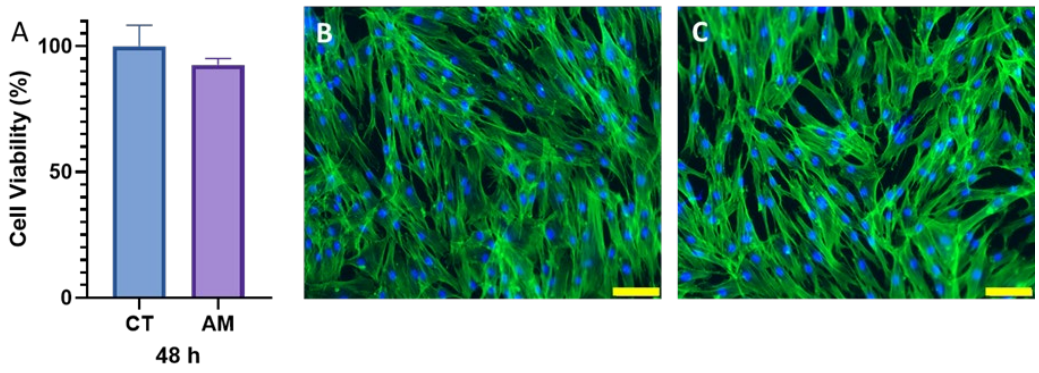

Figure 3. *The short-term cytocompatibility of HDFs at 48 h, was analysed using resazurin cell viability assay (A). Percent of cell viability of CTL compared with AM discs mean ± SD, p=0.21 (n = 3). Fluorescence microscopy merged images of HDFs after 48 h incubation stained with phalloidin for actin cytoskeleton (green) and DAPI for nucleus (blue), on CTL (B) and AM surface (C), scale bar represents 100µm.*

3.5.3 Evaluation of antibacterial performance (Bacterial viability by Live/Dead assay)

Images at the sample interface acquired by CLSM are shown in Figure 4, where viable bacteria are stained green and non-viable bacteria red. On the CTL surfaces, both *S. aureus* (Figure 4A) and *P. aeruginosa* (Figure 4C) appear fully viable across the entire concentration range.

When bacteria were cultured on the AM surfaces, large numbers of non-viable cells were observed, with *P. aeruginosa* undergoing notably increased cell death compared to *S. aureus* (Figure 4D and 4B, respectively). Quantitatively, the viability of *S. aureus* remained at 30% - 40% on the AM surface for lower inoculum concentrations, but above 10^5 CFU/disc, there was an increase in bacterial cell viability with each log increase in inoculum concentration (Figure 5A). For *P. aeruginosa* on the AM surfaces, less than 2% of bacteria remained viable at inoculum concentrations below 10^7 CFU/disc, but at inoculum concentrations above 10^7 CFU/disc, the viability of *P. aeruginosa* increased to approximately 10% (Figure 5B). The decrease in the number of viable bacteria on AM discs was statistically significant for all inoculum concentrations for both *S. aureus* and *P. aeruginosa* $p < 0.001$.

3.5.4 Evaluation of the full thickness of the biofilm

Z-stacked CLSM images generated for *S. aureus* and *P. aeruginosa* incubated on CTL and AM discs showing the spatial distribution of viable (green) and non-viable (red) cells are presented in Figure 6. The distribution of live and dead cells for both species when cultured on the CTL surfaces had a stochastic distribution through the thickness of the formed biomass (Figures 7A and 8A). Most bacteria were viable, consistent with what is observed in a typical biofilm. However, for the AM surface, there was a notably increased proportion of non-viable bacteria throughout the entire thickness of the biomass. Furthermore, there was a greater proportion of non-viable bacteria directly in contact with the AM surfaces, compared to the layer of biomass farthest from the surface (Figures 7B and 8B). Within the 2-µm layer adjacent to the surface, *S. aureus* viability was only 0.1% with an inoculum concentration of 10^6 CFU/disc and 76.9% at the highest bacterial inoculum concentration of 10^9 CFU/disc. However, at increasing distances from the surface, the effect of increasing the inoculum concentration was less pronounced e.g., in the layer of biomass farthest from contact with the AM surface, the proportion of viable bacteria increased from 75.7% at 10^6 CFU/disc to 89% for the 10^9 CFU/disc. Considering *P. aeruginosa,* greater than 90% of bacteria within the 2µm layer adjacent to the surface were non-viable for all inoculum concentrations. In the layer *of P. aeruginosa* biomass furthest from the surface, bacterial viability ranged from 19.6% to 11.3%, for inoculum concentrations of 10^6 CFU/disc and 10^9 CFU/disc, respectively (Figure 8).

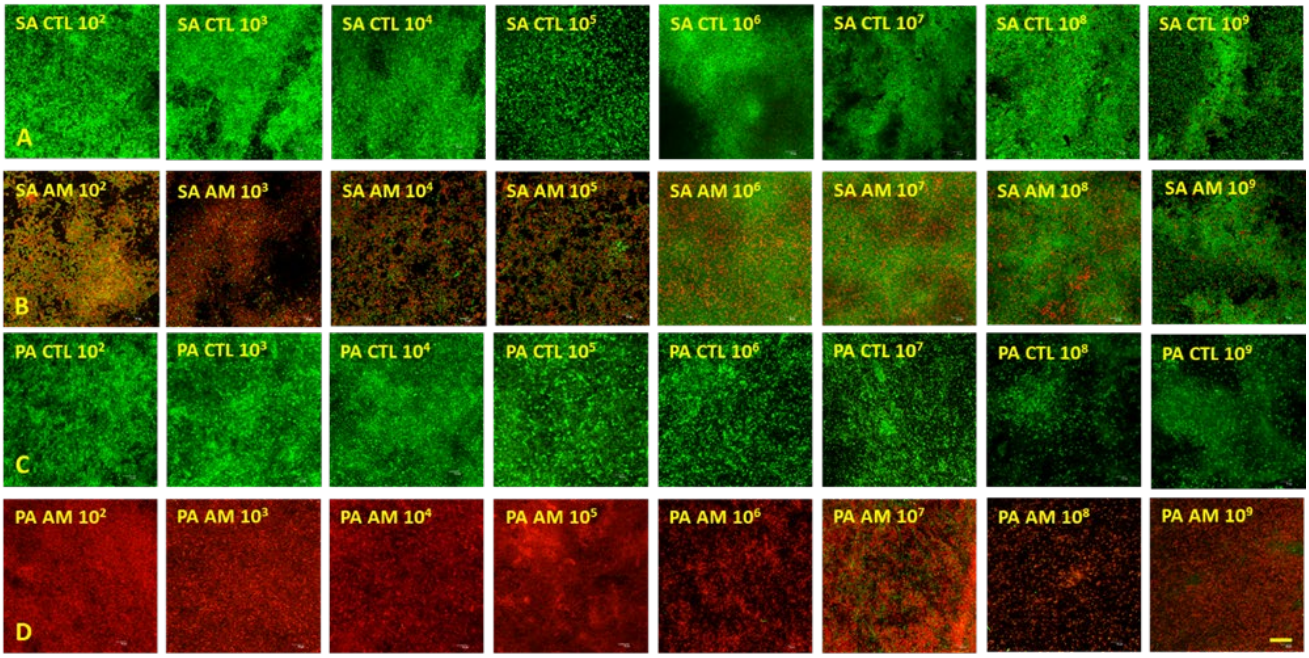

Figure 4. *Single-plane images of S. aureus and P. aeruginosa were acquired at the surface interface by CLSM. Fluorescently labelled using LIVE/DEAD® BacLight ™ Bacterial Viability Kit. A) S. aureus on Ti Alloy unetched CTL (SA CTL) and B) AM discs (SA AM). C) P. aeruginosa on Ti Alloy unetched CTL (PA CTL) and D) AM discs (PA AM) at 18 h after initial inoculum concentrations of 10^2 to 10^9 CFU/disc. yellow scale bar in the bottom right image represents 20µm, (n = 3).*

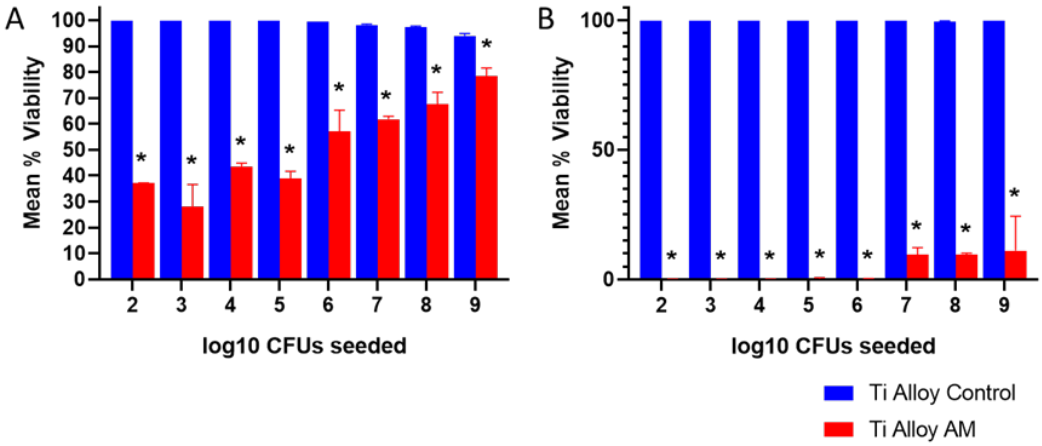

Figure 5. *Percent viability at 10-fold increasing concentrations of S. aureus (A) and P. aeruginosa (B) on AM and CTL discs 18 h after initial inoculation. Mean ± SD. Cell viability was quantified by staining with Live/Dead® BacLight™, mean ± SD (n = 3). Statistical significance was determined using the Holm-Sidak multiple comparison test for CTL versus AM samples for both S. aureus and P. aeruginosa, * p < 0.001*

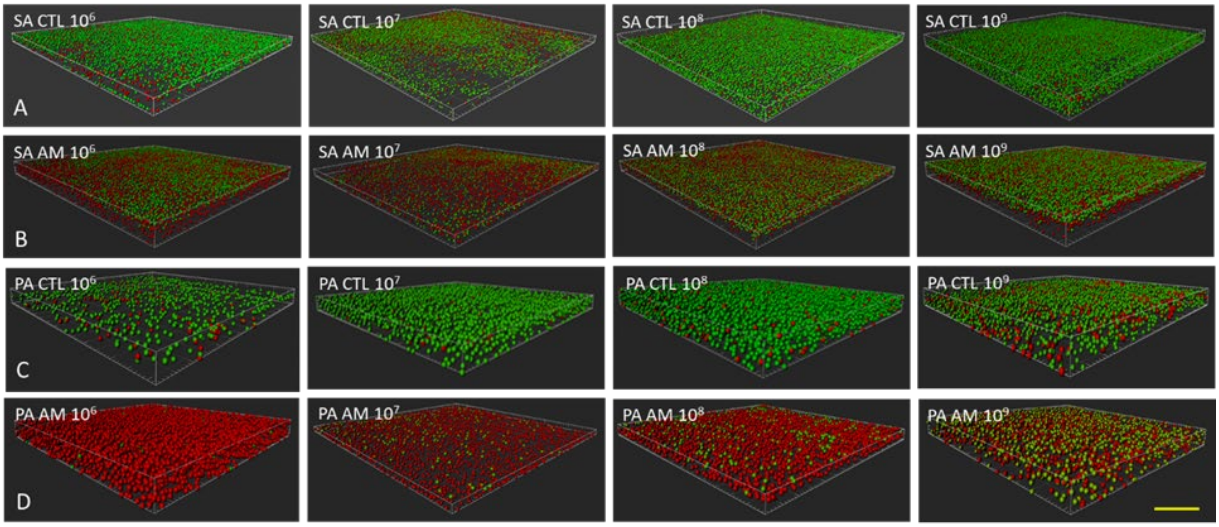

Figure 6. *Reconstructed modelling of z-stack images acquired from CLSM generated using Bitplane Imaris 3D image and analysis software shows the viability of bacteria through the thickness of the biomass 18 h after initial inoculation, where the bottom dying bacteria are in direct contact with the disc surface. A) S. aureus on Ti Alloy unetched CTL (SA CTL) and B) AM discs (SA AM). C) P. aeruginosa on Ti Alloy unetched CTL (PA CTL) and D) AM discs (PA AM) at the four highest inoculum concentrations 10^6 to 10^9 CFU/disc. The scale bar in the bottom right image represents 20µm, (n = 3).*

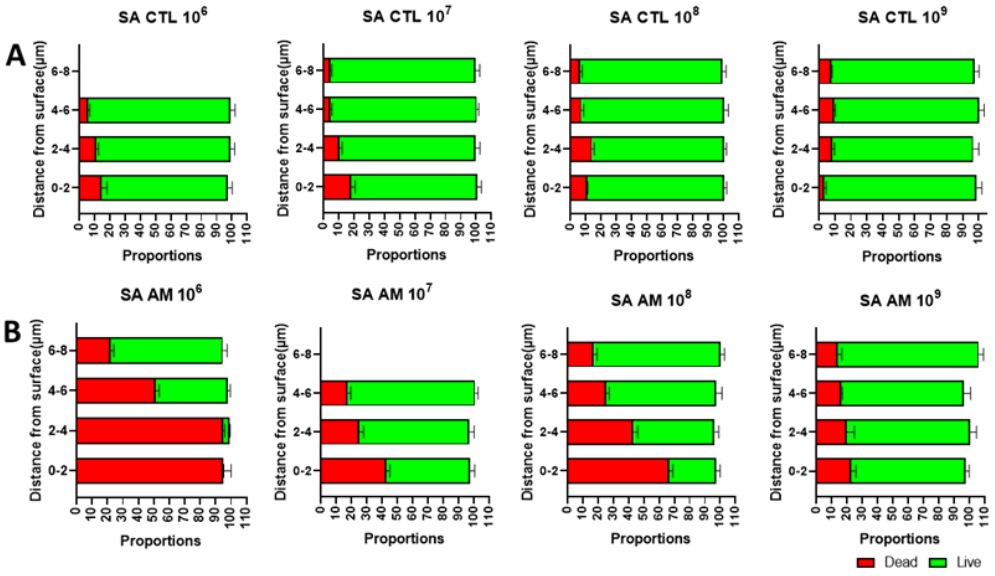

Figure 7. *The bar graphs indicate the live/dead percentage of the four highest inoculations, through each 2µm layer of biomass upwards from the surface, where green indicates viable and red indicates non-viable bacteria. S. aureus (SA) after 18h, through the full thickness of biomass adhered to A) SA CTL, and B) SA AM surfaces, mean ± SD (n = 3). See Table S2 in the supporting information for statistical significance.*

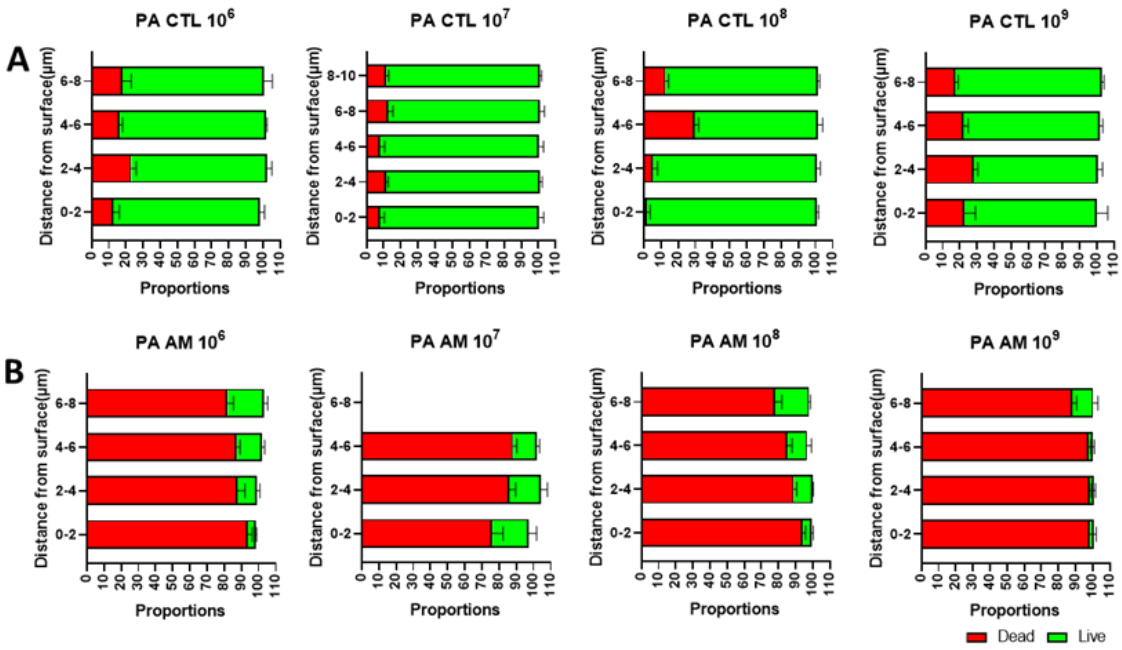

Figure 8. *Shows live/dead percentage of the four highest inoculations of P. aeruginosa (PA), through each 2µm layer of biomass upwards from the surface, where green indicates viable and red indicates non-viable bacteria. A) PA CTL, and B) PA AM surfaces, mean ± SD (n = 3). See Table S3 in the supporting information for statistical significance.*

3.5.5 Viability determined from colony enumeration (CFU counts)

For all inoculum concentrations, there was a greater than 2-log reduction (99.5%) of *S. aureus* growth on the AM surface compared to the CTL surface (2.5 log reduction for the lowest inoculum concentration to a 2-log reduction for the highest concentration, Figure 9A). The AM surface also had a greater efficacy in killing *P. aeruginosa* (Figure 9B). At the lower inoculum concentrations of 10^2 to 10^5 CFU/disc, the growth inhibition of *P. aeruginosa* on the AM surface was approaching a 5-log reduction relative to the CTL surface. Even at the highest inoculum concentration of 10^9 CFU/disc, there was still a 4-log reduction in viable bacteria on the AM surface relative to the CTL surface. SEM confirmed that no bacteria were left on the CTL or AM samples after vortexing and sonication.

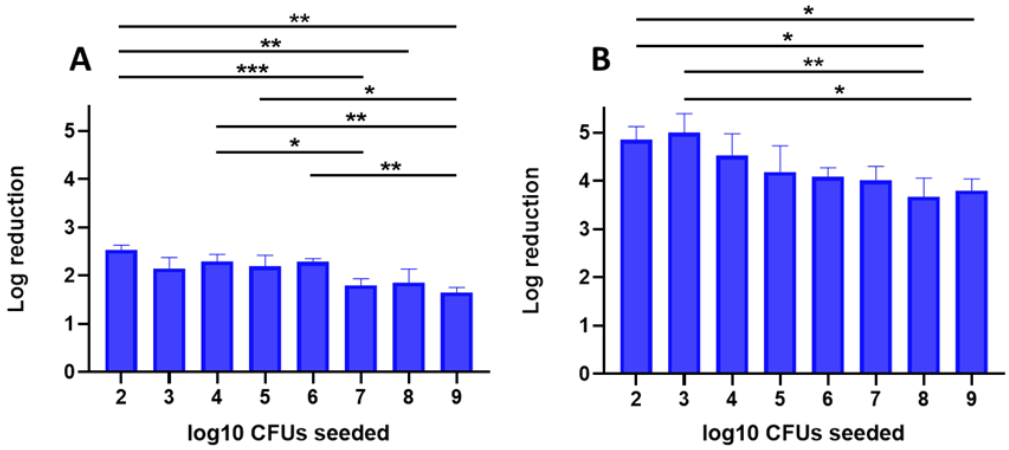

Figure 9. *Log reduction in viable bacteria on the AM surface, relative to the CTL surface after 18 h for A) S. aureus and B) P. aeruginosa. Bar graphs show relative log reduction in bacterial viability between surfaces with varying inoculum concentrations from 10^2 to 10^9. Mean ± SD (n = 3), * p < 0.05, **p < 0.001 and ***p < 0.001.*

3.5.6 SEM imaging of biofilm

Both *S. aureus* and *P. aeruginosa* grown on the CTL disc surfaces appeared healthy, showing no signs of cell damage (Figure 10). Furthermore, early biofilm formation was evident in the presence of extracellular polymeric (EPS) substances (Figures 10A and 10C). In contrast, there was no evidence of EPS or biofilm formation from bacteria inoculated on AM disc surfaces for all inoculum concentrations (Figure 10B and 10D). *P. aeruginosa* cells inoculated onto AM disc surfaces also appeared flattened and damaged (Figure 10D). These observations are consistent with cell membrane damage caused by the sharp features of the AM surface. *S. aureus* cells inoculated onto AM disc surfaces often displayed morphological changes including fragmentation (Figure 10B). These variances are likely due to the differences in the cell wall between the Gram-positive *S. aureus* and Gram-negative *P. aeruginosa.*

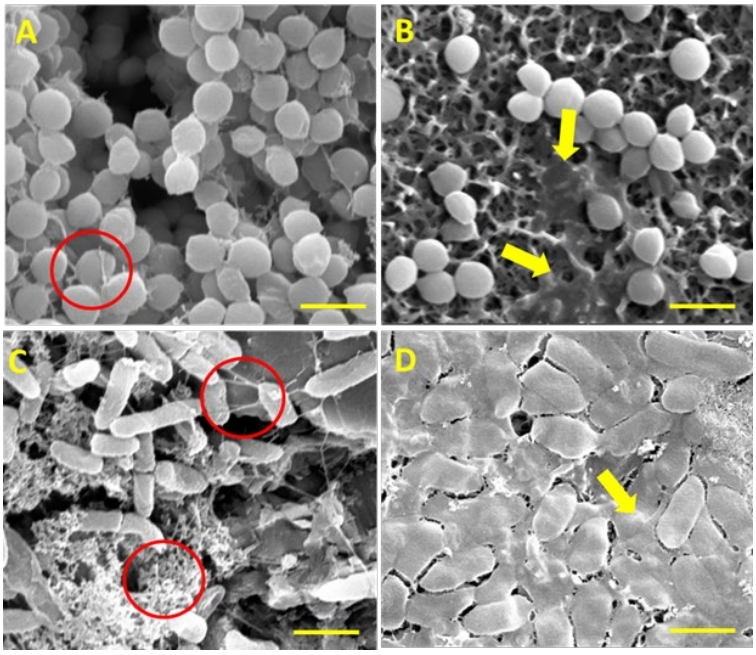

Figure 10. *Representative SEM Images of bacteria after 18-h incubation (10^6 CFU/disc initial inoculation concentration): S. aureus on Ti alloy (A) CTL S. aureus on AM surface (B) P. aeruginosa on Ti alloy CTL (C) and P. aeruginosa on AM surface (D). Red circles highlight early biofilm formation containing bacteria encapsulated in extracellular polymeric substances and fimbria adhesions, on unmodified titanium alloy CTL surfaces (A and C). Yellow arrows indicate lysed bacteria on the AM surfaces (B and D). SEM images were acquired at 25,000x magnification, 10kV, secondary electron mode and a working distance of 10mm. Scale bar = 1µm.*

Surface modifications at the nanoscale have shown potential in killing Gram-positive and Gram-negative bacteria, [33] but concentration-dependent experiments have not yet been performed. The concentration of bacteria that may attach to a titanium implant in a clinical environment is both uncertain and multifactorial and influenced by the implant type, the clinical setting, and patient factors [48-50]. Regardless, prior studies on the bactericidal efficacy of nanostructured surfaces have considered concentrations of bacteria that may be much greater than those that may occur clinically. We, therefore, evaluated the effect of the initial inoculum concentration of *S. aureus* and *P. aeruginosa* on the bactericidal efficacy of hydrothermally etched Ti6Al4V discs. We found a concentration-dependent effect for both species. For *S. aureus*, the killing efficacy of an AM surface remained at around 60% for concentrations from 10^2 CFU/disc to 10^5 CFU/disc. However, above concentrations of 10^5 CFU/disc, the killing efficiency incrementally decreased to approximately 25% at 10^9 CFU/disc. For *P. aeruginosa*, a more dramatic bactericidal effect was observed. The killing efficacy of an AM surface was close to 100% for concentrations from 10^2 to 10^5 CFU/disc, and even at the highest concentration of 10^9 CFU/disc, only approximately 10% of the cells remained viable.

For both bacteria, the biofilm depth profiling analysis revealed that on the AM surface, the greatest killing effect was at the interface between the nanostructured surface and the biomass, with a tapered reduction in killing further from the surface. These results are consistent with the previously reported mechanism of bacterial death induced by nanospiked surfaces. [33, 51]

In contrast, on the CTL surface, there was little difference in the viability of both types of bacteria in contact with the surface, or further away from the surface. Further evidence of preferential bacterial death adjacent to the surface itself was noted via SEM, where deformation and disruption of cell membranes were observed on the AM surface, but not on the CTL surface. There were notable differences in the concentration responses of *S. aureus* and *P. aeruginosa*, reflecting the challenge of killing Gram-positive bacteria. When compared to Gram-positive bacteria, the Gram-negative wall of *P. aeruginosa* has a 4-5-fold decrease in the peptidoglycan layer thickness, which is essential for structural integrity. The outer membrane of gram-negative bacteria comprises a phospholipid bilayer containing lipopolysaccharide, which is pivotal for the homeostasis of the periplasm of Gram-negative bacteria[52], and when damaged, the cell rapidly dies. [53] Gram-positive bacteria lack an outer membrane however, they express capsular polysaccharides. [54] The thick peptidoglycan layer and the capsular polysaccharide outer layer of gram-positive bacteria (such as *S. aureus*) provide a greater cell envelope stiffness than that of Gram-negative bacteria, thus exerting a protective role against mechanical-induced damage. [52, 55] For *P. aeruginosa,* excellent killing efficacy was demonstrated on the AM surface across a broad range of concentrations. For *S. aureus,* the killing efficacy of the AM surface decreased for inoculum concentrations greater than 10^6 CFU/disc. A potential mechanism to explain the decreased killing efficacy at higher concentrations is that at high inoculum concentrations, clusters of bacteria can form in the inoculum, with only the bacteria in direct contact with the surface undergoing cellular death. We also noted that killing efficacy decreased at increasing distances from the AM surface, particularly for *S. aureus*.

In contrast, several researchers have reported comparable killing efficacy on KOH hydrothermally etched titanium nanospikes. Wandiyanto, *et al.* [34] reported bacterial inactivation of 99 ± 0.7% for *P. aeruginosa* and 71.4 ± 13.6% for *S. aureus* at an inoculum concentration of approximately 10^8 CFU/disc however very few *S. aureus* were observed in CLSM images. An earlier study showed that 50% of *P. aeruginosa* and 20% of S. aureus were eliminated at an inoculum concentration of 3 x 10^8 CFU/disc, [32] somewhat similar to what we observed. Tsimbouri, *et al*. [56] generated hydrothermally etched titanium discs using 1M NaOH, which resulted in similar nanotopography and a 58% killing efficacy of *P. aeruginosa* after an 18-h incubation period inoculated with 6 x 10^8 CFU/disc. Similar nanostructures achieved using a chlorine-based, maskless plasma etched titanium, achieved a killing of 87.2 ± 2 % for *P. aeruginosa* and 72.5 ± 13 % for *S. aureus*, however, did not indicate the inoculation concentration. [5]

Biofilms are dynamic aggregates of bacterial cells embedded into a self-produced matrix with the ability to release planktonic cells, which may then attach to new sites. Given that nanostructured surfaces are passive in nature and do not elute biocidal agents into the biomass, it is logical to expect less cellular death and an increased propensity for cellular survival and biofilm formation further from the surface. Furthermore, if the nanostructured surface is covered by a layer of dead bacteria, there may be a masking effect, whereby the killing efficacy of the sharp nanostructures is reduced, allowing other bacteria to attach and grow on this layer of dead bacteria.

Such mechanisms require further study. Of note, however, we observed a population of dead cells in the upper layer of the bacterial biomass, even at high inoculum concentrations. An explanation for this could be the production of reactive oxygen species or programmed cell death due to an increased abundance of stress proteins upon the interaction of bacteria with sharp nanostructures. [58-60] These results suggest that there is an inoculum concentration threshold of approximately 10^6 CFU/disc, above which the killing efficacy of nanostructured surfaces may be diminished. In a sterile operating theatre environment, such a concentration is orders of magnitude above that which would be expected to contaminate a surgical site, stated as low as 10^2 CFU/cm^2. [61] We have demonstrated that a nanospiked Ti6AlV4 surface is highly biocidal against clinically relevant concentrations of Gram-positive and Gram-negative bacteria. Surface modification of Ti6Al4V implants to create nanostructures thus holds the potential to impair the ability of bacteria to colonize the implant and therefore potentially reduce the incidence of infection.

The significant interest in the antibacterial properties of surfaces containing sharp nanostructures points to a potential for application with future medical devices that reduce patient morbidity and mortality caused by infections. However, much future research is required to fully understand the remarkable properties of these materials and their safety. Our short-term cytocompatibility study using HDFs points to the absence of cytotoxicity and any adverse effects on cell adhesion, proliferation, or shape. This is a promising result; however, much work is required in the future to shed light on issues such as osteointegration, immunological consequences and fibrous encapsulation. The formation of debris from an implanted material is known to cause significant problems for patients. Our preliminary abrasion-induced wear studies presented in the supporting information suggest improved surface resistance to abrasion (Figure S1). This may suggest a reduced probability of debris formation and damage to patient wellbeing. Ultimately, before this surface modification can be used with commercial devices, there is a need for small and then large animal studies using appropriate infection models capable of determining the fate and safety of these nanostructured materials in an *in vivo* situation.

3.6 Conclusion

In this study, we examined the capacity of a contact-dependent nanostructured surface to resist increasing concentrations of bacteria. We utilized the process of hydrothermal etching to create a “spike-like” nanostructured surface topography on medical-grade titanium, showing good short-term cytocompatibility properties. We then challenged this antibacterial surface using increasing concentrations of *S. aureus* (Gram-positive) and *P. aeruginosa* (Gram-negative) from 10^2 CFU to 10^9 CFU/disc (surface area 0.78 cm^2). Analysis of the biomass formed on the surfaces demonstrated that even at high bacterial load, the nanostructures were very efficient in killing the first layer of bacteria. However, new bacteria were able to attach to and colonize the surface “masked” by the first layer of dead cells, particularly in the case of the Gram-positive *S. aureus*.

Nevertheless, it would be safe to assume that in a clinically sterile surgical theatre environment, the probability of contaminating such a device surface with a bacterial concentration greater than 10^6 CFU is relatively low. Thus, the type of contact-dependent bactericidal surface nano-modification investigated in this work could apply to a range of medical devices, acting to inhibit initial bacterial colonization of the implant and subsequent biofilm formation, thus contributing to lowering associated infection rates. Our study presents for the first time the effect of bacterial loading levels on the antibacterial efficacy of nanostructured surfaces. However, our study also points to the need for a future, more detailed investigation of the characteristics of the biofilm that forms. We have demonstrated that the surfaces have no cytotoxicity to primary fibroblast cells in the short term. In future studies, longer-term biocompatibility evaluations need to be carried out, including using bone marrow stromal cells and immune cells. The robustness of the surface features needs to be studied under the relevant standards for biomedical implants such as cyclic loading. Ultimately, the in vivo bactericidal efficacy and safety of this type of surface under different bacterial loads need to be evaluated using appropriate animal models.

3.7 Author Contributions

R.B., D.F. and A.H. designed, planned and performed the experiments. R.B. analyzed data and drafted the manuscript. N.N. and A.B. performed XPS and participated in data analysis. D.P. fabricated samples and assisted with the characterization of the nanotopography, D.B, T.B. initiated the design of the study and revised the manuscript. K.V. supervised the study and revised the manuscript.

3.8 Notes

The authors listed above declare no conflict of interest.

3.9 Acknowledgements

This study was co-funded by the Department of Industry, Science, Energy and Resources (Innovative Manufacturing CRC Ltd) Global Orthopaedic Technology Pty Ltd (IMCRC/GOT/130318). The authors acknowledge the funding and in-kind support from Corin Australia and the University of South Australia. The authors would also like to acknowledge the instruments and scientific and technical assistance of Microscopy Australia at the University of South Australia, Mawson Lakes Campus, a facility that is funded by the University, and State and Federal Governments.

3.10 Supporting Information

The Supporting Information is available free of charge at
https://pubs.acs.org/doi/10.1021/acsami.1c06919.
Additional information regarding the following: friction and wear analysis, conversion table between colony form units (CFU)/cm2 and CFU/disc and p-values comparing the biomass viability of CTL and AMK inoculated with *S. aureus* (figure 7) and *P. aeruginosa* (figure 8).

3.11 Supplementary Information

The *In Vitro* Bactericidal Efficacy of Nanostructured Ti6Al4V Surfaces is Bacterial Load Dependent

Richard Bright[1,2], Andrew Hayles[1,2], Daniel Fernandes[1], Rahul M Visalakshan[1], Neethu Ninan[1], Dennis Palms[1], Anouck Burzava[1], Dan Barker[3], Toby Brown[3], Krasimir Vasilev[1,2]. *

[1]STEM, University of South Australia, Mawson Lakes, Adelaide, 5095, South Australia, Australia. [2]Future Industries Institute, University of South Australia, Mawson Lakes, Adelaide, 5095, South Australia, Australia. [3]Corin Australia, Baulkham Hills, NSW 2153, Australia.
(*Corresponding author email: krasimir.vasilev@unisa.edu.au)

Methods and Materials

Friction and wear analysis. The pin-on-disk tribometer serves for the investigation and simulation of friction and wear processes under sliding conditions. The resistance against abrasive wear of the surface of CTL and AM titanium samples was assessed under a dry condition setup by a Pin-on-Disk tribometer (MT SERIES, Madrid, Spain) following ASTM G99-17 standards. A vertical load of 1N was applied under a constant sliding velocity of 100 RPM along a track radius of 2mm for 50 seconds. Penetration depth was measured by a Confocal Laser Microscope (Olympus OLS5000, Tokyo, Japan) using a 20x objective lens over a squared region of side length 650 um.

Results & Discussion

The HT etched surface modification acted as a hardened overlayer and reduced the penetration of the pin under a load of 1N for the same number of revolutions (Figure S1). Lower penetration could suggest a reduced probability of debris generation compared to the medical grade control.

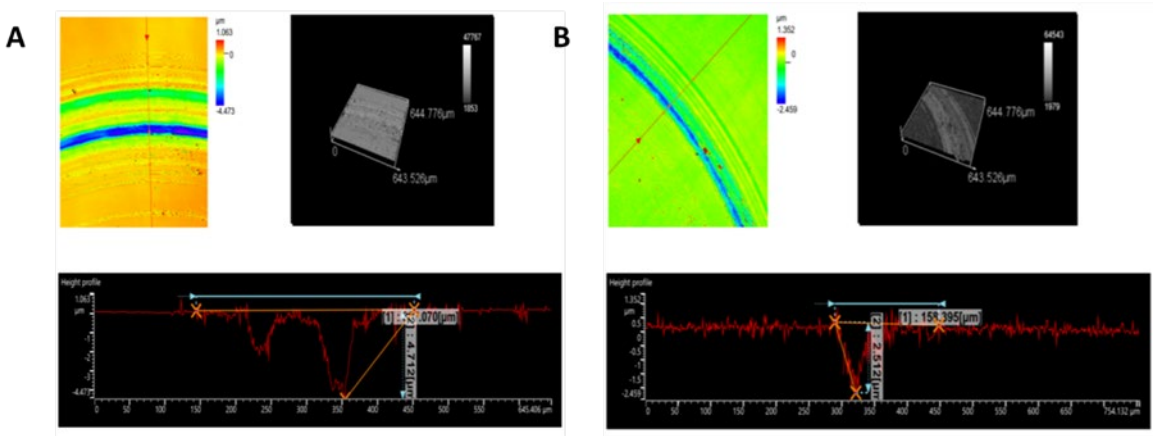

Figure S1. Comparison between etched (AMK) (A) and non-etched (CTL) (B) samples under a load of 1N for the same number of revolutions, a lower penetration depth was observed in etched samples (2.512 um) than its non-etched (4.712 um) counterparts.

CFU/cm^2	CFU/Titanium Alloy Disc
1.3 x 10^9	10^9
1.3 x 10^8	10^8
1.3 x 10^7	10^7
1.3 x 10^6	10^6
1.3 x 10^5	10^5
1.3 x 10^4	10^4
1.3 x 10^3	10^3
1.3 x 10^2	10^2

Table S1. *The table shows the conversion between colony form units (CFU)/cm^2 and CFU/disc, considering the surface area is 0.78cm^2/disc.*

S. aureus	Biofilm Slice	P value	Mean of CTL	Mean of AMK
10^6	0-2	0.000003	82.79	0.07667
	2-4	0.000003	88.21	4.0
	4-6	0.00002	93.55	46.72
	6-8	0.000003	0.0	72.71
10^7	0-2	0.000618	82.86	55.18
	2-4	0.003022	88.86	71.67
	4-6	0.001316	95.9	83.01
	6-8	0.000002	95.42	0.0
10^8	0-2	0.000061	82.86	30.95
	2-4	0.000372	88.86	53.01
	4-6	0.000973	95.9	72.35
	6-8	0.004532	95.42	82.94
10^9	0-2	0.002994	95.57	74.81
	2-4	0.133977	88.16	80.31
	4-6	0.077414	90.75	79.95
	6-8	0.353753	89.87	92.34

Table S2. *P-values and means, comparing biomass viability between unetched-CTL and AMK treated surface (figure 7), for the four highest inoculations of S. aureus Multiple t-tests were performed with post hoc analysis using Holm-Sidak method, (n=3). Only the three outer slices (2-4, 4-6 and 6-8 µm) on the 10^9 inoculation were non-significant. This suggests the surface has reached a bacterial saturation point and observing bacterial regrowth on the AMK.*

P. aeruginosa	**Biofilm Slice**	**P value**	**Mean of CTL**	**Mean of AMK**
10^6	0-2	0.000002	93.57	4.967
	2-4	0.000021	87.57	11.65
	4-6	0.000003	87.43	14.3
	6-8	0.000021	82.1	21.11
10^7	0-2	0.000023	92.62	20.96
	2-4	0.000014	89.54	18.17
	4-6	0.000004	92.46	13.81
	6-8	0.000002	88.25	0.0
	8-10	<0.000001	89.1	0.0
10^8	0-2	<0.000001	98.74	5.39
	2-4	<0.000001	94.97	10.77
	4-6	0.000011	71.62	11.62
	6-8	<0.000001	88.47	20.04
10^9	0-2	0.000035	77.35	1.95
	2-4	0.000005	72.47	2.267
	4-6	<0.000001	79.8	2.427
	6-8	0.000005	85.6	12.28

Table S3. *P-value and mean comparing, biomass viability between unetched-CTL and AMK treated surface (figure 7), for the four highest inoculations of P. aeruginosa Multiple t-tests, were performed with posthoc analysis using Holm-Sidak method, (n=3). AMK had statistically lower viability compared to the unetched-CTL surface.*

3.12 References

(1) Schierholz, J. M.; Beuth, J. Implant Infections: A Haven for Opportunistic Bacteria. *J Hosp Infect* **2001,** *49* (2), 87-93, DOI: 10.1053/jhin.2001.1052.

(2) Parvizi, J.; Gehrke, T.; International Consensus Group on Periprosthetic Joint, I. Definition of Periprosthetic Joint Infection. *J Arthroplasty* **2014,** *29* (7), 1331, DOI: 10.1016/j.arth.2014.03.009.

(3) Parvizi, J.; Gehrke, T.; Chen, A. F. Proceedings of the International Consensus on Periprosthetic Joint Infection. *The bone & joint journal* **2013,** *95-B* (11), 1450-2, DOI: 10.1302/0301-620X.95B11.33135.

(4) Davidson, D. J.; Spratt, D.; Liddle, A. D. Implant Materials and Prosthetic Joint Infection: The Battle with the Biofilm. *EFORT Open Rev* **2019,** *4* (11), 633-639, DOI: 10.1302/2058-5241.4.180095.

(5) Eka, A.; Chen, A. F. Patient-Related Medical Risk Factors for Periprosthetic Joint Infection of the Hip and Knee. *Ann Transl Med* **2015,** *3* (16), 233, DOI: 10.3978/j.issn.2305-5839.2015.09.26.

(6) Stoodley, P.; Kathju, S.; Hu, F. Z.; Erdos, G.; Levenson, J. E.; Mehta, N.; Dice, B.; Johnson, S.; Hall-Stoodley, L.; Nistico, L.; Sotereanos, N.; Sewecke, J.; Post, J. C.; Ehrlich, G. D. Molecular and Imaging Techniques for Bacterial Biofilms in Joint Arthroplasty Infections. *Clin Orthop Relat Res* **2005,** (437), 31-40, DOI: 10.1097/01.blo.0000175129.83084.d5.

(7) Cataldo, M. A.; Petrosillo, N.; Cipriani, M.; Cauda, R.; Tacconelli, E. Prosthetic Joint Infection: Recent Developments in Diagnosis and Management. *J Infect* **2010,** *61* (6), 443-8, DOI: 10.1016/j.jinf.2010.09.033.

(8) Boxma, H.; Broekhuizen, T.; Patka, P.; Oosting, H. Randomised Controlled Trial of Single-Dose Antibiotic Prophylaxis in Surgical Treatment of Closed Fractures: The Dutch Trauma Trial. *Lancet* **1996,** *347* (9009), 1133-7, DOI: 10.1016/s0140-6736(96)90606-6.

(9) Patzakis, M. J.; Wilkins, J. Factors Influencing Infection Rate in Open Fracture Wounds. *Clin Orthop Relat Res* **1989,** (243), 36-40.

(10) Metsemakers, W. J.; Kuehl, R.; Moriarty, T. F.; Richards, R. G.; Verhofstad, M. H. J.; Borens, O.; Kates, S.; Morgenstern, M. Infection after Fracture Fixation: Current Surgical and Microbiological Concepts. *Injury* **2018,** *49* (3), 511-522, DOI: 10.1016/j.injury.2016.09.019.

(11) Arciola, C. R.; Campoccia, D.; Montanaro, L. Implant Infections: Adhesion, Biofilm Formation and Immune Evasion. *Nat Rev Microbiol* **2018,** *16* (7), 397-409, DOI: 10.1038/s41579-018-0019-y.

(12) Arciola, C. R.; Campoccia, D.; Speziale, P.; Montanaro, L.; Costerton, J. W. Biofilm Formation in Staphylococcus Implant Infections. A Review of Molecular Mechanisms and Implications for Biofilm-Resistant Materials. *Biomaterials* **2012,** *33* (26), 5967-82, DOI: 10.1016/j.biomaterials.2012.05.031.

(13) Stoodley, P.; Conti, S. F.; DeMeo, P. J.; Nistico, L.; Melton-Kreft, R.; Johnson, S.; Darabi, A.; Ehrlich, G. D.; Costerton, J. W.; Kathju, S. Characterization of a Mixed Mrsa/Mrse Biofilm in an Explanted Total Ankle Arthroplasty. *FEMS Immunol Med Microbiol* **2011,** *62* (1), 66-74, DOI: 10.1111/j.1574-695X.2011.00793.x.

(14) Stoodley, P.; Nistico, L.; Johnson, S.; Lasko, L. A.; Baratz, M.; Gahlot, V.; Ehrlich, G. D.; Kathju, S. Direct Demonstration of Viable Staphylococcus Aureus Biofilms in an Infected Total Joint Arthroplasty. A Case Report. *J Bone Joint Surg Am* **2008,** *90* (8), 1751-8, DOI: 10.2106/JBJS.G.00838.

(15) Bidossi, A.; Bottagisio, M.; Savadori, P.; De Vecchi, E. Identification and Characterization of Planktonic Biofilm-Like Aggregates in Infected Synovial Fluids from Joint Infections. *Front Microbiol* **2020,** *11*, 1368, DOI: 10.3389/fmicb.2020.01368.

(16) Koseki, H.; Yonekura, A.; Shida, T.; Yoda, I.; Horiuchi, H.; Morinaga, Y.; Yanagihara, K.; Sakoda, H.; Osaki, M.; Tomita, M. Early Staphylococcal Biofilm Formation on Solid Orthopaedic Implant Materials: In Vitro Study. *PLoS One* **2014,** *9* (10), e107588, DOI: 10.1371/journal.pone.0107588.

(17) Toyofuku, M.; Inaba, T.; Kiyokawa, T.; Obana, N.; Yawata, Y.; Nomura, N. Environmental Factors That Shape Biofilm Formation. *Biosci Biotechnol Biochem* **2016,** *80* (1), 7-12, DOI: 10.1080/09168451.2015.1058701.

(18) Liu, Y.; Zhang, J.; Ji, Y. Environmental Factors Modulate Biofilm Formation by Staphylococcus Aureus. *Sci Prog* **2020,** *103* (1), 36850419898659, DOI: 10.1177/0036850419898659.

(19) Nandakumar, V.; Chittaranjan, S.; Kurian, V. M.; Doble, M. Characteristics of Bacterial Biofilm Associated with Implant Material in Clinical Practice. *Polym J* **2012,** *45* (2), 137-152, DOI: 10.1038/pj.2012.130.

(20) Izakovicova, P.; Borens, O.; Trampuz, A. Periprosthetic Joint Infection: Current Concepts and Outlook. *EFORT Open Rev* **2019,** *4* (7), 482-494, DOI: 10.1302/2058-5241.4.180092.

(21) Young, H.; Hirsh, J.; Hammerberg, E. M.; Price, C. S. Dental Disease and Periprosthetic Joint Infection. *J Bone Joint Surg Am* **2014,** *96* (2), 162-8, DOI: 10.2106/JBJS.L.01379.

(22) Cyteval, C.; Bourdon, A. Imaging Orthopedic Implant Infections. *Diagn Interv Imaging* **2012,** *93* (6), 547-57, DOI: 10.1016/j.diii.2012.03.004.

(23) Zimmerli, W.; Sendi, P. Orthopaedic Biofilm Infections. *APMIS* **2017,** *125* (4), 353-364, DOI: 10.1111/apm.12687.

(24) Spagnolo, A. M.; Ottria, G.; Amicizia, D.; Perdelli, F.; Cristina, M. L. Operating Theatre Quality and Prevention of Surgical Site Infections. *J Prev Med Hyg* **2013,** *54* (3), 131-137.

(25) Kapadia, B. H.; Berg, R. A.; Daley, J. A.; Fritz, J.; Bhave, A.; Mont, M. A. Periprosthetic Joint Infection. *Lancet* **2016,** *387* (10016), 386-394, DOI: 10.1016/S0140-6736(14)61798-0.

(26) Sharma, D.; Misba, L.; Khan, A. U. Antibiotics Versus Biofilm: An Emerging Battleground in Microbial Communities. *Antimicrob Resist Infect Control* **2019,** *8*, 76, DOI: 10.1186/s13756-019-0533-3.

(27) Sendi, P.; Zimmerli, W. Antimicrobial Treatment Concepts for Orthopaedic Device-Related Infection. *Clin Microbiol Infect* **2012,** *18* (12), 1176-84, DOI: 10.1111/1469-0691.12003.

(28) Wang, M.; Tang, T. Surface Treatment Strategies to Combat Implant-Related Infection from the Beginning. *J Orthop Translat* **2019,** *17*, 42-54, DOI: 10.1016/j.jot.2018.09.001.

(29) Narayana, S. V. V. S.; Srihari, S. V. V. A Review on Surface Modifications and Coatings on Implants to Prevent Biofilm. *Regen Eng Transl Med* **2019,** *6* (3), 330-346, DOI: 10.1007/s40883-019-00116-3.
(30) Lin, N.; Berton, P.; Moraes, C.; Rogers, R. D.; Tufenkji, N. Nanodarts, Nanoblades, and Nanospikes: Mechano-Bactericidal Nanostructures and Where to Find Them. *Advances in colloid and interface science* **2018,** *252*, 55-68, DOI: 10.1016/j.cis.2017.12.007.
(31) Bandara, C. D.; Singh, S.; Afara, I. O.; Wolff, A.; Tesfamichael, T.; Ostrikov, K.; Oloyede, A. Bactericidal Effects of Natural Nanotopography of Dragonfly Wing on Escherichia Coli. *ACS Appl Mater Interfaces* **2017,** *9* (8), 6746-6760, DOI: 10.1021/acsami.6b13666.
(32) Bhadra, C. M.; Truong, V. K.; Pham, V. T.; Al Kobaisi, M.; Seniutinas, G.; Wang, J. Y.; Juodkazis, S.; Crawford, R. J.; Ivanova, E. P. Antibacterial Titanium Nano-Patterned Arrays Inspired by Dragonfly Wings. *Sci Rep* **2015,** *5*, 16817, DOI: 10.1038/srep16817.
(33) Ivanova, E. P.; Hasan, J.; Webb, H. K.; Gervinskas, G.; Juodkazis, S.; Truong, V. K.; Wu, A. H.; Lamb, R. N.; Baulin, V. A.; Watson, G. S.; Watson, J. A.; Mainwaring, D. E.; Crawford, R. J. Bactericidal Activity of Black Silicon. *Nat Commun* **2013,** *4*, 2838, DOI: 10.1038/ncomms3838.
(34) Wandiyanto, J. V.; Tamanna, T.; Linklater, D. P.; Truong, V. K.; Al Kobaisi, M.; Baulin, V. A.; Joudkazis, S.; Thissen, H.; Crawford, R. J.; Ivanova, E. P. Tunable Morphological Changes of Asymmetric Titanium Nanosheets with Bactericidal Properties. *J Colloid Interface Sci* **2020,** *560*, 572-580, DOI: 10.1016/j.jcis.2019.10.067.
(35) Standard Test Method for Determining the Antimicrobial Activity of Antimicrobial Agents under Dynamic Contact Conditions: Astm E2149-10. In *American Society for Testing and Materials (ATSM)*, West Conshohocken, PA, USA, 2010.
(36) Crnich, C. J.; Pop-Vicas, A. E.; Hedberg, T. G.; Perl, T. M. Efficacy and Safety of a Novel Antimicrobial Preoperative Skin Preparation. *Infect Control Hosp Epidemiol* **2019,** *40* (10), 1157-1163, DOI: 10.1017/ice.2019.200.
(37) Roth, J. A.; Schwab, C.; Atkinson, A.; von Flüe, M.; Kettelhack, C.; Eckstein, F. S.; Battegay, M.; Klimke, S.; Frei, R.; Widmer, A. F. Are Three Antiseptic Paints Needed for Safe Preparation of the Surgical Field? A Prospective Cohort Study with 239 Patients. *Antimicrob Resist Infect Control* **2020,** *9* (1), 120, DOI: 10.1186/s13756-020-00780-z.
(38) Russotto, V.; Cortegiani, A.; Raineri, S. M.; Giarratano, A. Bacterial Contamination of Inanimate Surfaces and Equipment in the Intensive Care Unit. *J Intensive Care* **2015,** *3*, 54, DOI: 10.1186/s40560-015-0120-5.
(39) Fu Shaw, L.; Chen, I. H.; Chen, C. S.; Wu, H. H.; Lai, L. S.; Chen, Y. Y.; Wang, F. Factors Influencing Microbial Colonies in the Air of Operating Rooms. *BMC Infect Dis* **2018,** *18* (1), 4, DOI: 10.1186/s12879-017-2928-1.
(40) Jorand, F. P.; Debuy, S.; Kamagate, S. F.; Engels-Deutsch, M. Evaluation of a Biofilm Formation by Desulfovibrio Fairfieldensis on Titanium Implants. *Lett Appl Microbiol* **2015,** *60* (3), 279-87, DOI: 10.1111/lam.12370.

(41) Kinnari, T. J.; Peltonen, L. I.; Kuusela, P.; Kivilahti, J.; Könönen, M.; Jero, J. Bacterial Adherence to Titanium Surface Coated with Human Serum Albumin. *Otol Neurotol* **2005,** *26* (3), 380-4, DOI: 10.1097/01.mao.0000169767.85549.87.

(42) Bankier, C.; Cheong, Y.; Mahalingam, S.; Edirisinghe, M.; Ren, G.; Cloutman-Green, E.; Ciric, L. A Comparison of Methods to Assess the Antimicrobial Activity of Nanoparticle Combinations on Bacterial Cells. *PLoS One* **2018,** *13* (2), e0192093, DOI: 10.1371/journal.pone.0192093.

(43) Rabe, M.; Verdes, D.; Seeger, S. Understanding Protein Adsorption Phenomena at Solid Surfaces. *Advances in colloid and interface science* **2011,** *162* (1-2), 87-106, DOI: 10.1016/j.cis.2010.12.007.

(44) Prabu, V.; Karthick, P.; Rajendran, A.; Natarajan, D.; Kiran, M. S.; Pattanayak, D. K. Bioactive Ti Alloy with Hydrophilicity, Antibacterial Activity and Cytocompatibility. *Rsc Adv* **2015,** *5* (63), 50767-50777, DOI: 10.1039/c5ra04077a.

(45) Samree, K.; Srithai, P. U.; Kotchaplai, P.; Thuptimdang, P.; Painmanakul, P.; Hunsom, M.; Sairiam, S. Enhancing the Antibacterial Properties of Pvdf Membrane by Hydrophilic Surface Modification Using Titanium Dioxide and Silver Nanoparticles. *Membranes* **2020,** *10* (10), DOI: 10.3390/membranes10100289.

(46) Chouirfa, H.; Bouloussa, H.; Migonney, V.; Falentin-Daudré, C. Review of Titanium Surface Modification Techniques and Coatings for Antibacterial Applications. *Acta biomaterialia* **2019,** *83*, 37-54, DOI: 10.1016/j.actbio.2018.10.036.

(47) Huang, L.; Jing, S.; Zhuo, O.; Meng, X.; Wang, X. Surface Hydrophilicity and Antifungal Properties of Tio Films Coated on a Co-Cr Substrate. *BioMed Research International* **2017,** *2017*, 2054723, DOI: 10.1155/2017/2054723.

(48) Schömig, F.; Perka, C.; Pumberger, M.; Ascherl, R. Implant Contamination as a Cause of Surgical Site Infection in Spinal Surgery: Are Single-Use Implants a Reasonable Solution? - a Systematic Review. *BMC Musculoskelet Disord* **2020,** *21* (1), 634, DOI: 10.1186/s12891-020-03653-z.

(49) Koga, T.; Matsukubo, T.; Okuda, K.; Ishihara, K. Effect of Clinical Factors on Bacterial Contamination of Bone Chips Collected During Implant Surgery. *Implant Dent* **2013,** *22* (5), 525-9, DOI: 10.1097/ID.0b013e3182a2b8e3.

(50) Ribeiro, M.; Monteiro, F. J.; Ferraz, M. P. Infection of Orthopedic Implants with Emphasis on Bacterial Adhesion Process and Techniques Used in Studying Bacterial-Material Interactions. *Biomatter* **2012,** *2* (4), 176-94, DOI: 10.4161/biom.22905.

(51) Cao, Y.; Su, B.; Chinnaraj, S.; Jana, S.; Bowen, L.; Charlton, S.; Duan, P.; Jakubovics, N. S.; Chen, J. Nanostructured Titanium Surfaces Exhibit Recalcitrance Towards Staphylococcus Epidermidis Biofilm Formation. *Sci Rep* **2018,** *8* (1), 1071, DOI: 10.1038/s41598-018-19484-x.

(52) Silhavy, T. J.; Kahne, D.; Walker, S. The Bacterial Cell Envelope. *Cold Spring Harb Perspect Biol* **2010,** *2* (5), a000414, DOI: 10.1101/cshperspect.a000414.

(53) Heesterbeek, D. A. C.; Muts, R. M.; van Hensbergen, V. P.; de Saint Aulaire, P.; Wennekes, T.; Bardoel, B. W.; van Sorge, N. M.; Rooijakkers, S. H. M. Outer Membrane Permeabilization by the Membrane Attack Complex Sensitizes Gram-Negative Bacteria to Antimicrobial Proteins in Serum and Phagocytes. *PLoS Pathog* **2021,** *17* (1), e1009227, DOI: 10.1371/journal.ppat.1009227.
(54) Rohde, M. The Gram-Positive Bacterial Cell Wall. *Microbiol Spectr* **2019,** *7* (3), DOI: 10.1128/microbiolspec.GPP3-0044-2018.
(55) Harper, C. E.; Hernandez, C. J. Cell Biomechanics and Mechanobiology in Bacteria: Challenges and Opportunities. *APL Bioeng* **2020,** *4* (2), 021501, DOI: 10.1063/1.5135585.
(56) Tsimbouri, P. M.; Fisher, L.; Holloway, N.; Sjostrom, T.; Nobbs, A. H.; Meek, R. M.; Su, B.; Dalby, M. J. Osteogenic and Bactericidal Surfaces from Hydrothermal Titania Nanowires on Titanium Substrates. *Sci Rep* **2016,** *6*, 36857, DOI: 10.1038/srep36857.
(57) Linklater, D. P.; Juodkazis, S.; Crawford, R. J.; Ivanova, E. P. Mechanical Inactivation of Staphylococcus Aureus and Pseudomonas Aeruginosa by Titanium Substrata with Hierarchical Surface Structures. *Materialia* **2019,** *5*, DOI: 10.1016/j.mtla.2018.100197.
(58) Jenkins, J.; Mantell, J.; Neal, C.; Gholinia, A.; Verkade, P.; Nobbs, A. H.; Su, B. Antibacterial Effects of Nanopillar Surfaces Are Mediated by Cell Impedance, Penetration and Induction of Oxidative Stress. *Nat Commun* **2020,** *11* (1), 1626, DOI: 10.1038/s41467-020-15471-x.
(59) Bayles, K. W. Bacterial Programmed Cell Death: Making Sense of a Paradox. *Nature Reviews Microbiology* **2014,** *12* (1), 63-69, DOI: 10.1038/nrmicro3136.
(60) Allocati, N.; Masulli, M.; Di Ilio, C.; De Laurenzi, V. Die for the Community: An Overview of Programmed Cell Death in Bacteria. *Cell death & disease* **2015,** *6* (1), e1609, DOI: 10.1038/cddis.2014.570.
(61) Percin, D.; Sav, H.; Hormet-Oz, H. T.; Karauz, M. The Relationship between Holding Time and the Bacterial Load on Surgical Instruments. *Indian J Surg* **2015,** *77* (1), 16-18, DOI: 10.1007/s12262-012-0725-z.

(IF 10.16)

Bright R, Fernandes D, Wood J, Palms D, Burzava A, Ninan N, Brown T, Barker D, Vasilev K. Long-term antibacterial properties of a nanostructured titanium alloy surface: An *in vitro* study. Mater Today Bio. 2021 Dec 4;13:100176. DOI: 10.1016/j.mtbio.2021.100176 . PMID: 34938990; PMCID: PMC8661698.

CHAPTER 4:

LONG-TERM ANTIBACTERIAL PROPERTIES OF A NANOSTRUCTURED TITANIUM ALLOY SURFACE- AN *IN VITRO* STUDY

Richard Bright[1], Daniel Fernandes[1], Jonathan Wood[1], Dennis Palms[1], Anouck Burzava[1], Neethu Ninan[1], Toby Brown[2], Dan Barker[2] and Krasimir Vasilev[1*].

[1]Academic Unit of STEM, University of South Australia, Mawson Lakes, Adelaide, 5095, South Australia, Australia. [2]Corin Australia, Pymble, NSW 2073, Australia.
[*]Corresponding author's email address: krasimir.vasilev@unisa.edu.au

3.2 Graphical Abstract

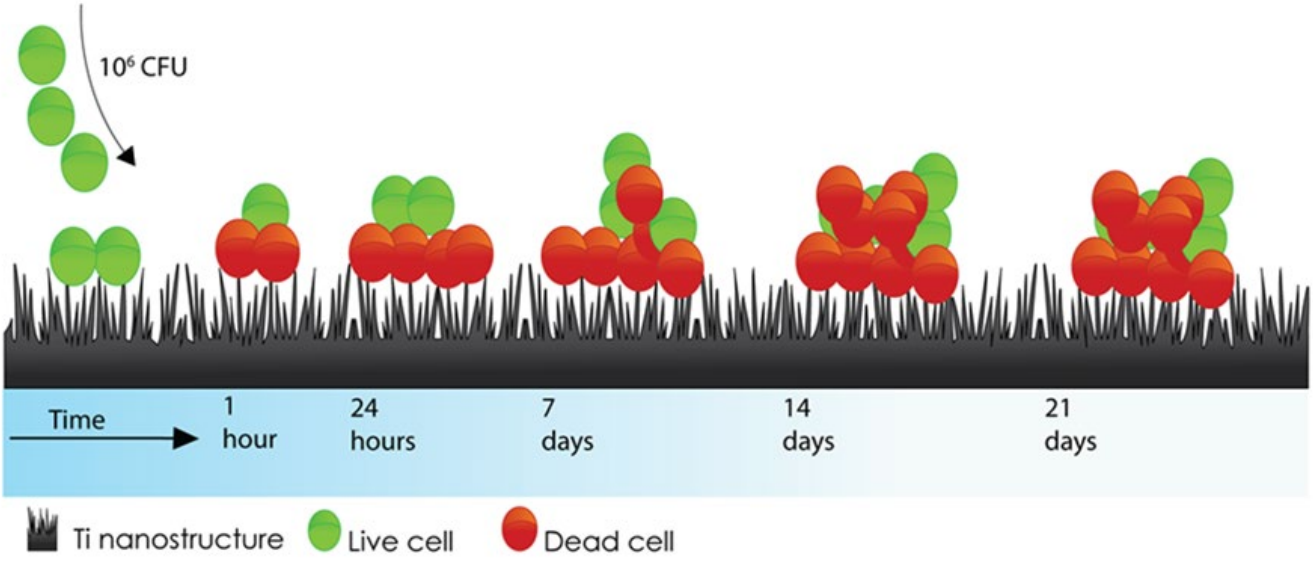

4.2 Abstract

The demand for joint replacement and other orthopaedic surgeries involving titanium implants is continuously increasing; however, 1% - 2% of surgeries result in costly and devastating implant-associated infections (IAIs). *Pseudomonas aeruginosa* and *Staphylococcus aureus* are two common pathogens known to colonise implants, leading to serious complications. Bioinspired surfaces with spike-like nanotopography have previously been shown to kill bacteria upon contact; however, the longer-term potential of such surfaces to prevent or delay biofilm formation is unclear. Hence, we monitored biofilm formation on control and nanostructured titanium disc surfaces over 21 days following inoculation with *Pseudomonas aeruginosa* and *Staphylococcus aureus*. We found a consistent 2-log or higher reduction in live bacteria throughout the time course for both bacteria. The biovolume on nanostructured discs was also significantly lower than control discs at all time points for both bacteria. Analysis of the biovolume revealed that for the nanostructured surface, bacteria were killed not just on the surface, but at locations above the surface. Interestingly, pockets of bacterial regrowth on top of the biomass occurred in both bacterial species, however, this was more pronounced for *S. aureus* cultures after 21 days. We found that the nanostructured surface showed antibacterial properties throughout this longitudinal study. To our knowledge this is the first *in vitro* study to show a reduction in the viability of bacterial colonisation on a nanostructured surface over a clinically relevant time frame, providing the potential to reduce the likelihood of implant-associated infections.

Keywords

Nanoprotrusions, nanostructures, nanospikes, antibacterial, biofilm, implant infection, biomimetic, implant-associated infections, orthopedic.

4.3 Introduction

Orthopaedic implants and other devices play a crucial role in restoring health, treating musculoskeletal disease, and ultimately saving patient lives [1]. Titanium alloy is widely used as a biomaterial to replace hard tissue, due to its mechanical bone-like properties, enhanced corrosion resistance and superior biocompatibility. [2] However, implant-associated infection (IAI) occurs in 1% - 2% of joint replacement [3, 4] and approximately 30% of open fracture reduction cases [5, 6], leading to notably increased morbidity, mortality, and treatment cost [7, 8]. IAI involves a series of complex interactions between the pathogen, the implant, and the host immune response. In the absence of a foreign body, tissue contamination by opportunistic pathogens is usually spontaneously cleared by host immune defences. However, the presence of an implant triggers a localised tissue response, which includes acute and chronic inflammation, a foreign body reaction, the formation of granulation tissue and, finally, fibrous encapsulation. In this early phase, bacteria may take advantage of the immunocompromised region around the implant to adhere, colonise and form a biofilm [9].

Ideally, in a concept termed ‘race to the surface’, host cells outcompete bacteria to colonise the implant surface, leading to favourable tissue integration – where the host immune system is better placed to prevent the onset of IAI [10, 11].

Bacteria adhere to implants by a process mediated by hydrophobic, electrostatic and van der Waals interactions, where they colonise the device surface to form a biofilm that can evade the immune response. A biofilm manifests, following a sequence of growth phases to become a multifaceted biological unit that is extremely difficult to treat, becoming resistant to systemic antibiotics [12-14]. An IAI results in an unresolved chronic inflammatory response, leading to tissue destruction and ultimately loosening of the bone-implant interface [15].

Treatment of an IAI usually involves the removal of the implant and associated cement, debridement of all devitalised tissue, and long-term antimicrobial treatment [16]. Sources of bacterial contamination implicated in IAI include the operating room environment, surgical equipment, clothing worn by medical staff, and bacteria on the patient’s skin and residing in the patient’s body [17-19]. The most common etiologic agents causing IAIs are *Staphylococcus aureus* (*S. aureus*), *Staphylococcus epidermidis (S. epidermidis)* [20], *Pseudomonas aeruginosa* (*P. aeruginosa*) [21], and *Escherichia coli* (*E. coli*) [22]. These bacteria are normally associated with skin and environmental microbiota but can quickly colonise implants leading to biofilm formation [23]. Four out of five IAIs are caused by *Staphylococcus* species*,* with *S. aureus* and *S. epidermidis* responsible for two out of three [20]. Drug-eluting coatings have been successfully attached to implants, including silver nanoparticles [24-26], antibacterial peptides [27, 28] and antibiotics [29], amongst others [30, 31]. However, these finite eluting treatments are generally short-acting and may harm eukaryotic cells, prompting attempts to find a safer and longer-lasting, non-eluting solution [32, 33]. Following the discovery that mechano-bactericidal nanostructures found on the wing of a dragonfly can kill a variety of bacterial species upon contact [34], it has been shown that titanium surfaces with a specific nanoarchitecture mimicking that of the dragonfly wing can also be highly effective in killing bacteria [34-36]. The mechano-bactericidal activity of nanostructured surfaces is governed by surface profile and is independent of surface chemistry. [37] Nanostructures with a high aspect ratio - with a length many times that of their width, mechanically disrupt the bacterial membrane. [38] Whilst nanostructured surfaces have shown antibacterial efficacy against Gram-positive species, Gram-negative species such as *P. aeruginosa* and *E. coli* are particularly vulnerable, due to differences in cell wall architecture [35, 39]. Several methods have been developed to fabricate nanostructures on titanium and its alloys, with antibacterial properties to enhance osteointegration. Some of these methods include anodization, [40] sol-gel [41] and hydrothermal etched titanium (HTE). [42] HTE stands out as the method of choice to fabricate TiO_2 due to; its simplicity, inexpensiveness, environmental friendliness and more importantly, the ability to generate a variety of nanoscale patterns. [42] Furthermore, the TiO_2 surface layer exhibits low solubility in water, which prevents substrate metal ions from dissolution, enhanced wear and fatigue resistance. [43]

A limitation of previous studies has been the short time frame over which bacteria were cultured on nanostructured surfaces, whereas biofilms are known to evolve over days and indeed weeks [36, 39, 44-46]. Moreover, reduced early bacterial viability as well as inhibited and/or delayed biofilm formation on the implant surface may promote improved host tissue integration in the early phase, which further reduces the likelihood of an IAI developing [47, 48]. The aim of this study was, therefore, to examine the antibacterial efficacy of a nanostructured titanium alloy on two clinically relevant pathogens (*S. aureus* and *P. aeruginosa*) over 21 days. We hypothesise that there will be a continuous, long-term disruption of biofilm growth and maturation on the antibacterial nanostructured implant surface, which may translate to implants with reduced occurrence of IAIs.

4.4 Materials and Methods

4.4.1 Fabrication of antibacterial Ti6Al4V surface

To create the study HTE surface, medical grade Ti6Al4V discs (10 mm diameter, 3 mm thickness) with a mirror-polished top surface and a RA of 0.1 µm (Hamagawa Industrial (M)76 SDN BHD, Kedah Malaysia), were hydrothermally etched, using 1M KOH in a stainless-steel reactor (autoclave; Parr Instrument Company, USA). After the chemical reaction, the vessels were cooled, and samples were cleaned in ultrapure water. After drying for 2 h at 70 °C, discs were heat treated inside a tubular furnace and cooled down overnight. As-received Ti6Al4V discs with a polished top surface were used as the control implant surface (CTL) in biofilm experiments. All samples were cleaned and sterilised at 121 °C for 20 min before use in biological experiments.

4.4.2 Characterisation of nanotopography by scanning electron microscopy (SEM) and atomic force microscopy (AFM)

The morphology of the HTE and CTL surfaces was characterised using scanning electron microscopy (SEM) (Zeiss Merlin FEG-SEM, Zeiss, Jena, Germany) at 2KV, 4.5 mm working distances with magnifications from 5 K to 50 K. Substrate surfaces were orientated at 45° relative to the horizontal plane in the SEM, where an oblique view reveals additional information about the nanotopography that cannot be assessed from a top-down perspective, such as approximate nanostructure height. Five samples were used to measure height, diameter and spacing between nanostructures. The height of the nanostructures was calculated using the distance between a perpendicular plane and the highest point of each spike, and the diameter was measured at mid-height in parallel orientation with the basal plane (25 spikes measured per sample). The measurements for spike height were corrected for the 45° stage tilt [49]. To determine the spacing between nanostructures, zero-degree tilted SEM images were analysed (n = 5), considering nanostructure tips in a 5 μm^2 field.

Analysis was performed using ImageJ software v1.53a (NIH, USA). The morphology of the HTE and CTL surfaces was also characterised in air, using atomic force microscopy (AFM). Data for 5 μm² surface area scans were acquired using a JPK NanoWizard III (JPK BioAFM, Berlin, Germany) with instrument-specific software v5, written in Linux Ubuntu (Canonical Ltd., London, UK). An NT-MDT NSG03 silicon nitride cantilever with a conical tip rated by the manufacturer (Spectrum Instruments Ltd, Moscow, Russia) at a radius of less than 10 nm and a half-side angle of 18° was used to perform amplitude modulation or tapping mode scans on HTE and CTL surfaces (n = 3). Initial calibration of the cantilever on a glass microscope slide derived a normal spring constant of 1.9 N/m and a deflection sensitivity of 86.8 kHz. Scanning parameters over a scan rate of 0.8 Hz were held constant at a setpoint of 22.8 nm and a drive amplitude of 0.3 V. Roughness values and 3D reconstructions were acquired using Gwyddion data analysis software version 2.54. (http://gwyddion.net/).

4.4.3 Contact angle analysis

The water contact angle (WCA) of the CTL and HTE samples (n = 3) was measured using a contact angle goniometer model RD-SDM02 (RD Support, Scotland, UK), to determine surface wettability. Contact angles were measured for five randomly placed drops on triplicate samples. Both CTL and HTE samples were placed on a flat surface to receive 4 μL of Milli-Q water and the WCA was measured within 20 s using the sessile drop analysis.

4.4.4 Chemical analysis of the surface by X-ray photoelectron spectroscopy (XPS)

XPS was employed to investigate the surface chemistry of the CTL and HTE samples (n = 3). Survey spectra were collected with a pass energy of 160 eV and high-resolution spectra were obtained using a 20-eV pass energy, with a monochromatic Al source run at 15 keV and 15 mA on a Kratos AXIS Ultra DLD spectrometer (Kratos Analytical Ltd, Manchester, UK). Survey spectra were documented over a 0−1100 eV range at 0.5 eV increments. CasaXPS software version 2.3.23 (www.casaxps.com, Teignmouth, UK) was used to process the spectra after curve fitting, and all binding energies were referenced to the carbon peak at 285.0 eV.

4.4.5 Energy-dispersive X-ray spectroscopy (EDS) for elemental analysis

HTE samples were dry cut with a CBN blade from More Superhard (Zhengzhou, China) at 300 rpm in a Struers Minitome (Willich, Germany). To compare the qualitative elemental analysis between the HTE surface and the subsurface, a Zeiss Merlin FEG-SEM (Zeiss, Jena, Germany) equipped with an EDS detector (Oxford Instruments X-MaxN (20 mm^2) EDS-Silicon Drift Detector) was used. Spectra were obtained, using an SE2 detector at 15 kV, 3 nA, a working distance of 10 mm, analytic mode and 10 K magnification, using AZTEC EDS software version 3.1 (Oxford Instruments, Oxfordshire, UK).

4.4.6 The short-term cytocompatibility of the HTE nanostructured surface

The ability of RAW 264.7 macrophage-like cells (ATCC® TIB-71™, VA, USA) to adhere and proliferate on the HTE surface was assessed by LIVE/DEAD® Viability/Cytotoxicity Kit for mammalian cells (Molecular Probes, Invitrogen, CA, USA), following the manufacturer's protocol. RAW 264.7 macrophage-like cells were cultured in Dulbecco's modified Eagle's medium (DMEM, ThermoFisher, MA, USA) supplemented with 10% fetal bovine serum (FCS; ThermoFisher, MA, USA) and 1% penicillin/streptomycin (ThermoFisher, MA, USA). Cells were seeded on HTE and CTL samples at 2.5 x 10^4 cells per well in a 48-well tissue culture plate and incubated at 37 °C in 95% humidity and 5% CO_2. After 48 h culturing on HTE and CTL samples in a 48-well tissue culture plate, the cells were washed gently with phosphate-buffered saline (PBS), followed by calcein AM/ EthD-1 working solution and incubated at room temperature for 30 min, then imaged by confocal laser scanning microscope (CLSM; Olympus, Tokyo, Japan). Calcein (Ex/Em 495/515 nm) will fluorescently stain live cells green, whereas EthD-1 (Ex/EM 495/635 nm) will stain cells with damaged membranes or dead cells, producing a bright red fluorescence upon binding to nucleic acids. Viability was quantified by counting red and green stained cells using ImageJ software v1.53a (NIH, USA). Cytotoxicity was further assessed using LDH-Glo™ Cytotoxicity Assay (Promega, WI, USA), to detect extracellular lactate dehydrogenase (LDH), a widely used marker in cytotoxicity studies due to its rapid release in tissue culture media upon disruption of the cell membrane [50, 51]. Briefly to quantify LDH release, 50 µL of media was added to 50 µL of LDH detection reagent in a 96-well opaque plate, mixed and incubated at room temperature for 30 min then luminescence read on a Synergy HTX multi-mode microplate reader (Biotek, VT, USA). Triplicate readings were normalised to cells grown on a tissue cultures plate (TCP). The formula used to calculate percent cytotoxicity was, $\% \, Cytotoxicity = \frac{Treatment\ LDH\ Release - Background}{Control\ LDH\ Release - Background} \ x\ 100.$

4.4.7 Bacterial culturing and biofilm growth protocols

P. aeruginosa, ATCC 15692 and *S. aureus*, ATCC 25923 glycerol stocks were plated onto Tryptone Soy Agar (TSA; Oxoid, ThermoFisher, MA, USA) plates and incubated for 18 h at 37 °C. Single colonies of each species were inoculated into Tryptone Soy Broth (TSB; Oxoid, ThermoFisher, MA, USA) and 5% FCS (TSBFCS; Gibco, ThermoFisher, MA, USA), and incubated overnight at 37 °C. The following day bacterial cultures were gram-stained to confirm purity and adjusted to 1 x 10^6 CFU/mL by adjusting to the associated 600 nm (OD_{600}) reading measured on a Nanodrop 2000C (ThermoFisher Scientific, MA, USA). An OD_{600} of 1 was determined to be approximately 1 x 10^9 CFU/mL by calibrating against colony forming units (CFU) for *P. aeruginosa* and *S. aureus* before the commencement of this study. Samples of HTE and CTL were inoculated in a 24-well plate with 1 mL of 1 x 10^6 CFU/mL of either *P. aeruginosa* or *S. aureus* for nine-time points (day 1-7, 14 and 21) and incubated with daily replenishment of TSBFCS, at 37 °C in a humid chamber on an orbital shaker (Ratek Instruments, VIC. Australia), on setting 6. At each time point, HTE and CTL samples were removed for analysis.

4.4.8 Quantitative antimicrobial test

The gold standard for enumerating bacteria is the colony-forming unit (CFU) method [52]. Briefly, at each time-point (days 1-7, 14 and 21), HTE and CTL discs were transferred into 1 mL PBS and vortexed for 15 s, followed by 2 min sonication then vortexed a further 15 s, and serially diluted. Serial dilutions were plated onto TSA plates and incubated for 18 h at 37 °C. Viable cell counts were performed on the HTE and CTL surfaces by the drop plate method [50]. The following day, colonies were counted, and CFUs determined for *P. aeruginosa* and *S. aureus* incubated on HTE and CTL discs [53]. Comparison between viability on the HTE and CTL samples was further used to determine log reduction, $\log_{10}(N_{CTL}/N_{HTE})$ and percent reduction for each time-point. To validate the complete removal of bacteria the HTE and CTL samples were imaged by SEM, post-CFU processing.

4.4.9 Bacteria live/dead assay

Bacterial cells attached to the surface of HTE and CTL samples were stained by Live/Dead® BacLight™ (Invitrogen, ThermoFisher MA, USA) according to the manufacturer's protocol. Briefly, a mixture containing Syto9 (Ex/Em 480/500 nm) and Propidium Iodide (PI; Ex/Em 490/635 nm) in equal proportions (1.5 µL of each per mL) in PBS was freshly prepared. Syto9 is taken up by all cells and binds with nucleic acids, staining the cell green. Whereas PI is unable to pass through the intact plasma membrane and is therefore only taken up by damaged cells allowing detection of both live (green) and compromised cell membrane integrity that is associated with cell death (red). The samples were immersed in the live/dead solution and incubated at room temperature for 15 min in the dark before microscopy.

4.4.10 Confocal laser scanning microscope analysis

Samples were imaged at each time point (days 1-7, 14 and 21), using three random images per sample. CTL and HTE samples were imaged for viability and biomass analysis, using an Olympus FV3000 CLSM (Olympus, Tokyo, Japan). Single-plane micrographs were used to determine viability by counting red and green stained cells using ImageJ software v1.53a (NIH, USA). Z-stack images were acquired for *S. aureus* and *P. aeruginosa* on days 7, 14 and 21. The viability and total biomass for the Z-stacks were also examined using Imaris 3D analysis software (Version 9.3.0, Bitplane, Zürich, Switzerland). The excitation/emission maxima of the LIVE/DEAD Bacterial Viability Kit dyes are 480/500 nm for SYTO 9 and 490/635 nm for PI.

4.4.11 SEM analysis of bacterial morphology

To prepare biological samples for SEM, samples were fixed in 1.25% glutaraldehyde and 4% paraformaldehyde in PBS containing 4% sucrose for 24 h. Next, they were washed in PBS, followed by dehydration in an ascending ethanol series from 50%, 70% and 100% ethanol.

Finally, samples were chemically dried using hexamethyldisilane (Sigma-Aldrich, MO, USA), mounted on aluminium stubs, sputter coated with 1 nm platinum, and imaged using a Zeiss Merlin FEG- SEM (Carl Zeiss, Jena, Germany).

4.4.12 Statistical analysis

Graphical data was represented by mean and standard deviation, n = 3. All statistical analyses were performed using GraphPad Prism version 9.0.0.0 for Windows (GraphPad Software, La Jolla California USA, www.graphpad.com). The data was analysed by multiple t-tests. Statistical significance was determined using the Holm-Sidak method, with alpha = 0.05, and significance levels were set at $p < 0.05$. All experimental procedures were performed in biological replicates (n = 3).

4.5 Results and Discussion

4.5.1 Characterisation of HTE nanostructure surface

Representative SEM micrographs depicting the nanostructured features of the CTL and HTE samples are shown in Figure 1A to 1D at 5, 50 and 200 K magnification, respectively. The CTL surface appeared smooth at lower magnification, however, at high magnification, machining marks and scratches due to the polishing process can be seen. The HTE surface exhibited hierarchal disordered spike-like nanostructures covering the entire surface. The height of the nanostructures was 348 ± 152 nm, and the diameter at mid-height was 98 ± 60 nm, signifying a high aspect ratio. The spacing between the individual nanostructures was 437 ± 46 nm. Nanostructures with similar dimensions have previously been shown to be effective at killing both Gram-positive and Gram-negative bacteria [35, 38].

The AFM image, presented in Figure 1E, confirmed machining marks due to polishing on the CTL surface. Nanostructures with peaks and valleys can also be seen in the AFM image from the HTE surface (Figure 1F), however, the fine details seen by SEM could not be resolved by AFM due to the well-known tip convolution effect [54]. The AFM images displayed greater roughness on the HTE surface compared to the CTL surface. The root mean square roughness (RMS), arithmetic roughness average (Ra) and surface area (SA) determined from the AFM images for the CTL surface were 5.13 nm, 4.15 nm and 25.14 μm^2, respectively, while for the HTE surface, these parameters were 236.3 nm, 175.5 nm and 64.64 μm^2 respectively. The surface area measured by AFM on the HTE sample increased 2.6-fold when compared to the CTL. It should be noted, however, that the tip convolution resulting from the cantilever tip side angle and scan velocity reduced the measured surface roughness values, especially towards surface features with comparable magnitude to the tip radius. The water contact angle for the control surface (61 ± 8°) was significantly greater than that of the HTE surface (5 ± 0.8°, $p = 0.003$, Figure 1G). The Wenzel [55] and Cassie–Baxter [56] equations state that adding surface roughness will enhance the wettability caused by the chemistry of the surface.

It is well known a water contact angle between 0° and 10° is categorised as superhydrophilic. [57] Generally, an increase in hydrophilicity is an imperative characteristic to improve biocompatibility and antibacterial properties of the HTE surface - where hydrophilic implant surfaces favour cell-implant contact, the initial phases of wound healing and a cascade of events leading to the osteogenesis [58-61].

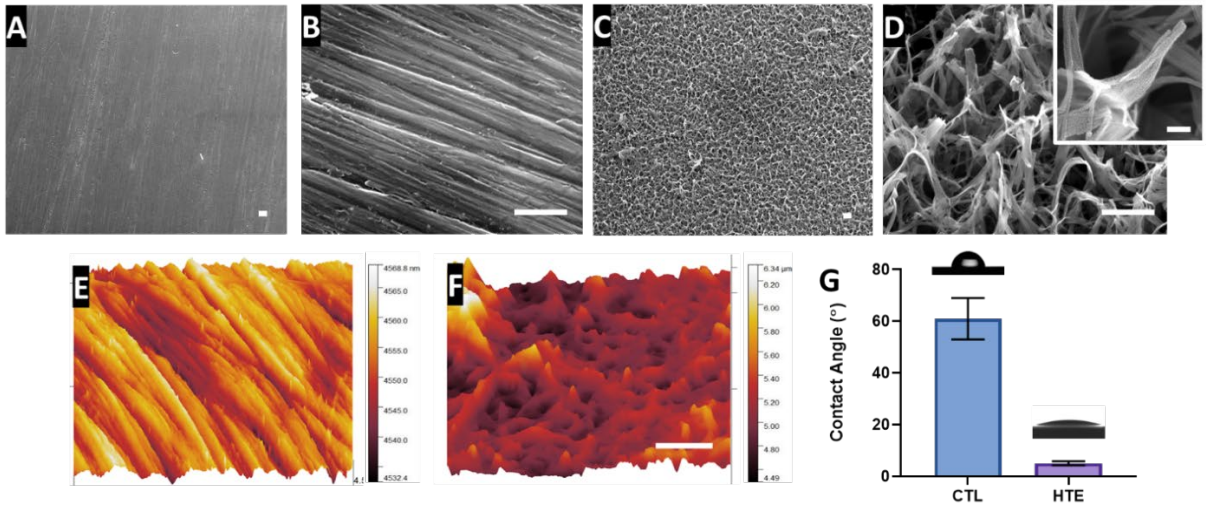

Figure 1. *SEM micrographs of unetched CTL (1A and 1B) showing effects of polishing, and the HTE surface (1C and 1 D) displaying hierarchal nanotopography (scale bar for figures 1A to 1D 500 nm). The inset image in 1 D shows the morphology of a single nanostructure at 200 K magnification (scale bar 100 nm). AFM-3D reconstructions showing nanotopological features of a 5 x 5 µm region on CTL (1E) and the superhydrophilic HTE surface (1F) (scale bar 1 µm). The bar graph represents the water contact angle for CTL and HTE surfaces mean ± SD (n = 3), p = 0.0003. Images above the bar graph demonstrate the wettability by the sessile drop method (1G). Nanostructure measurements, AFM and wettability can be found in supplementary information Table S1.*

4.5.2 Chemical analysis

The atomic percentage of elements detected on the CTL and HTE disc surfaces using XPS is shown in Figure 2A. There was a significant increase in oxygen and titanium atomic concentrations on the HTE surfaces compared to the untreated CTL (5.6%, p = 0.0003 and 5.1%, p = 0.0002 respectively). These results are consistent with the formation of a thicker oxide layer occurring during the hydrothermal etching process. The increased thickness of the oxide layer also meant that with the XPS sampling depth of 10 nm, vanadium and aluminium became barely detectable on HTE surfaces. Hydrothermal etching also reduced the presence of environmental contaminants such as carbon and nitrogen. Furthermore, a small amount of potassium was incorporated within the HTE surface, consistent with the use of KOH as the alkaline etchant.

Trace amounts of magnesium, calcium, and silicon, incorporated during the polishing and handling of the CTL samples, were detected on both CTL and HTE disc surfaces. Using EDS (Figure 2B and 2C), we confirmed the increase in oxygen content for the HTE surface, consistent with hydrothermal oxidation of the surface layer occurring during hydrothermal etching discussed above [42]. The three elements used in the manufacture of the Ti-alloy (i.e., Ti, Al, V) were also detectable in the EDS spectra.

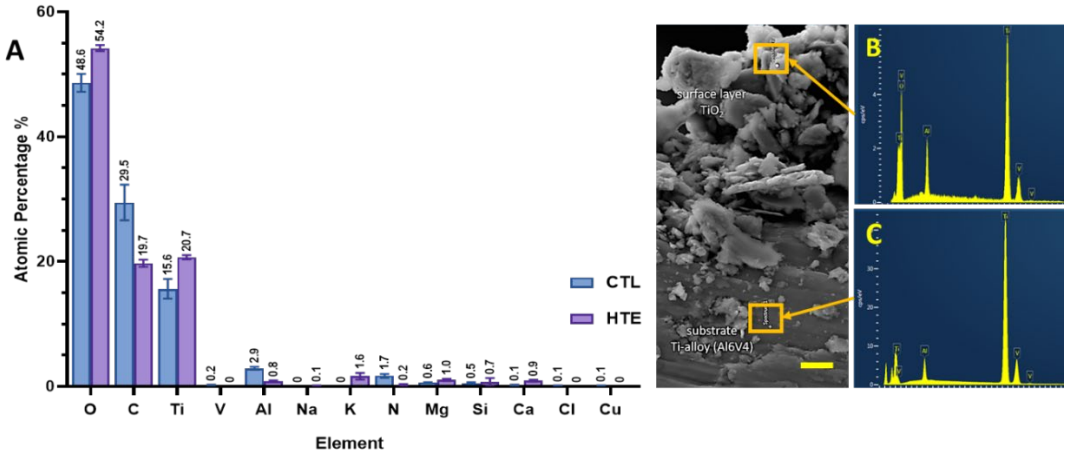

Figure 2. *Atomic percentages for CTL and HTE samples quantified by XPS, mean ± SD (n = 3). P-values for all elements detected can be found in supplementary information in Table S2 (2A). EDS spectra were measured on the HTE surface (2B) and substrate (2C) (scale bar 5 µm).*

4.5.3 *In vitro* cytotoxicity of Raw 264.7 cells to HTE treated surface

After biomaterial implantation, macrophages are one of the earliest host-cell responders [62]. We, therefore, used a RAW 264.7 macrophage-like, Abelson leukemia virus-transformed cell line derived from mice, to observe any short-term cytocompatibility to the HTE surface. Briefly, the viability of RAW 264.7 cells seeded onto CTL and HTE discs is shown in Figure 3A. After 48 h incubation, the percent viability for CTL and HTE discs was 95.8 ± 2.6% and 94.0 ± 4.2%, respectively ($p = 0.57$). Furthermore, after fluorescent staining with LIVE/DEAD® Viability/Cytotoxicity Kit, no red stained cells (indicating dead cells) were detected on the CTL or the HTE samples. Cells on both CTL and HTE samples appeared healthy and had comparable morphology. The cells were approximately 60% confluent after 48 h on both CTL (Figure 3B) and HTE samples (Figure 3C).

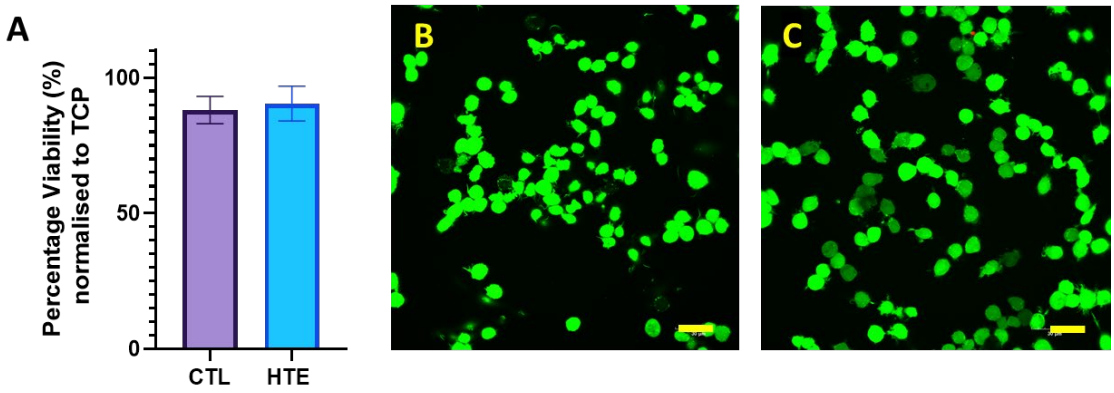

Figure 3. *Viability of RAW 264.7 macrophage-like cells determined by LDH-Glo™ Cytotoxicity Assay, normalised to RAW 264.7 macrophages grown directly on TCP. The mean ± SD percentage viability for RAW 264.7 macrophages incubated on CTL samples was 95.8 ± 2.6% and for HTE samples was 94.0 ± 4.2% (mean ± SD), p = 0.57, n = 3 (3A). The confocal images of RAW 264.7 macrophages incubated on the CTL (3B) and HTE (3C) for 48 h, stained with LIVE/DEAD™ Viability/Cytotoxicity Kit, for mammalian cells (scale bars 30 μm).*

4.5.4 Bacterial viability analysis

To assess the viability of bacterial populations on the CTL and HTE surfaces, we used the LIVE/DEAD® BacLight™ Bacterial Viability Kit [63]. Representative live/dead images of *P. aeruginosa* and *S. aureus* at days 1, 3, 7, 14 and 21 are shown in Figures 4 and 5, respectively. When *P. aeruginosa* was cultured on HTE surfaces, the bacterial viability was only 0.97 ± 0.06% after 24 h. Longer incubation times resulted in marginally higher mean viability, which never exceeded 4%. (Figure 6A). For *S. aureus*, there was an initial cell viability of 26.0 ± 0.9% after 24 h incubation. On day 3, *S. aureus* viability was at its lowest (6.8 ± 3.1%), with viability increasing to 36.2 ± 2.7% by day 7, and then 40.9 ± 4.3%, by day 21 (Figure 6B). In contrast, the viability for *S. aureus* and *P. aeruginosa* did not drop below 90% throughout the 21-day study on the CTL surface (Figures 6A and 6B).

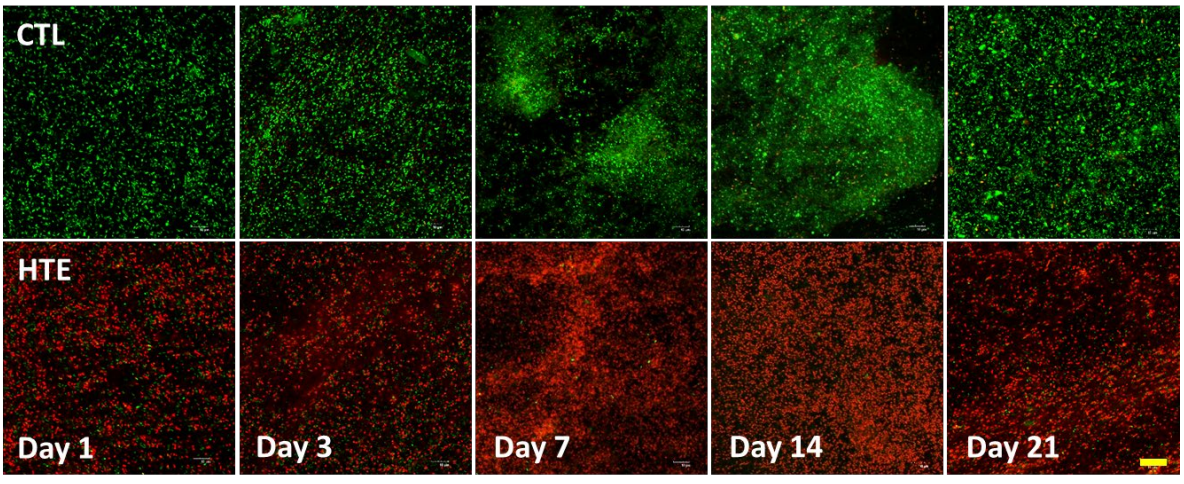

Figure 4. *Confocal microscopy images of P. aeruginosa after staining with LIVE/DEAD® BacLight™ Bacterial Viability Kit incubated on CTL and HTE surfaces at five representative time points over 21 days. Live cells stain fluorescent green, whereas bacteria with damaged membranes stain fluorescent red. The top panels represent as-received CTL, and the bottom panels represent the matching time point HTE samples incubated with P. aeruginosa (scale bar 20 µm), (n = 3).*

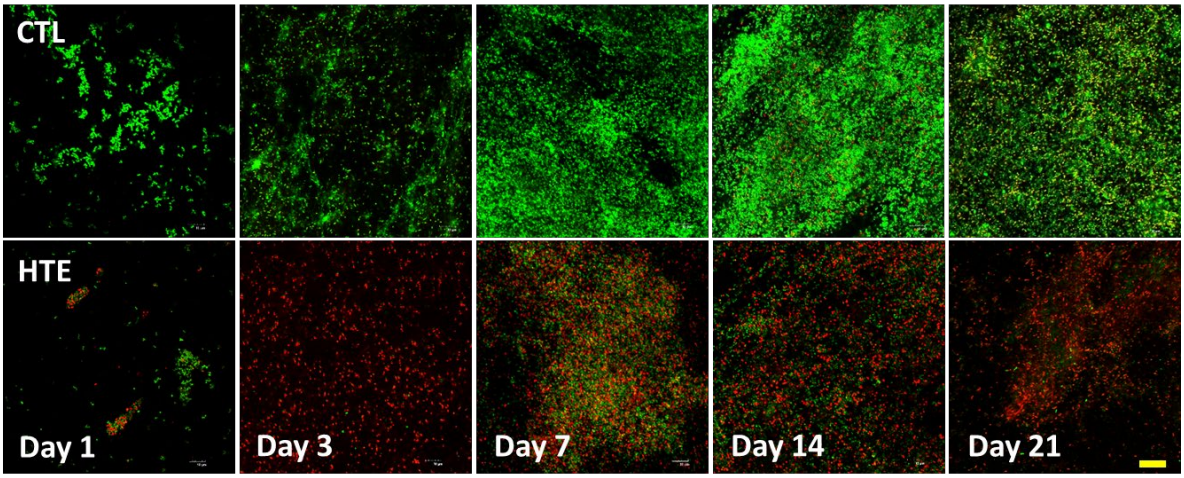

Figure 5. *Confocal microscopy images of S. aureus after staining with LIVE/DEAD® BacLight™ Bacterial Viability Kit incubated on CTL and HTE at five representative time points over 21 days. Live cells stain fluorescent green, whereas bacteria with damaged membranes stain fluorescent red. The top panels represent as-received CTL, and the bottom panels represent the matching time point HTE samples incubated with S. aureus (scale bar 20 µm), (n = 3).*

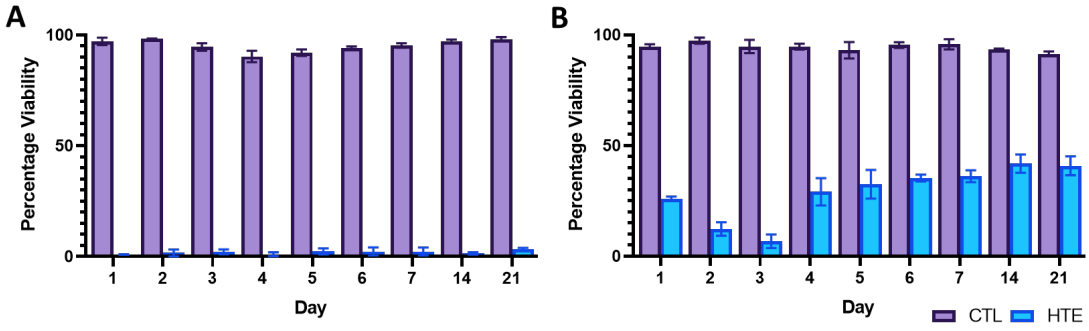

Figure 6. *The viability of P. aeruginosa (6A) and S. aureus (6B) was determined from the live/dead staining over 21 days on CTL and HTE surfaces, mean ± SD (n = 3). To compare CTL and HTE surfaces, multiple comparisons using the Holm-Sidak method revealed a significance of p < 0.0001 at all-time points. A table of p-values can be found in the supplementary information (Tables S2 and S3).*

To analyse the biovolume on the CTL and HTE surfaces, we prepared Z-stack surface rendered 3-D models for *P. aeruginosa* (Figure 7) and *S. aureus* on days 7, 14 and 21 (Figure 8). Bacterial viability was also quantified at the three time points (days 7, 14 and 21) using 3D rendered biovolume Z-stack images obtained from the same samples used for single-plane fluorescence imaging. Each of the three time points represented an additional week of biofilm colonisation for *P. aeruginosa* (Figure 7H) and *S. aureus* (Figure 8H). *P. aeruginosa* incubated on the CTL samples showed significantly greater biovolume compared to the HTE samples on days 7, 14 and 21 ($p = 0.003$, $p = 0.006$ and $p = 0.003$ respectively, Figure 7G). There was minimal evidence of clusters of live bacteria, associated with the formation of biofilm [64], on the HTE surfaces. Rather, there were thick areas of dead bacteria evident on these samples, most prominent on days 14 and 21.

Although there was some increase in *P. aeruginosa* biovolume on the HTE surface by day 21, this was still less than half the biovolume on the CTL surface on day 7. While the viability of *P. aeruginosa* remained above 90% on the CTL surfaces out to day 21, from day 7 to day 14, the viability on the HTE surface remained below 25% (21.1 ± 3.7% at day 7, decreasing to 18.1 ± 3.5% at day 14), with most cells in contact with the surface killed at day 21. Interestingly, there was evidence of minor bacterial recolonisation above the previously killed bacteria on the HTE surface, which may partially explain the slight recovery in *P. aeruginosa* viability through the biovolume to 42.4 ± 5.2% by day 21 (Figure 7H). Similarly, to *P. aeruginosa*, there was significantly less *S. aureus* biovolume on the HTE surfaces compared to the CTL surfaces at days 7, 14 and 21 ($p = 0.002$, $p = 0.01$ and $p = 0.01$ respectively, Figure 8G). Again, by day 21, there was less than half the biovolume of *S. aureus* on the HTE surface compared to that on the CTL surface on day 7. Pockets of *S. aureus* recolonisation were evident away from the surface, particularly noticeable on days 14 and 21 (Figure 8E and 8F), where total viability increased from 35.0 ± 6.2% at day 7, 53.1 ± 3.0% at day 14, to 63.4 ± 4.2% at day 21 (Figure 8H).

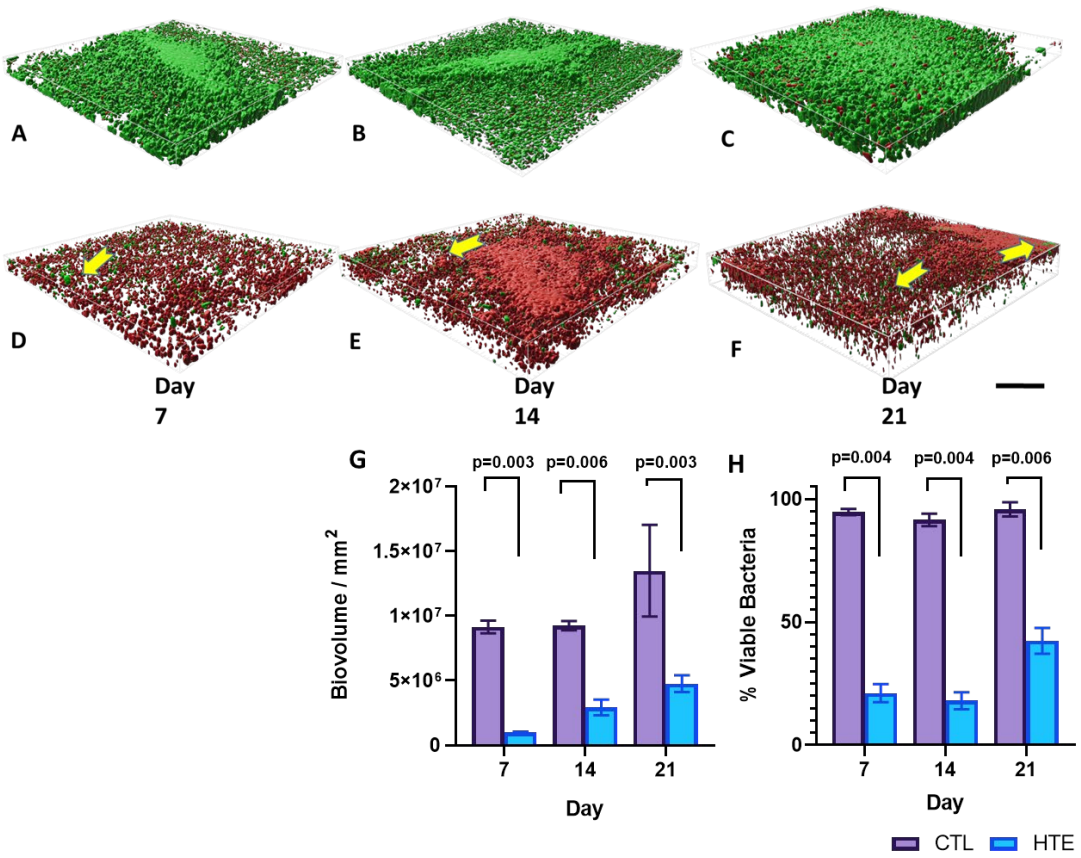

Figure 7. *Representative Z-stack rendered biofilm 3D-images of P. aeruginosa on CTL and HTE surfaces for day 7 (Figure 7A and 7D, respectively), 14 (Figure 7B and 7E, respectively) and 21 (Figure 7C and 7F, respectively). Biovolume of P. aeruginosa incubated on CTL and HTE for day 7, 14 and 21 (Figure 7G) mean ± SD, (n = 3). Yellow arrows highlight pockets of bacterial recolonisation on top of dead biofilm (scale bar 30 µm), images signify an area of 0.01 mm^2 (n = 3).*

The viability of P. aeruginosa (Figure 7H) at three time points was calculated from biovolume using multiple t-tests followed by the Holm-Sidak method, with alpha = 0.05. Each column represents mean ± SD, (n = 3).

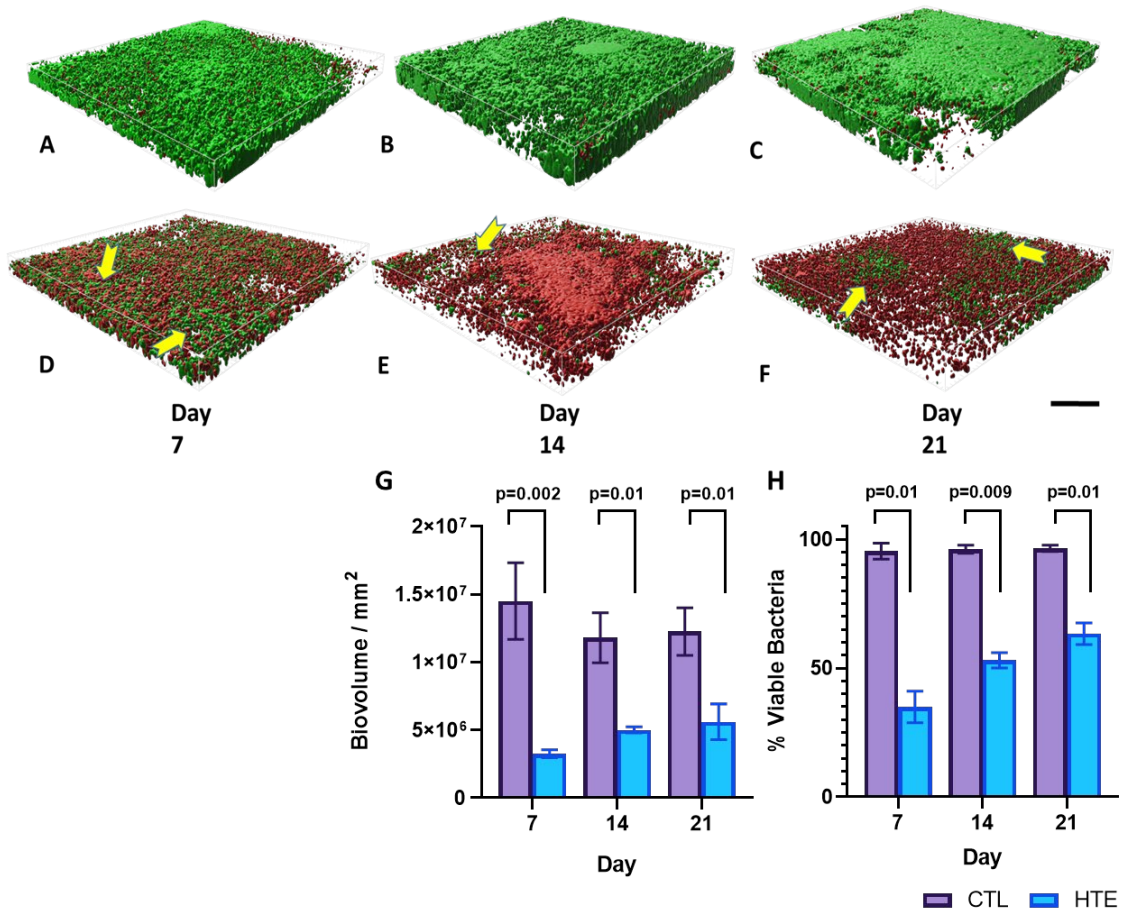

Figure 8. *Representative Z-stack rendered biofilm 3D-images of S. aureus on CTL and HTE samples for day 7 (Figure 8A and 8D, respectively), 14 (Figure 8B and 8E, respectively) and 21 (8C and 8F, respectively). Biovolume of S. aureus incubated on CTL and HTE for days 7, 14 and 21 (6G) Mean ± SD, n = 3. Yellow arrows depict pockets of bacterial recolonisation on top of dead bacteria (scale bar 30 µm), images signify an area of 0.01 mm² (n = 3). The viability of S. aureus (8H) at three time points was calculated from biovolume using multiple t-tests followed by the Holm-Sidak method, with alpha = 0.05. Each column represents mean ± SD, (n = 3).*

Using the drop plate method, the HTE surface showed a 1.9 – 2.5 log reduction in CFUs for *P. aeruginosa*, with the highest log reduction recorded on day 2 (2.5 log reduction). In contrast, *S. aureus* displayed a 1.5 – 2.5 log reduction in CFUs (Figure 9A). The maximum log reduction for *S. aureus* on the HTE surface was on day 3, consistent with data from live/dead staining (Figure 6B). After day 3, the HTE samples incubated with *S. aureus* showed a consistently lower log reduction compared to *P. aeruginosa* until the end of the study, particularly on days 5, 6 and 14 ($p < 0.05$). Both *P. aeruginosa* and *S. aureus* showed CFU counts in the range of 2-4 orders of magnitude higher on the CTL than on the HTE surface throughout the 21-day study (Figure 9B and 9C). There was a notable increase in log reduction on *S. aureus* incubated on HTE samples at day 3, in agreement with live/dead viability (Figures 5 and 6B).

The unexpected finding that *S. aureus* showed a delayed maximum killing on the HTE surface at day 3 could be a function of the difference in membrane structure between Gram-positive and Gram-negative bacteria [65].

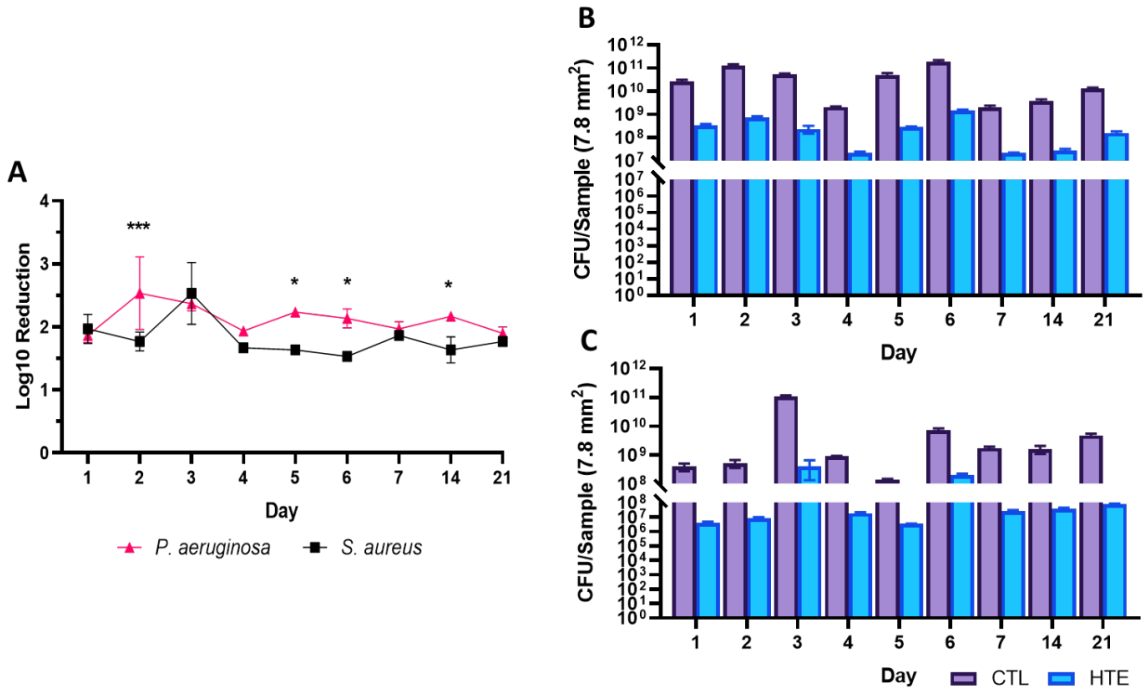

Figure 9. *Log reduction of P. aeruginosa and S. aureus incubated on HTE surface over 21 days. Mean ± SD, (n = 3) and * = p < 0.05 and *** = p < 0.001 (9A). CFUs per sample for P. aeruginosa (9B) and S. aureus (9C) on CTL and HTE surface mean ± SD, (n = 3). A table of p-values can be found for Figures 9A, 9B and 9C in the supplementary information (Table S4, Table S5 and Table S6, respectively).*

4.4.5 Morphology of *P. aeruginosa* and *S. aureus* on CTL and HTE surfaces

To gain further insights into differences between the interaction of *P. aeruginosa* and *S. aureus* with CTL and HTE surfaces over time, SEM micrographs were acquired over 21 days. For bacteria incubated on the HTE surface, there were distinct differences in morphology from days 7-21 compared to CTL surfaces. *P. aeruginosa* and *S. aureus* had almost completely colonised the CTL surfaces by day 7, with increasing cell density and little evidence of cell damage by day 21. The morphology of *P. aeruginosa* remained non-deformed, regular rod-shaped, and attached to the surface by pili on CTL surfaces (Figure S1). Similarly, *S. aureus* incubated on CTL surfaces, appeared spherical, with little evidence of membrane disruption, increasing in density and surface coverage, with notable mushroom-shaped formations indicative of biofilm formation by day 21 [64]. Further evidence that a mature biofilm had formed on the CTL surfaces by day 7 is the extensive extra polymeric substance (EPS) [66], which increased in density by day 21.

In contrast, both bacterial species remained in small clusters on the HTE surfaces out to day 21, with continued evidence of cell rupture. Examples of lysed, flattened, and fragmented *P. aeruginosa* can be seen in Figure 10, and the ruffled and fragmented morphology of *S. aureus* can be seen in Figure 11. The inset images in Figure S1 demonstrate membrane piercing by the nanostructures, consistent with other reports where both Gram-negative and Gram-positive bacteria have been killed on comparable surfaces at earlier time points [37, 67]. As confirmed by live/dead viability assays (Figures 4 and 6A) and CFU counts (Figure 10), *P. aeruginosa* appeared to be inflicted with more cellular damage than *S. aureus* due to the nanostructures on the HTE surface. Significantly, we observed minimal EPS produced by both bacteria and fewer cells on the HTE surfaces compared to CTL samples at all time points (Figure 10 and Figure 11, A-C). During biofilm formation, EPS is vital to the shift in cell state from adhered planktonic cells to a recalcitrant mature biofilm, where bacteria within the biofilm are more resistant to antibacterial drugs and host immune responses [68, 69]. Cao *et al.* [70] reported similar findings on nanostructured titanium alloy towards *S. epidermidis*, where biofilm formation was delayed for up to 6 days. However, to the authors' knowledge, this is the first study that demonstrates delayed biofilm formation for *P. aeruginosa* and *S. aureus* on a nanostructured surface for 21 days.

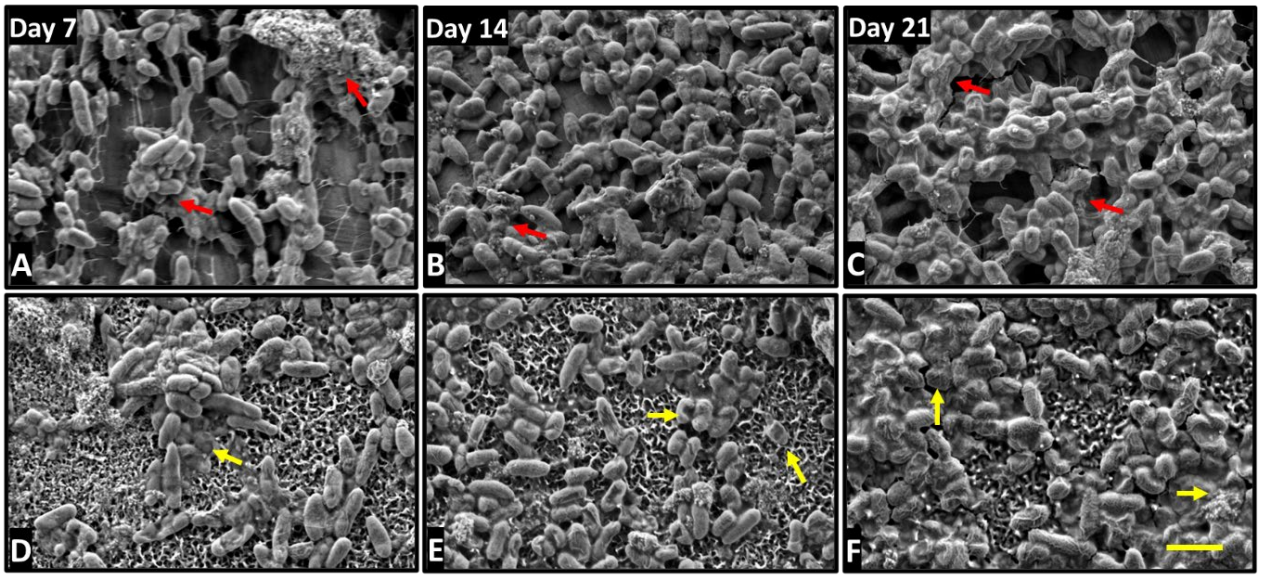

Figure 10. *SEM micrographs of P. aeruginosa incubated for 7, 14 and 21 days on CTL (A-C) and HTE surfaces (D-F). Yellow arrows highlight irregular morphology and dead cells: and red arrows show EPS-covering bacteria. The scale bar bottom left represents 2µm.*

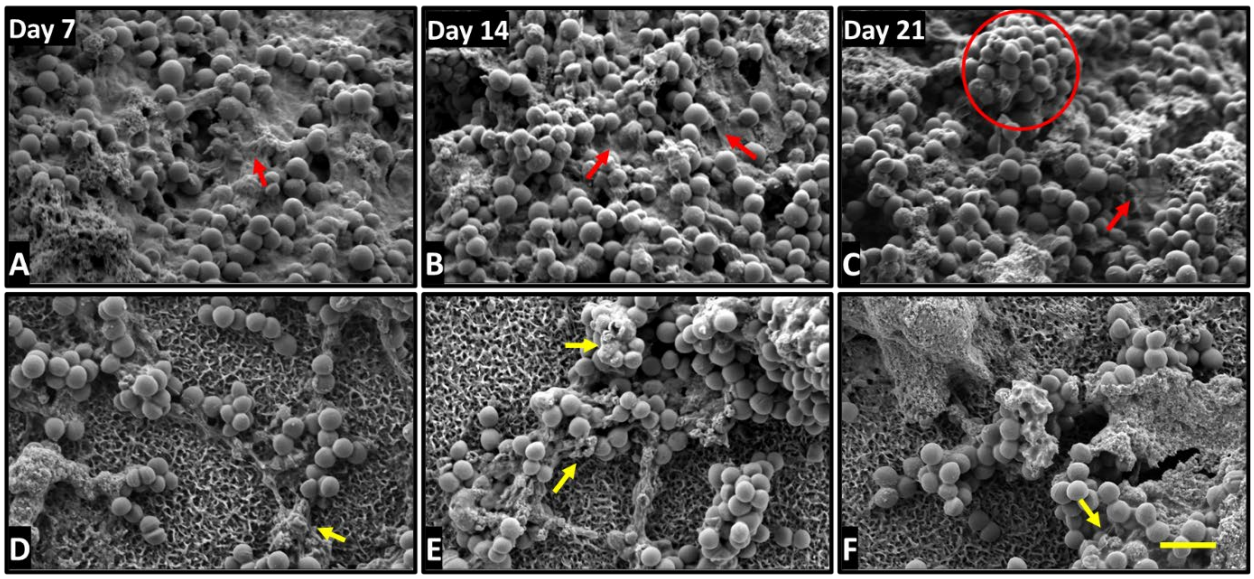

Figure 11. *SEM micrographs of S. aureus incubated for 7, 14 and 21 days on CTL (A-C) and HTE surfaces (D-F). Arrows highlight irregular morphology and dead cells; Red arrows show EPS covering bacteria: The red circle highlights the formation of mushroom-shaped biofilm. The scale bar bottom left represents 2µm.*

Bioinspired nanostructured surfaces have previously been reported to show antibacterial efficacy against pathogens involved in IAIs [34, 35, 38, 71]. However, this is the first study to examine the efficacy of such a surface for extended periods. We evaluated the efficacy of the nanostructures against two pathogens commonly associated with IAIs, i.e., the Gram-negative *P. aeruginosa* and the Gram-positive *S. aureus,* over 21 days. We observed a sustained high killing rate on the HTE surface for both *P. aeruginosa* and *S. aureus* of approximately 97% and 60% by live/dead analysis on day 21, respectively. Analysis of biovolume demonstrated that *P. aeruginosa* and *S. aureus* remained only approximately 60% and 40% viable by day 21, respectively, where most live bacteria were away from the surface. Conversely, *P. aeruginosa* and *S. aureus* incubated on CTL surfaces remained greater than 95% viable throughout the study, both at the interface with the surface and throughout the full thickness of the biomass. There was a consistent 2-log reduction in viability for both bacteria on the HTE surface compared to CTL throughout the study. SEM images provided further evidence of a mechano-bactericidal effect of the spike-like nanostructures, also shown by other researchers at early time points [37, 67], however, our study showed that this effect was prolonged, with far fewer bacteria colonising the surface on the HTE samples compared to CTL samples out to day 21. By day 21, there remained a lack of EPS on HTE surfaces, where flattened, disrupted, and fragmented bacteria were observed. In contrast, both bacteria appeared to have formed mature biofilms on the CTL surfaces. Taken together, these results confirm our hypothesis that the antibacterial nanostructured implant surface disrupted biofilm growth and maturation over a long period.

Although the HTE surface was effective at killing both bacteria in this study, it appeared more so against *P. aeruginosa*, which may reflect the differences between Gram-negative and Gram-positive bacteria. It is well known that Gram-negative bacteria are less rigid than their Gram-positive counterparts, predominately due to the thinner peptidoglycan layer present in the cell wall, thus rendering them vulnerable to contact killing by the spike-like nanostructures [65, 72]. Although Gram-positive bacteria lack an outer membrane, they are characterised by a thick peptidoglycan layer and protective capsular polysaccharide outer layer, providing greater cell wall rigidity and increased resistance to mechanically induced killing than Gram-negative bacteria [73, 74]. The rate of cell division may also be a vital contributing factor to the difference in the killing rate observed between Gram-negative and Gram-positive bacteria on the HTE surface. During cytokinesis, a complex hierarchical assembly of proteins forms at the mid-cell known as the divisome [75]. This remodelling may alter the bacterial turgor pressure [76, 77] and cell wall integrity [78, 79], resulting in heightened killing on the HTE surface of bacteria which divide more rapidly. The doubling time for *P. aeruginosa* can be as low as 25 min [80], in contrast to 1 h for *S. aureus* [81]. The differences in doubling the time between the two bacteria may be an additional influence on the killing rate on the HTE surface, as reported in this study and by other researchers [36, 42, 44, 82].

Importantly, we observed substantial volumes of dead bacteria throughout the biomass, away from the HTE surface over 21 days. It is likely that not all these dead bacteria visible throughout the biomass came directly into contact with the nanostructured surface. Stress-induced programmed cell death (PCD) may explain how a passive non-eluting surface may induce bacterial cell death at some distance away from the surface. PCD refers to the genetically encoded cascade of events leading to cell death and may be initiated by cellular stress, for example, oxidative stress [83, 84]. Although PCD is a well-understood phenomenon within eukaryotic cells, there are emerging studies that show PCD has been conserved throughout evolution in prokaryotic cells [85, 86]. A biofilm may induce PCD within cells that are undergoing excessive environmental stresses, such as contact killing with a nanostructured surface, to favour the survival of the colony [86, 87]. While the majority of the biovolume appeared to be constituted from dead bacteria on the HTE surfaces, there were observable pockets of live cells remerging on top of previously killed cells, particularly evident for *S. aureus* on days 14 and 21. Additionally, stressed cells in contact with the HTE surface may express extracellular death factor (EDF), which has been implicated in PCD in Gram-negative bacteria, mainly studied in *E. coli* [88, 89].

Furthermore, gene expression may be modulated by the nanostructures, perhaps resulting in biofilm disaggregation. Quorum-sensing genes, which synchronise the biofilm allowing it to behave like a multicellular organism, may be modulated, thus affecting biofilm formation over time. Potential downregulation in quorum sensing and biofilm-associated genes may inhibit the formation of biofilm on the HTE surface, though this warrants further investigation.

Unravelling a complete mechanistic picture of the effect of surface nanostructures on bacterial attachment, growth, colonisation, and biofilm establishment is a complex task that will require the efforts of much ongoing research. However, this work details pioneering experiments that demonstrate the capacity of surfaces containing disordered spike-like nanostructures to sustain antibacterial properties over an extended period. Clinically, such an implant surface may not only act as a deterrent to bacterial aggregation and biofilm formation, but it may also provide host tissue with more time to win the race to the surface, in turn reducing the likelihood of an IAI.

4.6 Conclusion

In this study, we characterised the physicochemical and antibacterial properties of hydrothermally etched nanostructures over extended periods. A short-term cytocompatibility study using RAW 264.7 macrophage-like cells showed no adverse effects on morphology, viability, and proliferation. Following culture on HTE surfaces, *P. aeruginosa* did not exceed 4% viability over 21 days, whereas *S. aureus* viability reduced to 6.8 ± 3.1% by day 3, then increased to approximately 40% by day 21. In contrast, both bacterial species remained above 95% viable on CTL surfaces throughout the study. Total biovolume and measured viability were also significantly lower on the HTE surfaces for both bacteria at all time points. SEM imaging confirmed contact killing of bacteria on the nanostructures, as well as a lack of mature, organised biofilm forming on the HTE, surfaces over longer time points. Although additional research is required to fully understand the mechanisms underpinning the long-term antibacterial properties of surfaces containing sharp nanostructures, including an *in vivo* model, this study points to the potential of such surfaces to be applied to medical devices and ultimately contribute to reducing the rates of IAI.

4.7 Author Contributions

R.B. and D.F. designed, planned, and performed the experiments. R.B. analysed data and drafted the manuscript. D.F. fabricated samples. J.W., A.B., N.N. and D.P. performed the surface characterisation and participated in data analysis, D.F., D.B. and T.B. initiated the design of the study and revised the manuscript. K.V. supervised the study and revised the manuscript.

4.8 Declaration of Competing Interest

The authors listed above declare no conflict of interest or personal relationships that could have appeared to influence the work reported in this paper.

4.9 Acknowledgements

This study was co-funded by the Department of Industry, Science, Energy and Resources (Innovative Manufacturing CRC Ltd) Global Orthopaedic Technology Pty Ltd (IMCRC/GOT/130318).

The authors acknowledge the funding and in-kind support from Corin Australia and the University of South Australia. The authors would also like to acknowledge the instruments and scientific and technical assistance of Microscopy Australia at the University of South Australia, Mawson Lakes Campus, a facility that is funded by the University, and State and Federal Governments. RB thanks Andrew Hayles for his assistance in the graphical abstract. KV thanks NHMRC for Fellowship GNT1194466 and ARC for grant DP180101254.

4.10 Supporting Information

Supplementary data to this article can be found online at
https://doi.org/10.1016/j.mtbio.2021.100176
Additional information regarding the following**:** XPS elemental analysis, mean and p-values for CTL and HTE for figure 2 (Table S1). A table of p-values for live/dead viability analysis for *P. aeruginosa* (Table S2) and *S. aureus* (Table S3) from Figure 5A and 5B respectively. Mean log-reduction scores and associated p-values (Table S4) from Figure 9A. P-values for percent viability calculated from colony forming unit analysis for *P. aeruginosa* (Table S5) and *S. aureus* (Table S6), from Figure 9B and 9C respectively. Lastly, SEM micrographs for P. aeruginosa from Figure 10A (Figure S1) and S. aureus from Figure 10B (Figure S2) were incubated on CTL and HTE surfaces for 7, 14 and 21 days.

4.11 Data Availability

The data that support the findings of this study are available from the corresponding author, [KV], upon reasonable request.

4.12 Supplementary Material

Long-Term Antibacterial Properties of a Nanostructured Titanium Alloy Surface: An *In Vitro* Study

Richard Bright[1], Daniel Fernandes[1], Jonathan Wood[1], Dennis Palms[1], Anouck Burzava[1], Neethu Ninan[1], Toby Brown[2], Dan Barker[2] and Krasimir Vasilev[1*].

[1]Academic Unit of STEM, University of South Australia, Mawson Lakes, Adelaide, 5095, South Australia, Australia. [2]Corin Australia, Pymble, NSW 2073, Australia.

[*]Corresponding author email address: krasimir.vasilev@unisa.edu.au

Keywords: Nanoprotrusions, nanospikes, antibacterial, biofilm, biofouling, implant infection, orthopedic.

Table S1. *Topography measured by SEM. RMS, Ra and surface area were measured by AFM and wettability was measured using a contact angle goniometer (Figure 1B).*

Characteristic	CTL	HTE
Spike Height		348± 52 nm
Diameter		98±60 nm
Spacing		437±46 nm
RMS	5.13 nm	236.3 nm
Ra	4.15 nm	175.5 nm
Surface Area	25.1 μm^2	64.6 μm^2
Wettability	61±8°	5±0.8°

Table S2. *XPS elemental analysis, mean p-values compare all elements detected between CTL and HTE surface. Statistical significance was determined using multiples t-tests, followed by post hoc Holm-Sidak multiple comparison test, with alpha = 0.05. (Figure 2A).*

Elements	CTL		HTE		
	Mean	SD	Mean	SD	p-value
O	48.6	2.5	54.2	0.9	0.000030
C	29.5	4.9	19.7	1.0	<0.000001
Ti	15.6	2.7	20.7	0.6	0.000148
V	0.2	0.1	0.0	0.0	0.999839
Al	2.9	0.4	0.8	0.2	0.433299
Na	0.0	0.0	0.1	0.1	0.999899
K	0.0	0.0	1.6	0.9	0.706060
N	1.7	0.5	0.2	0.3	0.774516
Mg	0.6	0.1	1.0	0.3	0.999351
Si	0.5	0.3	0.7	1.2	0.999899
Ca	0.1	0.2	0.9	0.3	0.988274
Cl	0.1	0.1	0.0	0.0	0.999899
Cu	0.1	0.1	0.0	0.0	0.999899

Table S3. *P-values for P. aeruginosa viability (%) determined by live/dead staining over 21 days, comparing CTL to HTE. Statistical significance was determined using multiple t-tests followed by the post hoc Holm-Sidak method, with alpha = 0.05. (Figure 6A).*

Day	Mean CTL	Mean HTE	p-value
1	97.1	0.9	<0.000001
2	98.2	1.7	<0.000001
3	94.6	2.2	<0.000001
4	90.3	1.1	<0.000001
5	92.0	2.4	<0.000001
6	94.1	2.3	<0.000001
7	95.2	2.2	<0.000001
14	97.2	1.5	<0.000001
21	98.1	3.2	<0.000001

Table S4. *p-values for S. aureus viability (%) determined by live/dead staining over 21 days, comparing CTL to HTE. Statistical significance was determined using multiple t-tests following the Holm-Sidak method, with alpha = 0.05, n=3. (Figure 6B).*

Day	Mean CTL	Mean HTE	p-value
1	94.8	26.0	<0.000001
2	97.4	12.3	0.000002
3	94.8	6.8	0.000004
4	94.7	29.1	0.000055
5	93.0	32.5	0.000148
6	95.4	35.3	<0.000001
7	95.8	36.2	0.000008
14	93.4	41.8	0.000027
21	91.47	40.9	0.000037

Table S5. *Mean log-reduction scores and associated p-values for P. aeruginosa and S. aureus, incubated on CTL to HTE surfaces for each time point. Significance was determined by multiple t-tests following the Holm-Sidak method, with alpha = 0.05. (Figure 9A)*

Day	Log-reduction *P. aeruginosa*	Log Reduction *S. aureus*	p-value
1	1.867	1.967	0.8269
2	2.533	1.767	0.0007
3	2.367	2.533	0.8084
4	1.933	1.667	0.4996
5	2.233	1.633	0.0102
6	2.133	1.533	0.0102
7	1.967	1.867	0.8269
14	2.167	1.633	0.0220
21	1.900	1.767	0.8269

Table S6. *Mean CFU per sample (surface area 0.78 cm^2) and p-values for P. aeruginosa, incubated over 21 days, comparing CTL to HTE. Statistical significance was determined using multiple t-tests corrected for multiple comparisons using the Holm-Sidak method, with an alpha = 0.05, n = 3. (Figure 9B).*

Day	CFU / CTL Disc	CFU / HTE Disc	p-value
1	2.70E+10	3.47E+08	0.002183
2	1.30E+11	7.30E+08	0.001354
3	5.30E+10	2.37E+08	0.000888
4	2.10E+09	2.23E+07	0.000032
5	5.10E+10	2.80E+08	0.002775
6	1.87E+11	1.43E+09	0.002775
7	2.00E+09	2.17E+07	0.002775
14	3.87E+09	2.80E+07	0.001919
21	1.31E+10	1.59E+08	0.000819

Table S7. *Mean CFU per sample (surface area 7.8 mm^2) and p-values for S. aureus, incubated over 21 days, comparing CTL to HTE. Statistical significance was determined using multiple t-tests corrected for multiple comparisons using the Holm-Sidak method, with an alpha = 0.05, n = 3. (Figure 9C).*

Day	CFU / CTL Disc	CFU / HTE Disc	p-value
1	3.97E+08	4.07E+06	0.013953
2	5.20E+08	8.83E+06	0.013953
3	1.05E+11	4.00E+08	0.000924
4	9.10E+08	1.90E+07	0.000035
5	1.40E+08	3.30E+06	0.000151
6	7.37E+09	2.07E+08	0.001704
7	1.77E+09	2.50E+07	0.000924
14	1.60E+09	3.60E+07	0.013953
21	4.83E+09	8.13E+07	0.001341

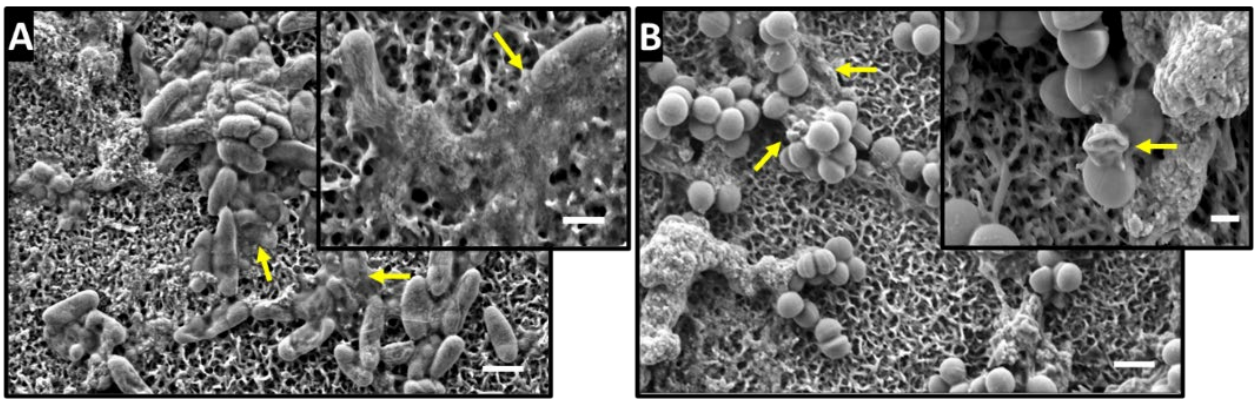

Figure S1. *SEM micrographs depicting P. aeruginosa (A) and S. aureus (B) at day 7 post-incubation on HTE samples. Inset images show higher magnification images demonstrating irregular morphology, dead cells, and cellular debris, highlighted by the yellow arrows. Scale bars in the main images represent 1µm, and the inset scale bar represents 500 nm (Figures 10 & 11).*

4.13 References

[1] P.H. Long, Medical devices in orthopedic applications, Toxicol Pathol 36(1) (2008) 85-91.

[2] Q. Zheng, L. Mao, Y. Shi, W. Fu, Y. Hu, Biocompatibility of Ti-6Al-4V titanium alloy implants with laser microgrooved surfaces, Materials Technology (2020) 1-10.

[3] R.O. Darouiche, Treatment of infections associated with surgical implants, N Engl J Med 350(14) (2004) 1422-9.

[4] T.F. Moriarty, R. Kuehl, T. Coenye, W.J. Metsemakers, M. Morgenstern, E.M. Schwarz, M. Riool, S.A.J. Zaat, N. Khana, S.L. Kates, R.G. Richards, Orthopaedic device-related infection: current and future interventions for improved prevention and treatment, EFORT Open Rev 1(4) (2016) 89-99.

[5] M.J. Patzakis, J. Wilkins, Factors influencing infection rate in open fracture wounds, Clin Orthop Relat Res (243) (1989) 36-40.

[6] H. Boxma, T. Broekhuizen, P. Patka, H. Oosting, Randomised controlled trial of single-dose antibiotic prophylaxis in surgical treatment of closed fractures: the Dutch Trauma Trial, Lancet 347(9009) (1996) 1133-7.

[7] D. Hernández-Vaquero, M. Fernández-Fairen, A. Torres, A.M. Menzie, J.M. Fernández-Carreira, A. Murcia-Mazon, E. Guerado, L. Merzthal, Treatment of periprosthetic infections: an economic analysis, ScientificWorldJournal 2013 (2013) 821650.

[8] F.S. Haddad, A. Ngu, J.J. Negus, Prosthetic Joint Infections and Cost Analysis?, Adv Exp Med Biol 971 (2017) 93-100.

[9] J.M. Anderson, Future challenges in the in vitro and in vivo evaluation of biomaterial biocompatibility, Regen Biomater 3(2) (2016) 73-7.

[10] A.G. Gristina, Biomaterial-centered infection: microbial adhesion versus tissue integration, Science 237(4822) (1987) 1588-95.

[11] L. Chu, Y. Yang, S. Yang, Q. Fan, Z. Yu, X.L. Hu, T.D. James, X.P. He, T. Tang, Preferential Colonization of Osteoblasts Over Co-cultured Bacteria on a Bifunctional Biomaterial Surface, Front Microbiol 9 (2018) 2219.

[12] E. Roilides, M. Simitsopoulou, A. Katragkou, T.J. Walsh, How Biofilms Evade Host Defenses, Microbiol Spectr 3(3) (2015).

[13] C.W. Hall, T.F. Mah, Molecular mechanisms of biofilm-based antibiotic resistance and tolerance in pathogenic bacteria, FEMS Microbiol Rev 41(3) (2017) 276-301.

[14] T.F. Mah, G.A. O'Toole, Mechanisms of biofilm resistance to antimicrobial agents, Trends Microbiol 9(1) (2001) 34-9.

[15] E. Seebach, K.F. Kubatzky, Chronic Implant-Related Bone Infections-Can Immune Modulation be a Therapeutic Strategy?, Front Immunol 10 (2019) 1724.

[16] R. Trebse, V. Pisot, A. Trampuz, Treatment of infected retained implants, J Bone Joint Surg Br 87(2) (2005) 249-56.

[17] F. Schömig, C. Perka, M. Pumberger, R. Ascherl, Implant contamination as a cause of surgical site infection in spinal surgery: are single-use implants a reasonable solution? - a systematic review, BMC Musculoskelet Disord 21(1) (2020) 634.
[18] C. Yue, B. Zhao, Y. Ren, R. Kuijer, H.C. van der Mei, H.J. Busscher, E.T. Rochford, The implant infection paradox: why do some succeed when others fail? Opinion and discussion paper, Eur Cell Mater 29 (2015) 303-10; discussion 310-3.
[19] J.M. Schierholz, J. Beuth, Implant infections: a haven for opportunistic bacteria, J Hosp Infect 49(2) (2001) 87-93.
[20] M. Ribeiro, F.J. Monteiro, M.P. Ferraz, Infection of orthopedic implants with emphasis on bacterial adhesion process and techniques used in studying bacterial-material interactions, Biomatter 2(4) (2012) 176-194.
[21] P. Brouqui, M.C. Rousseau, A. Stein, M. Drancourt, D. Raoult, Treatment of Pseudomonas aeruginosa-infected orthopedic prostheses with ceftazidime-ciprofloxacin antibiotic combination, Antimicrob Agents Chemother 39(11) (1995) 2423-5.
[22] L. Crémet, A. Broquet, B. Brulin, C. Jacqueline, S. Dauvergne, R. Brion, K. Asehnoune, S. Corvec, D. Heymann, N. Caroff, Pathogenic potential of Escherichia coli clinical strains from orthopedic implant infections towards human osteoblastic cells, Pathog Dis 73(8) (2015) ftv065.
[23] A.L. Cogen, V. Nizet, R.L. Gallo, Skin microbiota: a source of disease or defence?, Br J Dermatol 158(3) (2008) 442-55.
[24] A. Sobolev, A. Valkov, A. Kossenko, I. Wolicki, M. Zinigrad, K. Borodianskiy, Bioactive Coating on Ti Alloy with High Osseointegration and Antibacterial Ag Nanoparticles, ACS Appl Mater Interfaces 11(43) (2019) 39534-39544.
[25] H. Haidari, Z. Kopecki, R. Bright, A.J. Cowin, S. Garg, N. Goswami, K. Vasilev, Ultrasmall AgNP-Impregnated Biocompatible Hydrogel with Highly Effective Biofilm Elimination Properties, ACS Appl Mater Interfaces 12(37) (2020) 41011-41025.
[26] A. Ravindran Girija, S. Balasubramanian, R. Bright, A.J. Cowin, N. Goswami, K. Vasilev, Ultrasmall Gold Nanocluster Based Antibacterial Nanoaggregates for Infectious Wound Healing, ChemNanoMat 5(9) (2019) 1176-1181.
[27] M. Riool, A. de Breij, J.W. Drijfhout, P.H. Nibbering, S.A.J. Zaat, Antimicrobial Peptides in Biomedical Device Manufacturing, Front Chem 5 (2017) 63.
[28] S.S. Griesser, M. Jasieniak, K. Vasilev, H.J. Griesser, Antimicrobial Peptides Grafted onto a Plasma Polymer Interlayer Platform: Performance upon Extended Bacterial Challenge, Coatings 11(1) (2021) 68.
[29] F. Jahanmard, F.M. Dijkmans, A. Majed, H.C. Vogely, B.C.H. van der Wal, D.A.C. Stapels, S.M. Ahmadi, T. Vermonden, S. Amin Yavari, Toward Antibacterial Coatings for Personalized Implants, ACS Biomater Sci Eng 6(10) (2020) 5486-5492.
[30] K. Vasilev, Nanoengineered Antibacterial Coatings and Materials: A Perspective, Coatings 9(10) (2019) 654.

[31] K. Vasilev, J. Cook, H.J. Griesser, Antibacterial surfaces for biomedical devices, Expert Rev Med Devices 6(5) (2009) 553-67.
[32] V.J. Suhardi, D.A. Bichara, S. Kwok, A.A. Freiberg, H. Rubash, H. Malchau, S.H. Yun, O.K. Muratoglu, E. Oral, A Fully Functional Drug-Eluting Joint Implant, Nat Biomed Eng 1 (2017).
[33] A.E. Eltorai, J. Haglin, S. Perera, B.A. Brea, R. Ruttiman, D.R. Garcia, C.T. Born, A.H. Daniels, Antimicrobial technology in orthopedic and spinal implants, World J Orthop 7(6) (2016) 361-9.
[34] E.P. Ivanova, J. Hasan, H.K. Webb, G. Gervinskas, S. Juodkazis, V.K. Truong, A.H. Wu, R.N. Lamb, V.A. Baulin, G.S. Watson, J.A. Watson, D.E. Mainwaring, R.J. Crawford, Bactericidal activity of black silicon, Nat Commun 4 (2013) 2838.
[35] R. Bright, A. Hayles, D. Fernandes, R.M. Visalakshan, N. Ninan, D. Palms, A. Burzava, D. Barker, T. Brown, K. Vasilev, In Vitro Bactericidal Efficacy of Nanostructured Ti6Al4V Surfaces is Bacterial Load Dependent, ACS Appl Mater Interfaces 13(32) (2021) 38007-38017.
[36] J.V. Wandiyanto, T. Tamanna, D.P. Linklater, V.K. Truong, M. Al Kobaisi, V.A. Baulin, S. Joudkazis, H. Thissen, R.J. Crawford, E.P. Ivanova, Tunable morphological changes of asymmetric titanium nanosheets with bactericidal properties, J Colloid Interface Sci 560 (2020) 572-580.
[37] E.P. Ivanova, D.P. Linklater, M. Werner, V.A. Baulin, X. Xu, N. Vrancken, S. Rubanov, E. Hanssen, J. Wandiyanto, V.K. Truong, A. Elbourne, S. Maclaughlin, S. Juodkazis, R.J. Crawford, The multi-faceted mechano-bactericidal mechanism of nanostructured surfaces, Proc Natl Acad Sci U S A 117(23) (2020) 12598-12605.
[38] D.P. Linklater, M. De Volder, V.A. Baulin, M. Werner, S. Jessl, M. Golozar, L. Maggini, S. Rubanov, E. Hanssen, S. Juodkazis, E.P. Ivanova, High Aspect Ratio Nanostructures Kill Bacteria via Storage and Release of Mechanical Energy, ACS Nano 12(7) (2018) 6657-6667.
[39] J. Jenkins, J. Mantell, C. Neal, A. Gholinia, P. Verkade, A.H. Nobbs, B. Su, Antibacterial effects of nanopillar surfaces are mediated by cell impedance, penetration and induction of oxidative stress, Nat Commun 11(1) (2020) 1626.
[40] G. Eaninwene, 2nd, C. Yao, T.J. Webster, Enhanced osteoblast adhesion to drug-coated anodized nanotubular titanium surfaces, Int J Nanomedicine 3(2) (2008) 257-64.
[41] T. Nichol, J. Callaghan, R. Townsend, I. Stockley, P.V. Hatton, C. Le Maitre, T.J. Smith, R. Akid, The antimicrobial activity and biocompatibility of a controlled gentamicin-releasing single-layer sol-gel coating on hydroxyapatite-coated titanium, Bone Joint J 103-b(3) (2021) 522-529.
[42] J. Vishnu, K.M. V, V. Gopal, C. Bartomeu Garcia, P. Hameed, G. Manivasagam, T.J. Webster, Hydrothermal treatment of etched titanium: A potential surface nano-modification technique for enhanced biocompatibility, Nanomedicine 20 (2019) 102016.
[43] K. Ma, R. Zhang, J. Sun, C. Liu, Oxidation Mechanism of Biomedical Titanium Alloy Surface and Experiment, International Journal of Corrosion 2020 (2020) 1678615.
[44] C.M. Bhadra, V.K. Truong, V.T. Pham, M. Al Kobaisi, G. Seniutinas, J.Y. Wang, S. Juodkazis, R.J. Crawford, E.P. Ivanova, Antibacterial titanium nano-patterned arrays inspired by dragonfly wings, Sci Rep 5 (2015) 16817.

[45] D.T. Elliott, R.J. Wiggins, R. Dua, Bioinspired antibacterial surface for orthopedic and dental implants, J Biomed Mater Res B Appl Biomater 109(7) (2021) 973-981.
[46] S. Ferraris, A. Cochis, M. Cazzola, M. Tortello, A. Scalia, S. Spriano, L. Rimondini, Cytocompatible and Anti-bacterial Adhesion Nanotextured Titanium Oxide Layer on Titanium Surfaces for Dental and Orthopedic Implants, Front Bioeng Biotechnol 7 (2019) 103.
[47] S.M. Shiels, K.M. Bedigrew, J.C. Wenke, Development of a hematogenous implant-related infection in a rat model, BMC Musculoskelet Disord 16 (2015) 255.
[48] C.R. Arciola, D. Campoccia, L. Montanaro, Implant infections: adhesion, biofilm formation and immune evasion, Nat Rev Microbiol 16(7) (2018) 397-409.
[49] Q. Shi, S. Roux, F. Latourte, F. Hild, D. Loisnard, N. Brynaert, Measuring topographies from conventional SEM acquisitions, Ultramicroscopy 191 (2018) 18-33.
[50] S. Kaja, A.J. Payne, Y. Naumchuk, P. Koulen, Quantification of Lactate Dehydrogenase for Cell Viability Testing Using Cell Lines and Primary Cultured Astrocytes, Curr Protoc Toxicol 72 (2017) 2.26.1-2.26.10.
[51] M.H. Cho, A. Niles, R. Huang, J. Inglese, C.P. Austin, T. Riss, M. Xia, A bioluminescent cytotoxicity assay for assessment of membrane integrity using a proteolytic biomarker, Toxicol In Vitro 22(4) (2008) 1099-106.
[52] S.S. Kumar, A.R. Ghosh, Assessment of bacterial viability: a comprehensive review on recent advances and challenges, Microbiology (Reading) 165(6) (2019) 593-610.
[53] C. Bankier, Y. Cheong, S. Mahalingam, M. Edirisinghe, G. Ren, E. Cloutman-Green, L. Ciric, A comparison of methods to assess the antimicrobial activity of nanoparticle combinations on bacterial cells, PLoS One 13(2) (2018) e0192093.
[54] J. Canet-Ferrer, E. Coronado, A. Forment-Aliaga, E. Pinilla-Cienfuegos, Correction of the tip convolution effects in the imaging of nanostructures studied through scanning force microscopy, Nanotechnology 25(39) (2014) 395703.
[55] R.N. Wenzel, Surface Roughness and Contact Angle, The Journal of Physical and Colloid Chemistry 53(9) (1949) 1466-1467.
[56] A.B.D. Cassie, S. Baxter, Wettability of porous surfaces, Transactions of the Faraday Society 40(0) (1944) 546-551.
[57] H.K. Webb, R.J. Crawford, E.P. Ivanova, Wettability of natural superhydrophobic surfaces, Adv Colloid Interface Sci 210 (2014) 58-64.
[58] S. Arango-Santander, A. Pelaez-Vargas, S.C. Freitas, C. García, A novel approach to create an antibacterial surface using titanium dioxide and a combination of dip-pen nanolithography and soft lithography, Sci Rep 8(1) (2018) 15818.
[59] M. Rabe, D. Verdes, S. Seeger, Understanding protein adsorption phenomena at solid surfaces, Adv Colloid Interfac 162(1-2) (2011) 87-106.
[60] J.O. Abaricia, A.H. Shah, R.M. Musselman, R. Olivares-Navarrete, Hydrophilic titanium surfaces reduce neutrophil inflammatory response and NETosis, Biomater Sci 8(8) (2020) 2289-2299.

[61] S.C. Sartoretto, J.A. Calasans-Maia, Y.O.D. Costa, R.S. Louro, J.M. Granjeiro, M.D. Calasans-Maia, Accelerated Healing Period with Hydrophilic Implant Placed in Sheep Tibia, Braz Dent J 28(5) (2017) 559-565.
[62] J. Kzhyshkowska, A. Gudima, V. Riabov, C. Dollinger, P. Lavalle, N.E. Vrana, Macrophage responses to implants: prospects for personalized medicine, J Leukoc Biol 98(6) (2015) 953-62.
[63] P. Stiefel, S. Schmidt-Emrich, K. Maniura-Weber, Q. Ren, Critical aspects of using bacterial cell viability assays with the fluorophores SYTO9 and propidium iodide, BMC Microbiol 15 (2015) 36.
[64] T. Bjarnsholt, M. Alhede, M. Alhede, S.R. Eickhardt-Sørensen, C. Moser, M. Kühl, P. Jensen, N. Høiby, The in vivo biofilm, Trends Microbiol 21(9) (2013) 466-74.
[65] T.J. Silhavy, D. Kahne, S. Walker, The bacterial cell envelope, Cold Spring Harb Perspect Biol 2(5) (2010) a000414-a000414.
[66] Y. Li, P. Xiao, Y. Wang, Y. Hao, Mechanisms and Control Measures of Mature Biofilm Resistance to Antimicrobial Agents in the Clinical Context, ACS Omega 5(36) (2020) 22684-22690.
[67] D.P. Linklater, V.A. Baulin, S. Juodkazis, R.J. Crawford, P. Stoodley, E.P. Ivanova, Mechano-bactericidal actions of nanostructured surfaces, Nat Rev Microbiol 19(1) (2021) 8-22.
[68] S. Aggarwal, P.S. Stewart, R.M. Hozalski, Biofilm Cohesive Strength as a Basis for Biofilm Recalcitrance: Are Bacterial Biofilms Overdesigned? Microbiol Insights 8(Suppl 2) (2015) 29-32.
[69] J.F. González, M.M. Hahn, J.S. Gunn, Chronic biofilm-based infections: skewing of the immune response, Pathogens and disease 76(3) (2018) fty023.
[70] Y. Cao, B. Su, S. Chinnaraj, S. Jana, L. Bowen, S. Charlton, P. Duan, N.S. Jakubovics, J. Chen, Nanostructured titanium surfaces exhibit recalcitrance towards Staphylococcus epidermidis biofilm formation, Sci Rep 8(1) (2018) 1071.
[71] A. Tripathy, P. Sen, B. Su, W.H. Briscoe, Natural and bioinspired nanostructured bactericidal surfaces, Adv Colloid Interface Sci 248 (2017) 85-104.
[72] M. Arnoldi, M. Fritz, E. Bäuerlein, M. Radmacher, E. Sackmann, A. Boulbitch, Bacterial turgor pressure can be measured by atomic force microscopy, Phys Rev E Stat Phys Plasmas Fluids Relat Interdiscip Topics 62(1 Pt B) (2000) 1034-44.
[73] K. O'Riordan, J.C. Lee, Staphylococcus aureus capsular polysaccharides, Clin Microbiol Rev 17(1) (2004) 218-234.
[74] C.E. Harper, C.J. Hernandez, Cell biomechanics and mechanobiology in bacteria: Challenges and opportunities, APL Bioeng 4(2) (2020) 021501-021501.
[75] O. Bohuszewicz, J. Liu, H.H. Low, Membrane remodelling in bacteria, J Struct Biol 196(1) (2016) 3-14.
[76] M. Osawa, H.P. Erickson, Turgor Pressure and Possible Constriction Mechanisms in Bacterial Division, Front Microbiol 9 (2018) 111-111.
[77] C. Coltharp, J. Buss, T.M. Plumer, J. Xiao, Defining the rate-limiting processes of bacterial cytokinesis, Proc Natl Acad Sci U S A 113(8) (2016) E1044-53.

[78] A.J. Egan, R.M. Cleverley, K. Peters, R.J. Lewis, W. Vollmer, Regulation of bacterial cell wall growth, Febs j 284(6) (2017) 851-867.
[79] H. Strahl, L.W. Hamoen, Membrane potential is important for bacterial cell division, Proc Natl Acad Sci U S A 107(27) (2010) 12281-6.
[80] A.E. LaBauve, M.J. Wargo, Growth and laboratory maintenance of Pseudomonas aeruginosa, Curr Protoc Microbiol Chapter 6 (2012) Unit-6E.1.
[81] A.K. Szafrańska, V. Junker, M. Steglich, U. Nübel, Rapid cell division of Staphylococcus aureus during colonization of the human nose, BMC Genomics 20(1) (2019) 229.
[82] P.M. Tsimbouri, L. Fisher, N. Holloway, T. Sjostrom, A.H. Nobbs, R.M. Meek, B. Su, M.J. Dalby, Osteogenic and bactericidal surfaces from hydrothermal titania nanowires on titanium substrates, Sci Rep 6 (2016) 36857.
[83] Y. Hong, J. Zeng, X. Wang, K. Drlica, X. Zhao, Post-stress bacterial cell death mediated by reactive oxygen species, Proc Natl Acad Sci U S A 116(20) (2019) 10064-10071.
[84] B. Ezraty, A. Gennaris, F. Barras, J.F. Collet, Oxidative stress, protein damage and repair in bacteria, Nat Rev Microbiol 15(7) (2017) 385-396.
[85] K.W. Bayles, Bacterial programmed cell death: making sense of a paradox, Nat Rev Microbiol 12(1) (2014) 63-9.
[86] N. Allocati, M. Masulli, C. Di Ilio, V. De Laurenzi, Die for the community: an overview of programmed cell death in bacteria, Cell Death Dis 6(1) (2015) e1609.
[87] H. Engelberg-Kulka, B. Sat, M. Reches, S. Amitai, R. Hazan, Bacterial programmed cell death systems as targets for antibiotics, Trends Microbiol 12(2) (2004) 66-71.
[88] M. Belitsky, H. Avshalom, A. Erental, I. Yelin, S. Kumar, N. London, M. Sperber, O. Schueler-Furman, H. Engelberg-Kulka, The Escherichia coli extracellular death factor EDF induces the endoribonucleolytic activities of the toxins MazF and ChpBK, Mol Cell 41(6) (2011) 625-35.
[89] H. Engelberg-Kulka, S. Amitai, I. Kolodkin-Gal, R. Hazan, Bacterial programmed cell death and multicellular behavior in bacteria, PLoS Genet 2(10) (2006) e135-e135.

(IF 12.26)

Bright R, Hayles A, Wood J, Palms D, Brown T, Barker D, Vasilev K. Surfaces Containing Sharp Nanostructures Enhance Antibiotic Efficacy. Nano Lett. 2022 Aug 24;22(16):6724-6731. DOI: 10.1021/acs.nanolett.2c02182 . Epub 2022 Jul 28. PMID: 35900125.

CHAPTER 5:

SURFACES CONTAINING SHARP NANOSTRUCTURES ENHANCE ANTIBIOTIC EFFICACY

Richard Bright, Andrew Hayles, Jonathan Wood, Dennis Palms, Toby Brown, Dan Barker and Krasimir Vasilev*

Keywords

Nanostructures, biomimetics, hydrothermally etching, antibacterial, antibiotics, implant-associated infections.

TABLE OF CONTENTS

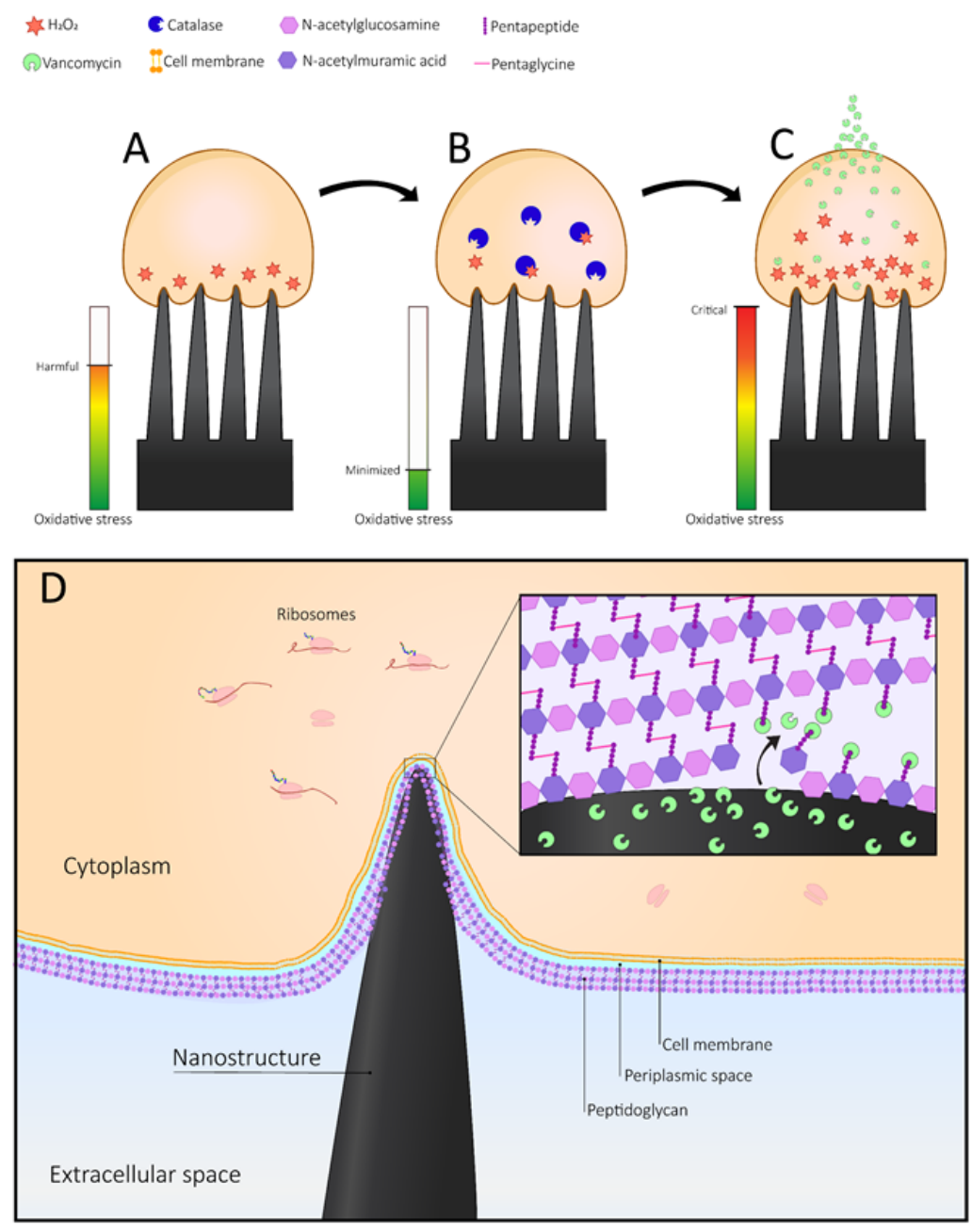

Scheme 1. *The interaction between Staphylococcus aureus and the hydrothermally etched sharp nanostructures sensitizes the surviving bacteria to a clinically relevant antibiotic, vancomycin. Furthermore, a sub-clinical dose of the antibiotic was able to eliminate the remaining bacteria. We propose a mechanism for this antibacterial synergy, involving enhanced oxidative stress, and impeded defenses of the bacterial cell against ROS and cell wall damage*.

5.2 ABSTRACT

The ever-increasing rate of medical device implantations is met by a proportionately high burden of implant-associated infections. These types of infections are notoriously difficult to treat due to the resistant nature of bacterial biofilms and their capacity to evade the immune system. To mitigate this threat, much research has been directed toward the development of antibacterial surface modifications by various means. One recent approach that has attracted significant attention involves surfaces containing sharp nanostructures capable of killing bacteria upon contact. Herein, we report that the mechanical interaction between Staphylococcus aureus and such surface nanostructures leads to a sensitization of the pathogen to the glycopeptide antibiotic vancomycin. We demonstrate that this is due to cell wall damage and impeded bacterial defences against reactive oxygen species. The results of this study promise to be impactful in the clinic, as the combination of nanostructured antibacterial surfaces and antibiotics commonly used in hospitals may improve antimicrobial therapy strategies, helping clinicians to prevent and treat implant-associated infections using reduced antibiotic concentrations instead of relying on invasive revision surgeries with often poor outcomes.

5.3 INTRODUCTION

Surgically implanted medical devices are being utilized at an ever-increasing rate. [1] Unfortunately, implant-associated infections (IAI) are a persistent threat that causes considerable morbidity and mortality. [2] Mortality rates associated with IAI can exceed 25%, depending on the implant type and its location. [3] Once pathogenic bacteria establish on a solid implant surface, they quickly alter their genetic profile to shift toward a biofilm phenotype. Bacterial biofilm is a complex, metabolically heterogeneous aggregation of surface-attached bacterial cells embedded in a matrix of extracellular polymeric substances (EPS). [4] Once in the biofilm state, bacteria can withstand harsh environmental conditions and evade the host immune system. Perhaps the most problematic is the fact that bacteria in biofilms can withstand up to 1000-fold higher concentrations of antibiotics compared to their planktonic counterparts. [5] The consequence of such high antibiotic tolerance is an inability to eradicate IAI with antibiotics alone. Therefore, IAI necessitates invasive surgeries to debride the surrounding tissue and replace the implant, [6] which carries the added risk of further complications and a high probability of re-infection. [7]

The severity of the problem triggered much research directed toward devising innovative antibacterial surface modification approaches. [7] A recent strategy that attracted significant attention involves the fabrication of nanoscale structures that kill bacteria upon contact by mechanical interactions, thus inhibiting biofilm formation. [8, 9] This type of mechano-bactericidal effect was first observed in Nature on the wing surface of cicadas. [10, 11] Bioinspired mechano-bactericidal topographies have since been applied to synthetic materials based on silicon and titanium. [9, 12]

The bactericidal mechanism of these surfaces has been attributed to a combination of cell membrane penetration by the sharp nanostructures, leading to cell rupture, [13] as well as the intracellular generation of reactive oxygen species (ROS) and subsequent oxidative stress. [14] While such surfaces have been demonstrated to be particularly effective at killing Gram-negative bacteria such as *Pseudomonas aeruginosa*, Gram-positive bacteria such as *Staphylococcus aureus* with highly rigid cell walls have been demonstrated to be more difficult to completely eradicate. [15] Therefore, this study aimed to investigate whether delivery of an antibiotic to remaining bacteria not already killed due to contact with a nanostructured surface may improve overall antibacterial efficacy.

With consideration to the purported bactericidal mechanisms of nanostructured surfaces, we hypothesized that the mechanical interactions would also lead to an increased sensitivity of bacteria to vancomycin, a glycopeptide antibiotic that inhibits cell wall biosynthesis. This may occur through two potential routes. Firstly, bacterial cells that are not directly penetrated and killed during initial contact with the protruding nanostructures may still have distorted cell walls with exposed inner layers of peptidoglycan, allowing increased binding of vancomycin to the D-Ala-D-Ala component of peptidoglycan. [16, 17] Secondly, as a bactericidal antibiotic, vancomycin ultimately leads to cell death through the means of oxidative stress. [18] Thus, there could be a potential complementary action between vancomycin and bactericidal nanostructured surfaces, as the oxidative stress generated by the nanostructures may be amplified by the oxidative stress associated with the antibiotic treatment. In this report, we present a major finding pointing to synergistic cooperation between an antibiotic that is commonly used in the clinical setting and a surface containing sharp nanostructures, and how together they can be used to fight IAI.

5.4 RESULTS AND DISCUSSION

5.4.1 Characterization and Cytocompatibility of HTE-Ti.

The presence of sharp nanostructures on the hydrothermally etched titanium (HTE-Ti) surface was confirmed by SEM. Comparative images with control as-received titanium (AR-Ti) are shown in Figure 1A and Figure 1B (Macroscopic images of AR-Ti and HTE-Ti discs, together with complementary SEM images of AR-Ti and HTE-Ti samples are shown in Figure S1 and Figure S2). The HTE-Ti nanoprotrusions were approximately perpendicular to the surface and measured at 348 ± 152 nm in height and had a mean diameter of 98 ± 60 nm at mid-height. Such nanostructures with heights greater than 200 nm and a high aspect ratio are required for optimal bactericidal activity. [19] Spacing between the nanostructures was 437 ± 46 nm.

The arithmetic average (Ra) and mean square roughness (RMS) were determined from the AFM images to be 175.5 nm and 236.3 nm for HTE-Ti and 4.2 nm and 5.13 nm for AR-Ti. The surface nanostructures also resulted in a significant increase in the surface area (SA) from 25.1 μm^2 for AR-Ti to 64.6 μm^2 for HTE-Ti. The HTE-Ti surface was superhydrophilic, having a water contact angle of 5° ± 0.8° compared to 61° ± 8° of AR-Ti. Both the roughness and hydrophilicity of the HTE-Ti

surface are attractive properties for intra-osseous implant applications, as both properties promote protein adsorption and osteogenesis. [20]

EDX analysis (Figure 1H and Figure1I) detected indicative elements used in the manufacture of titanium alloy (titanium, aluminium, and vanadium) in the bulk material (spectrum 2). Analysis of the nanostructured outermost layer (spectrum 1) obtained after hydrothermal treatment indicated a thickening of the oxide layer confirmed by an increase in oxygen content and the absence of vanadium. [21] A transitional layer was also observed (spectrum 3) between the nanostructure and the bulk material, which had a reduction in aluminium and an increase in oxygen content compared to the bulk material.

To verify the cytocompatibility of the HTE-Ti surface toward eukaryotic cells, an LDH-Glo™ cytotoxicity assay was performed using RAW 264.7 macrophage-like cells (**Figure 1J**). There was no significant difference in viability between cells cultured on AR-Ti and HTE-Ti (88.1 ± 5.0 and 90.4 ± 6.4 respectively, p = 0.64), indicating that the modified nanostructured surface supports host cells as well as the control polished surface.

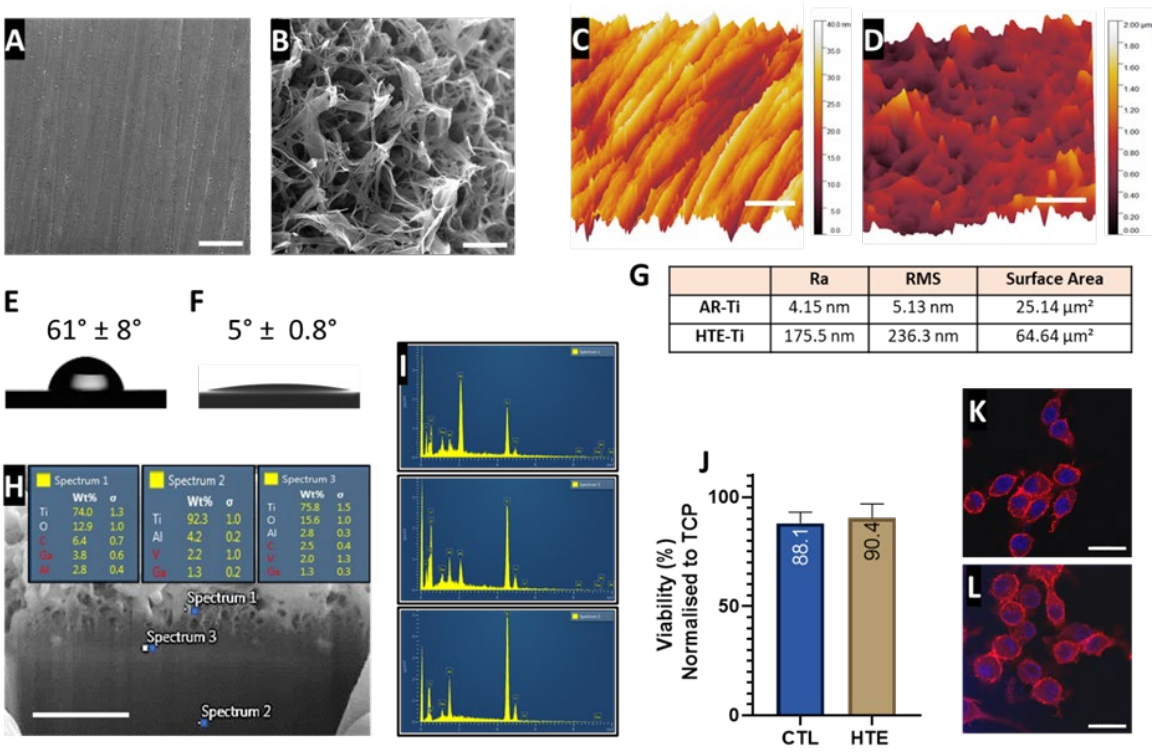

Figure 1. *Surface characterization and cytocompatibility. SEM micrographs of AR-Ti (A) and HTE-Ti (B) scale bars represent 500 nm. AFM images of AR-Ti (C) and HTE-Ti (D), scale bars equal 1 µm. The water contact angle of AR-Ti (E) and HTE-Ti, data represents mean ± SD and n =3 (F). Surface roughness analysis (G). EDX measurement of elemental composition (Wt.%) of HTE-Ti, nanostructures (Spectrum 1), the underlying oxide layer (Spectrum 3) and bulk (Spectrum 2) (H) scale bar = 500nm, and spectral analysis for nanostructures (Spectrum 1), underlying oxide layer (Spectrum 3) and bulk (Spectrum 2) (I).*

LDH-based viability of AR-Ti and HTE-Ti, 88.1 ± 5.0% and 90.4 ± 6.4% (mean ± SD) respectively, p = 0.64 and n =3 (J) and actin/DAPI stained fluorescence micrographs of RAW 264.7 macrophage-like cells on AR-Ti and HTE-Ti, scale bar = 20 μm (K and L respectively).

5.4.2 The Bactericidal Activity of HTE-Ti

To determine the baseline efficacy of HTE-Ti as a bactericidal surface, samples were challenged with 4 medically relevant pathogens (Figure S3). The viability determined from live/dead analysis for *Escherichia coli* (*E. coli*, ATCC 11303), *Pseudomonas aeruginosa* (*P. aeruginosa*, ATCC 15692), *Staphylococcus epidermidis* (*S. epidermidis*, ATCC 35984) and *Staphylococcus aureus* (*S. aureus*, ATCC 25923) incubated on AR-Ti surface for 18 h was 92.6 ± 5.2%, 97.4 ± 11.4%, 95.8 ± 8.9% and 97.4 ± 7.8%, respectively and on the HTE-Ti surface was 18.2 ± 4.1%, 5.3 ± 0.9%, 34.5 ± 3.6% and 35.1 ± 11.2%, respectively (Table 1). *S. aureus* was the pathogen showing the greatest capacity to overcome the mechano-bactericidal nature of the surface, exhibiting a 2-log reduction over 14 days (Figure S4). *S. aureus* is also a major clinical challenge, as some strains carry methicillin resistance genes which nullify many first-choice antibiotics. Furthermore, the formation of *S. aureus* biofilm promotes the emergence of methicillin-resistant cells utilizing horizontal gene transfer. [22]

Table 1. *The bactericidal activity of HTE-Ti against implanted device-related pathogens and their prevalence in IAI. The viability data was tabulated as mean ± SD and n = 3.*

Pathogen	Gram-stain	IAI burden (%)	Viability on HTE-Ti (%)
E. coli	Gram-negative	2.4-5.3 [23]	18.2 ± 4.1
P. aeruginosa	Gram-negative	6.1-10.5% [23]	5.3 ± 0.9
S. epidermidis	Gram-positive	Up to 66% [24]	34.5 ± 3.6
S. aureus	Gram-positive	Up to 66% [24]	35.1 ± 11.2

5.4.3 Vancomycin Treatment of Mature *S. Aureus* Biofilm On HTE-Ti.

To understand the effect of the nanostructured surface on the susceptibility of *S. aureus* to antibiotics, firstly we cultured *S. aureus* on the AR-Ti and HTE-Ti surfaces for 3 days. Then, the surviving *S. aureus* was treated with vancomycin at concentrations ranging from 5 to 100 μg/mL (representing 5-100x MIC, see Figure S5) for 7 consecutive days (Figure 2 and Figure S6). At this concentration range, the vancomycin dosage is below that used clinically. For example, orthopedic device-related infections are recommended to be treated with an initial intravenous vancomycin dosage of up to 30 mg/kg. [25] This equates to a blood concentration of 467 μg/mL assuming a body weight of 70 kg and blood volume of 4.5 L.

Without vancomycin treatment, *S. aureus* maintained the viability of approximately 80% on the AR-Ti surfaces during the 7-day time course, while on the HTE-Ti surfaces viability reduced to 20% by day 7. The presence of 5, 25 and 50 µg/mL vancomycin had only a marginal effect on *S. aureus* viability for both surfaces. A further increase in vancomycin concentration to 75 and 100 µg/mL allowed for the total clearance of remaining viable cells on the HTE-Ti surface, however, *S. aureus* still retained viability between 20-40% on the AR-Ti surface even after 7 days. These results supported the hypothesis that antibiotic treatment of *S. aureus* on a nanostructured implant surface has improved efficacy compared to on a control polished surface.

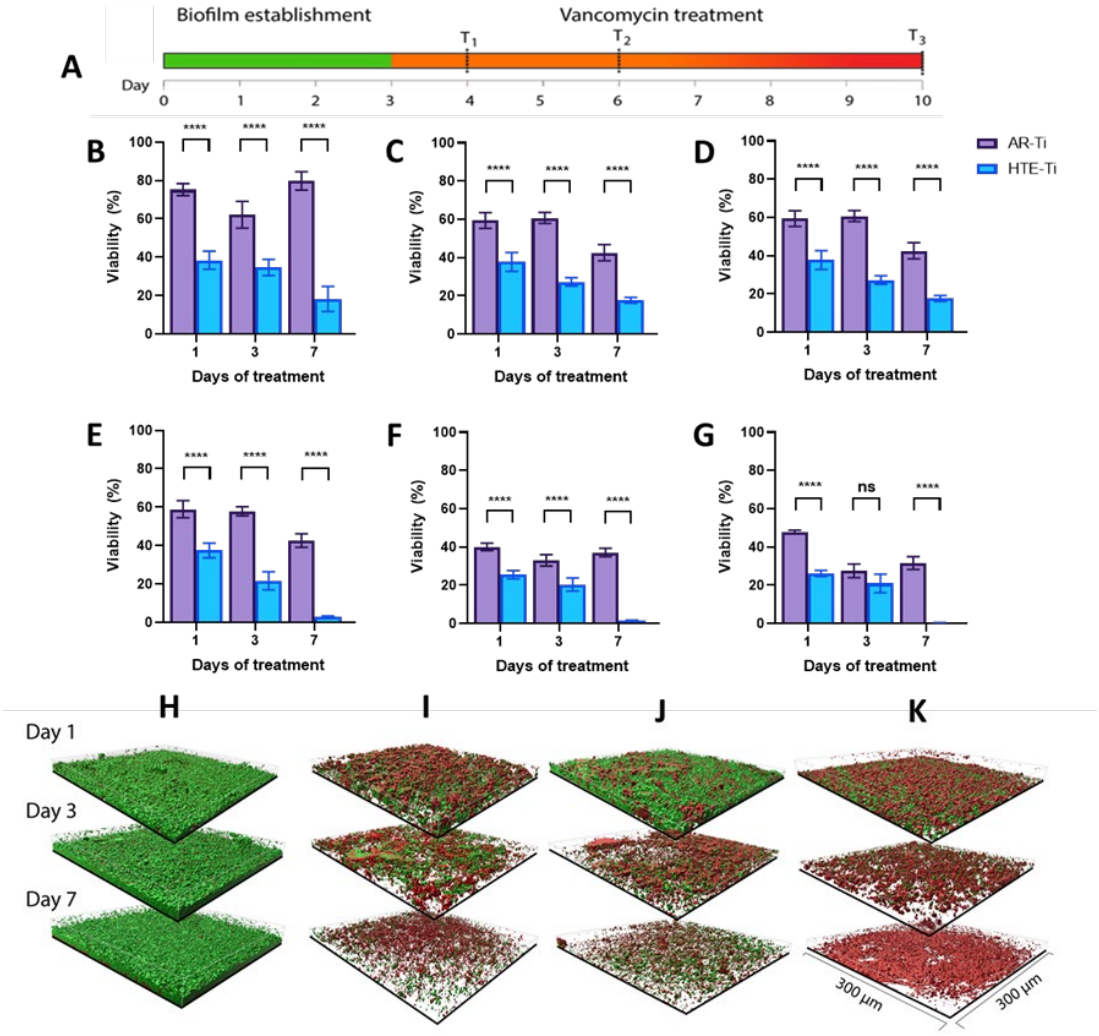

Figure 2. *Mature S. aureus biofilm was treated with vancomycin for 7 days. An illustrated timeline of biofilm establishment (first 3 days) and the follow-up treatment of days (A). Time course viability study of S. aureus in the absence of vancomycin (B), or vancomycin at 5 µg/mL (C), 25 µg/mL (D), 50 µg/mL (E), 75 µg/mL (F) or 100 µg/mL (G). 3D Z-stack representations of biofilm viability during treatment course on AR-Ti and HTE-Ti without vancomycin treatment (H and I), and with 75 µg/mL (J and K). **** represents p < 0.0001 and ns = non-significant. All data represent mean ± SD and n = 3.*

Cell morphology was analyzed using SEM (Figure 3, Figure S7 and Figure S8). On the AR-Ti surface, without vancomycin, there was a noticeable presence of deposited EPS and cells appeared to have a typical smooth coccoid morphology indicative of mature biofilm formation (Figure 3A). In the presence of 75 µg/mL vancomycin, a small proportion of cells appeared flaccid or shrivelled (Figure 3B). On the HTE-Ti surface, without vancomycin, the lack of EPS and evidence of fragmentation in the remaining cells suggests inhibited biofilm formation due to the antimicrobial effects of the surface (Figure 3C). After treatment with 75 µg/mL vancomycin, the cells on the HTE-Ti surface appeared predominately shrivelled and wrinkled (Figure 3D). Further, debris from lysed cells appeared to be sunken into the nanostructured surface consistent with the contact-killing mechanisms reported for these types of surfaces. [10, 26] This study of cell morphologies under different conditions using SEM confirms the cell viability analysis presented in Figure 2.

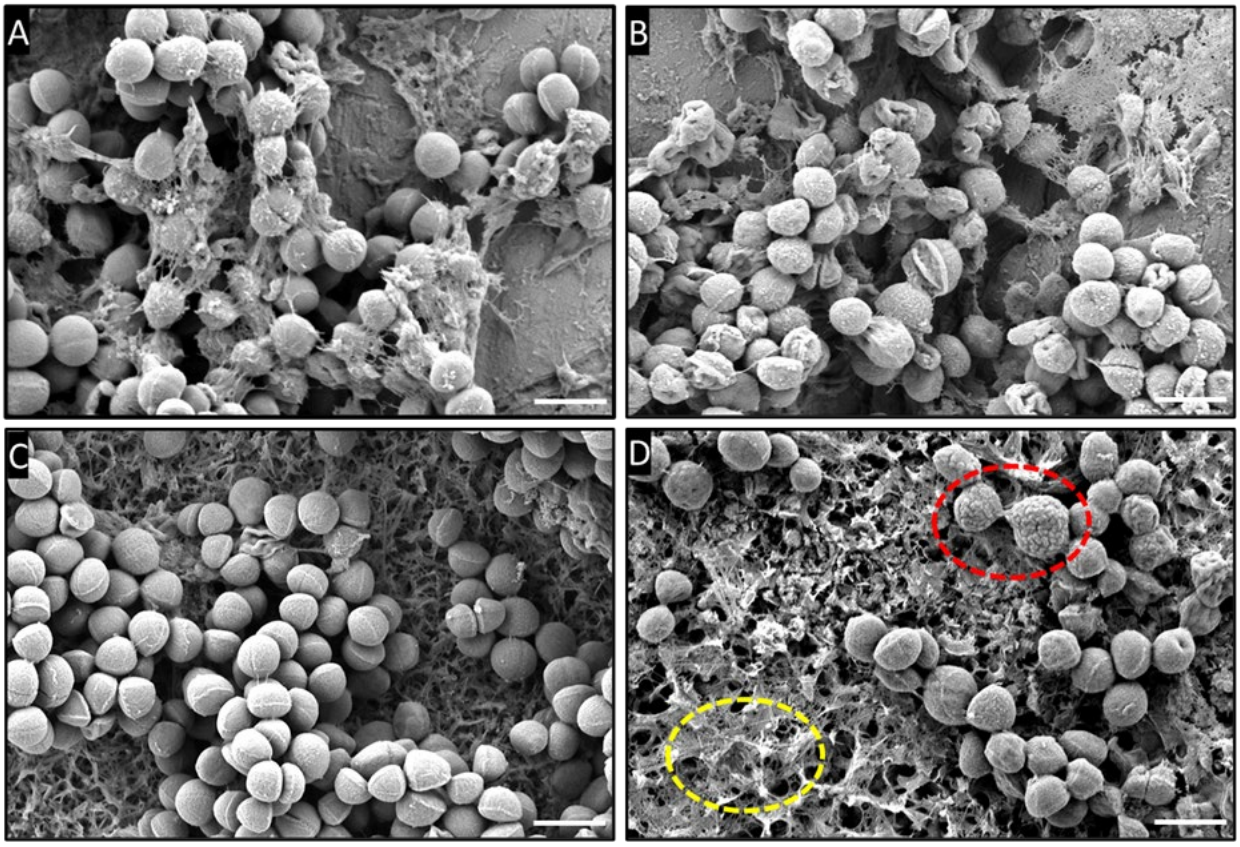

Figure 3. *SEM analysis of S. aureus after 7 days incubation on AR-Ti without vancomycin (A) and treated with 75 µg/mL vancomycin (B), and HTE-Ti without vancomycin (C) and treated with 75 µg/mL vancomycin (D). The red dashed circle highlights an example of shrivelled morphology, and the yellow dashed circle highlights cell debris between nanostructures. Scale bars = 1 µm. Further, SEM micrographs are provided in Supplementary Figure S7 & Figure S8.*

5.4.4 Mechanism of Improved Vancomycin Efficacy

Next, we questioned whether the improved vancomycin efficacy is simply due to the lower number of viable bacteria adhered to the HTE-Ti surface or whether there is synergistic activity between antibiotic treatment and physical features of the bactericidal surface on adhered bacteria viability. Our first hypothesis was that bacteria that have not already been killed by day 3 due to contact with the sharp surface nanostructures, may still have damaged cell walls, and thus be more susceptible to antibiotic treatment compared to those on the AR-Ti surface.

To investigate this, we generated cross-sections of *S. aureus* incubated on both surfaces and imaged them using SEM (Figure 4). On the AR-Ti surface, the *S. aureus* cells appeared undisturbed and free of any deformation. In contrast, on the HTE-Ti surface, the adhered *S. aureus* cell morphologies appeared severely distorted against the nanostructures beneath them. Therefore, it is conceivable that the mechanical interaction between the nanostructured surface and *S. aureus,* causing the cells to become significantly distorted, results in sufficient cell wall damage, to allow vancomycin to bind with D-Ala-D-Ala in the exposed peptidoglycan. Cell wall damage may then promote the cell to reinforce its peptidoglycan layer, allowing for additional vancomycin binding during biosynthesis. [16, 27]

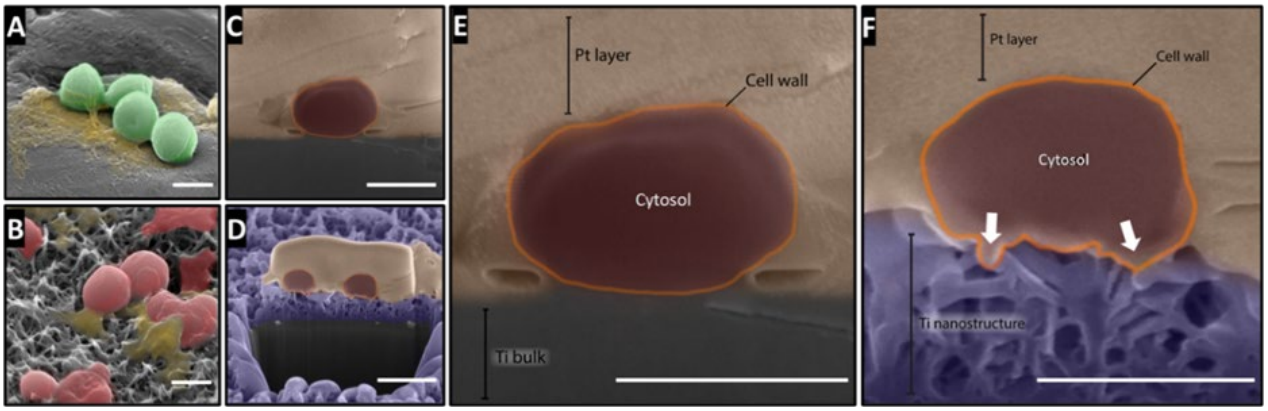

Figure 4. *Influence of surface morphology at the nanoscale on the bacterial cell wall. 'False' coloured FIB-SEM analysis of S. aureus on AR-Ti A) and HTE-Ti B) imaged at 52° stage tilt. In cross-sections of S. aureus on AR-Ti (C and E) and HTE-Ti (D and F), white arrows highlight cell wall deformation. Scale bars = 500 nm. Refer to Figure S9 for non-coloured original images.*

Our second hypothesis was that oxidative stress associated with cell wall deformation was amplified by the presence of vancomycin and that this could account for the excess cell death on the HTE-Ti surface. To investigate this, we first used a ROS-Glo kit to measure the presence of H_2O_2 in *S. aureus* on the AR-Ti and HTE-Ti surfaces (Figure 5A – Figure 5C).

Without vancomycin treatment, cells on the HTE-Ti surface showed a 21% increase in H_2O_2 concentration compared to cells on the AR-Ti surface on day 1 (p = 0.008). However, by day 3, the H_2O_2 concentration was identical between both surfaces, and it remained equal for the remainder of the study. When the cells were treated with vancomycin, the H_2O_2 concentration was identical between both surfaces for the first 3 days, but by day 7, it was 18% higher on the HTE-Ti surface (p = 0.03). These data follow the trend in cell viability presented in Figure 2. It should be noted that during the first 3 days of vancomycin treatment at 75 µg/mL (Figure 2F), the viability of *S. aureus* on the HTE-Ti surface remained unchanged, but by day 7, the entire biofilm had been eradicated. This timeline corresponds to the increase in H_2O_2 concentration on HTE-Ti.

To generate further insights into these results, we performed gene expression analysis targeting *katA*, a gene that encodes the catalase enzyme in *S. aureus* (Figure 5D and Figure 5E). Catalase is responsible for converting H_2O_2 into H_2O and O_2 to mitigate oxidative stress exposure. We analyzed the expression of *katA* on the samples collected on day 7, as the viability analysis suggested that day 7 was the critical point at which cells were eradicated on HTE-Ti but remained viable on AR-Ti. In the absence of vancomycin, *katA* had a 50% upregulation on the HTE-Ti compared to the AR-Ti (Figure 5D). This is unsurprising as it has been established that oxidative stress is induced when *S. aureus* is incubated on a mechano-bactericidal surface. [14] However, there was no detectable *katA* expression on the vancomycin-treated samples (Figure 5E). This is consistent This is consistent with the known role of vancomycin to downregulate *katA* in *S. aureus*.[40]

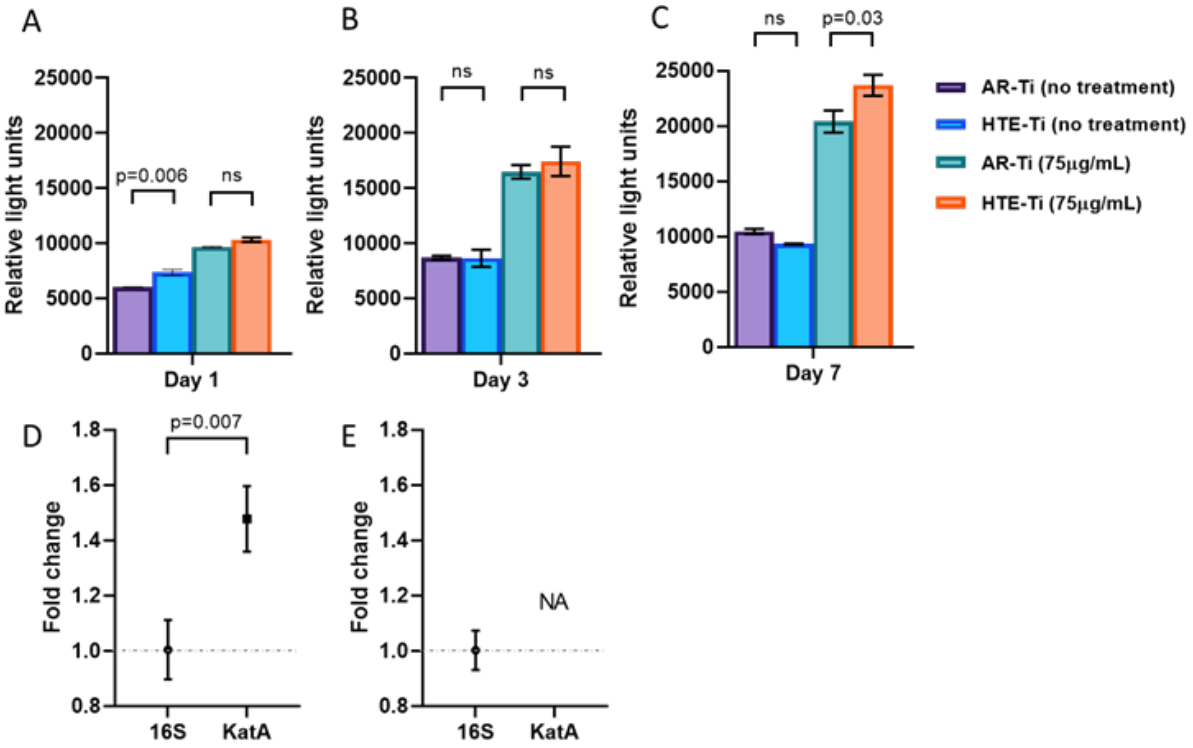

Figure 5. *Intracellular oxidative stress response. Luminescence measurements proportionate to H_2O_2 concentration at days 1, 3 and 7 (A, B, and C, respectively). Relative gene expression of katA after 7 days on untreated HTE-Ti samples (D) and samples treated with vancomycin at 75 µg/mL (E). NA = not available because there was no expression detected. All data graphed as mean ± SD and n = 3.*

When the relative gene expression results are connected with the ROS-Glo and viability assays, a plausible mechanism for antibacterial synergy begins to emerge (Schematic 1). The mechanical interaction between *S. aureus* and the nanostructures provides a constant stimulus that induces the formation of ROS. To counter this oxidative stress, *S. aureus* upregulates the expression of *katA*. In the absence of vancomycin, the enzyme appears to be sufficient to minimize ROS levels, as is evident by the ROS-Glo analysis. However, when *S. aureus* is treated with vancomycin, the cell catalase response is impeded, leading to two important consequences. Firstly, the mechanically induced ROS generation becomes unmasked as catalase is no longer able to eliminate H_2O_2. Secondly, the presence of vancomycin itself further causes oxidative stress by its own mechanism, [28] which is independent of the nanostructured surface. These two factors help to explain the synergistic antibacterial action between vancomycin and the HTE-Ti surface. Beyond this, the deformed cell wall observed by the cross-sectional analysis in Figure 4 suggests that vancomycin may be able to bind to exposed D-Ala-D-Ala between the layers of peptidoglycan more easily. As cell wall stress triggers the cell to reinforce peptidoglycan, [29] this may allow for an opportunity for further vancomycin binding, which prevents cell wall reinforcement by inhibiting cross-linkage between peptidoglycan layers. [17]

5.5 CONCLUSIONS

Recently, considerable focus has been directed toward research and development of mechano-bactericidal surface modifications to protect medical devices from bacterial colonization. While these surfaces have shown promising *in vitro* bactericidal activity, alone, they are unable to kill 100% of bacterial cells upon contact, and a proportion of viable bacteria typically remain. In the present study, we have demonstrated that the remaining cells can be effectively eliminated by vancomycin at sub-clinical dosages, [25] and the combined antibacterial activities of vancomycin and the titanium nanostructures on the HTE-Ti surface appear to be synergistic.

We have provided evidence of enhanced oxidative stress and changes in *katA* expression associated with this dual-antibacterial strategy. Based on these findings, we have proposed a mechanism for this antibacterial synergy, involving enhanced oxidative stress, and impeded defences of the bacterial cell against ROS and cell wall damage. Antibiotic prophylactic and post-surgical treatments will likely remain the predominant clinical means to fight infections.

In this context, this study is important because it demonstrates that nanoengineered antibacterial surfaces can improve the efficacy of antibiotics, and in this way, decrease major side effects from high-dose antibiotics and ease the burden of devastating implant-associated infections.

5.6 Experimental Section

5.6.1 Fabrication of TI6AL4V Nanostructured Surface

Coupons of Ti6Al4V (discs 10 mm in diameter and 3 mm in height) were mirror-polished and etched in a stainless-steel reactor (Parr Instrument Company, USA), using 1M KOH aqueous solution. Based on preliminary optimization experiments to investigate the generation of distinct nanostructures, the reactor was kept sealed at 150 °C inside an oven for 4 h. After etching, the vessels were cooled down in flowing water and the samples were rinsed and immersed in ultrapure water, and then dried. Next, the discs were heat treated inside a tubular furnace and cooled down overnight until room temperature (RT). As-received Ti6Al4V discs were used as the control surface (AR-Ti) and the hydrothermally etched titanium surface (HTE-Ti) was the experimental surface. All samples were cleaned and sterilized at 121 °C for 20 min before use.

5.6.2 Surface Characterization

Scanning Electron Microscope (SEM), Atomic Force Microscopy (AFM), Energy-dispersive X-ray spectroscopy (EDX) and Wettability: The nanotopography of the AR-Ti and HTE surfaces was characterized using scanning electron microscopy (SEM) (Zeiss Merlin FEG-SEM, Zeiss, Jena, Germany) at 2KV, 4 mm working distance with magnifications ranging from 5 K to 50 K. Samples were tilted to 45° in the SEM, where an oblique view reveals additional information about the nanotopography that cannot be assessed from a top-down perspective. The nanostructures upon the HTE-Ti surface were assessed for height, diameter and spacing between nanostructures. The height of the nanostructures was calculated using the distance between a perpendicular plane and the highest point of each spike, and the diameter was measured at mid-height in parallel orientation with the basal plane. The measurements for spike height were corrected for the 45° stage tilt. [1] The spacing between nanostructures was analyzed by measuring the density of nanostructure tips in a 5 μm^2 field. Analysis was performed using ImageJ software v1.53a (NIH, USA).

The AR-Ti and HTE-Ti surfaces were further characterized using atomic force microscopy (AFM). Data acquisition for 5 μm^2 surface area scans was achieved using a JPK NanoWizard III (JPK BioAFM, Berlin, Germany) with instrument-specific software, written in Linux Ubuntu, version 5 (Canonical Ltd., London, United Kingdom). A silicon nitride cantilever (NT-MDT NSG03) with a conical tip with a radius < 10 nm and a half side angle of 18° (Spectrum Instruments Ltd, Moscow, Russia) was used to perform amplitude modulation and tapping mode scans on AR-Ti and HTE-Ti surfaces. Calibration of the cantilever on a glass microscope slide resulted in a deflection sensitivity of 86.8 kHz and a spring constant of 1.9 N/m.

Scanning parameters were held constant at a set point of 22.8 nm and a drive amplitude of 0.3 V, over a scan rate of 0.8 Hz. Average Roughness (Ra), root mean square (RMS) roughness, surface area (SA) and 3-D reconstructions were acquired using Gwyddion data analysis software version 2.54. (http://gwyddion.net/)

HTE-Ti samples were loaded into an FEI DualBeam FIB-SEM (Thermo Scientific, MA, USA) equipped with a silicon drift energy dispersive x-ray spectroscopy detector. The stage was stage tilted 52° before ion beam milling. The surface was milled to reveal the oxide surface layer and sub-surface material, using a gallium ion beam at an accelerated voltage of 10 kV, a working distance of 4 mm and a beam current of 2.6 nA and 0.46 nA. Spectra were obtained, using “spot” mode at 10 kV, 0.17 nA, a working distance of 4 mm and 30 K magnification, using AZTEC EDS software version 3.1 (Oxford Instruments, Oxfordshire, UK).

The wettability or water contact angle (WCA) of the AR-Ti and HTE-Ti samples was measured using a contact angle goniometer model RD-SDM02 (RD Support, Scotland, United Kingdom), to determine surface wettability. Both AR-Ti and HTE-Ti samples were placed on a flat surface to receive a 4 µL aliquot of Milli-Q water and the WCA was measured within 20 s using the sessile drop analysis. Contact angles were measured for five randomly placed drops on triplicate samples. A contact angle above 90° is deemed to have poor wetting and is termed hydrophobic. Conversely, a contact angle below 90°, is described as hydrophilic. [2]

5.6.3 Cytocompatibility and Morphology

To assess short-term cytocompatibility and cellular morphology upon the HTE-Ti surface, RAW 264.7 murine macrophage-like cells (ATCC® TIB-71™, VA, USA) were used, as macrophages are one of the first mammalian cell types to adhere and respond to biomaterials upon implantation. RAW 264.7 macrophage-like cell cultures were maintained in Dulbecco’s Modified Eagle Medium supplemented with 10% v/v fetal bovine serum (FBS; Life Technologies, California, USA), 1% penicillin (100 U mL^{-1}) and streptomycin (100 µg mL^{-1}) (Life Technologies, California, USA) at 37 °C and 5% CO_2 with 95% humidity. RAW 264.7 macrophage-like cells were seeded at 2.5 x 10^5 cells/well in a 48-well plate and incubated for 72 h at 37 °C and 5% CO_2. LDH-Glo™ Cytotoxicity Assay (Promega, WI, USA), detects extracellular lactate dehydrogenase (LDH), a marker of cytotoxicity, released in tissue culture media upon disruption of the cell membrane. [3-4] Following the manufacturer's instructions LDH was quantified by combining 50 µL of cell culture supernatant and 50 µL of LDH detection reagent in a 96-well opaque plate (Corning, MA, USA), mixed and incubated at RT for 30 min. Luminescence was then read on a Synergy HTX multi-mode microplate reader (Biotek, VT, USA). Readings were normalized to cells grown on a tissue culture plate (TCP). RAW 264.7 murine macrophage-like cells, incubated on AR-Ti and HTE-Ti samples (72 h at 37 °C and 5% CO_2), cells were fluorescently stained with TRITC-conjugated Phalloidin and DAPI (Millipore, MA, USA) to observe the cellular structures, actin cytoskeleton and nuclei.

After samples were fixed, and permeabilized with 0.1% Triton x-100, they were stained with TRITC-conjugated Phalloidin (60 ng/mL; Ex/Em 540/565 nm) and DAPI (100 ng/mL; Ex/Em 358/461 nm). Samples were inverted onto a glass coverslip and imaged by an Olympus FV3000 confocal laser scanning microscope (CLSM; Olympus, Tokyo, Japan).

5.6.4 Cultures and Conditions

Isolate colonies of *Staphylococcus aureus* (ATCC 25923) were aseptically transferred from tryptone soy agar (TSA) to 10 mL of tryptone soy broth (TSB) and incubated until late-log phase (approx. 18 h) at 37 °C. Cell concentration was measured by absorbance at 600 nm in the cuvette reader of a NanoDrop™ 2000c (ThermoFisher, MA, USA), and the optical density was adjusted to 1 (approx. 1 x 10^9 CFU/mL) by dilution.

5.6.5 MIC Establishment

The minimum inhibitory concentration (MIC) of vancomycin was established according to CLSI standards (CLSI 2012). Briefly, an overnight culture of *S. aureus* (ATCC 25923) was inoculated to a final concentration of 5 x 10^5 CFU/mL into the wells of a 96-well microtiter plate (Sarstedt, Nümbrecht, Germany) containing cation-adjusted Mueller-Hinton broth (CAMHB; ThermoFisher, MA, USA) supplemented with vancomycin (Sigma, MI, USA) at two-fold decreasing concentrations from 64 to 0.0625 µg/mL. MIC was determined to be the lowest concentration at which there was no absorbance (600 nm) reading greater than the background reading. The protocol was repeated with tryptic soy broth TSB; ThermoFisher, MA, USA) supplemented with 5% v/v fetal bovine serum (TSBFBS) to verify that the vancomycin activity was comparable across both growth media.

5.6.6 Surface Inoculation and Vancomycin Treatment

Sterile AR-Ti and HTE-Ti (Ti6Al4V) discs (10 mm^2) were placed into the wells of a 24-well tissue culture plate (Sarstedt, Nümbrecht, Germany). Each disc surface was inoculated with 50 µL of the preculture of *S. aureus* containing 10^6 CFU. The discs were incubated for 3 h at 37 °C in a humid chamber to allow for cell adhesion. The discs were then immersed in 1 mL of TSBFBS and placed back in the incubator. The samples were incubated for 3 days, and the growth media was replaced every 24 h. After 3 days of biofilm establishment the samples were treated with TSBFBS supplemented with the relevant concentrations of vancomycin, media plus vancomycin replaced every 24 h for a further 7 days.

5.6.7 Live/Dead® Baclight™ Biofilm Viability Assay

At each of the 3 time points the biofilm samples were stained with Live/Dead®BacLight™ (Invitrogen, MA, USA). Samples representing each condition were transferred to a fresh 24-well tissue culture plate and immersed in a solution containing equal proportions of Syto9 and Propidium Iodide (PI) at 1.5µL/mL in phosphate-buffered saline (PBS).

Syto9 permeants to all cells, and stains nucleic acid green; PI stains nucleic acid red, but it is impermeant to the cell membrane, thus it only stains cells with damaged cell walls. The samples were incubated for 15 min at RT in the dark. The biofilm of each sample was imaged with an Olympus FV3000 CLSM (Olympus, Tokyo, Japan) immediately after staining. The CLSM was set up to image simultaneously the live cells green (Syto9, Ex/ Em 480/500 nm) and dead cells red (PI, Ex/Em 490/635 nm), using a dual emission filter. Random triplicate areas of the biofilm samples were chosen for the generation of three-dimensional Z-stack images. The viability of biofilm samples was determined by importing the Z-stack images into Imaris 3D analysis software (Version 9.3.0, Bitplane, Zürich, CHE) and using the 'spots' tool to quantify numbers of green and red fluorescent spots with a diameter of approximately 1 µm. Colony forming determination (CFU) and log reduction data (Figure S4) were done as previously reported.[5-6] Briefly, discs were vortexed for 15 s, followed by 2 min sonication then vortexed for a further 15 s, and serially (1:10) diluted. Serially diluted samples (10 µL), in triplicate, were dropped onto TSA plates and incubated for 18 h at 37 °C. The following day, colonies were counted, and CFUs determined. Log reduction was determined using the subsequent formula; $\text{Log}_{10}\left(\frac{AR-Ti}{HTE-Ti}\right)$. SEM confirmed the complete removal of bacteria by this method.

5.6.8 ROS-GLO™ H_2O_2 Quantification

Inoculation and vancomycin treatment were carried out with the same protocol as the viability assay described above, except the samples were immersed in 200 µL media in 48-well plates (Sarstedt, Nümbrecht, Germany). Before measurement at each time point, the growth media was discarded and replenished to a total volume of 200 µL, with supplemented ROS-Glo™ H_2O_2 Assay (Promega, WI, USA) substrate according to the manufacturer's protocol. The plate was placed back in the incubator for a further 6 h to allow for the substrate to react with H_2O_2 to generate and accumulate the luciferin precursor. The discs were then aseptically removed from the plates and placed in 500 µL RNA*later* (Ambion, TX, USA) to be stored at -30 ˚C for later qPCR analysis. The remaining culture media was transferred to a 96-well white flat bottom microtiter plate (Corning, MA, USA) in duplicate 100 µL aliquots. The ROS-Glo™ Detection Solution was mixed with each well according to the manufacturer's protocol. The plate was incubated for 20 min in the dark at RT and then the luminescence signal was read by a Synergy HTX plate reader (BioTek, VT, USA) using an integration time of 1 s and a settling time of 0.15 s.

5.6.9 RNA Extraction and Quantitative Real-Time PCR

Cells were detached from AR-Ti and HTE-Ti samples by sonication for 2 min followed by a 30 s pulse on a vortex in a 5 mL tube. The resultant cell suspension was pelleted at 12,000g for 5 min and the supernatant was discarded. The pellet was resuspended in the lysis buffer provided in the RiboPure RNA Purification Kit (Invitrogen, MA, USA). The RNA extraction was carried out according to the manufacturer's instructions.

Quantity and purity of RNA were determined using a NanoDrop 2000c Spectrophotometer (ThermoFisher, MA, USA). PCR master mixes were assembled using the SuperScript III Platinum One-Step qRT-PCR Kit (Invitrogen, MA, USA). Primers were added at a concentration of 10 µM. Template RNA (1ng) was added to each reaction in 1 µL aliquots. No-template control received 1 µL of RNAse-free H_2O in its place. Reverse transcription and amplification were carried out in 1 step in a Rotor-Gene Q Thermocycler (version 2.1.0, QIAGEN, Hilden, Germany) with the program: 3 min at 50 °C; 5 min at 95 °C; 40 cycles of 95 °C for 15 s and 60 °C for 30 s. The signal was acquired at 60 °C. A melt curve was generated at 1° intervals between 72 and 95 °C. Amplification specificity was verified by melting curve analysis. The *katA* qPCR data were normalized to the *16S* internal reference gene. The normalized data were used to calculate fold-change expression between HTE-Ti and AR-Ti using the Livak method ($2^{-\Delta\Delta Ct}$). [7] Primer sequences for *katA* and *16S* are presented in Table S1.

5.6.10 Scanning Electron Microscopy (SEM)

Another set of AR-Ti and HTE-Ti samples was inoculated and treated identically and in parallel to those used in the viability analysis. At each time point, samples from this set of discs were transferred to a fixative solution of PBS containing 1.25% glutaraldehyde, 4% paraformaldehyde and 4% sucrose for 1h. Samples were then gently washed in PBS and dehydrated in a series of increasing concentrations of ethanol (50, 70 and 100% v/v) for 10 min at each step, followed by a 1:1 mixture of pure ethanol and hexamethyldisilazane (HMDS, Sigma-Aldrich, MA, USA) for 20 min and finally 100% HMDS for 20 min. AR-Ti and HTE-Ti samples were left to dry in a fume cabinet for 2 h, mounted on aluminium stubs using double-sided carbon tape and then sputter-coated with 2 nm of platinum. Samples were imaged with a Zeiss Merlin FEG-SEM, (Microscopy Australia, University of South Australia; Zeiss, Jena, Germany) at an accelerating voltage of 2 kV, a secondary electron detector, a working distance of 4.5 mm and magnifications ranging from 5K to 25K magnifications.

5.6.10 Focused Ion Beam (FIB) Milling

Dual-focused ion beam-scanning electron microscopy (FIB-SEM) is a powerful method for *in-situ* cross-sectional sample preparation and imaging, visualizing the interaction of the bacteria-titanium interface. [8] AR-Ti and HTE-Ti samples incubated with *S. aureus* for 18 h, were loaded into an FEI DualBeam FIB-SEM (Thermo Scientific, MA, USA), and the stage was tilted to 52°, with a working distance of 4 mm under high vacuum conditions.

Before ion beam milling, bacteria of interest were coated with platinum (1µm), to protect the nanomorphology using an accelerated voltage of 10 kV and a 0.46 nA current. Cross sections were then milled with a focused ion beam (gallium) at a depth of 5 µm with an accelerated voltage of 10 kV and a 2.6 nA current, followed by a current of 0.46 nA for further refinement.

SEM images of the cross-section exposing the interface between bacteria and titanium surface (AR-Ti and HTE-Ti), were acquired using an electron beam accelerating voltage of 10 kV, 0.17 nA, SE mode and a working distance of 4 mm.

5.6.11 Statistical Analysis

Statistical analysis was performed using GraphPad Prism version 8.1.1.1 for Windows (GraphPad Software, La Jolla California USA, www.graphpad.com). Gene expression fold change and LDH viability data were analyzed using an unpaired t-test, and bacterial viability by multiple t-tests was corrected for multiple comparisons using the Holm-Sidak method. Lastly, ROS analysis was performed using one-way ANOVA corrected for multiple comparisons followed by Holm-Sidak posthoc analysis, with 95% confidence intervals. Significance levels were set at $p < 0.05$. All experimental procedures were performed in replicates (n = 3) and reported as mean ± standard deviation (SD).

5.7 Supporting Information

The Supporting Information is available free of charge at
https://pubs.acs.org/doi/10.1021/acs.nanolett.2c02182
Experimental methods, and supporting figures including titanium disc macro images (Figure S1) SEM micrographs (Figure S2), live/dead staining of *E. coli*, *P. aeruginosa*, *S. epidermidis* and *S. Aureus* (Figure S3), CFU data for *S. Aureus* (Figure S4), MIC of vancomycin against S. aureus (Figure S5), Z-stack rendered biofilm 3D-images of *S. aureus* biofilm treated with vancomycin for 7 days (Figure S6), further SEM images of *S. aureus* biofilm after 7 days incubation on AR-Ti treated with vancomycin (Figure S7 and S8), non-coloured original FIB cross-section images (Figure S9) and primers used in expression study (Table S1).

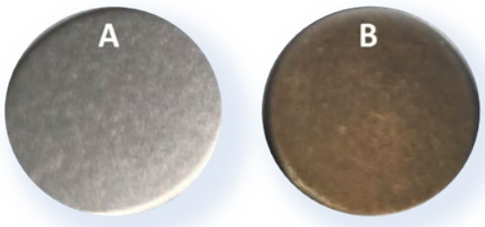

Figure S1. *Coupons of Ti6Al4V discs 10 mm in diameter and 3 mm in height, AR-Ti (A) and HTE-Ti (B).*

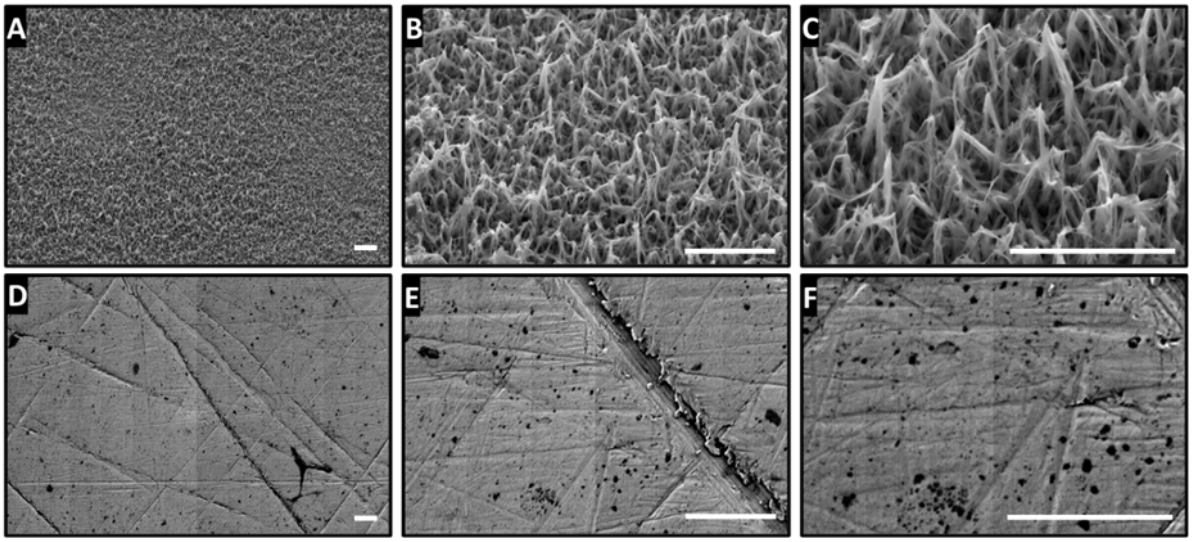

Figure S2. *SEM micrographs of HTE-Ti (A-C) and AR-Ti (D-F) were acquired at 45° stage tilt. Scale bar = 2 µm.*

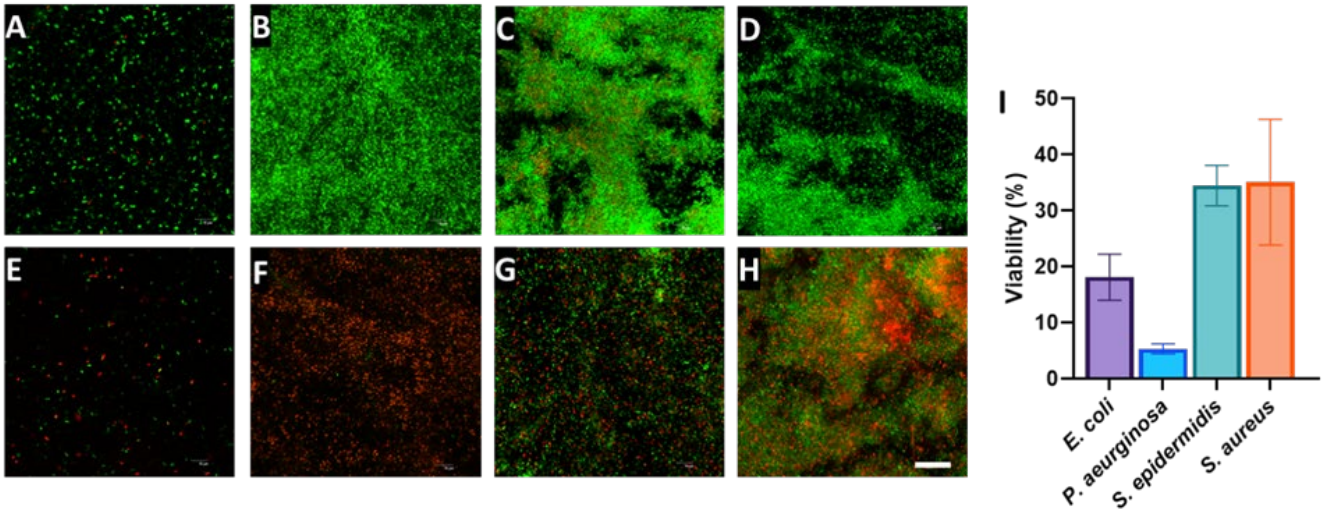

Figure S3. *Live/dead-stained confocal micrographs of E. coli (A and E), P. aeruginosa (B and F), S. epidermidis (C and G) and S. aureus (D and H). The top row represents bacteria incubated for 20 h on the AR-Ti surface, and the bottom row bacteria incubated for 20 h on the HTE-Ti surface. Scale bar in panel H = 20 µm. Viability determined from live/dead images for HTE-Ti, mean ± SD, n=3, (I).*

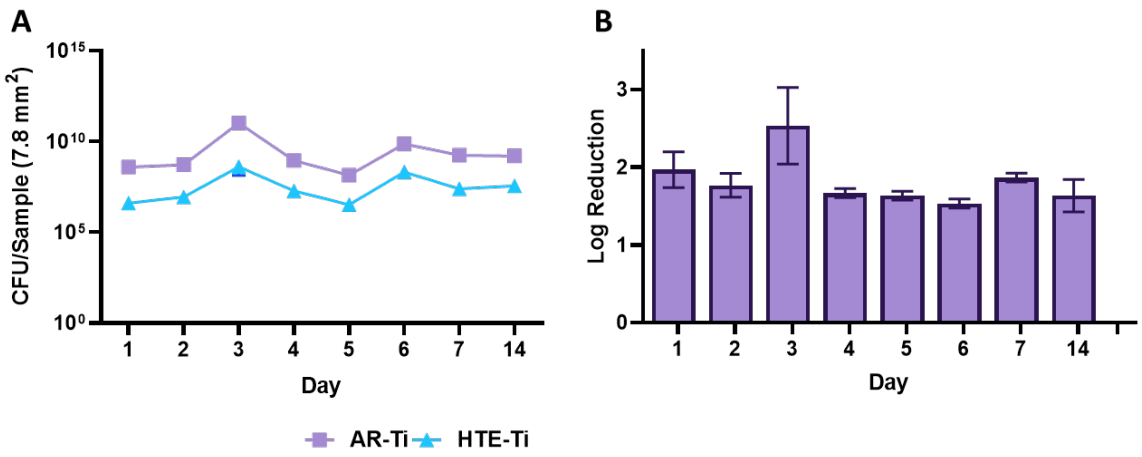

Figure S4. *Colony forming units (CFU) of S. aureus incubated on AR-Ti and HTE-Ti over 14 days (A). Log reduction of S. aureus incubated on AR-Ti and HTE surfaces over 14 days. Log Reduction of S. aureus incubated on HTE-Ti over 14 days, where log reduction = log10 (a/b) with a = AR-Ti CFU and b = HTE-Ti CFU. Reported as mean ± SD and n=3 (B).*

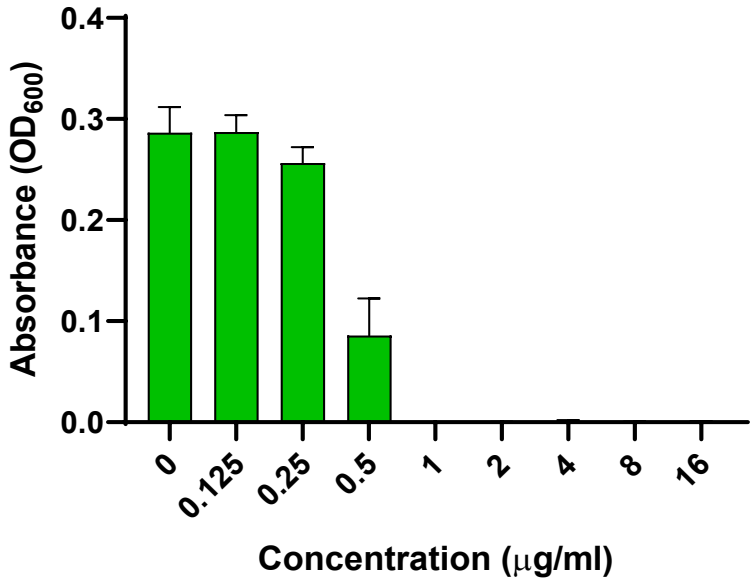

Figure S5. *MIC establishment of vancomycin against Staphylococcus aureus ATCC 25923.*

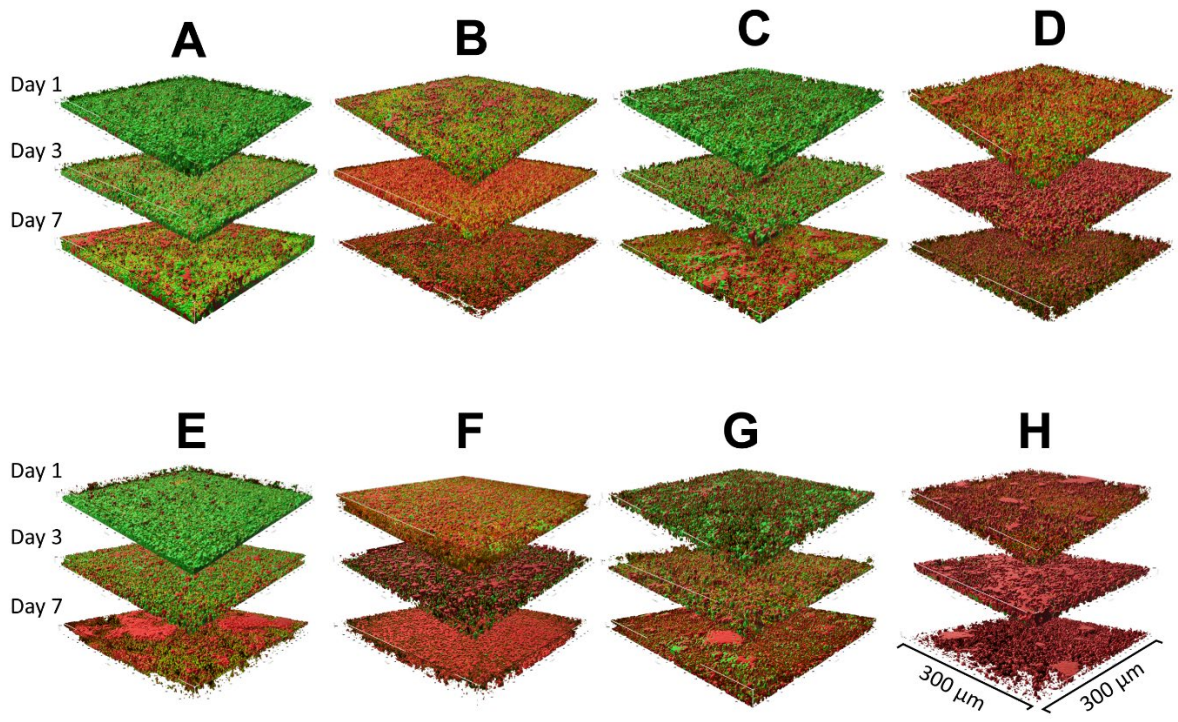

Figure S6. *Representative Z-stack rendered biofilm 3D images of S. aureus biofilm treated with vancomycin for 7 days. (A) = CTL, 5 µg/mL (B) = AM 5 µg/mL, (C) = CTL 25µg/mL, (D) = AM 25µg/mL, (E) = CTL 50 µg/mL, (F) = AM 50 µg/mL, (G) = CTL 100 µg/mL and (H) = AM 100 µg/mL.*

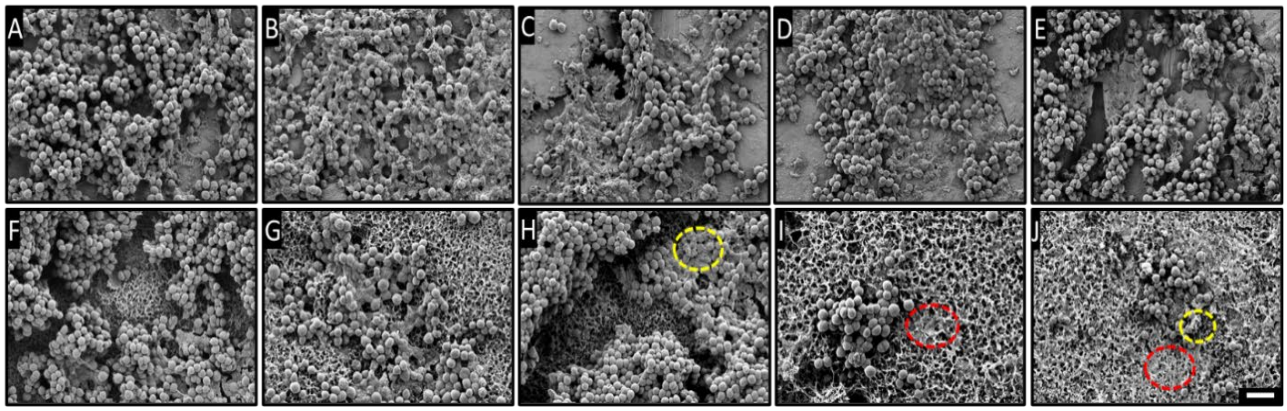

Figure S7. *SEM analysis of S. aureus biofilm after 7 days incubation on AR-Ti treated with no vancomycin (A), or 5 µg/mL (B), 25 µg/mL (C), 75 µg/mL (D) and 100µg/mL (E) vancomycin treatments, respectively. SEM micrographs of S. aureus incubated on HTE-Ti with no vancomycin (F), or 5 µg/mL (G), 25 µg/mL (H), 50 µg/mL, 75 µg/mL (I) and 100µg/mL (J) vancomycin treatments, respectively. Red dashed circles highlight an example of shrivelled morphology and yellow dashed circles highlight cell debris between nanostructures. Scale bar in the bottom right panel (J) = 2 µm.*

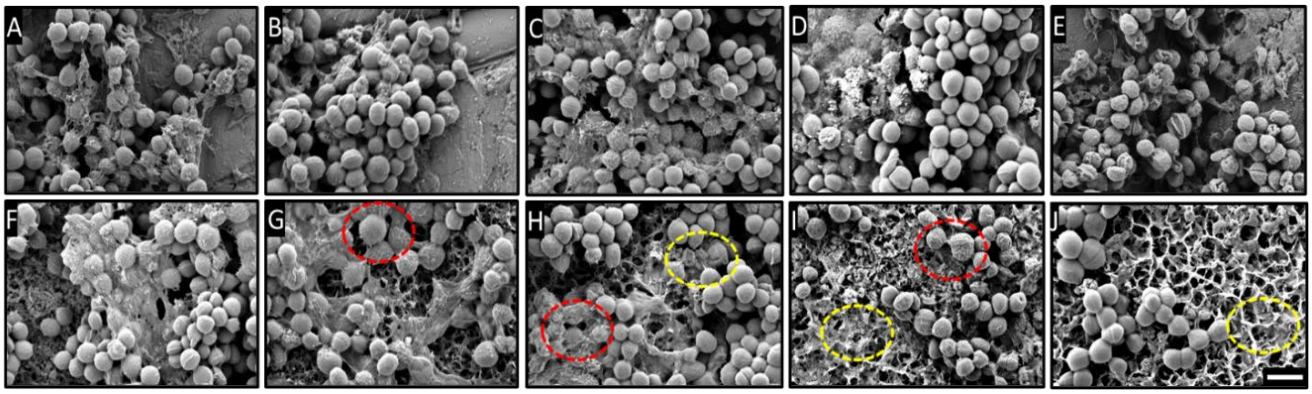

Figure S8. *Higher magnification SEM micrographs of S. aureus biofilm after 7 days incubation on AR-Ti treated with no vancomycin (A), or 5 µg/mL (B), 25 µg/mL (C), 75 µg/mL (D) and 100µg/mL (E) vancomycin treatments, respectively. SEM micrographs of S. aureus incubated on HTE-Ti with no vancomycin (F), or 5 µg/mL (G), 25 µg/mL (H), 50 µg/mL, 75 µg/mL (I) and 100µg/mL (J) vancomycin treatments, respectively. Red dashed circles highlight an example of shrivelled morphology and yellow dashed circles highlight cell debris between nanostructures. Scale bar in the bottom right panel (J) = 1 µm.*

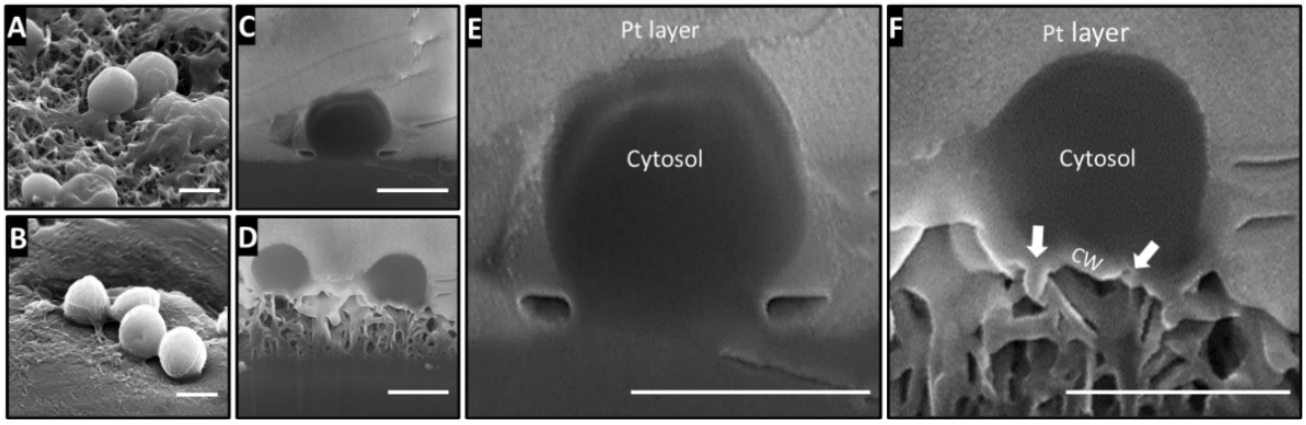

Figure S9. *Non-coloured original SEM images of S. aureus on AR-Ti (A) and HTE-Ti (B) imaged at 52° stage tilt. FIB Cross-sections of S. aureus on AR-Ti (C and E) and HTE-Ti (D and F). Scale bars = 500 nm, white arrows highlight cell wall deformation, Pt layer = platinum layer, CW = cell wall.*

Table S1. *Primers used in relative gene expression study.*

Gene target		Sequence (5' – 3')
16S [9]	F	ACGGTCTTGCTGTCACTTATA
	R	TACACATATGTTCTTCCCTAATAA
katA [10]	F	GGAGCGTGACATTCGAGGAT
	R	GACCCGTCCAGAAATCCCAG

5.8 REFERENCES

(1) Shi, Q.; Roux, S.; Latourte, F.; Hild, F.; Loisnard, D.; Brynaert, N. Measuring Topographies from Conventional Sem Acquisitions. Ultramicroscopy 2018, 191, 18-33.

(2) Yuan, Y.; Lee, T. R. Contact Angle and Wetting Properties. In Surface Science Techniques; Bracco, G.; Holst, B., Eds.; Springer Berlin Heidelberg: Berlin, Heidelberg, 2013; pp 3-34.

(3) Smith, S. M.; Wunder, M. B.; Norris, D. A.; Shellman, Y. G. A Simple Protocol for Using a Ldh-Based Cytotoxicity Assay to Assess the Effects of Death and Growth Inhibition at the Same Time. PLoS One 2011, 6 (11), e26908-e26908.

(4) Kaja, S.; Payne, A. J.; Naumchuk, Y.; Koulen, P. Quantification of Lactate Dehydrogenase for Cell Viability Testing Using Cell Lines and Primary Cultured Astrocytes. Curr Protoc Toxicol 2017, 72, 2.26.1-2.26.10.

(5) Bright, R.; Hayles, A.; Fernandes, D.; Visalakshan, R. M.; Ninan, N.; Palms, D.; Burzava, A.; Barker, D.; Brown, T.; Vasilev, K. In Vitro Bactericidal Efficacy of Nanostructured Ti6al4v Surfaces Is Bacterial Load Dependent. ACS Appl Mater Interfaces 2021, 13 (32), 38007-38017.

(6) Naghili, H.; Tajik, H.; Mardani, K.; Razavi Rouhani, S. M.; Ehsani, A.; Zare, P. Validation of Drop Plate Technique for Bacterial Enumeration by Parametric and Nonparametric Tests. Vet Res Forum 2013, 4 (3), 179-183.

(7) Livak, K. J.; Schmittgen, T. D. Analysis of Relative Gene Expression Data Using Real-Time Quantitative Pcr and the 2(-Delta Delta C(T)) Method. Methods 2001, 25 (4), 402-8.

(8) Antoniou, N.; Rykaczewski, K.; Uchic, M. D. In Situ Fib-Sem Characterization and Manipulation Methods. MRS Bulletin 2014, 39 (4), 347-352.

(9) Johnson, E. J.; Zemanick, E. T.; Accurso, F. J.; Wagner, B. D.; Robertson, C. E.; Harris, J. K. Molecular Identification of Staphylococcus Aureus in Airway Samples from Children with Cystic Fibrosis. PLOS ONE 2016, 11 (1), e0147643.

(10) Kadiyala, U.; Turali-Emre, E. S.; Bahng, J. H.; Kotov, N. A.; VanEpps, J. S. Unexpected Insights into Antibacterial Activity of Zinc Oxide Nanoparticles against Methicillin Resistant Staphylococcus Aureus (Mrsa). Nanoscale 2018, 10 (10), 4927-4939.

Author Contributions

R.B., K.V., D.B., and T.B. conceptualized, designed, and planned the study. R.B. and A.H. performed experiments and analyzed and interpreted the data. R.B., A.H., and K.V. wrote and revised the paper. J.W. and D.P. performed the surface characterization and participated in data analysis. K.V. supervised the study. All authors have read and agreed to the published version of the manuscript.

Notes

The authors declare no competing financial interest.

ACKNOWLEDGMENTS

This study was co-funded by the Department of Industry, Science, Energy and Resources (Innovative ManufacturingCRC Ltd) Global Orthopaedic Technology Pty Ltd (IMCRC/ GOT/130318). The authors acknowledge the funding and in-kind support from Corin Australia and the University of South Australia. The authors also acknowledge the instruments and scientific and technical assistance of Microscopy Australia at the University of South Australia, Mawson Lakes Campus, a facility that is funded by the University, and State and Federal Governments. K.V. thanks the NHMRC for Fellowship GNT1194466 and the ARC for grant DP180101254.

Data Availability Statement

The data that support the findings of this study are available from the corresponding author upon reasonable request.

5.9 REFERENCES

1 Montanaro, L. et al. Scenery of Staphylococcus implant infections in orthopedics. Future Microbiol 6, 1329-1349, doi:10.2217/fmb.11.117 (2011).

2 Fischbacher, A. & Borens, O. Prosthetic joint infections: mortality rate over the last ten years. Orthopaedic Proceedings 99-B, 40-40, doi:10.1302/1358-992X.2017.22.040 (2017).

3 Lenguerrand, E. et al. Risk factors associated with revision for prosthetic joint infection following knee replacement: an observational cohort study from England and Wales. Lancet Infect Dis 19, 589-600, doi:10.1016/s1473-3099(18)30755-2 (2019).

4 VanEpps, J. S. & Younger, J. G. Implantable Device-Related Infection. Shock 46, 597-608, doi:10.1097/SHK.0000000000000692 (2016).

5 Flemming, H.-C. et al. Biofilms: an emergent form of bacterial life. Nature Reviews Microbiology 14, 563-575, doi:10.1038/nrmicro.2016.94 (2016).

6 Olsen, I. Biofilm-specific antibiotic tolerance and resistance. European Journal of Clinical Microbiology & Infectious Diseases 34, 877-886, doi:10.1007/s10096-015-2323-z (2015).

7 Hansen, E. N., Zmistowski, B. & Parvizi, J. Periprosthetic joint infection: what is on the horizon? Int J Artif Organs 35, 935-950, doi:10.5301/ijao.5000145 (2012).

8 Widmer, A. F. New developments in diagnosis and treatment of infection in orthopedic implants. Clin Infect Dis 33 Suppl 2, S94-106, doi:10.1086/321863 (2001).

9 Vasilev, K., Cook, J. & Griesser, H. J. Antibacterial surfaces for biomedical devices. Expert Rev Med Devices 6, 553-567, doi:10.1586/erd.09.36 (2009).

10 Bright, R. et al. Long-term antibacterial properties of a nanostructured titanium alloy surface: An in vitro study. Materials Today Bio 13, 100176, doi: https://doi.org/10.1016/j.mtbio.2021.100176 (2022).

11 Bright, R. et al. In Vitro Bactericidal Efficacy of Nanostructured Ti6Al4V Surfaces is Bacterial Load Dependent. ACS Appl Mater Interfaces 13, 38007-38017, doi:10.1021/acsami.1c06919 (2021).

12 Linklater, D. P. et al. Mechano-bactericidal actions of nanostructured surfaces. Nat Rev Microbiol 19, 8-22, doi:10.1038/s41579-020-0414-z (2021).

13 Ivanova, E. P. et al. Natural bactericidal surfaces: mechanical rupture of Pseudomonas aeruginosa cells by cicada wings. Small 8, 2489-2494, doi:10.1002/smll.201200528 (2012).

14 Bhadra, C. M. et al. Antibacterial titanium nano-patterned arrays inspired by dragonfly wings. Scientific Reports 5, 16817, doi:10.1038/srep16817 (2015).

15 Ivanova, E. P. et al. Bactericidal activity of black silicon. Nat Commun 4, 2838, doi:10.1038/ncomms3838 (2013).

16 Das Ghosh, L., Hasan, J., Jain, A., Sundaresan, N. R. & Chatterjee, K. A nanopillar array on black titanium prepared by reactive ion etching augments cardiomyogenic commitment of stem cells. Nanoscale 11, 20766-20776, doi:10.1039/C9NR03424B (2019).

17 Jaggessar, A. et al. Mechanical, bactericidal and osteogenic behaviours of hydrothermally synthesised TiO(2) nanowire arrays. J Mech Behav Biomed Mater 80, 311-319, doi: 10.1016/j.jmbbm.2018.02.011 (2018).
18 Jaggessar, A. & Yarlagadda, P. Modelling the growth of hydrothermally synthesised bactericidal nanostructures, as a function of processing conditions. Mater Sci Eng C Mater Biol Appl 108, 110434, doi: 10.1016/j.msec.2019.110434 (2020).
19 Jenkins, J. et al. Antibacterial effects of nanopillar surfaces are mediated by cell impedance, penetration and induction of oxidative stress. Nat Commun 11, 1626, doi:10.1038/s41467-020-15471-x (2020).
20 Lin, N., Berton, P., Moraes, C., Rogers, R. D. & Tufenkji, N. Nanodarts, nanoblades, and nanospikes: Mechano-bactericidal nanostructures and where to find them. Adv Colloid Interface Sci 252, 55-68, doi: 10.1016/j.cis.2017.12.007 (2018).
21 Wang, F., Zhou, H., Olademehin, O. P., Kim, S. J. & Tao, P. Insights into Key Interactions between Vancomycin and Bacterial Cell Wall Structures. ACS Omega 3, 37-45, doi:10.1021/acsomega.7b01483 (2018).
22 Dengler, V., Meier, P. S., Heusser, R., Berger-Bächi, B. & McCallum, N. Induction kinetics of the Staphylococcus aureus cell wall stress stimulon in response to different cell wall active antibiotics. BMC Microbiology 11, 16, doi:10.1186/1471-2180-11-16 (2011).
23 Kohanski, M. A., Dwyer, D. J., Hayete, B., Lawrence, C. A. & Collins, J. J. A common mechanism of cellular death induced by bactericidal antibiotics. Cell 130, 797-810, doi:10.1016/j.cell.2007.06.049 (2007).
24 Hayles, A. et al. Hydrothermally etched titanium: a review on a promising mechano-bactericidal surface for implant applications. Materials Today Chemistry 22, 100622, doi:https://doi.org/10.1016/j.mtchem.2021.100622 (2021).
25 Clainche, T. L. et al. Mechano-Bactericidal Titanium Surfaces for Bone Tissue Engineering. ACS Applied Materials & Interfaces 12, 48272-48283, doi:10.1021/acsami.0c11502 (2020).
26 Pinotti, F. E., de Oliveira, G. J. P. L., Aroni, M. A. T., Marcantonio, R. A. C. & Marcantonio Jr, E. Analysis of osseointegration of implants with hydrophilic surfaces in grafted areas: A Preclinical study. Clinical Oral Implants Research 29, 963-972, doi:https://doi.org/10.1111/clr.13361 (2018).
27 Anitha, V. C., Banerjee, A. N., Joo, S. W. & Min, B. K. Morphology-dependent low macroscopic field emission properties of titania/titanate nanorods synthesized by alkali-controlled hydrothermal treatment of a metallic Ti surface. Nanotechnology 26, 355705, doi:10.1088/0957-4484/26/35/355705 (2015).
28 Kriegeskorte, A. & Peters, G. Horizontal gene transfer boosts MRSA spreading. Nature Medicine 18, 662-663, doi:10.1038/nm.2765 (2012).
29 McCarthy, H. et al. Methicillin resistance and the biofilm phenotype in Staphylococcus aureus. Frontiers in Cellular and Infection Microbiology 5, doi:10.3389/fcimb.2015.00001 (2015).

30 Arciola, C. R., Campoccia, D. & Montanaro, L. Implant infections: adhesion, biofilm formation and immune evasion. Nat Rev Microbiol 16, 397-409, doi:10.1038/s41579-018-0019-y (2018).

31 Ribeiro, M., Monteiro, F. J. & Ferraz, M. P. Infection of orthopedic implants with emphasis on bacterial adhesion process and techniques used in studying bacterial-material interactions. Biomatter 2, 176-194, doi:10.4161/biom.22905 (2012).

32 Liu, C. et al. Clinical Practice Guidelines by the Infectious Diseases Society of America for the Treatment of Methicillin-Resistant Staphylococcus aureus Infections in Adults and Children. Clinical Infectious Diseases 52, e18-e55, doi:10.1093/cid/ciq146 (2011).

33 Sendi, P. & Zimmerli, W. Antimicrobial treatment concepts for orthopaedic device-related infection. Clin Microbiol Infect 18, 1176-1184, doi:10.1111/1469-0691.12003 (2012).

34 Park, K. J., Chapleau, J., Sullivan, T. C., Clyburn, T. A. & Incavo, S. J. 2021 Chitranjan S. Ranawat Award: Intraosseous vancomycin reduces periprosthetic joint infection in primary total knee arthroplasty at 90-day follow-up. The Bone & Joint Journal 103-B, 13-17, doi:10.1302/0301-620X.103B6.BJJ-2020-2401.R1 (2021).

35 Tripathy, A., Sen, P., Su, B. & Briscoe, W. H. Natural and bioinspired nanostructured bactericidal surfaces. Advances in Colloid and Interface Science 248, 85-104, doi:https://doi.org/10.1016/j.cis.2017.07.030 (2017).

36 Kang, H.-K. & Park, Y. Glycopeptide Antibiotics: Structure and Mechanisms of Action. jbv 45, 67-78, doi:10.4167/jbv.2015.45.2.67 (2015).

37 Wang, Y. et al. Catalase Expression Is Modulated by Vancomycin and Ciprofloxacin and Influences the Formation of Free Radicals in Staphylococcus aureus Cultures. Appl Environ Microbiol 81, 6393-6398, doi:10.1128/AEM.01199-15 (2015).

38 Balibar, C. J. et al. cwrA, a gene that specifically responds to cell wall damage in Staphylococcus aureus. Microbiology (Reading) 156, 1372-1383, doi:10.1099/mic.0.036129-0 (2010).

39 Bright, R. et al. Bio-Inspired Nanostructured Ti-6Al-4V Alloy: The Role of Two Alkaline Etchants and the Hydrothermal Processing Duration on Antibacterial Activity. Nanomaterials (Basel) 12, doi:10.3390/nano12071140 (2022).

40 Shi, Q. et al. Measuring topographies from conventional SEM acquisitions. Ultramicroscopy 191, 18-33, doi:10.1016/j.ultramic.2018.04.006 (2018).

41 Yuan, Y. & Lee, T. R. in Surface Science Techniques (eds Gianangelo Bracco & Bodil Holst) 3-34 (Springer Berlin Heidelberg, 2013).

42 Smith, S. M., Wunder, M. B., Norris, D. A. & Shellman, Y. G. A simple protocol for using a LDH-based cytotoxicity assay to assess the effects of death and growth inhibition at the same time. PLoS One 6, e26908-e26908, doi:10.1371/journal.pone.0026908 (2011).

43 Kaja, S., Payne, A. J., Naumchuk, Y. & Koulen, P. Quantification of Lactate Dehydrogenase for Cell Viability Testing Using Cell Lines and Primary Cultured Astrocytes. Curr Protoc Toxicol 72, 2.26.21-22.26.10, doi:10.1002/cptx.21 (2017).
44 Naghili, H. et al. Validation of drop plate technique for bacterial enumeration by parametric and nonparametric tests. Vet Res Forum 4, 179-183 (2013).
45 Livak, K. J. & Schmittgen, T. D. Analysis of relative gene expression data using real-time quantitative PCR and the 2(-Delta Delta C(T)) Method. Methods 25, 402-408, doi:10.1006/meth.2001.1262 (2001).
46 Antoniou, N., Rykaczewski, K. & Uchic, M. D. In situ FIB-SEM characterization and manipulation methods. MRS Bulletin 39, 347-352, doi:10.1557/mrs.2014.58 (2014).

ACS APPLIED BIO MATERIALS

(IF 4.8)

Bright R, Hayles A, Wood J, Palms D, Barker D, Vasilev K. Interplay between Immune and Bacterial Cells on a Biomimetic Nanostructured Surface: A "Race for the Surface" Study. ACS Appl Bio Mater. 2023 Jun 29. doi: 10.1021/acsabm.3c00351. Epub ahead of print. PMID: 37384836.

CHAPTER 6:

THE INTERPLAY BETWEEN IMMUNE AND BACTERIAL CELLS ON A BIOMIMETIC NANOSTRUCTURED SURFACE – A 'RACE FOR THE SURFACE' STUDY

Richard Bright [1], Andrew Hayles [1], Jonathan Wood [2], Dennis Palms [1], Dan Barker [3] and Krasimir Vasilev [1,2] *

[1] College of Medicine and Public Health, Flinders University, Bedford Park, SA 5042, Australia.

[2] Academic Unit of STEM, University of South Australia, Mawson Lakes, Adelaide, SA 5095, Australia.

[3] Corin Australia, Sydney, NSW 2153, Australia

[*] Corresponding author email address: krasimir.vasilev@flinders.edu.au

Keywords

Competitive colonisation, antibacterial, biocompatible, macrophage, bioinspired

6.1 Graphical Abstract (TOC)

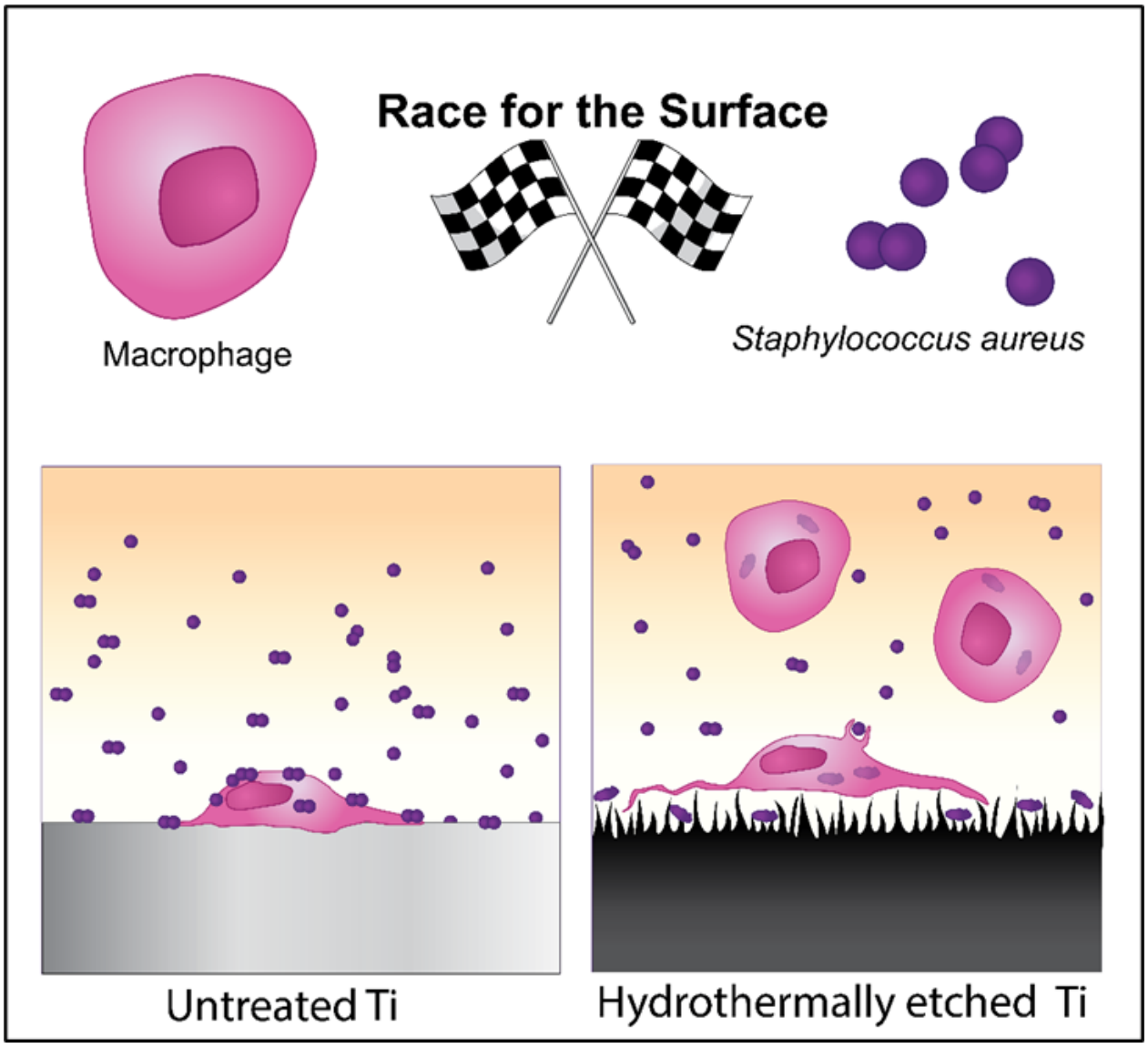

Schematic 1. We investigated the interaction between the Gram-positive pathogen *S. aureus* and a macrophage cell line on a nanostructured titanium surface – also known as the 'race for the surface', which is of key importance for successful medical device procedure outcomes. We showed that macrophages can outcompete Staphylococcus aureus on the nanostructured surface.

6.2 Abstract

Biomaterial-associated infection is an ever-increasing risk with devasting consequences for patients. Considerable research has been undertaken to address this issue by imparting antibacterial properties to the surface of biomedical implants. One approach that generated much interest over recent years was the generation of bioinspired bactericidal nanostructures. In the present report, we investigated the interplay between macrophages and bacteria on antibacterial nanostructured surfaces to determine the outcome of the so-called 'race for the surface'. Our results showed that macrophages - can indeed outcompete *Staphylococcus aureus* via multiple mechanisms. The early generation of reactive oxygen species by macrophages, down-regulation of bacterial virulence gene expression and the bactericidal nature of the nanostructured surface itself collectively acted to help the macrophage to win the race. This study highlights the potential of nanostructured surfaces to reduce infection rates and improve the long-term success of biomedical implants. This work can also serve as guidance to others to investigate in vitro host-bacteria interactions on other candidate antibacterial surfaces.

6.3 Introduction

Biomaterial-associated infection (BAI) is a serious problem for many medical device implantation procedures.[1] These infections are mainly due to the locally compromised host defence and the availability of a substrate to which bacteria can attach and form biofilms.[2] Often, BAIs cannot be resolved by conventional means, predominately due to the bacterial biofilm mode of growth, which protects the infecting organisms against the host immune system[3] and antibiotic treatment.[4] Pathogens can be introduced on an implant surface perioperatively, contiguously or via a hematogenous source.[5] *Staphylococcus spp.* encompasses approximately two-thirds of all pathogens in orthopaedic implant infections,[6] and are the principal etiological agents of two major types of infection causing septic arthritis and osteomyelitis, which involve the inflammatory destruction of joint and bone.[7] When bacteria come into contact with a biomaterial during implantation, the fate of the implant is determined by a race between bacteria trying to establish a biofilm, and the host cells trying to integrate the implant and kill bacteria. This concept was described in 1987 by the orthopaedic surgeon Anthony G. Gristina, who devised the phrase "race for the surface".[8] Host cells "win" the race if they successfully establish on the implant and occupy its surface area, leading to tissue integration around the implant and thus a minimized risk of bacterial colonization. Alternatively, bacteria may win the race by successfully establishing a biofilm on the solid implant surface before it can be encapsulated by host tissue. Once the biofilm is formed, it is extremely difficult to eradicate the pathogen from the implant, and the implant will inevitably fail and require to be replaced.

To tackle the problem of bacterial contamination of implantable devices, many different approaches have been developed.[9] One such method uses sharp nanoscale protrusions to kill bacteria on contact by mechanical interaction. This phenomenon is commonly referred to as the mechano-bactericidal effect.[10] Antibacterial nanostructures were first observed on cicada and dragonfly wings, then later translated to various synthetic material surfaces.[11] Such nanostructures may enhance the performance of many medical devices because they can be fabricated on a range of different medically relevant materials, such as titanium. For titanium nanostructures, a common and facile method for nanostructure fabrication is hydrothermal etching (HTE).[12] HTE titanium (HTE-Ti) nanostructures have been shown to be effective against both fungi[13] and bacteria (Gram-positive and Gram-negative)[14] for an extended period of time.[15] Furthermore, similar nanostructured surfaces have shown excellent cytocompatibility with human macrophage[15], fibroblast cells,[14a] and osteoblast-like cells.[16] Recently, an *in vivo* sheep model study compared implants having surfaces modified with antibacterial nanostructures to the gold standard hydroxyl apatite-coated devices. The study reported enhanced bone integration with the antibacterial nanostructured implants.[17] A mechanistic explanation of this finding was provided by a recent study that interrogated the composition of protein corona on antibacterial nanostructured titanium alloy surface and found enrichment in key cell adhesion proteins such as vitronectin. Furthermore, proteins that were related to immune response were also modulated in a way that leads to a reduction of inflammation.[18]

Macrophages are one of the first cell types that interact with an implanted biomaterial. The outcome of this interaction strongly impacts the subsequent cascade of events that determine the healing process and implant performance.[19] Upon attachment to biomaterials, macrophages become activated and attempt to phagocytose the implanted biomaterial. Subsequent cytokine release directs the inflammatory and wound-healing response to the biomaterial.[20] If the biomaterial is biocompatible, host tissue will integrate without impediment, thereby preventing future bacterial colonization. Macrophages also produce and release reactive oxygen species (ROS), reactive nitrogen species (RNS) and cytokines in response to a foreign body, including a bacterial challenge.[21]

One important missing piece of knowledge is related to how immune cells interact with bacteria on such antibacterial nanostructured surfaces. The hypothesis underpinning this work is that antibacterial surface modification would benefit immune cells in their effort to eliminate pathogens. To test this, we designed and performed co-culture studies employing RAW 264.7 macrophage-like cells as representatives of some of the early innate immune cells arriving at an implanted biomaterial surface, as well as *Staphylococcus aureus* (S. *aureus*) as an example of a major pathogen known to cause severe implant-associated infections. To understand the associated mechanisms, we also performed a differential gene expression analysis of *S. aureus* interacting with the surfaces involved in this study.

6.4 Results and Discussion

6.4.1. Characterization of the Hydrothermally Etched Surface

Before the biological experiments, the topographical, chemical, and physical properties of nanostructured HTE-Ti and as received titanium (AR-Ti) controls were characterized (**Figure 1**). Scanning electron microscopy (SEM) analysis revealed that while the AR-Ti had only macroscale features resulting from the polishing process, the HTE-Ti surface had developed sharp nanostructures. The dark appearance of the HTE-Ti samples (**Figure 1D**) is due to the trapping of the light by the surface nanostructures and is seen with other systems, such as the well-known black silicon nanostructured surface.[11a] The mean nanostructure height was 365 ± 135 nm, while the diameter at mid-height was 85 ± 48 nm. The spacing between nanostructures was 460 ± 64 nm. These values are comparable to those previously reported using the same fabrication process [12a, 14b] Atomic force microscopy (AFM) measurements were used to quantify the increase in roughness and surface area of the HTE-Ti samples (**Figures 1E, 1F and Table S1**). The roughness of the HTE-Ti surface was defined in terms of the root-mean-square (RMS) and arithmetic roughness average (Ra) over 5 x 5 μm scans, which returned values of 84.88 nm and 67.20 nm, respectively. In comparison, the untreated AR-Ti surface had an RMS of 54.90 nm and a Ra of 39.68 nm. The surface area in the 25 μm^2 scan was measured to be 49.8 μm^2 on the HTE-Ti surface and 25.84 μm^2 on the AR-Ti surface.

The elemental composition of the nanostructured HTE-Ti and AR-Ti control surfaces was characterized using an energy dispersive spectrometer (EDS) (**Figures 1H and 1I**). The results showed a decrease in vanadium and an increase in oxygen in the outermost layer of HTE-Ti, consistent with a thicker oxide layer (TiO_2) formed during the hydrothermal etching process. A minor presence of potassium was also detected in the HTE-Ti samples, which can be attributed to the use of KOH as the alkaline etchant of choice. The wettability of the samples was determined via sessile drop water contact angle analysis, which resulted in values of 57 ± 3° and 8 ± 3° ($p < 0.0001$) on the AR-Ti and HTE-Ti samples, respectively (**Figure 1G and Table S2**). This indicates that the HTE-Ti sample was substantially more hydrophilic. The increased hydrophilicity is reported to be a beneficial property for endosseous implants because it promotes protein adsorption, which is necessary for initial macrophage attachment [22] and bone integration.[23]

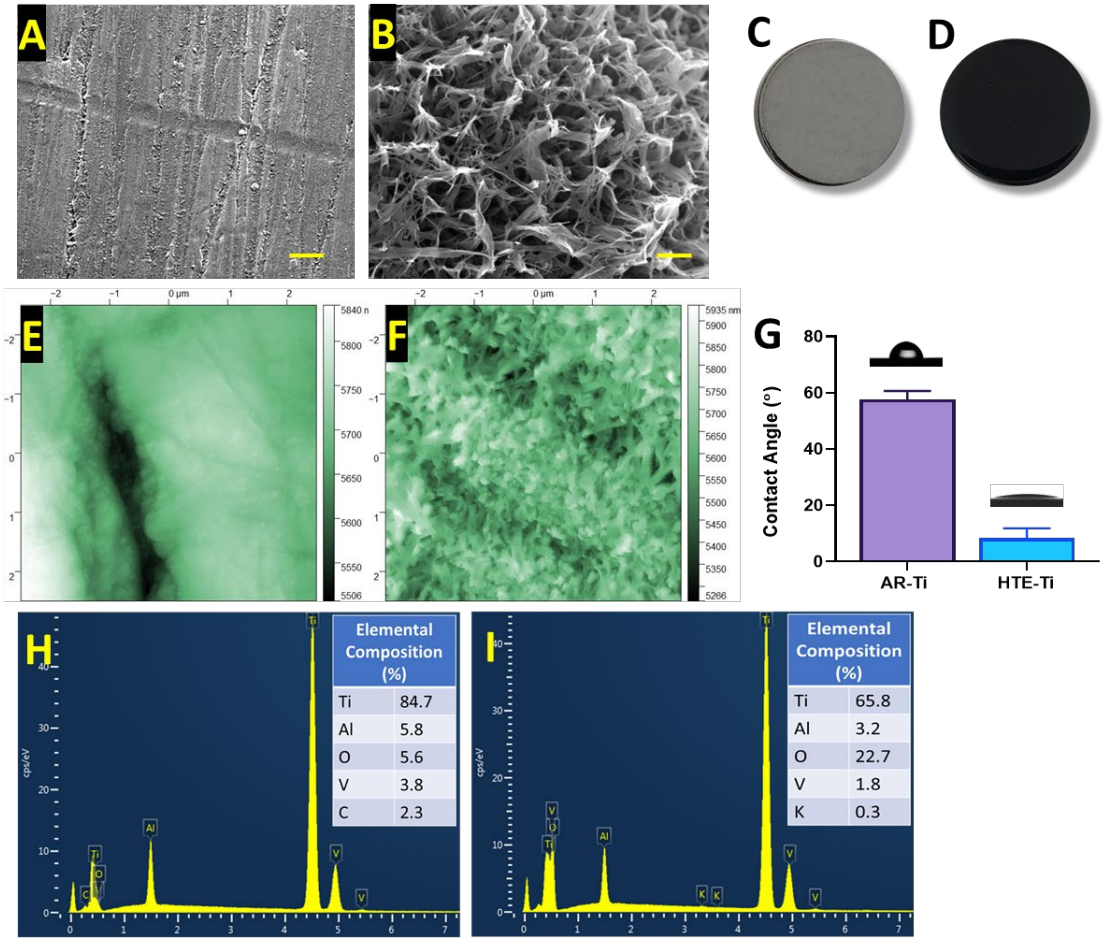

Figure 1. *Characterization of the AR-Ti (A) and HTE-Ti (B) surface by SEM, scale bars represent 500 nm. Photographs showing the appearance of the AR-Ti (C) and HTE-Ti (D) discs used in the experiments. AFM images of AR-Ti (E) and HTE-Ti (F). Water contact angle on both AR-Ti and HTE-Ti surfaces, mean ± SD, n = 3 (G). EDS spectra together with percent elemental composition of AR-Ti (H) and HTE-Ti (I).*

6.4.2 Bacterial Viability Alone and in Competitive Colonisation with Macrophages

Before investigating the outcome of the competitive colonisation between *S. aureus* and macrophages, the baseline efficacy of HTE-Ti against *S. aureus* was measured using Live/Dead fluorescence analysis over 7 days (**Figures 2A, 2B and Table S3**). On the AR-Ti surface, *S. aureus* maintained a viability of approximately 95% over the 7 days of incubation. On the HTE-Ti surface, after the first day of incubation, the viability of *S. aureus* was approximately 34%, decreasing to 15% on day 3, and recovering back to 36% by day 7. These measurements were consistent with a previously reported longitudinal viability analysis using HTE-Ti.[15] This baseline efficacy data is useful because it confirms the long-term efficacy of the nanostructured surface. The fluorescence-based viability data was also compared to viable cell counts using colony enumeration, which revealed colony-forming units (CFU) reductions between 1 and 1.5 logarithms throughout the time course.

Having established the baseline efficacy of the HTE-Ti surface against *S. aureus*, we set out to determine the outcome of competitive colonisation between macrophages and *S. aureus*. The experimental design was aimed at emulating a clinical case in which an implant is contaminated with bacteria before implantation. Thus, we inoculated the samples with *S. aureus* at 10^3 CFU/mL, with a multiplicity of infection (MOI) of 0.01, for 3 h before introducing macrophages.

The viability of *S. aureus* was then measured over 7 days using viable cell counts and reported as the logarithmic reduction of CFU between the AR-Ti and HTE-Ti surfaces (**Figure 2C and Table S4**). Interestingly, the logarithmic reduction of *S. aureus* was significantly increased in the presence of macrophages. After the first day of co-colonisation, *S. aureus* was reduced by 2.6 logarithms ($p < 0.001$), and by day 7, the logarithmic reduction was 3.6 ($p < 0.0001$). This is encouraging because it indicates that the combined effect of the nanostructures and the antibacterial actions of macrophages resulted in an enhanced bactericidal effect.

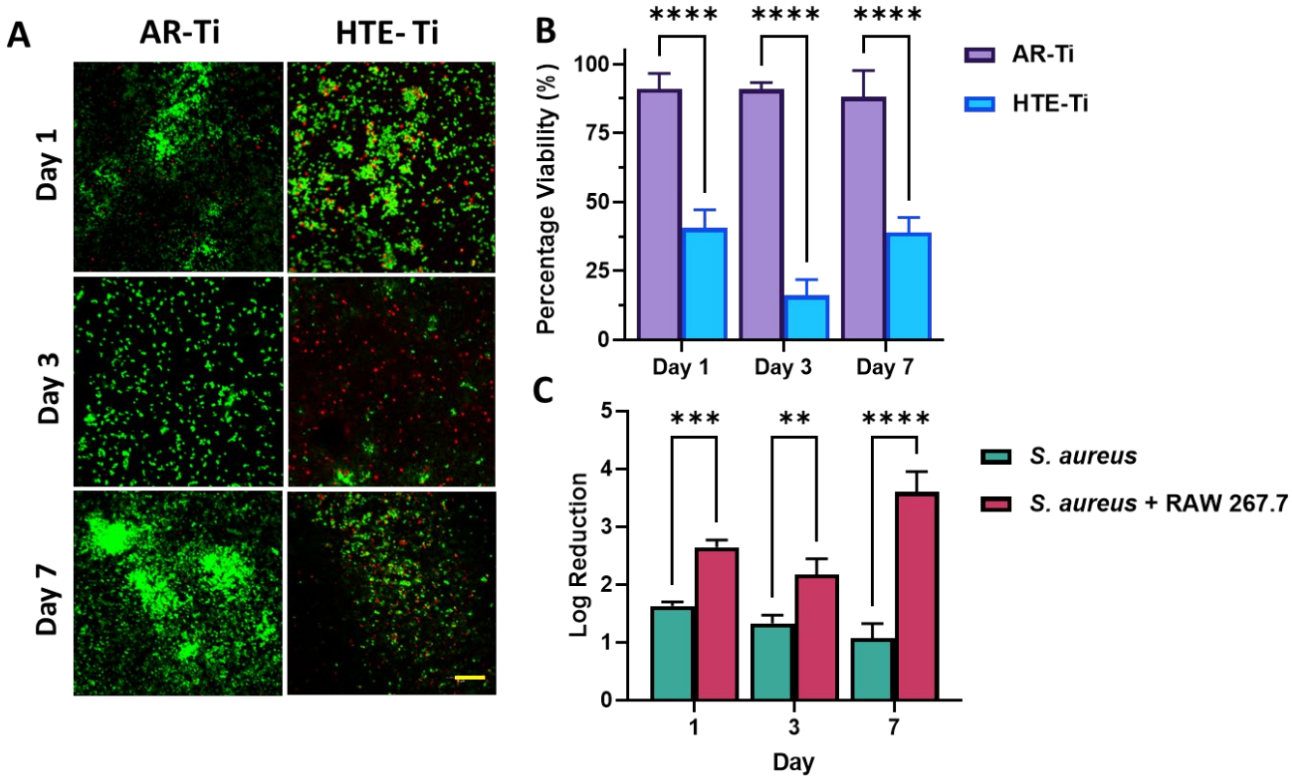

Figure 2. *Bacterial viability confocal micrographs, scale bar represents 10 µm (A), viability determined from live dead imaging of S. aureus incubated on HTE-Ti and AR-Ti surfaces, mean ± SD, n = 3 (B) and log reduction of S. aureus alone and co-cultured with RAW 264.7 macrophage-like cells, mean ± SD, n = 3 (C). ** p < 0.01, *** p < 0.001 and ****p < 0.0001.*

6.4.3 Co-culture Viability by Lactate Dehydrogenase (LDH) Assay and Morphology by CLSM

To quantify the viability of the RAW 264.7 macrophage-like cells, alone or in co-culture, we used an LDH cytotoxicity kit (**Figure 3B**). Viability analysis showed no statistically significant changes in macrophage viability on the nanostructured HTE-Ti or AR-Ti surfaces throughout the 7 days of incubation. However, macrophage viability drastically decreased over 7 days when the cells were co-cultured with *S. aureus* on the AR-Ti surface. This effect was not observed for macrophages co-cultured with *S. aureus* on the HTE-Ti surface, and instead, the viability was no different to their viability when cultured alone. This data supports the phalloidin / DAPI staining fluorescence analysis and reaffirms that macrophages remain resilient in the presence of *S. aureus* on the nanostructured surface, but not on the untreated AR-Ti surface.

To further investigate the interaction between *S. aureus* and RAW 264.7 macrophage-like cells on the nanostructured surface, we used TRITC-phalloidin (staining F-actin) and DAPI (staining DNA) to visualize the morphology and phagocytic behaviour of the macrophages (**Figures 3C – 3J**). When RAW 264.7 macrophage-like cells were cultured alone, we observed an expansion of the cell population on both surfaces over the 7 days, indicating that the culture conditions were adequate. Interestingly, after 1 day of incubation in the co-culture samples, we observed macrophages surrounded by *S. aureus* cells, however, very few bacteria were internalized. Notably, there appeared to be a much denser arrangement of *S. aureus* cells on the AR-Ti surface in comparison to the HTE-Ti (**Figures 3G and 3H**). On day 7, there was a dramatic change in the ratio and organisation of bacterial and macrophage cells on both surfaces. On the AR-Ti surface, there was an absence of macrophages, while DAPI staining found abundant evidence of *S. aureus*. In comparison, on the HTE-Ti surface, macrophages were in abundance, and most bacteria appeared to be internalized within the macrophages. This is strong evidence that macrophages are unable to out-compete *S. aureus* on the untreated AR-Ti surface but can compete strongly on the nanostructured surface. Thus, any *S. aureus* cells fortunate enough to survive nanostructure-induced lysis are phagocytosed and killed by the antimicrobial actions of macrophages. Day 3 confocal images can be viewed in the supplementary information **Figure S3**.

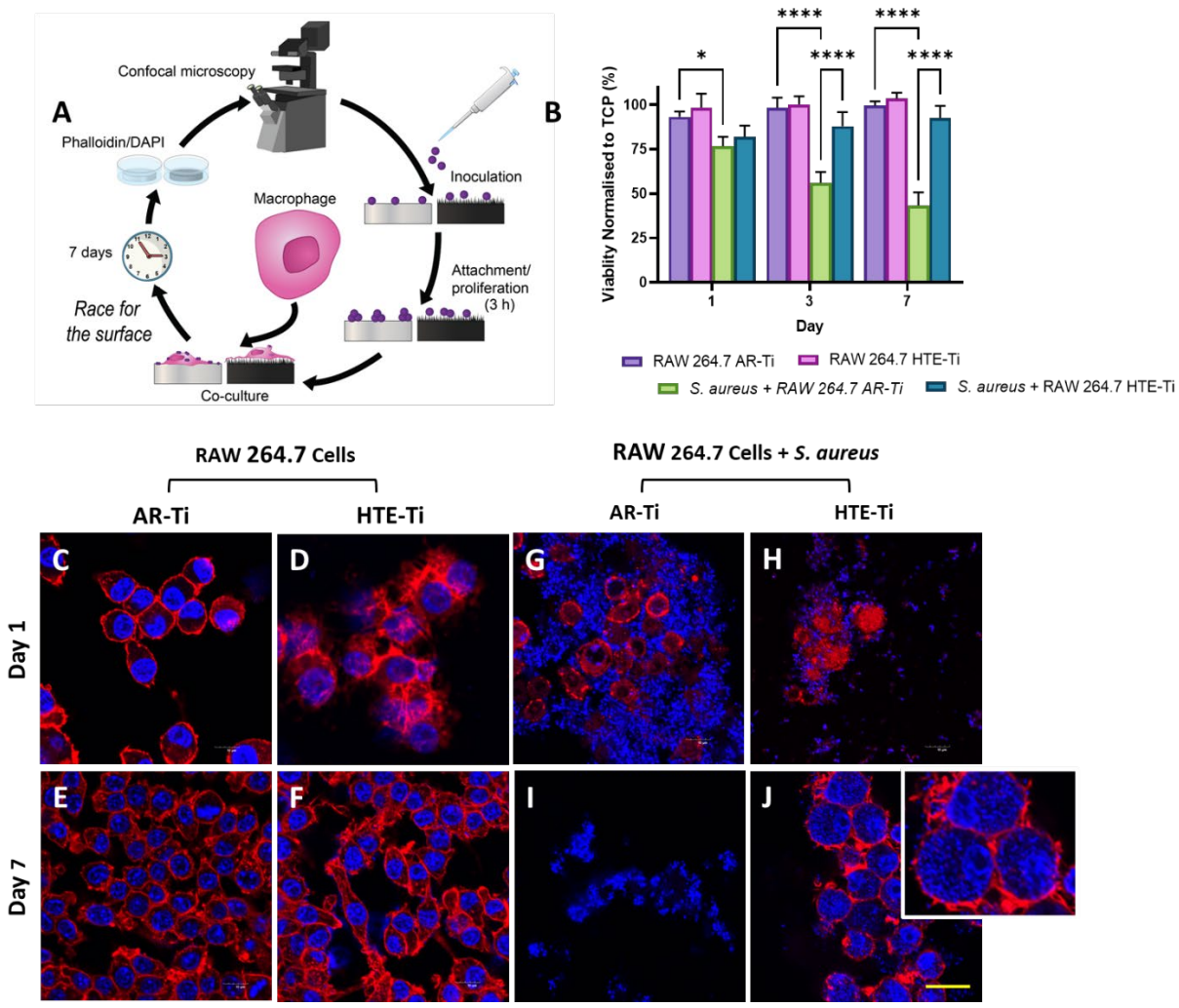

Figure 3. *The pre-infection co-culture protocol (A). LDH viability normalized to tissue culture plate (TCP) at days 1, 3 and 7 (B). * $p < 0.05$, **** $p < 0.0001$, mean ± SD, n = 3. The morphological behaviour of RAW 264.7 macrophage-like cells only at day 1 (C and D) and day 7 (E and F) and co-cultures of RAW 264.7 macrophage-like cells and S. aureus at day 1 (G and H) and day 7 (I and J) on the HTE-Ti and AR-Ti surfaces evaluated by actin staining with phalloidin (red) and nuclei counterstained with DAPI (blue). Inset higher magnification image in (H) demonstrates internalisation of S. aureus by RAW 264.7 macrophage-like cells. The scale bar in the bottom right panel represents 20 µm.*

6.4.4 ROS Generation by RAW 264.7 macrophage-like cells on HTE-Ti

ROS generation is a key response of macrophages when interacting with foreign objects. ROS plays a critical role in macrophage polarization towards an M1 proinflammatory phenotype.[24] Representative CLSM images of ROS-activated DCF stained RAW 264.7 macrophage-like cells incubated on both surfaces are shown in **Figures 4A - 4D**. In the presence of ROS, DCF-DA is deacetylated to highly fluorescent DCF (**Figure 4E**).[25]

RAW 264.7 macrophage-like cells on the HTE-Ti surface showed a significant increase in ROS generation compared to cells incubated on AR-Ti at 24 h (**Figure 4F)** ($p < 0.001$). However, when RAW 264.7 macrophage-like cells were incubated for 72 h on the HTE-Ti surface, their ROS generation was reduced to the same level as the cells incubated on the AR-Ti surface (**Figure 4F**). Mechanically induced ROS release by macrophages activates Mst1/2 to protect the cells against oxidative damage.[26] Additionally, an increase in intracellular ROS also influences cell proliferation, differentiation, and migration, which may help to shift the balance to favour the survival of macrophages over bacteria.[27] ROS generated by macrophages kills internalised bacteria by oxidative burst mediated by NADPH oxidase, a major component of the innate immune system.[28] Previous reports have determined that mechanically induced intracellular ROS generation is a primary antibacterial mechanism of the mechano-bactericidal effect of nanostructured surfaces. [29] Thus, when co-cultured with macrophage-like cells, *S. aureus* cells face the cumulative action of mechanically induced intracellular ROS generation alongside the enhanced oxidative environment within the macrophage. These factors may act synergistically to undermine bacteria and tip the scales in favour of the macrophage in the 'race for the surface'.

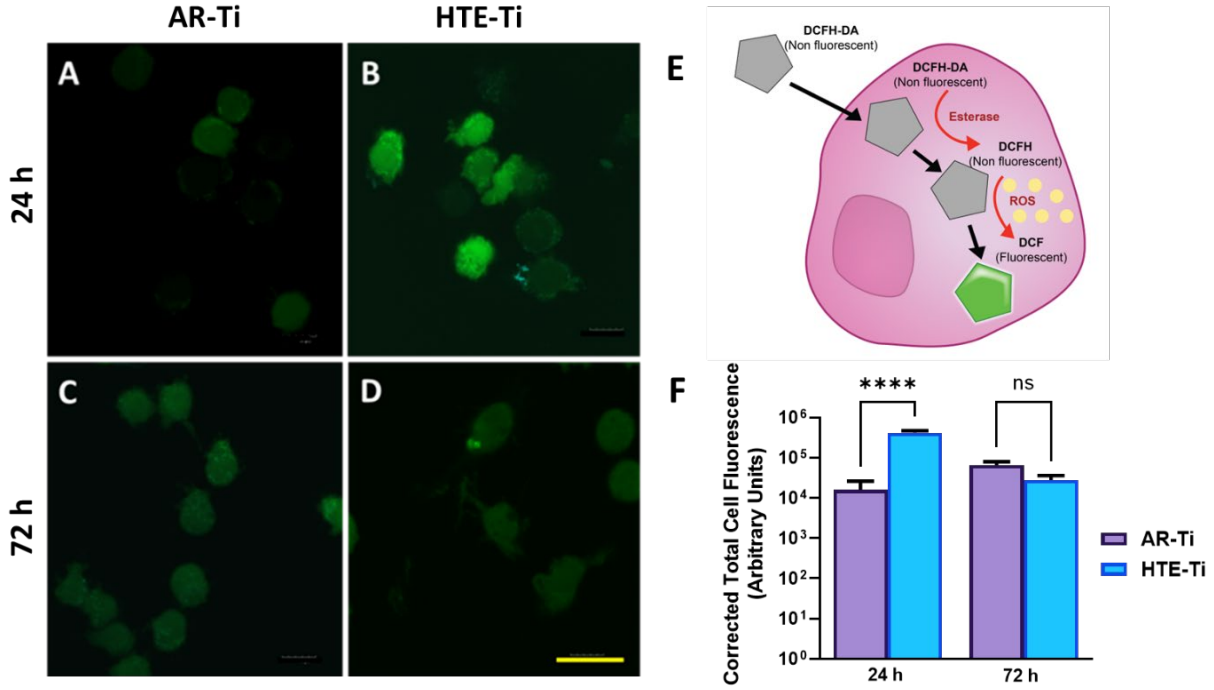

Figure 4. *CLSM fluorescent micrographs of RAW 264.7 macrophage-like cells treated with DCF-DA, incubated for 24 h on AR-Ti (A) and HTE-Ti (B), and 72 h on AR-Ti (C) and HTE-Ti (D). The scale bar represents 20 µm. The formation of fluorescent DCF from DCFH-DA to detect cellular levels of ROS (E). Corrected total cell fluorescence quantified from CLSM images (C), *** p < 0.0001, ns represents non-significance, mean ± SD, n = 3.*

6.4.5 SEM of Co-cultures of S. aureus and RAW 264.7 Macrophage-Like Cells at Day 7

To provide further support to our results, we used SEM imaging to analyse the morphology and organisation of *S. aureus* and RAW 264.7 macrophage-like cells on the surfaces, either separately or in a competitive culture, after 7 days of incubation (**Figure 5 and S4**). Visually, the *S. aureus* cells on the nanostructured HTE-Ti surface appeared sparse and frequently appeared shrivelled and deformed (**Figure 5B**, red arrows). The RAW 264.7 macrophage-like cells had typical healthy morphology on both AR-Ti and HTE-Ti when incubated without bacteria (**Figures 5C and 5D**). However, when co-colonized with *S. aureus* on the AR-Ti surface, the macrophage cells could not be visualized and instead appeared to be covered by *S. aureus* cells (**Figures 5E and 5F**). This contrasts with what was observed on the HTE-Ti surface, where the macrophage cells had typical healthy morphology while *S. aureus* cells were almost completely absent. The SEM observations closely correlate with the phalloidin / DAPI stain shown in **Figure 3**, which showed macrophages with internalized *S. aureus* cells on the HTE-Ti surface and a lack of macrophages on the AR-Ti surface.

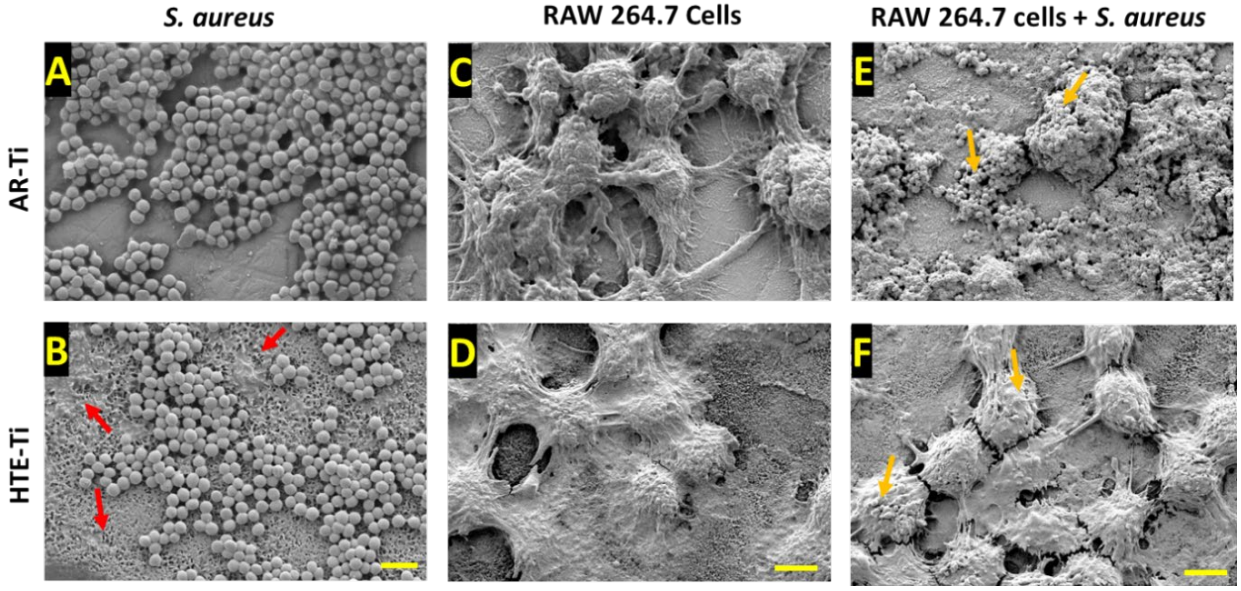

Figure 5. *SEM micrographs of S. aureus incubated for 7 days on AR-Ti (A) and HTE-Ti (B), red arrows highlighting dead bacteria and cell debris on the HTE-Ti surface, scale bar represents 2 µm. RAW 264.7 macrophage-like cells incubated for 7 days on AR-Ti (C) and HTE-Ti (D). The scale bar represents 5 µm. RAW 264.7 macrophage-like cells co-cultured with S. aureus for 7 days on AR-Ti (E) and HTE-Ti (F), orange arrows highlighting bacteria attached to RAW 264.7 macrophage-like cells, scale bars represent 5 µm.*

6.4.6 Differential Gene Expression (DGE) Analysis of S. aureus Incubated on HTE-Ti Nanostructures

To generate an understanding of how the nanostructured surface influences the gene expression of *S. aureus*, leading to inhibition of its competitive advantage against macrophages, we performed a DGE analysis of *S. aureus* on the HTE-Ti and AR-Ti surfaces. The study was designed to measure the change in expression profile when planktonic cells attach to either an untreated AR-Ti or an HTE-Ti nanostructured surface. From the analysis, a selection of genes was identified to be relevant to the competition between *S. aureus* and macrophages **(Table 1)**. A group of genes relevant to cell division was identified to be uniquely upregulated on the AR-Ti surface. During the process of cell division, bacteria must disassemble and reform their peptidoglycan wall to accommodate the growth of the daughter cell.[30] On the AR-Ti surface, *S. aureus* uniquely upregulated genes involved in the hydrolysis of peptidoglycan (*lytM*, *isaA*, and 3 CHAP-domain containing proteins), as well as the formation of new peptidoglycan or its components (*murD*, *datA*, alanine racemase, homoserine dehydrogenase). This suggests that *S. aureus* is more likely to rapidly divide and establish on the AR-Ti surface, in comparison to the nanostructured HTE-Ti surface. This analysis suggests that the reduced rate of peptidoglycan biosynthesis in cells attached to the HTE-Ti surface provides a competitive advantage for macrophages, supporting our observations.

Another key process in the competition between *S. aureus* and macrophages is the capacity of the pathogen to evade the host's immune response. Macrophages are phagocytic cells that engulf and destroy bacterial pathogens by exposing them to ROS, which damages proteins and nucleic acids.[31] This leads to the impairment of various cellular functions and ultimately the death of the pathogen.[32] Several differentially expressed genes were identified which may tip the balance in favour of macrophages on the nanostructured HTE-Ti surface. We observed a differential expression of genes associated with capsule biosynthesis. A capsule is an outer layer of polysaccharides that enables the evasion of phagocytosis by masking identifiable pathogen-associated cell surface structures.[33] On the nanostructured surface, we observed a downregulation of *capA*, which codes for a capsular biosynthesis protein. This suggests that on the nanostructured HTE-Ti surface *S. aureus* is less able to produce capsule, and therefore more likely to be recognized and engulfed by macrophages. Additionally, we observed an upregulation of genes associated with oxidative damage and repair on the AR-Ti samples. The *SOD1* gene encodes superoxide dismutase, which works to minimize oxidative stress by eliminating superoxide.[34] The effect of this is accompanied by the action of *msrA,* which codes for a protein that repairs methionine residues on proteins following exposure to oxidative stress, thus protecting bacteria from adverse conditions.[35] Overall, the differential expression of capsule biosynthesis and oxidative damage repair genes signals that on the nanostructured HTE-Ti surface *S. aureus* is less able to evade phagocytosis, and once *S. aureus* becomes engulfed by a macrophage, the bacterium may be more sensitive to the subsequent oxidative burst attack.

A further interesting difference in gene expression is related to the Panton-Valentine leukocidin (PVL), which functions as a pore-forming toxin. The PVL toxin targets macrophages, among other host cells, and inserts into the cytoplasmic membrane to create pores, leading to either necrosis or apoptosis.[36] The bi-component toxin is encoded by two genes, *LukF-PV,* and *LukS-PV*. While *LukS-PV* was commonly upregulated on both surfaces, the *LukF-PV* counterpart was only upregulated on the untreated AR-Ti surface. As both components are required for the toxin to function,[36] this difference in expression suggests that the PVL toxin is functionally upregulated only in *S. aureus* cells attached to the AR-Ti surface, and not the nanostructured HTE-Ti surface. This, therefore, supports the observation that *S. aureus* was able to out-compete macrophages on the untreated titanium surface but failed to do that on the nanostructured surface. The mechanistic model is depicted in **Schematic 1**.

Table 1. *The differentially expressed genes of S. aureus may influence the competition between macrophages and S. aureus on the nanostructured surface. Accession numbers can be found in Table S5.*

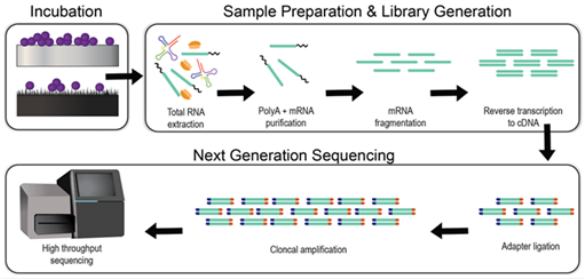

Gene/Function	Expression			
	AR-Ti		HTE-Ti	
	Regulation	Fold change	Regulation	Fold change
Cell Division				
Lytic Transglycosylase – *IsaA*	Up	1.7	---	N/A
Amidase domain-containing protein	Up	2.1	---	N/A
3 CHAP- domain containing protein	Up	2.0	---	N/A
Amidohydrolase family protein	Up	1.2	---	N/A
Glycine-glycine endopeptidase *LtyM*	Up	1.2	---	N/A
UDP-N-acetylmuramoyl-L-alanine D glutamase ligase *murD*	Up	1.0	---	N/A
Amino-acid transaminase *DatD*	Up	1.4	---	N/A
Alanine racemase *Alr*	Up	0.6	---	N/A
Homoserine dehydrogenase *HSD*	Up	3.2	---	N/A
Capsule Biosynthesis				
Polysaccharide biosynthesis protein	Up	1.0	---	N/A
Capsular polysaccharide type 5/8 biosynthesis protein *CapA*	---	N/A	Down	0.8
Redox Defenses				
Superoxide dismutase *SOD1*	Up	2.4	---	N/A
Peptide-methionine (S)-S-oxide reductase *MsrA*	Up	2.2	---	N/A
Toxins				
LukS-PV	Up	2.3	Up	2.3
LukF-PV	Up	2.4	---	N/A

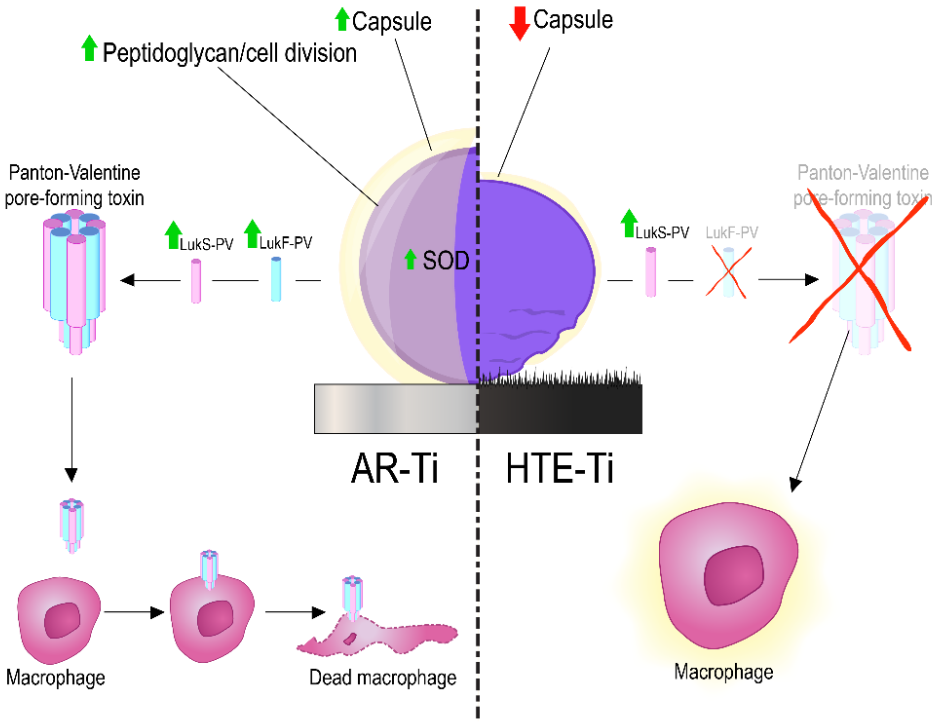

Schematic 1. *Highlights the downregulation of superoxide dismutase (SOD), capsule and LukF-PV expression, leading to bacterial cell death, and the increase in survivorship of macrophages, when co-cultured on the nanostructured HTE-Ti surface.*

The results from this study provide evidence that the HTE-Ti nanostructured surface not only exhibited antibacterial properties but also synergistically worked with macrophages, revealing the bifunctionality of such nanostructured surfaces. When macrophages were incubated on the nanostructured surface pre-infected with *S. aureus*, the RAW 264.7 cells were able to attach and proliferate, ultimately outcompeting the bacteria. In contrast, macrophages were completely outcompeted by *S. aureus* when cultured on the untreated AR-Ti control samples. The results of this work indicate that appropriately tailored nanostructured surfaces may not only act as a deterrent to bacterial colonisation but may also provide an advantage for the host immune system to win the 'race for the surface', in turn reducing the rate of occurrence of BAI. This is an important finding in the fight against this type of infection, which is among the most complicated and difficult to treat, often resulting in amputations or mortality. This work points to opportunities for researchers from the fields of (bio)materials engineering, nano and biotechnology, biology, microbiology, and medicine to join efforts to design surfaces that can help mammalian cells and tissue win the "race for the surface" and design experiments that help to completely understand the associated phenomena.

6.5 Conclusion

We investigated the interaction between the Gram-positive pathogen *S. aureus* and a macrophage cell line on a nanostructured titanium surface. Characterization of the surface showed sharp nanostructures with a high aspect ratio, and a significant increase in roughness, surface area and wettability when compared to the untreated control surface. Bactericidal analysis showed the surface was able to kill most bacteria upon contact. When bacteria were co-cultured with macrophages distinctly different results were seen of the AR-Ti control and the HTE-Ti. Bacteria were able to completely overwhelm the macrophages on the AR-Ti surface. On the contrary, macrophages dominated bacteria on the HTE-Ti surface. A mechanistic understanding was derived via differential gene expression analysis demonstrating changes in the expression of key virulence factors when bacteria are cultured on an AR-Ti or a nanostructured HTE-Ti surface. The results from this work demonstrate that surface nano-structuring with sharp features can help immune cells win the 'race for the surface' and better protect implanted biomaterials from infections.

6.6 Experimental Section

6.6.1 Fabrication of Hydrothermally Etched Titanium Alloy

Coupons of Ti6Al4V (discs 10 mm in diameter and 3 mm in height) polished to a roughness average (Ra) of 0.5 µm were etched in a stainless-steel reactor (Parr Instrument Company), using 1 M KOH aqueous solutions. The reactors were kept sealed at 150 °C inside an oven for 5 h.[18] After the initial etching process, the reactors were cooled, and the samples were rinsed and immersed in ultrapure water. After drying, discs were heat-treated (annealed) inside a tubular furnace and cooled overnight. Before performing biological experiments, the samples were cleaned and then sterilized in an autoclave at 121 °C for 20 min.

6.6.2 Characterisation of the HTE-Ti Surface

HTE-Ti surface characterization included SEM, AFM, EDS, and Contact Angle. Measurements of nanostructures present on HTE-Ti samples were measured using micrographs obtained on an SEM (Zeiss Merlin FEG-SEM, Jena, Germany), equipped with a secondary electron (SE) detector, at 2 KV, a working distance of 4 mm, 45° stage tilt and magnifications ranging from 5–50 K. SEM micrographs were imported into ImageJ 1.53t (NIH, MD, USA) to measure dimensions.

AR-Ti and HTE-Ti surfaces were further characterized using AFM performed in air using a Bruker Dimension Icon. AFM analysis was performed on the surfaces using an NT-MDT NSG03 silicon nitride cantilever with a conical tip quoted by the manufacturer with a radius < 10 nm and a half side angle of 18° (Spectrum Instruments Ltd, Moscow, Russia) was used in PeakForce mode. Preliminary calibration of the cantilever using a glass slide obtained a normal spring constant of 2.0 N m^{-1} and a deflection sensitivity of 94.4 nm V^{-1}. PeakForce amplitude over a 5 x 5 µm image was set at 150 nm with a frequency of 2 kHz, a lift height of 34 nm, and a scan rate of 8.84 µm s^{-1}.

Average Roughness (Ra), root mean square (RMS) roughness, surface area (SA) and 3-D reconstructions were acquired using Gwyddion data analysis software version 2.54 (http://gwyddion.net/, Czech Metrology Institute, Jihlava, Czechia).

Energy Dispersive Spectrometer (EDS) spectra were acquired using spot mode at 10kV, 0.17 nA, magnification of 10K and a working distance of 4 mm on the HTE-Ti and AR-Ti surfaces using AZTEC EDS software version 3.1 (Oxford Instruments, Oxfordshire, UK).

Water contact angle, θ was measured on HTE-Ti and AR-Ti surfaces by the sessile drop method, [47] using a goniometer RD-SDM02 (RD Support, Scotland, UK). The contact angle from Milli-Q water was measured in triplicate by a tangent fitting approach using the plugin Contact_Angle.jar for ImageJ software (NIH, MD, USA).

6.6.3 Bacterial Culture

S. aureus ATCC25923 (ATCC, VA, USA) was plated onto tryptone soy agar (TSA, Oxoid, ThermoFisher, Waltham, MA, USA) and incubated overnight at 37 °C. After overnight incubation, a single colony was inoculated into Dulbecco's Modified Eagle Medium (DMEM, ThermoFisher, MA, USA) supplemented with 10% (v/v) foetal bovine serum (FBS; Life Technologies, CA, USA) and incubated overnight at 37 °C. Cultures were then diluted to a final concentration of 2 x 10^3 CFU/mL. Before sample inoculation, it was determined by calibrating against CFU that an optical density of 1 measured at OD_{600} was approximately 10^9 CFU/mL. *S. aureus* from plates and cultures were routinely Gram-stained to check for purity. To determine the bacterial viability, nanostructured HTE-Ti and AR-Ti samples were inoculated in a 48-well plate with 500 µL (10^3 CFU/well) of *S. aureus* in DMEM supplemented with 10% (v/v) FBS and incubated at 37 °C, 5% CO_2 with 95% humidity, and analysed for viability at days 1, 3 and 7, with daily media replenishment. Bacterial cultures were incubated on an orbital shaker (Ratek Instruments, VIC. Australia), at 100 RPM, to simulate hydrodynamic conditions.

6.6.4 Live Dead Analysis – Viability

Samples were transferred to a sterile 24-well plate and immersed in LIVE/DEAD® BacLight™ Bacterial Viability Kit reagents (Invitrogen, ThermoFisher, MA, USA), with an equal proportion of Syto9 and Propidium Iodide at 1.5 µL/mL (of each) in phosphate-buffered saline (PBS). The immersed samples were incubated in the dark for 15 minutes at room temperature and then imaged with an Olympus FV3000 confocal laser scanning microscope (CLSM, Olympus, Tokyo, Japan). The excitation and emission spectra for Syto9 and Propidium Iodide were set at 480/500 and 490/635 nm, respectively. Micrographs were taken at 3 random locations on each sample. Cell viability was determined by counting the number of green and red stained cells using ImageJ v1.53 (NIH, USA), and using the following calculation: viability = ($\frac{green\ cells}{total\ cells}$ x 100).

6.6.5 Colony Enumeration

Samples were individually placed in 5 mL screw-cap tubes and immersed in 1 mL sterile PBS. Cells were detached from the samples by 2 mins sonication followed by 30 seconds vortex. The resultant cell suspension was serially diluted in 10-fold increments, and 10 µL of each dilution was aliquoted onto a fresh TSA plate in triplicate and incubated at 37°C for 20h. Colonies were counted the following day to determine the number of viable CFU retrieved per sample. The reduction in viable cells was calculated by $Log\frac{CFU(AR-Ti)}{CFU(HTE-Ti)}$, where CFU(AR-Ti) and CFU(HTE-Ti) are the CFU recovered from the AR-Ti and HTE-Ti samples, respectively.

6.6.6 RAW 264.7 Macrophage-Like Cell Culture

The RAW 264.7 cell line (ATCC® TIB-71, VA, USA) are macrophage-like cells, originating from a transformed cell line derived from BALB/c mice. These cells are described as an appropriate model of macrophages.[48] RAW 264.7 macrophage-like cells were cultured in DMEM supplemented with 10% (v/v) FBS, 100 units/mL penicillin and 100 µg/mL streptomycin (Life Technologies, CA, USA). Cells were maintained at 37 °C, 5% CO_2 and 95% humidity. The medium was replenished daily until the cells reached 80% confluency, before use.

6.6.7 Co-culture Pre-Infection Procedure

To mimic a contaminated implant model, *S. aureus* was inoculated on HTE-Ti and AR-Ti samples followed by RAW 264.7 macrophage-like cells. Initially, the HTE-Ti and AR-Ti samples were inoculated with *S. aureus* at an MOI of 0.01[49, 50] (10^3 CFU/disc of *S. aureus*) into a 48-well plate and incubated for 3 hours at 37 °C before the addition of the RAW 264.7 macrophage-like cells. This period is known as the “decisive period” and is considered critical for the initiation of medical implant-associated infections.[51] Next, the media was removed and RAW 264.7 macrophage-like cells (10^5 cells/disc) in 500 µL of DMEM supplemented with 10% (v/v) FBS, were added to each sample pre-inoculated with *S. aureus*. All co-culture experiments were incubated at 37°C, 5% CO_2 and 95% humidity on an orbital shaker at 100 RPM, and assessed on days 1, 3 and 7 with daily media replenishment.

6.6.8 Cell Attachment, Morphology and Cytotoxicity on the Nanostructured Surface

To assess cell attachment and morphology of RAW 264.7 macrophage-like cells co-cultured with *S. aureus* and alone on the HTE-Ti and AR-Ti surfaces, fluorescent staining was used to visualize the cytoskeleton and nuclei of the cells. Briefly, samples were fixed with 4% paraformaldehyde for 1 h. Following fixation, cells were permeabilized with 0.1% Triton X-100 (Sigma-Aldrich, MO, USA), and then stained with TRITC-Phalloidin (Ex/Em 540/565, ThermoFisher, MA, USA) and 4',6-diamidino-2-phenylindole (DAPI; Ex/Em 359/461, ThermoFisher MA, USA).

Fluorescence images were captured using an Olympus FV3000 confocal laser scanning microscope (CLSM; Olympus, Tokyo, Japan). Cytotoxicity was also evaluated using LDH-Glo™ Cytotoxicity Assay (Promega, WI, USA) following the manufacturer's instructions. Lactate dehydrogenase (LDH), is a widely used marker in cytotoxicity/viability studies due to its rapid release in tissue culture media upon disruption of the cell membrane.[52, 53] Briefly, LDH was quantified by adding 50 µL of media and 50 µL of LDH detection reagent in a 96-well white plate and incubated for 30 min at room temperature. Next, the luminescence was read on a Synergy HTX multi-mode microplate reader (Biotek, VT, USA). Readings were normalized to cells grown on tissue cultures plate (TCP). The formula used to calculate percent viability was, $\% \, Viability = \left(\frac{Treatment}{TCP}\right) x \, 100$.

6.6.9 Macrophage Generation of Reactive Oxygen Species (ROS) on Nanostructures

RAW 264.7 macrophage-like cells were seeded at 2 x10^5/sample in a 48-well plate on the HTE-Ti and AR-Ti discs in 500µL of DMEM supplemented with 10% (v/v) FBS and incubated at 37°C 5%, CO_2 and 95% humidity for 24 h and 72 h. Next, the culture media was replaced with an equal volume of 10 µm 2',7'-Dichlorodihydrofluorescein diacetate (DCF-DA, Sigma, MA, USA) in PBS and incubated at 37°C, 5% CO_2 and 95% humidity for 30 min. Finally, the samples were washed with PBS and intracellular ROS was detected using a confocal laser scanning microscope (CLSM; Olympus, Tokyo, Japan). Cellular oxidized DCF, *2′,7′*-dichlorofluorescein (primarily by H_2O_2), was imaged using an excitation of 490 nm and emission of 520 nm and the corrected total cell fluorescence was determined from three random images per time-point, using ImageJ software version 1.53t (NIH, Maryland, USA).

6.6.10 Cell Morphology by SEM

Overnight cultures of *S. aureus* and co-cultures of *S. aureus* and RAW 264.7 macrophage-like cells incubated on HTE-Ti and AR-Ti samples were fixed for 1 h with 4% paraformaldehyde, 1.25% glutaraldehyde, and 4% sucrose in PBS. Following fixation, they were washed in PBS, followed by dehydration in ethanol, ascending from 50% (v/v) to 100% (v/v) and further chemically dried using hexamethyldisilazane (HMDS; Sigma-Aldrich, MO, USA). Samples were then mounted on aluminium stubs using carbon tape, sputter-coated with 5 nm platinum, and imaged using a Zeiss Merlin FEG-SEM (Zeiss, Jena, Germany).

6.6.11 Differential Gene Expression Analysis

Bacterial cells were retrieved from HTE-Ti and AR-Ti samples (n = 4), after 20 h at 37 °C following the same sonication and vortex method described for colony enumeration. The cell suspension was pelleted by centrifugation at 3000 g and resuspended in RNA extraction buffer, provided in the RiboPure™- Bacteria Kit (Life Technologies, ThermoFisher, MA, USA).

High throughput sequencing of samples was performed using MGI DNBSEQ G400 equipped with a PE100 flow cell (MGI Tech Co., Ltd, Shenzhen, China). Stranded polyA libraries were prepared using Tecan Universal Prokaryotic RNA-seq (Tecan Group Ltd, Männedorf, Switzerland). Illumina to MGI Library Conversion was done using MGIEasy Universal Library Conversion Kit (Part No. MGI1000004155, MGI Tech Co., Ltd, Shenzhen, China). Next, RNA-seq data pre-processing was carried out using an in-house pre-processing workflow, using MultiQC for quality reporting, alignment to the *S. aureus* assembly (GCA_000756205.1) using STAR,[54] and gene expression quantification using FeatureCounts.[55] Overall, alignment was good (~85%) and library sizes were large (over 12M/sample), making them suitable for downstream analysis in R. Differential gene expression (DE) analysis was completed using the Limma-Voom (v.3.52.0) method. [56, 57] Two different comparisons were defined to analyse genes that are differentially expressed across three conditions (planktonic vs AR-Ti or planktonic vs HTE-Ti). Significant differential expressed genes (DEGs) were identified for each comparison (FDR-adjusted p-value < 0.05).

6.6.12 Statistical Analysis

Graphical data was represented by mean and standard deviation. All statistical analysis were performed using GraphPad Prism version 9.0.0.0 for Windows (GraphPad Software, La Jolla California USA, www.graphpad.com). The water contact angle was analysed using a two-tailed unpaired t-test. Two-way ANOVA, corrected for multiple comparisons using the Bonferroni method, was used for live-dead viability, log reduction, LDH viability and ROS staining intensity analysis. A *p*-value ≤ 0.05 was deemed statically significant, and all experiments were performed in triplicate, except for *S. aureus* DGE analysis, which was $n = 4$.

6.7 Supporting Information

The Supporting Information is available free of charge at https://pubs.acs.org/doi/10.1021/acsabm.3c00351.

6.8 Acknowledgements

The authors acknowledge the funding and in-kind support from Corin Australia and the University of South Australia. The authors would also like to acknowledge the instruments assistance of Microscopy Australia, a facility that is funded by the University, and State and Federal Governments. We would also like to acknowledge the contribution of the South Australian Genomics Centre (SAGC) in the generation of data used in this publication. K.V. thanks NHMRC for Fellowship GNT1194466 and ARC for grant DP180101254

6.9 Conflict of Interest

All authors declare that they have no conflicts of interest.

6.10 Author Contributions

R.B., K.V., D.B., and conceptualized, designed, and planned the study. R.B. performed experiments and analyzed and interpreted the data. R.B., A.H., and K.V. wrote. and revised the paper. J.W. and D.P. performed the surface. characterization and participated in data analysis. K.V. supervised the study. All authors have read and agreed to the published version of the manuscript.

6.11 Data Availability Statement

The data that support the findings of this study are available from the corresponding author upon reasonable request.

6.12 Supplementary Information

The Interplay Between Immune and Bacterial Cells on a Biomimetic Nanostructured Surface – A 'Race for the Surface' Study

Richard Bright [1,*], Andrew Hayles [1], Jonathan Wood [2], Dennis Palms [1], Dan Barker [3] and Krasimir Vasilev [1,2*]

[1] College of Medicine and Public Health, Flinders University, Bedford Park, SA 5042, Australia.

[2] Academic Unit of STEM, University of South Australia, Mawson Lakes, Adelaide, SA 5095, Australia

[3] Corin Australia, Sydney, NSW 2153, Australia

[*] Correspondence: richard.bright@flinders.edu.au; krasimir.vasilev@flinders.edu.au

Table S1. *AFM post-analysis data on AR-Ti (A) and HTE-Ti surfaces (B).*

A

Moment-Based	
Average value:	5.694 µm
RMS roughness (Sq):	54.90 nm
RMS (grain-wise):	54.90 nm
Mean roughness (Sa):	39.68 nm
Skew (Ssk):	-0.6375
Excess kurtosis:	1.289
Order-Based	
Minimum:	5.506 µm
Maximum:	5.840 µm
Median:	5.699 µm
Maximum peak height (Sp):	0.146 µm
Maximum pit depth (Sv):	0.188 µm
Maximum height (Sz):	0.334 µm
Hybrid	
Projected area:	25.00 μm^2
Surface area:	25.84 μm^2
Volume:	142.4 μm^3
Variation:	5.370 μm^2
Inclination θ:	1.18 deg
Inclination φ:	0.43 deg

B

Moment-Based	
Average value:	5.606 µm
RMS roughness (Sq):	84.88 nm
RMS (grain-wise):	84.88 nm
Mean roughness (Sa):	67.20 nm
Skew (Ssk):	-30.22×10^{-3}
Excess kurtosis:	0.03875
Order-Based	
Minimum:	5.266 µm
Maximum:	5.935 µm
Median:	5.607 µm
Maximum peak height (Sp):	0.329 µm
Maximum pit depth (Sv):	0.340 µm
Maximum height (Sz):	0.669 µm
Hybrid	
Projected area:	25.00 μm^2
Surface area:	49.79 μm^2
Volume:	140.2 μm^3
Variation:	40.38 μm^2
Inclination θ:	4.39 deg
Inclination φ:	21.24 deg

Table S2. *Water contact angle on AR-Ti and HTE-Ti surfaces, mean ± SD, n =3 and p-value determined using an unpaired two-tailed t-test.*

Surface	Mean ± SD	*p*-value
AR-Ti	57.7 ± 3.1	
HTE-Ti	8.3 ± 3.5	$p < 0.0001$

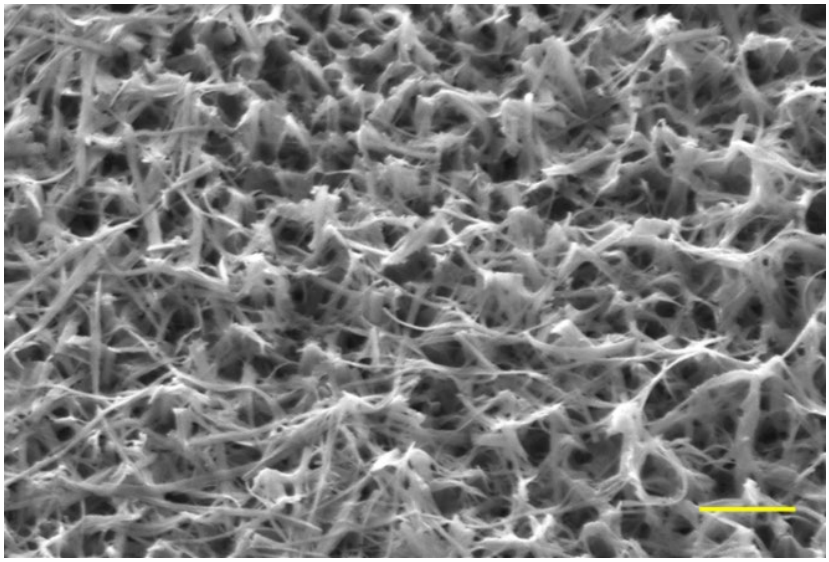

Figure S1. *SEM microphage of the HTE-Ti sample, validating removal of all bacteria after sonication/vortex method for CFU counts. Image acquired at 50 K magnification, 4 mm WD, 2 KV using secondary electron detector, scale bar represents 500 µm.*

Table S3. *Viability of S. aureus alone on AR-Ti and HTE-Ti surfaces, determined from live dead imaging, for days 1, 3 and 7. Before investigating competitive colonisation between S. aureus and macrophages, the baseline efficacy of HTE-Ti against S. aureus was measured using Live/Dead fluorescence analysis over 7 days. Data represents mean ± SD and p values.*

Day	AR-Ti	SD	HTE-Ti	SD	p -Value
1	94.8	1.0	34.4	4.3	<0.0001
3	94.8	3.0	15.1	3.3	<0.0001
7	95.8	2.3	36.2	2.7	<0.0001

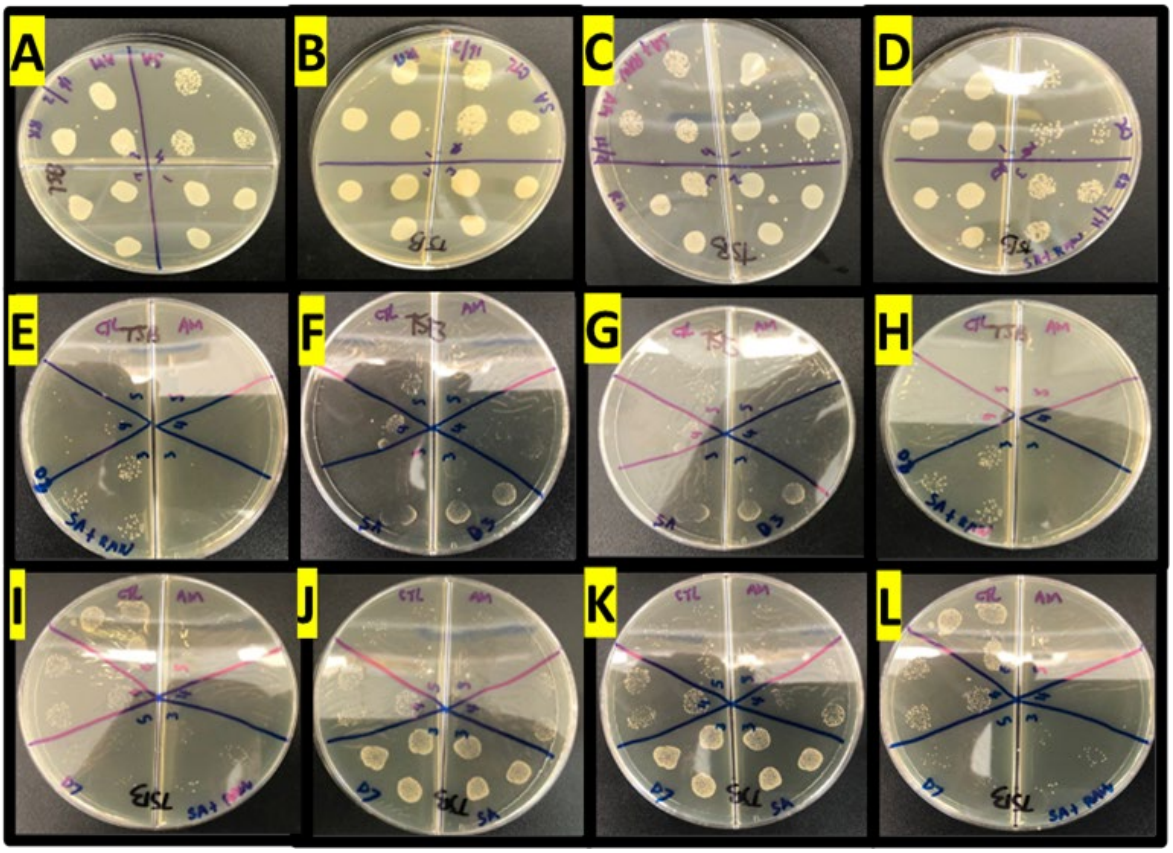

Figure S2. *Images of plates showing CFU for S. aureus alone and co-cultured with RAW 264.7 macrophage-like cells on AR-Ti or HTE-Ti discs. Day 1 (A – D), Day 2 (E – H and Day 7 (I – L).*

Table S4. *Log reduction of S. aureus alone and co-cultured with RAW 264.7 macrophage-like cells on HTE-Ti samples, mean ± SD and p-values.*

Day	*S. aureus*		S. aureus + RAW 264.7		
	Mean	SD	Mean	SD	p - values
1	1.6	0.1	2.6	0.1	0.0004
3	1.3	0.1	2.2	0.3	0.0018
7	1.1	0.2	3.6	0.4	<0.0001

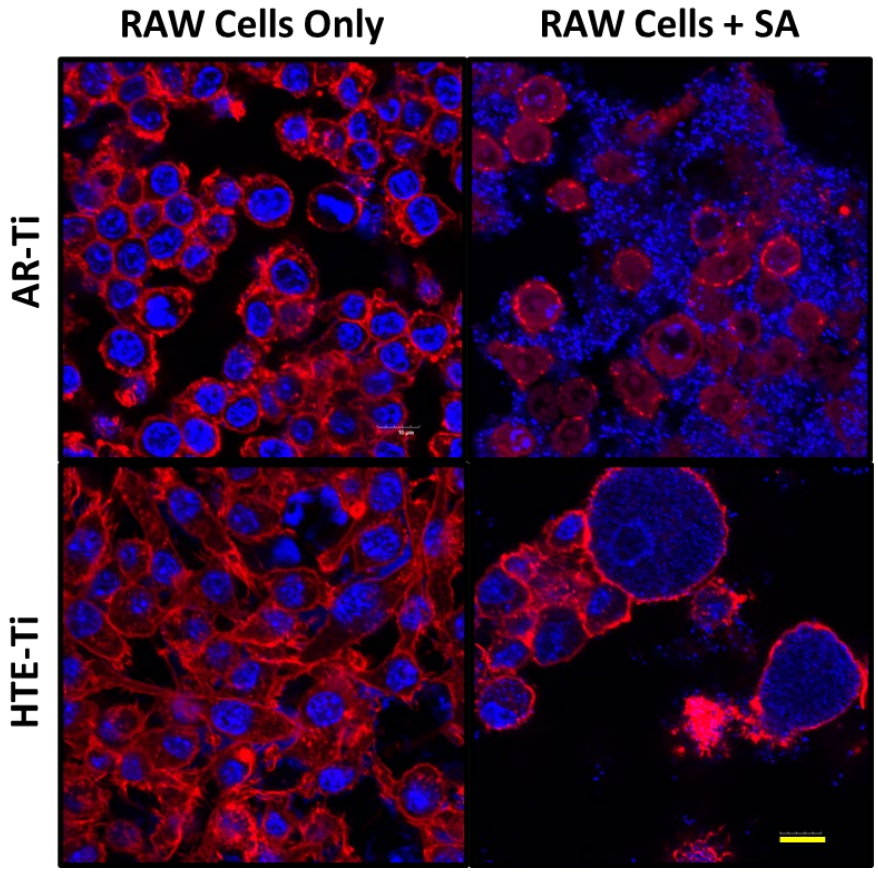

Figure S3. *Morphology of RAW 264.7 macrophage-like cells (RAW Cells Only) on AR-Ti and HTE-Ti surfaces, and co-cultures of RAW 264.7 macrophage-like cells and S. aureus at day 3, evaluated by actin staining with phalloidin (red) and nuclei counterstained with DAPI (blue). The scale bar represents 10 µm.*

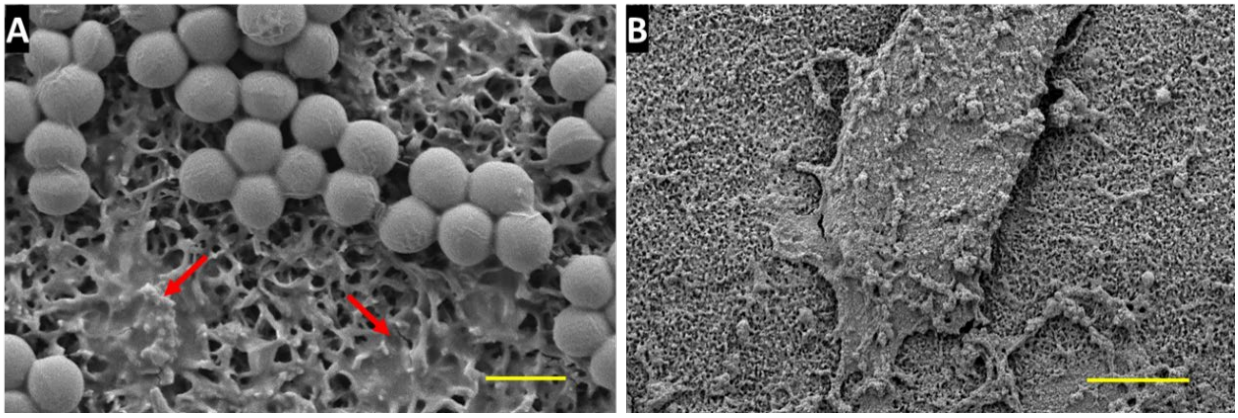

Figure S4. *SEM micrograph of S. aureus incubated on HTE-Ti surface at day 7, red arrows highlight dead bacteria and scale bar equal 1 µm (A), and a single RAW 264.7 macrophage-like cell co-cultured with S. aureus for 7 days. The surface of the cell appears to have bacteria embedded in the cell membrane; the scale bar represents 10 µm (B).*

Table S5. *Accession numbers for differential expression (DE) of S. aureus genes between AR-Ti and HTE-Ti samples. All genes differentially expressed were statistically significant p < 0.05, n = 4.*

Gene/Function	Expression			
	CTL		HTE	
	Regulation	Fold change	Regulation	Fold change
Cell Division				
Lytic transglycosylase *IsaA* KQ76_RS13190	Up	1.7	---	N/A
Amidase domain-containing protein KQ76_RS13615	Up	2.1	---	N/A
CHAP domain-containing protein KQ76_RS01150	Up	2.0	---	N/A
Amidohydrolase family protein KQ76_RS13245	Up	1.2	---	N/A
Glycine-glycine endopeptidase *LytM* KQ76_RS01125	Up	1.2	---	N/A
UDP-N-acetylmuramoyl-L-alanine D glutamase ligase *murD* KQ76_RS05595	Up	1.0	---	N/A
Amino-acid transaminase *DatD*	Up	1.4	---	N/A
Alanine racemase *Alr*	Up	0.6	---	N/A
Homoserine dehydrogenase *HSD*	Up	3.2	---	N/A
Capsule Biosynthesis				
Polysaccharide biosynthesis protein KQ76_RS08970	Up	1.0	---	N/A
Capsular polysaccharide type 5/8 biosynthesis protein *CapA* KQ76_RS00490	---	N/A	Down	0.8
Redox Defences				
Superoxide dismutase *SOD1* KQ76_RS07950	Up	2.4	---	N/A
Peptide-methionine (S)-S-oxide reductase *MsrA* KQ76_RS06935	Up	2.2	---	N/A
Toxins / Protease				
LukS-PV KQ76_RS07290	Up	2.3	Up	2.3
LukF-PV KQ76_RS07285	Up	2.4	---	N/A
Staphopain A KQ76_RS09980	Up	5.1	---	N/A
Staphopain B KQ76_RS04860	Up	5.6	Up	4.6

6.13 References

[1] a)M. Jamal, W. Ahmad, S. Andleeb, F. Jalil, M. Imran, M. A. Nawaz, T. Hussain, M. Ali, M. Rafiq, M. A. Kamil, J Chin Med Assoc 2018, 81, 7; b)M. Ribeiro, F. J. Monteiro, M. P. Ferraz, Biomatter 2012, 2, 176; c)V. Kandi, S. Vadakedath, Cureus 2020, 12, e12267.

[2] W. Zimmerli, P. Sendi, Semin Immunopathol 2011, 33, 295.

[3] a)C. R. Arciola, D. Campoccia, L. Montanaro, Nat Rev Microbiol 2018, 16, 397; b)U. Dapunt, G. M. Hänsch, C. R. Arciola, Materials (Basel) 2016, 9, 387.

[4] B. Li, T. J. Webster, J Orthop Res 2018, 36, 22.

[5] A. Trampuz, W. Zimmerli, Injury 2006, 37, S59.

[6] W. F. Oliveira, P. M. S. Silva, R. C. S. Silva, G. M. M. Silva, G. Machado, L. Coelho, M. T. S. Correia, J Hosp Infect 2018, 98, 111.

[7] A. M. Edwards, R. C. Massey, Trends Microbiol 2011, 19, 184.

[8] A. G. Gristina, Science 1987, 237, 1588.

[9] a)K. Vasilev, J. Cook, H. J. Griesser, Expert Rev Med Devices 2009, 6, 553; b)X. Yang, J. Hou, Y. Tian, J. Zhao, Q. Sun, S. Zhou, Sci China Technol Sci 2022, 65, 1000; c)K. Vasilev, Coatings 2019, 9, 654.

[10] D. P. Linklater, V. A. Baulin, S. Juodkazis, R. J. Crawford, P. Stoodley, E. P. Ivanova, Nature Reviews Microbiology 2021, 19, 8.

[11] a)E. P. Ivanova, J. Hasan, H. K. Webb, G. Gervinskas, S. Juodkazis, V. K. Truong, A. H. Wu, R. N. Lamb, V. A. Baulin, G. S. Watson, J. A. Watson, D. E. Mainwaring, R. J. Crawford, Nat Commun 2013, 4, 2838; b)C. M. Bhadra, V. Khanh Truong, V. T. H. Pham, M. Al Kobaisi, G. Seniutinas, J. Y. Wang, S. Juodkazis, R. J. Crawford, E. P. Ivanova, Scientific Reports 2015, 5, 16817.

[12] a)R. Bright, A. Hayles, J. Wood, N. Ninan, D. Palms, R. M. Visalakshan, A. Burzava, T. Brown, D. Barker, K. Vasilev, Nanomaterials 2022, 12, 1140; b)A. Hayles, J. Hasan, R. Bright, D. Palms, T. Brown, D. Barker, K. Vasilev, Materials Today Chemistry 2021, 22, 100622.

[13] A. Hayles, R. Bright, J. Wood, D. Palms, P. Zilm, T. Brown, D. Barker, K. Vasilev, Advanced Materials Interfaces 2022, 9, 2102353.

[14] a)R. Bright, A. Hayles, D. Fernandes, R. M. Visalakshan, N. Ninan, D. Palms, A. Burzava, D. Barker, T. Brown, K. Vasilev, ACS Appl Mater Interfaces 2021, 13, 38007; b)R. Bright, A. Hayles, J. Wood, D. Palms, T. Brown, D. Barker, K. Vasilev, Nano Lett 2022, 22, 6724.

[15] R. Bright, D. Fernandes, J. Wood, D. Palms, A. Burzava, N. Ninan, T. Brown, D. Barker, K. Vasilev, Mater Today Bio 2021, 13, 100176.

[16] K. Martins de Sousa, D. P. Linklater, B. J. Murdoch, M. Al Kobaisi, R. J. Crawford, R. Judge, S. Dashper, A. J. Sloan, D. Losic, E. P. Ivanova, ACS Applied Bio Materials 2023, Epub.

[17] C. F. Jones, R. D. Quarrington, H. Tsangari, Y. Starczak, A. Mulaibrahimovic, A. L. S. Burzava, C. Christou, A. J. Barker, J. Morel, R. Bright, D. Barker, T. Brown, K. Vasilev, P. H. Anderson, Clin Orthop Relat Res 2022, 480, 2232.

[18] D. M. Rivera-Chacon, M. Alvarado-Velez, C. Y. Acevedo-Morantes, S. P. Singh, E. Gultepe, D. Nagesha, S. Sridhar, J. E. Ramirez-Vick, J Biomed Nanotechnol 2013, 9, 1092.
[19] J. Kzhyshkowska, A. Gudima, V. Riabov, C. Dollinger, P. Lavalle, N. E. Vrana, J Leukoc Biol 2015, 98, 953.
[20] J. M. Anderson, A. Rodriguez, D. T. Chang, Semin Immunol 2008, 20, 86.
[21] J. E. Arce Miranda, J. L. Baronetti, M. G. Paraje, Eur J Clin Microbiol Infect Dis 2021, 40, 2563.
[22] D. Kosoff, J. Yu, V. Suresh, D. J. Beebe, J. M. Lang, Lab Chip 2018, 18, 3011.
[23] a)F. E. Pinotti, G. J. P. L. de Oliveira, M. A. T. Aroni, R. A. C. Marcantonio, E. Marcantonio Jr, Clinical Oral Implants Research 2018, 29, 963; b)T. L. Clainche, D. Linklater, S. Wong, P. Le, S. Juodkazis, X. L. Guével, J.-L. Coll, E. P. Ivanova, V. Martel-Frachet, ACS Applied Materials & Interfaces 2020, 12, 48272.
[24] H. Y. Tan, N. Wang, S. Li, M. Hong, X. Wang, Y. Feng, Oxid Med Cell Longev 2016, 2016, 2795090.
[25] X. Chen, Z. Zhong, Z. Xu, L. Chen, Y. Wang, Free Radic Res 2010, 44, 587.
[26] P. Wang, J. Geng, J. Gao, H. Zhao, J. Li, Y. Shi, B. Yang, C. Xiao, Y. Linghu, X. Sun, X. Chen, L. Hong, F. Qin, X. Li, J. S. Yu, H. You, Z. Yuan, D. Zhou, R. L. Johnson, L. Chen, Nat Commun 2019, 10, 755.
[27] M. Canton, R. Sánchez-Rodríguez, I. Spera, F. C. Venegas, M. Favia, A. Viola, A. Castegna, Front Immunol 2021, 12, 734229.
[28] M. Herb, M. Schramm, Antioxidants (Basel) 2021, 10, 313.
[29] a)J. Jenkins, J. Mantell, C. Neal, A. Gholinia, P. Verkade, A. H. Nobbs, B. Su, Nat Commun 2020, 11, 1626; b)M. Olivi, E. Zanni, G. De Bellis, C. Talora, M. S. Sarto, C. Palleschi, E. Flahaut, M. Monthioux, S. Rapino, D. Uccelletti, S. Fiorito, Nanoscale 2013, 5, 9023.
[30] A. J. F. Egan, J. Errington, W. Vollmer, Nature Reviews Microbiology 2020, 18, 446.
[31] L. Cavinato, E. Genise, F. R. Luly, E. G. Di Domenico, P. Del Porto, F. Ascenzioni, Frontiers in Microbiology 2020, 11, 326.
[32] B. Ezraty, A. Gennaris, F. Barras, J.-F. Collet, Nature Reviews Microbiology 2017, 15, 385.
[33] a)B. F. Cress, J. A. Englaender, W. He, D. Kasper, R. J. Linhardt, M. A. Koffas, FEMS Microbiol Rev 2014, 38, 660; b)T. J. Foster, J. A. Geoghegan, V. K. Ganesh, M. Höök, Nat Rev Microbiol 2014, 12, 49.
[34] a)J. Treffon, D. Chaves-Moreno, S. Niemann, D. H. Pieper, T. Vogl, J. Roth, B. C. Kahl, Cell Microbiol 2020, 22, e13158; b)M. H. Karavolos, M. J. Horsburgh, E. Ingham, S. J. Foster, Microbiology (Reading) 2003, 149, 2749.
[35] V. K. Singh, K. Singh, K. Baum, Antioxidants (Basel) 2018, 7, 128.
[36] A. L. Genestier, M. C. Michallet, G. Prévost, G. Bellot, L. Chalabreysse, S. Peyrol, F. Thivolet, J. Etienne, G. Lina, F. M. Vallette, F. Vandenesch, L. Genestier, J Clin Invest 2005, 115, 3117.

[37] M. Medale, D. Brutin, NPJ Microgravity 2021, 7, 30.
[38] B. Taciak, M. Białasek, A. Braniewska, Z. Sas, P. Sawicka, Ł. Kiraga, T. Rygiel, M. Król, PLoS One 2018, 13, e0198943.
[39] a)S. Zaatreh, K. Wegner, M. Strauß, J. Pasold, W. Mittelmeier, A. Podbielski, B. Kreikemeyer, R. Bader, PLoS One 2016, 11, e0151534; b)M. Martínez-Pérez, A. Conde, M. A. Arenas, I. Mahíllo-Fernandez, J. J. de-Damborenea, R. Pérez-Tanoira, C. Pérez-Jorge, J. Esteban, Colloids Surf B Biointerfaces 2019, 173, 876.
[40] M. Emmerson, New Horiz-Sci Pract 1998, 6, S3.
[41] a)P. Kumar, A. Nagarajan, P. D. Uchil, Cold Spring Harb Protoc 2018, 2018; b)M. C. Cox, R. Mendes, F. Silva, T. F. Mendes, A. Zelaya-Lazo, K. Halwachs, J. J. Purkal, I. A. Isidro, A. Félix, E. R. Boghaert, C. Brito, Sci Rep 2021, 11, 18571.
[42] A. Dobin, C. A. Davis, F. Schlesinger, J. Drenkow, C. Zaleski, S. Jha, P. Batut, M. Chaisson, T. R. Gingeras, Bioinformatics 2013, 29, 15.
[43] Y. Liao, G. K. Smyth, W. Shi, Bioinformatics 2014, 30, 923.
[44] a)M. E. Ritchie, B. Phipson, D. Wu, Y. Hu, C. W. Law, W. Shi, G. K. Smyth, Nucleic Acids Res 2015, 43, e47; b)C. W. Law, Y. Chen, W. Shi, G. K. Smyth, Genome Biol 2014, 15, 29.

7.1 Conclusions and Future Work

7.1 Conclusion

The growing demand for titanium-based implants has led to an increase in implant-associated infections and some instances poor integration. To address this issue, researchers are developing novel anti-infective technologies that can reduce the risk of infection and improve host integration. These technologies include the use of antimicrobial coatings, nanomaterials, and drug-eluting coatings. The nanoscale topography observed on cicada and dragonfly wings is being used as a model for the development of synthetic materials that can kill bacteria on contact. These materials are designed to mimic the nanostructures found on the wings of these insects, which are known to be effective at repelling bacteria and enhancing bone integration. Various approaches have been employed to duplicate and augment the efficacy of these innate antimicrobial surfaces.

One such method which is known as alkaline hydrothermal etching, is a cheap and moderately simple process used to etch a variety of materials, including silicon, gallium arsenide, and other semiconductor materials. The process involves immersing the material in a heated alkaline solution, typically sodium hydroxide (NaOH) or potassium hydroxide (KOH). The alkaline solution reacts with the material, causing it to etch away. The etching rate is typically controlled by adjusting the temperature and concentration of the alkaline solution. The purpose of this research project was to assess the suitability of hydrophilic hydrothermally etched nanostructured surfaces to be utilized for orthopaedic and dental implants. Strategies to enhance, suppress, or qualitatively shape the immune response are of importance for diverse biomedical applications such as biomaterials. This project will be aimed at further assessing the suitability of a hydrothermally etched nanomodified surface to be implemented on titanium-based implants to minimize implant-associated infection and enhance osteointegration.

This work consists of four aims. The first aim (chapter 2) was to investigate the role of etching time and the choice of cation (sodium and potassium) in the alkaline heat treatment on the topographical, physical, and bactericidal properties of the resulting modified titanium surfaces. Intriguingly, the NaOH surface was more effective at eliminating Gram-negative pathogens, while the KOH surface was more effective against the Gram-positive strains. The optimal etching times to effectively eliminate both gram-positive and gram-negative bacteria were 4 h for sodium hydroxide (NaOH) and 5 h for potassium hydroxide (KOH). Through this study, it was determined that a 5 h KOH treatment resulted in an optimal surface against both Gram-negative and Gram-positive bacteria. Subsequent experiments utilized this treatment (chapters 3 – 6).

The second aim (chapter 3) was to evaluate the load-dependent antibacterial efficacy of nanostructures inoculated with *Staphylococcus. aureus* or *Pseudomonas aeruginosa* at concentrations ranging from 10^2 to 10^9 colony-forming units per sample.

As expected, the bactericidal efficiency decreased with increasing bacterial concentrations, with decreases in bacterial viability noted for *Staphylococcus aureus* above 10^5 CFU/disc and 10^6 CFU/disc for *Pseudomonas aeruginosa.* Surprisingly, biofilm depth analysis revealed a decrease in bacterial viability in the 2µm layer furthest from the nanostructured surface. This work contributed to refining the most effective bacterial dosage for chapters 4-6.

The third aim (chapter 4) of the study was to evaluate the formation of biofilm on titanium discs with and without nanostructures, for 21 days after introducing *Pseudomonas aeruginosa* and *Staphylococcus aureus*. The nanostructured surface consistently demonstrated remarkable antibacterial properties throughout the entire duration of this longitudinal investigation. Upon observing that *S. aureus* exhibited a higher survival rate when incubated on the nanostructured surface compared to *P. aeruginosa*, the decision was made to utilize S. aureus in the fourth aim.

The fourth aim (chapter 5) involved examining the potential elimination of surviving *S. aureus* using a sub-clinical dose of vancomycin, a glycopeptide antibiotic. The findings revealed that when Staphylococcus aureus encountered surface nanostructures, it resulted in increased susceptibility of the pathogen to the antibiotic. This enhanced vulnerability was attributed to damage to the bacterial cell wall and compromised defence mechanisms against reactive oxygen species.

The final aim (chapter 6) was to investigate the interaction between macrophages and bacteria on the nanostructured surface to understand the outcome of the competitive process known as the 'race for the surface'. The results demonstrated that macrophages possess the ability to outcompete *Staphylococcus aureus* through multiple mechanisms. The early generation of reactive oxygen species by macrophages, the inhibition of bacterial virulence gene expression, and the bactericidal characteristics of the nanostructured surface all played a combined role in ensuring the triumph of macrophages in this competitive race. This study brings us a step closer to an in vivo model, with plans to conduct it using a rat model of implant infection.

In addition, various cell lines were evaluated for their biocompatibility throughout the study, including the THP-1 human leukemia monocytic cell line, RAW264.7 mouse macrophage, human dermal fibroblast (HDF), dental pulp stem cells, and MG63 osteoblast-like cells. Impressively, all these cell lines demonstrated outstanding biocompatibility and displayed anti-inflammatory potential when exposed to the nanostructured surface. Bacterial cells typically exhibit a significantly smaller size, ranging from 0.2 to 2.0 micrometres in diameter, in comparison to mammalian cells. Furthermore, bacterial cells possess a robust cell wall composed of peptidoglycan, providing structural integrity and protection against external factors. In contrast, mammalian cells lack a cell wall and are generally 10 to 100 times larger than bacterial cells. These distinctive characteristics allow mammalian cells to thrive on nanostructured surfaces while effectively eliminating bacteria upon contact.

This thesis delves into the exploration of hydrothermal etched nanostructures for designing, fabricating, and evaluating biomaterials with enhanced antibacterial properties and improved host integration. Furthermore, this research contributes to expanding our understanding and paves the way for the clinical implementation of these advancements.

7.2 Future Work

This thesis has focused extensively on validating HTE-Ti as an effective surface modification for reducing implant-associated infections and improving osseointegration. The findings presented in this study demonstrate promising potential. However, before large-scale commercialization can commence, additional data is required. The following points highlight key areas of future research necessary to successfully translate this promising technology into clinical practice:

1. *Comprehensive Validation*: Additional research is necessary to thoroughly validate the efficacy of HTE-Ti as a surface modification for combating infections and its potential to enhance osseointegration. This entails conducting comprehensive studies utilizing various implant materials, designs, and infection models to assess their performance in diverse scenarios.
2. *Infection Prevention Strategies*: Exploring the synergistic effects of HTE-Ti with other infection prevention strategies, such as antimicrobial coatings or drug-eluting materials, can enhance its anti-infective properties. Investigating combination therapies can provide valuable insights into developing more robust implant systems.
3. *Biocompatibility Assessment*: Conducting thorough biocompatibility studies is essential to ensure that HTE-Ti does not induce adverse reactions or compromise the host's immune response. Detailed evaluations of the material's interaction with surrounding tissues, inflammation levels, and long-term biocompatibility are crucial steps in establishing its safety profile.
4. *In Vitro Models*: While the existing data exhibits promising findings, the primary consideration when evaluating a novel biomaterial revolves around its safety and effectiveness within the intended biological application. In this thesis, comprehensive cytocompatibility assessments have been performed using diverse mammalian cell lines to evaluate their interaction with the HTE-Ti surface. Encouragingly, these interactions have resulted in positive outcomes, with no significant decrease in cell viability observed. However, it is important to note that these results alone do not offer a comprehensive understanding of the surface's biosafety. It is imperative to explore the biocompatibility of the surface within the intricate environment of a mammalian host.

   The interplay between blood components on the HTE-Ti surface holds promise for enhancing bactericidal performance through strengthened attachment between bacteria and the nanoscale protrusions. However, it is important to acknowledge that in an in vivo environment, the interaction of blood components, such as cells and proteins, may have an opposing effect by covering or concealing the nanoprotrusions, potentially reducing their effectiveness. Although cytocompatibility measurements on mammalian cell lines have shown promising results. Conducting additional research is crucial to assess the biocompatibility and bactericidal effectiveness of the HTE-Ti surface in animal models.

This emphasizes the importance of conducting appropriate animal studies to gather valuable insights and address essential questions before progressing to human clinical trials.

5. *Clinical Trials*: Rigorous clinical trials involving a diverse patient population and different types of implants are necessary to evaluate the safety and efficacy of HTE-Ti in real-world settings. These trials should assess infection rates, patient outcomes, implant stability, and the overall performance of HTE-Ti over an extended period.
6. *Long-Term Follow-up*: Long-term monitoring of patients with HTE-Ti-modified implants is crucial to assess the durability of the surface modification and its long-lasting effects on infection prevention and osseointegration. This data would provide insights into its performance and efficacy over extended periods of implantation.
7. *Standardization and Regulation*: Developing standardized protocols and guidelines for the production, characterization, and clinical application of HTE-Ti is essential. Engaging regulatory authorities early in the process will help ensure compliance with safety, quality, and ethical standards, facilitating its eventual regulatory approval and commercialization.
8. *Cost-effectiveness Analysis*: Performing thorough cost-effectiveness analyses is crucial to assess the economic feasibility of HTE-Ti biomaterials as a viable solution on a larger scale. Evaluating the potential reduction in healthcare costs associated with infections and analysing the economic impact on healthcare systems are essential steps for the successful adoption of these materials in the market.

By addressing these research areas, we can bridge the gap between the current promising evidence and the realization of HTE-Ti nanostructured implants as a clinical reality. Ultimately, this technology has the potential to significantly minimize implant-associated infections, enhance osseointegration, and improve patient outcomes in numerous clinical settings.

COMPENDIUM OF CO-AUTHORED PAPERS PUBLISHED THROUGHOUT MY PHD JOURNEY

1. Visalakshan RM, **Bright R**, Burzava ALS, Barker AJ, Simon J, Ninan N, Palms D, Wood J, Martínez-Negro M, Morsbach S, Mailänder V, Anderson PH, Brown T, Barker D, Landfester K, Vasilev K. Antibacterial Nanostructured Surfaces Modulate Protein Adsorption, Inflammatory Responses, and Fibrous Capsule Formation. ACS Appl Mater Interfaces. 2023 Jan 11;15(1):220-235. doi: 10.1021/acsami.2c13415. Epub 2022 Nov 23. PMID: 36416784.

2. Hayles, A., **Bright, R**., Hasan, J., Wood, J., Palms, D., Barker, D., Vasilev, K., Dual Species Bacterial Challenge of a Biomimetic Nanostructured Surface. Adv. Mater. Interfaces 2022, 9, 2201583. https://doi.org/10.1002/admi.202201583

3. Hasan J, **Bright R**, Hayles A, Palms D, Zilm P, Barker D, Vasilev K. Preventing Peri-implantitis: The Quest for a Next Generation of Titanium Dental Implants. ACS Biomater Sci Eng. 2022 Nov 14;8(11):4697-4737. doi: 10.1021/acsbiomaterials.2c00540. Epub 2022 Oct 14. PMID: 36240391.

4. Wood J, Hayles A, **Bright R**, Palms D, Vasilev K, Hasan J. Nanomechanical tribological characterisation of nanostructured titanium alloy surfaces using AFM: A friction vs velocity study. Colloids Surf B Biointerfaces. 2022 Sep; 217:112600. doi: 10.1016/j.colsurfb.2022.112600. Epub 2022 May 30. PMID: 35665641.

5. Jones CF, Quarrington RD, Tsangari H, Starczak Y, Mulaibrahimovic A, Burzava ALS, Christou C, Barker AJ, Morel J, **Bright R**, Barker D, Brown T, Vasilev K, Anderson PH. A Novel Nanostructured Surface on Titanium Implants Increases Osseointegration in a Sheep Model. Clin Orthop Relat Res. 2022 Nov 1;480(11):2232-2250. doi: 10.1097/CORR.0000000000002327. Epub 2022 Aug 24. PMID: 36001022.

6. Hayles, A., **Bright, R**., Wood, J., Palms, D., Zilm, P., Brown, T., Barker, D., Vasilev, K., Spiked Nanostructures Disrupt Fungal Biofilm and Impart Increased Sensitivity to Antifungal Treatment. Adv. Mater. Interfaces 2022, 9, 2102353. https://doi.org/10.1002/admi.202102353

7. Hayles, A.; Hasan, J.; **Bright, R**.; Wood, J.; Palms, D.; Zilm, P.; Barker, D.; Vasilev, K. Spiked Titanium Nanostructures That Inhibit Anaerobic Dental Pathogens. ACS Applied Nano Materials 2022.

8. A. Hayles, J. Hasan, **R. Bright**, D. Palms, T. Brown, D. Barker, K. Vasilev, Hydrothermally etched titanium: a review on a promising mechano-bactericidal surface for implant application. Materials Today Chemistry, Volume 22, 2021, 100622,ISSN 2468 5194,https://doi.org/10.1016/j.mtchem.2021.100622.